Durham E-Theses

Synthesis and characterization of alkali-metal reduced polycyclic aromatic hydrocarbon based materials

STEFANCIC, ALES

Synthesis and characterization of alkali-metal reduced polycyclic aromatic hydrocarbon based materials

Aleš Štefančič

A Thesis presented for the degree of

Doctor of Philosophy

Department of Chemistry

Durham University

July 2017

Synthesis and characterization of alkali-metal reduced polycyclic aromatic hydrocarbon based materials

Aleš Štefančič

Submitted for the degree of Doctor of Philosophy

July 2017

Abstract

The reduction chemistry of polycyclic aromatic hydrocarbon (PAH) based materials is well established and has been investigated for more than a century. A frequently applied reduction method is treatment of the PAH by alkali metals, where an electron from the alkali metal is transferred to the π-system of the PAH. Recently it has been found that these reduced species can possess intriguing magnetic and electronic properties in the solid state, e.g. pentacene derivatives are excellent organic semiconductors and triphenylides are low-dimensional antiferromagnets.

This topic has also attracted considerable attention since superconductivity was reported in alkali-metal reduced PAHs synthesised by solid-state techniques. However, the unavailability of well-crystalline and single-phase materials, which would permit the unambiguous identification of the superconducting phase and disclose the origin of superconductivity, has severely hindered progress in this research direction.

In this thesis the reduction of PAHs with potassium, rubidium and caesium metals was carried out in aprotic coordinating organic solvents. Single crystalline and polycrystalline phase-pure, solvent containing- and solvent-free reduction products were successfully isolated for the first time. Crystal structures were determined with single-crystal and powder X-ray diffraction, magnetism was studied with Superconducting Quantum Interference Device (SQUID) magnetometry and electron paramagnetic resonance (EPR) spectroscopy, and charge transfer was followed with infrared (IR) and Raman spectroscopies. The synthesised materials exhibit a variety of magnetic properties, spanning canted-antiferromagnetism, ferromagnetism, low-dimensional magnetism and diamagnetism. A detailed structural analysis was performed in order to establish magnetostructural correlations. This study has expanded the family of well characterised alkali-metal reduced PAH based materials and gives an insight into the structures and magnetism of this family of compounds.

Declaration

I hereby declare that no part of this thesis has been submitted elsewhere for any other degree or qualification and it is all my own work unless referenced to the contrary in the text.

Signature:

Acknowledgments

Table of Contents

List of Figures

1 Chapter 1 – Introduction

1.1 Polycyclic aromatic hydrocarbons

Polycyclic aromatic hydrocarbons (PAHs) are organic nonpolar compounds consisting of six-membered rings fused together. The carbon atoms comprising those rings are sp^2-hybridised, forming fully conjugated and planar molecules. Some of the known PAHs are presented in Figure 1. The smallest PAH is called naphthalene (**1** in Figure 1) and is composed of two benzene rings. PAHs comprising three benzene rings possess trivial names, they are called anthracene (**2**) and phenanthrene (**3**) and some of those made up from four benzene rings are tetracene (**4**), chrysene (**6**), triphenylene (**7**) and pyrene (**5**). As it is apparent, benzene rings can be fused together in different fashions and establish a family of molecules with a variety of shapes and sizes.
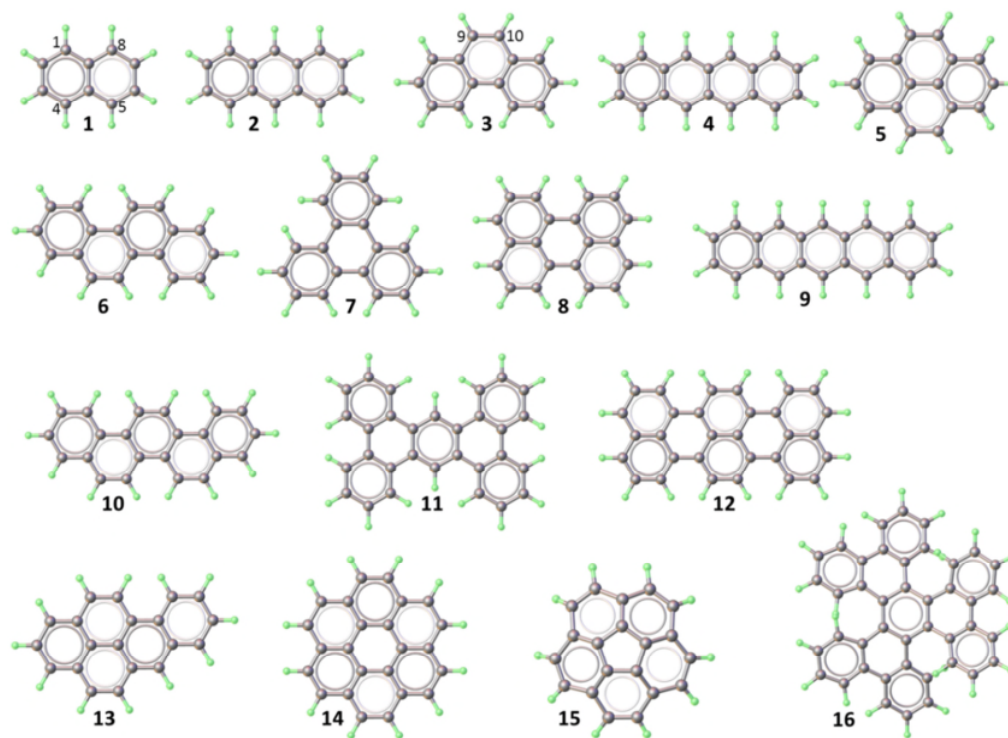
Figure 1: Representation of some known PAHs. Carbon atoms are shown as grey spheres, while hydrogen atoms are shown as pale green spheres. The benzene rings containing dark grey, pale grey and no circles contain three, two/one and zero double bonds, respectively, in the resonant structure with the highest amount of fully benzenoid rings.

According to IUPAC nomenclature [1] names of bigger PAHs can be derived from benzene or the trivial names of small PAHs. For instance, by adding three benzene rings to a phenanthrene molecule at three different positions (denoted with Latin letters) the name of tribenzo[c,fgh,j]phenanthrene can be derived as shown in Figure 2. However, PAHs can be very big molecules, composed of a large number of benzene rings (> 40), where the naming becomes difficult to manage. Therefore, alternative names such as supernaphthalene [2] and superphenalene [3,4] are used in the literature for big PAHs that resemble naphthalene and phenalene.
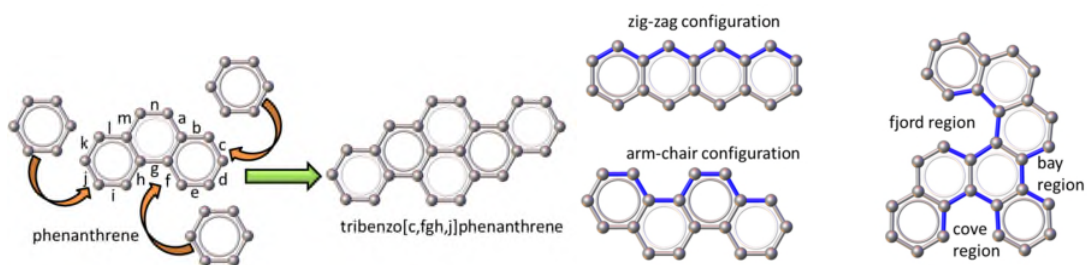
Figure 2: Constructing a tribenzo[c,fgh,j]phenanthrene by adding three benzene rings to phenanthrene and naming it according to IUPAC nomenclature.

Figure 3: The periphery of PAHs represented by colouring of C-C bonds in blue.

Benzene rings can be fused together in a variety of fashions, forming different types of peripheries of PAH molecules such as zig-zag and arm-chair configurations, and bay, cove and fjord regions as depicted in Figure 3. The geometry of fused benzene rings has a profound influence on their stability/reactivity and they can be divided into acenes, phenacenes, K-region PAHs, rylenes, fully benzenoide PAHs and non-planar PAHs. These six groups of PAHs show a different degree of aromaticity, which determines the stability of PAH systems. The term 'aromaticity' is more than 150 years old [5,6,7] and is yet not fully investigated and understood, and therefore remains an active research topic [8, 9, 10, 11, 12, 13]. At this stage it is worth citing Milan Randić [8]: *'There is no doubt that the term "aromaticity" is one of the most widely used terms in chemistry. At the same time, "aromaticity" may well be one of the most widely misused terms in chemistry, not by being attributed to compounds that do not qualify as aromatic, but by becoming so unspecified that it is applied to too many compounds*

that show widely different physico-chemical properties.' The scope of thesis in terms of this aromaticity is going to be limited to Clar's rule [14] in order to present the stability of different PAHs. According to this rule, the systems where the highest amount of π-electrons can be grouped in sextets, $6n$, are going to be most stable.

Acenes represent a group of PAHs where benzene rings are fused in a linear way forming a zig-zag edge configuration, PAHs **1, 2, 4** and **9** in Figure 1. By drawing a resonance structure as shown in Figure 4, only one benzene ring can possess a sextet of π-electrons. Low aromatic stabilisation results in a high reactivity of acenes. Actually they are the most reactive among all the six groups stated above and their reactivity increases with increasing amount of benzene rings. For example, pentacene (**9**) is considerably air sensitive, because it oxidises to 6,13-pentacenequinone, changing from purple to green colour.
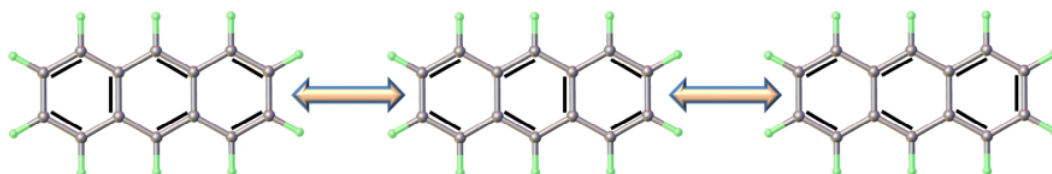
Figure 4: Three possible resonance structures of anthracene (**2**) showing that only one ring can possess six π-electrons, while the other two rings possess only four per ring. Colour code: C grey and H pale green.

In phenacenes, the benzene rings form an armchair edge configuration as shown in Figure 3. According to resonance structures every second benzene ring contains a sextet of π-electrons, and therefore, phenacenes are more stable than acenes due to additional aromatic stabilisation. The middle benzene ring in phenanthrene (**3**) possesses two π-electrons and forms a so-called K-region which is chemically reactive. Therefore, the 9 and 10 positions are susceptible for oxidation, halogenation and reduction. Phenanthrene (**3**), chrysene (**6**) and picene (**10**) (Figure 1) are some representatives of the phenacene family.

The rylenes can be viewed as polynaphthalenes, where two or more naphthalene molecules are fused together either on 1 and 8 or 4 and 5 positions (Figure 1). In terms

of aromatic stability they can be placed between acenes and phenacenes. Perylene (**8**) and terrylene (**12**) shown in Figure 1 belong to the rylene family.

The K-region PAHs, such as pyrene (**5**) and coronene (**14**) depicted in Figure 1, can be viewed as phenanthrene and perylene with additional benzene rings annulated in their bay regions. Their aromatic stability is approximately the same as that observed in phenacenes.

Fully benzenoid PAHs possess the highest aromaticity and are, therefore, the most stable. These PAHs consist solely of benzene rings containing either benzene rings with π-electron sextets or rings without π-electrons in their resonant structures. Triphenylene (**7**) and tetrabenzoanthracene (**11**), shown in Figure 1, are two representatives of the fully benzenoid PAH family.

The stability of PAHs can be also followed by ultraviolet-visible spectroscopy. The higher energy needed for exciting electrons from the HOMO (highest occupied molecular orbital) to the LUMO (lowest unoccupied molecular orbital) implies higher aromatic stability [15]. The absorption p-bands (corresponding to this excitation) for tetracene (4), chrysene (6), pyrene (5) and triphenylene (7), the members of different PAH families with the same number of benzene rings, are 480, 320, 334 and 285 nm respectively. This indicates that triphenylene with three fully benzenoid rings requires more energy for its electrons to be excited from the HOMO to the LUMO than tetracene with only one fully benzenoid ring. The absorption bands and fluorescence bands of most PAHs shown in Figure 1 are gathered in Table 1.

Table 1: The absorption and fluorescence bands of selected PAHs [15].

PAH	Absorption (nm)	Fluorescence (nm)
Anthracene (**2**)	380; 255	400; 500
Tetracene (**4**)	480; 285	475; 513; 555
Pentacene (**9**)	600; 300	610
Phenanthrene (**3**)	330; 293; 345	350
Chrysene (**6**)	320; 267; 360	374; 388
Picene (**10**)	330; 287; 386	380
Perylene (**8**)	440; 255	435; 465
Terrylene (**12**)	560; 270	575; 612
Pyrene (**5**)	334; 272; 372	370; 400
Coronene (**14**)	340; 305; 375	420; 500
Triphenylene (**7**)	285; 260; 320	355; 370
Dibenzopyrene (**11**)	329; 289; 376	383

The characteristic absorption and fluorescence spectra of individual PAHs can serve as a fingerprint for unambiguous determination of that particular compound [16, 17].

Non-planar PAHs can be realised by either introducing a five-member ring or fjord/cove region. The former causes the curvature of PAHs, e.g., exchanging the six-member ring with a five-member one in the middle of coronene (**14**) yields bowl shaped corannulene (**15**). By adding 12 five-member rings the carbon sheet bearing the conjugated electron system can be closed into sphere-shape fullerenes. The introduction of fjord region (comprised of six carbon atoms, as shown in Figure 3) induces the steric crowding of hydrogen atoms, which causes the twisting of the whole PAH molecule and the formation of the so-called helicene structure. The representative of bowl shape PAHs, corannulene (**15**), and fjord region PAHs, hexabenzotriphenylene (**16**) are depicted in Figure 1.

When PAHs are assembled in a crystal structure they adopt specific packing motifs because of $\pi\cdots\pi$ interactions. The π system above and below the benzene rings in PAHs consists of delocalised electrons, and therefore, possesses a negative charge ($\pi^{\delta-}$), while hydrogen atoms in the benzene ring plane possess a positive charge ($H^{\delta+}$). This leads to a quadrupole charge distribution as shown in Figure 5a. This charge distribution establishes two attractive and one repulsive interactions between neighbouring PAH units when changing the orientation of the molecules. Attractive force arises in edge-to-face or T-shape and offset face-to-face or slipped stacking and

repulsive in face-to-face or eclipsed face-to-face stacking as depicted in Figure 5b, 5c and 5d, respectively [18, 19,20].
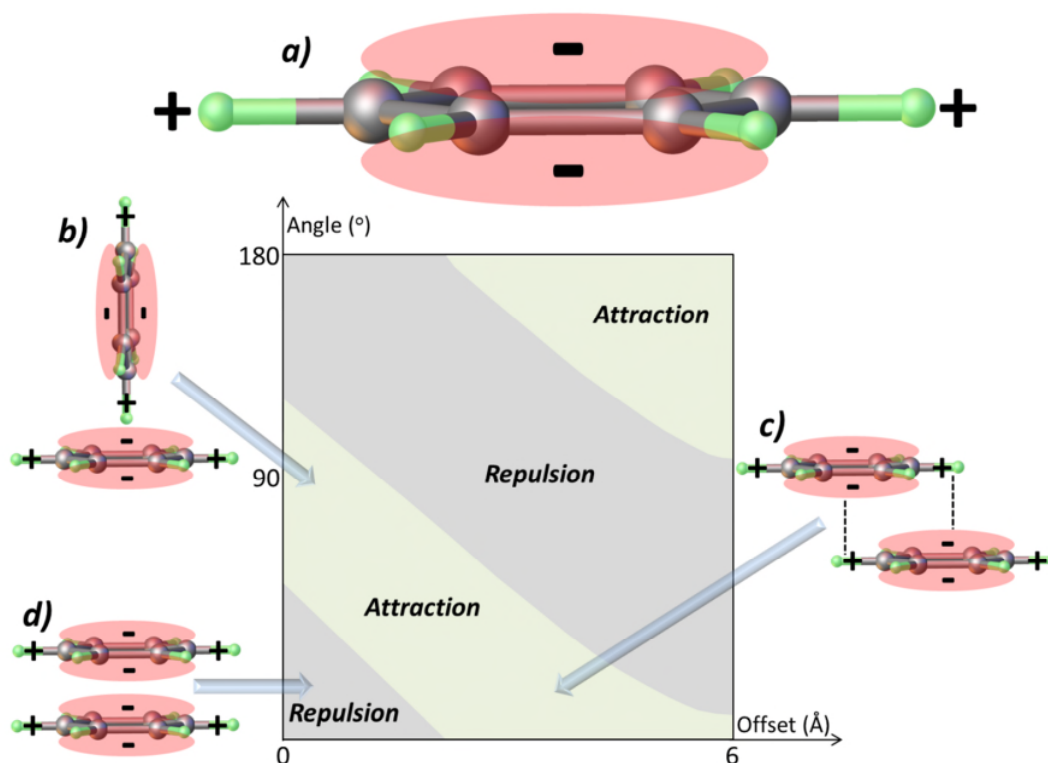
Figure 5: a) a quadrupole charge distribution in a benzene molecule. Pale red ellipsoids above and below the benzene ring plane show delocalised electrons in a π-cloud. The positive charges of the hydrogen atoms in the benzene ring plane are also shown. b), c) and d) represent edge-to-face, offset face-to-face and face-to-face interactions, respectively. The chart in the middle depicts the attractive and repulsive interactions between two PAH molecules as a function of orientation [19]. Colour code: C grey and H pale green.

The above stated interactions result in four basic packing motifs; herringbone, sandwich-herringbone, gamma (γ) and beta (β), observed in PAHs [18, 21, 22]. The majority of planar PAHs, such as acenes and phenacenes, adopt a herringbone packing motif. For instance, this most common packing motif is observed in naphthalene as shown in Figure 6 (upper left panel). The naphthalene molecules are tilted at *ca.* 51° with respect to each other, where hydrogen atoms face the π cloud of neighbouring molecules. Therefore, the edge-to-face interactions, $H^{\delta+}\cdots\pi^{\delta-}$, are predominant in the herringbone packing motif. Some other PAHs adopting a herringbone packing motif

6

reported in the literature [21] are anthracene (**2**), phenanthrene (**3**), triphenylene (**7**), benzanthracene, chrysene (**6**), benzo[c]phenanthrene, picene (**10**) and dibenzanthracene.

The sandwich-herringbone packing motif was observed in pyrene as depicted in Figure 6 (right upper panel). Two pyrene molecules form a sandwich-like arrangement, where these two molecules are offset by ca. 1.7 Å, enabling offset face-to-face interactions. Furthermore, the pyrene molecules in the first sandwich-like arrangement face the other pyrene molecules in a neighbouring sandwich-like arrangement at an angle of ca. 83°, establishing edge-to-face interactions. Based on this, it can be concluded that offset face-to-face and edge-to-face interactions are present in the sandwich-herringbone packing motif. Additional PAHs adopting the sandwich-herringbone packing motif are perylene (**8**), benzperylene, dinaphthoanthracene and quaterrylene [21].
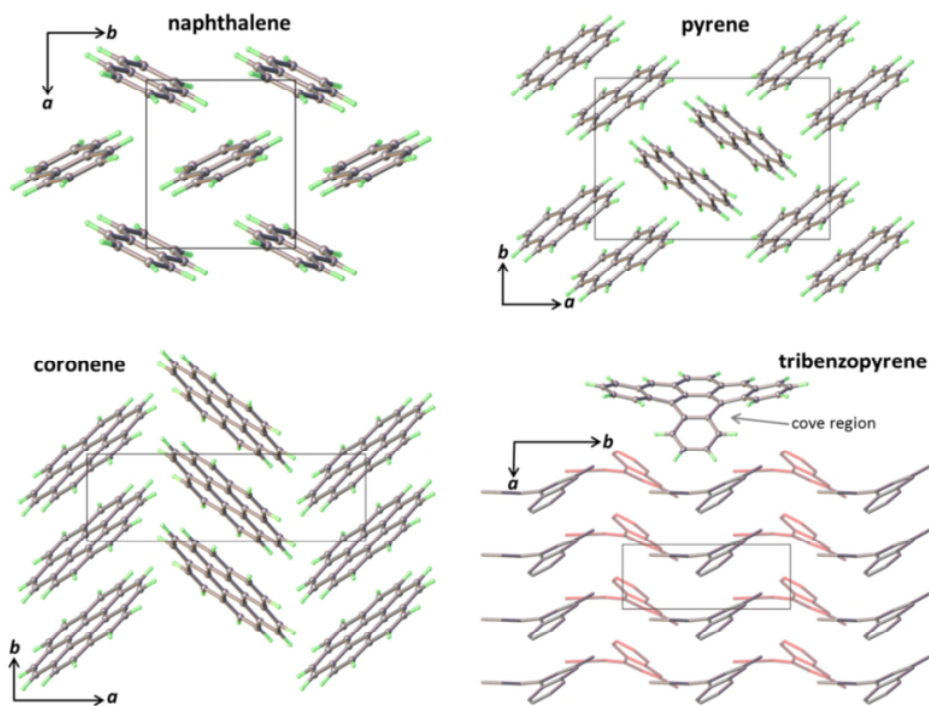
Figure 6: Representation of four basic packing motifs observed in PAHs: herringbone in naphthalene (upper left panel), sandwich-herringbone in pyrene (upper right panel), gamma (γ) in coronene (bottom left panel) and beta (β) in tribenzopyrene (bottom right panel) [21]. All structures are projected along the [001] crystallographic direction. Hydrogen atoms are omitted, C-C bonds are presented as tubes and neighbouring stacks are shown in red for clarity in tribenzopyrene packing motif. Colour code: C grey and H pale green.

The bottom left panel in Figure 6 represents the gamma (γ) packing motif in the crystal structure of coronene (**14**). The neighbouring coronene molecules that form chains along the crystallographic *b* direction are shifted by ca. 3.2 Å, indicating that the offset face-to-face interactions are the predominant one in this packing motif. Additional stabilisation of the crystal structure is achieved by the edge-to-face interactions between coronene molecules in neighbouring chains. This packing motif was also observed in benzopyrene (**13**), dibenzoperylene, benzobisanthrene, dibenzocoronene, ovalene, hexabenzocoronene and kekulene [21].

The beta (β) packing motif is formed in PAHs where strong offset face-to-face interactions are present and edge-to-face interactions do not contribute much to the stabilisation of the crystal structure. This packing motif is mainly observed in non-planar PAHs, such as tribenzopyrene, where the non-planarity originates from cove regions as shown in Figure 6 (bottom right panel). Violanthrene, tetrabenzoperylene, diphenanthroperylene, anthrabenzonaphthopentacene and diperinaphthyleneanthracene are also some representatives, where the packing motif was found [21].

The semiconducting nature of polycyclic aromatic hydrocarbons and their derivatives undoubtedly renders them as one of the most outstanding and promising materials of our time. Their use is growing exponentially in research fields of optical dyes [23, 24, 25], liquid crystals [4, 26, 27, 28] and organic electronics [29, 30, 31, 32], such as photovoltaic [33, 34], organic field-effective transistors (OFETs) [35, 36], organic light-emitting diodes (OLEDs) [37, 38, 39] and molecular electronics [40, 41, 42, 43, 44]. Organic electronics, spanning organic solar cells, OFETs, OLEDs and molecular electronics, is arguably one of the hottest research topics in chemistry. This topic is rapidly evolving especially due to demands of industry, and a variety of compounds, described in the above literature, are already integrated in devices.

Despite all the outstanding properties found in those materials, the PAHs also have a grim side, which throws a shadow on the above stated research topics. The correlation between PAHs and human cancer dates back to 1775, when Sir Percival Pott (surgeon to St. Bartholomew's Hospital in London) linked the high occurrence of scrotal cancer in chimney sweepers with occupation exposure to soot [45], which is known to contain

a variety of PAHs. In the last century there were numerous studies investigating the influence of PAHs on the development of cancer in humans [46, 47, 48]. Thus far it was established that several PAHs are genotoxic and induce mutations, while smaller PAHs are co-carcinogens that affect cancer progression and promotion. The genotoxicity is connected with the structure of the PAH molecule, although it is still a subject of debate [47]. PAHs containing bay, K and fjord regions can be metabolised by enzymes to diol epoxides, quinolones and radical cations, which form adducts with DNA molecule [46, 48, 49, 50], as shown in Figure 7. Small PAHs with 2 to 4 fused benzene rings can dysregulate gap junction channels, preventing normal cell division, and therefore, initiate cancerous cell replication [52]. Several PAHs, *e.g.* naphthalene (**1**), phenanthrene (**3**), pyrene (**5**), anthracene (**2**), chrysene (**6**), coronene (**14**), acenaphthene, acenaphthylene, benzo[a]anthracene, benzo[a]pyrene (**13**), benzo[e]pyrene and dibenzo[a,e]pyrene, are listed, regulated and monitored by the European Food Safety Authority, the Agency for Toxic Substances and the Disease Registry and Environmental Protection Agency, due to proven carcinogenicity of these PAHs. The health risk associated with PAHs and their accessibility, *i.e.* they can be found in fossil fuels, or produced by incomplete combustion of organic compounds, renders them as one of the major pollutants [53,54].
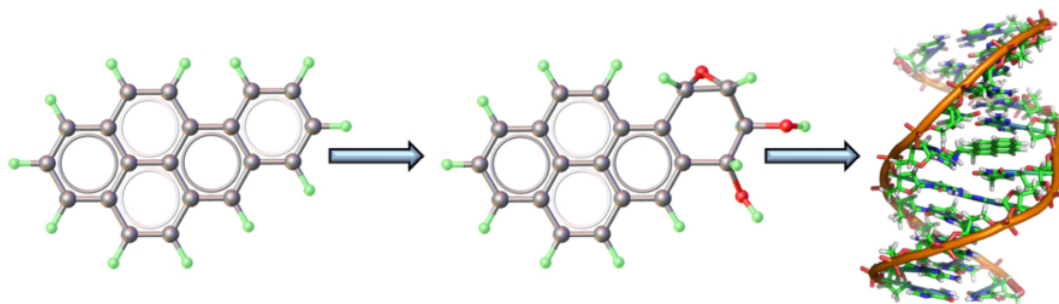
Figure 7: A schematic interpretation of mutagenic effect of benzo[a]pyrene. Benzo[a]pyrene (left side) is metabolised by enzymes to benzo[a]pyrene-7,8-dihydrodiol-9,10-epoxide (middle), which forms an adduct with DNA molecule (right side [51]).

1.2 Reduction chemistry of PAHs and magnetic properties of radical anions

The reduction chemistry of PAHs is more than a century old and Wilhelm Johann Schlenk (1879-1943) is one of the most well-known pioneers of this chemistry. He synthesised the first alkali-metal reduced PAH (disodium anthracide) in 1914, by reacting two moles of sodium with one mole of anthracene in diethyl ether [55]. It has to be noted that all alkali-metal reduced PAHs are extremely air-sensitive and due to this Wilhelm Schlenk designed special glassware, allowing him to manipulate air-sensitive materials [56]. Actually, the glassware he designed made him one of the most recognisable men among chemists, because every chemist is acquainted with the 'Schlenk line' and 'Schlenk techniques'. A brief description of his scientific path is described in the literature, Wilhelm Schlenk: The Man Behind the Flask [57].

In the following decades the reduction chemistry of PAHs developed into an interesting research topic, where two main streams were followed. The first stream was the synthesis of PAH radical anions and their investigation using ultraviolet-visible spectroscopy and conduction measurements, while the second stream was the usage of the radical anions as precursors for synthesis of PAH derivatives (*e.g.* via Birch reduction) and as strong reducing agents [58, 59, 60, 61, 62, 63, 64, 65, 66, 67]. The synthesis of radical anions and dianions of PAHs can be achieved if one of the reactants and product is soluble in a chosen solvent, therefore two synthetic paths are usually utilised. The most commonly used is the reaction of alkali or alkaline earth metals with PAHs in aprotic coordinating organic solvents, *e.g.* diethyl (Et_2O) and dimethyl (Me_2O) ether, tetrahydrofuran (THF), dimethoxyethane (DME, glyme), bis(2-methoxyethyl) ether (diglyme), tetramethylethylenediamine (TMEDA) and pentamethyldiethylenetriamine (PMDTA). In this case PAHs are completely or partially soluble and the reduced species are completely soluble, meaning that the reaction occurs on the surface of the metal. Therefore, the surface of the metal needs to be oxide- and hydroxide-free. The second path involves the dissolution of alkali and alkaline earth metals and reduced species. This can be achieved in protic strongly coordinating solvents such as liquid ammonia and methylamine. However, the reduced species act as a very strong base and can abstract the hydrogen atom (proton) from

ammonia, and therefore, form hydrogenated PAH and alkali amide as shown in Figure 8. The abstraction of a proton renders this process less favourable for production and characterisation of radical anions, but it is more suitable for production of PAH derivatives, Arthur Birch extensively used this process for synthesis of reduced organic compounds in the 1940's [68].
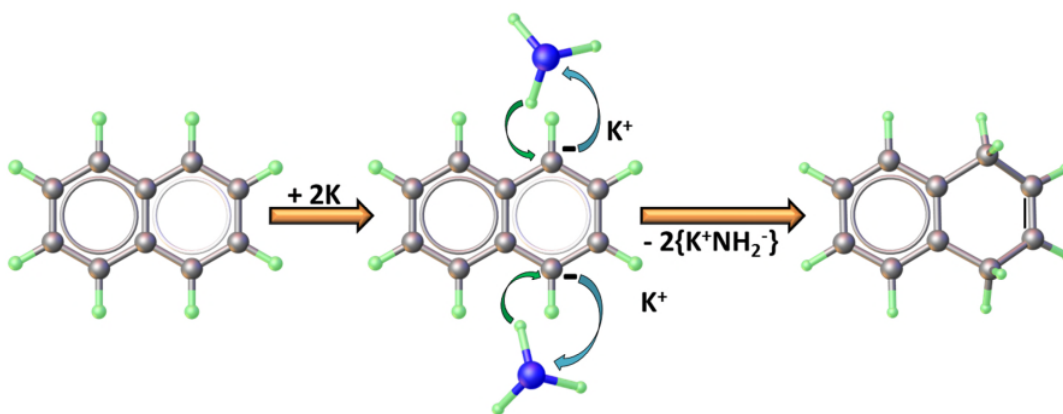
Figure 8: The scheme representing the formation of dipotassium naphthalide followed by reduction of dianion in the presence of ammonia to 1,4-dihydronapthalene and potassium amide. Colour code: C grey, N blue and H pale green.

All solutions of radical anions are deeply coloured (*e.g.* naphthalides are green, phenanthrides are olive green, anthracides are brilliant blue, triphenylides are lavender and perylides are dark blue) and conduct electricity [61]. The electron transfer from alkali metal to the LUMO of the PAH molecule, changes its electron structure and the colour of the solution originates from LUMO-LUMO+1 electron transitions, which occurs in the visible spectrum. Additionally, the visible spectra can serve as a fingerprint of PAH radical anions [63].

The availability of high-quality glove boxes along with rapid progress in computational power allowed the handling of highly air-sensitive alkali-metal reduced PAHs in the solid state and their characterisation by single crystal X-ray diffraction in the 1990's. The crystallisation of these compounds usually proceeds in a way such that a stoichiometric amount of solvent is incorporated in the lattice. According to two comprehensive review articles [69, 70], nearly 100 solvent-containing alkali-metal reduced PAHs were successfully isolated as solids and investigated by single crystal X-

ray diffraction. Solid radical anions of PAHs with one unpaired electron per PAH unit can potentially give rise to intriguing magnetic and electronic properties, *e.g.* antiferromagnetic, ferromagnetic, metallic or even superconducting states. However, only a small amount of those materials were probed by magnetometry or electron paramagnetic resonance (EPR). Until recently, the magnetic properties were investigated only in potassium naphthalide ($K_2(C_{10}H_8)_2(THF)$) [71] and potassium anthracide ($K_4(C_{14}H_{10})_3(THF)_6$) [72]. In the $K_2(C_{10}H_8)_2(THF)$ a long-range antiferromagnetic ordering with T_N of 28.6 K and in the $K_4(C_{14}H_{10})_3(THF)_6$ anthracide an aggregate with a triplet ground state were observed.

In the same period that organometallic chemists started isolating and characterising single crystals of alkali-metal reduced PAHs, solid-state chemists and condensed-matter physicists became interested in the solvent free compounds. However, according to the literature those two scientific communities (organometallic chemists and solid-state chemists/ condensed-matter physicists) barely interacted with each other. The discovery of superconductivity in potassium fulleride (K_3C_{60}) [73] in 1991 triggered a search for new carbon based molecules, which could become superconducting upon reduction. The observation of an insulator to conductor transition in potassium-doped pentacene (**9**) [74] and the theoretical results that the superconducting critical temperature (T_C) increases with the inverse number of π electrons in PAH molecules [75] (Figure 9a), initiated a long quest of solid-state chemists and condensed-matter physicists to synthesise PAH-based superconductors. The synthesis route they have followed was different from that of the organometallic chemists and mimicked the synthesis of alkali metal fullerides. In 2010 superconductivity was reported in potassium doped picene (**6**) [76] with T_C of 18 K. Shortly after that the superconductivity in potassium doped phenanthrene (**3**) [77] (T_C = 5 K), potassium doped coronene (reported T_C = 3.5, 7, 11 and 15 K, as well) [78] and potassium doped 1,2:8,9-dibenzopentacene (T_C = 33.1 K) [79] were reported and a correlation between the number of benzene rings and T_C was abstracted, as shown in Figure 9b.
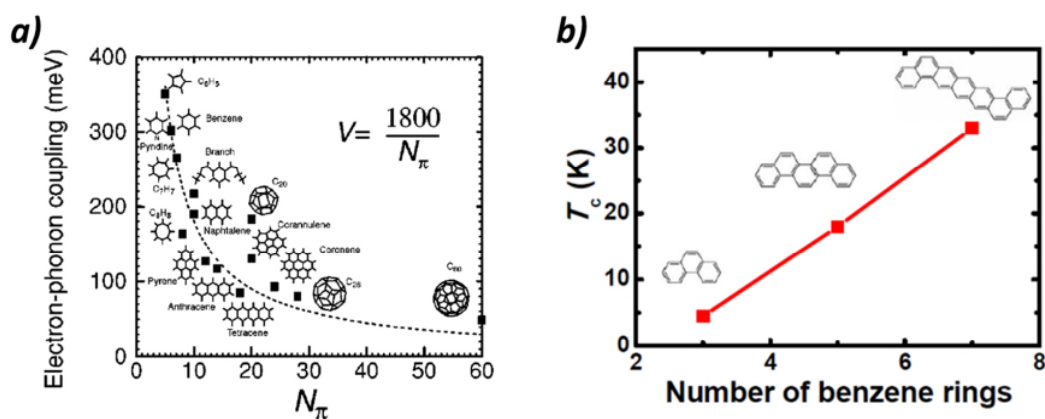
Figure 9: a) The correlation between electron-phonon coupling strength *vs.* number of π electrons in PAHs, where the T_C should increase with a decreasing number of π electrons [75]. b) Correlation between superconducting transition temperature (T_C) *vs.* number of benzene rings in potassium reduced PAHs [79].

These publications ignited the whole research field and in the following years superconductivity was also reported in samarium-doped picene (T_C = 4 K), phenanthrene (T_C = 5, 5.2, 4.4 K reported) and chrysene (**6**) with T_C of 5 K [80], strontium- and barium-doped phenanthrene with T_C of 5.6 and 5.4 K respectively [81], barium-doped anthracene (**2**) with T_C of 35 K [82], potassium-doped pentacene (T_C = 4.5 K) [83]. More recently superconductivity with T_C as high as 123 K in potassium-doped p-terphenyl was reported [84]. Basic information about most of the reported PAH based superconductors is gathered in Table 2.

The continuing observations of superconductivity in various alkali and alkaline earth metal reduced PAHs inspired theoretical physicists and chemists to perform a variety of calculations in order to shed light on the crystal structure and electronic properties of these superconducting materials. Moreover, they attempted to provide a theoretical background, which would elucidate the origin of superconductivity in these compounds. Some of those results are represented in the literature [85, 86, 87, 88, 89, 90, 91].

Despite all of the excitement of this research topic it has to be stressed that the identity of the superconducting phases and the origin of putative superconductivity remain unknown. All these superconducting materials exhibit low crystallinity, which prevents the unambiguous determination of their crystal structure. Several

13

superconducting temperatures for the same material along with a small shielding fraction and the observation of metal hydrides indicate the multi-phase nature of these materials. However, the most concerning fact is the lack of reproducibility of these materials inside this research community and in some case inside the same research group. All these issues severely hampered the progress of this research topic.

Table 2: Alkali- and alkaline earth metal-reduced superconducting PAHs along with their basic properties: nominal stoichiometry of metal used, annealing temperature and time, superconducting transition temperature and shielding fraction (describing the amount of superconducting phase).

Compound	x	Annealing temperature (K)	Annealing time (days)	T_c (K)	Shielding fraction (%)	Ref.
$K_x$picene	3.3	440	21	6.9	15	[76]
$K_x$picene	3.3	440	11	18	1.2	[76]
$K_x$picene	3.0	673	10	14	3.9	[92]
Rb_xpicene	3.1	570	6.7	6.9	10	[76]
Rb_xpicene	3.8	523	14	11	14	[92]
Ca_xpicene	1.5	773	42	7	1.25	[78]
Sm_xpicene	1	693	4	4	trace	[80]
$K_x$phenanthrene	3	473	1	4.95	5.3	[77]
Rb_xphenanthrene	3	513	7	4.75	6.7	[77]
Sr_xphenanthrene	1.5	503	8	5.6	39.5	[81]
Ba_xphenanthrene	1.5	503	8	5.4	65.4	[81]
Sm_xphenanthrene	1	513	4	5, 5.2, 4.4	trace	[80]
$K_x$dibenzopentacene	3.17	573-623	7-20	28.2	5.5	[79]
$K_x$dibenzopentacene	3.45	573-623	7-20	33.1	3.2	[79]
$K_x$dibenzopentacene	3	573-623	7-20	7.4	3.6	[79]
Sm_xchrysene	1	603	4	7.4	3.6	[80]
$K_x$coronene	3	-	-	3.5, 7, 11, 15	trace	[78]
Ba_xanthracene	1	RT, NH_3 (lq)	0.25	35	trace	[82]
$K_x$pentacene	3	523	1.5	4.5	0.5	[83]
$K_x$terphenyl	3	443-533	1-7	123	-	[84]

Moreover, the inability to reproduce those results, despite the immense effort of groups worldwide, induced frustration and opened up a dispute in this scientific community. It is argued here that purely mimicking the solid state reactions used for the synthesis of alkali and alkaline earth metal intercalated fullerenes and graphite is not appropriate for the PAH-based materials. In the case of fullerides and intercalated graphite, the solid state reaction at elevated temperatures or reactions in liquid ammonia and methylamine followed by an annealing process, yielded well-defined polycrystalline materials. There the alkali and alkaline earth metal cations were successfully intercalated in the interstices/voids present in the crystal structure

without breaking the crystal structure of pristine materials, as shown in Figure 10. By utilising the above stated methods, a variety of superconducting fullerides [73, 93, 94, 95, 96, 97, 98] and intercalated graphite [99,100] were synthesised with superconducting transition temperatures as high as 38 and 11.5 K respectively.
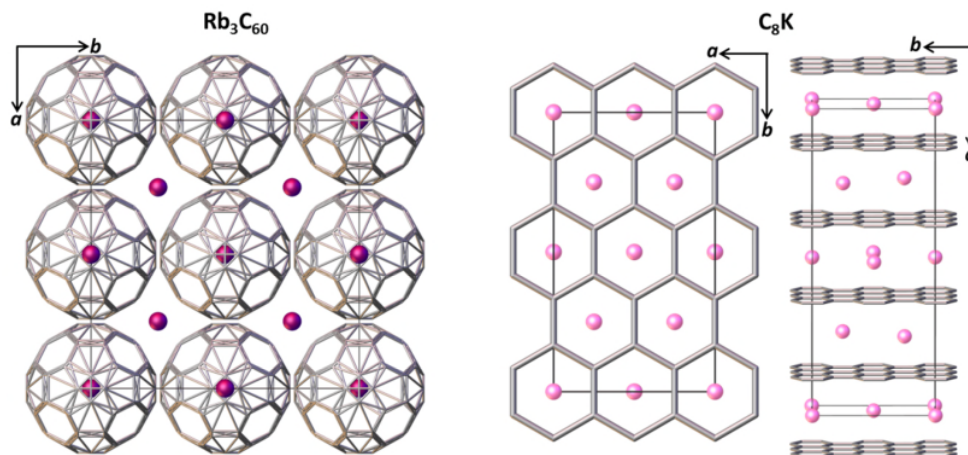
Figure 10: On the left side is a presentation of Rb_3C_{60} along the crystallographic *c* direction, where rubidium cations occupy the interstices between C_{60}^{3-} moieties (the disorder of C_{60} is shown producing a seemingly fourfold rotational symmetry of the molecules). The presentation of C_8K structure along the crystallographic [001] and [100] directions, depicted on the right side, shows the intercalation of potassium cations between graphite layers. Colour code: Rb violet; K lilac and C grey.

In contrast to fullerene and graphite, PAHs contain hydrogen atoms which can be abstracted in the presence of strong reducing agent at elevated temperatures (Figure 11) or PAH can be hydrogenated in the presence of strongly coordinating protic solvents, *e.g.* ammonia and methylamine (Figure 8). The abstraction of hydrogen from the PAH molecule leads to the formation of very reactive radical species, which are prone to attack the double bond of the neighbouring PAH molecule, yielding various polymeric PAH compounds. Based on the observed alkali hydride in various samples, this seems a valid explanation.
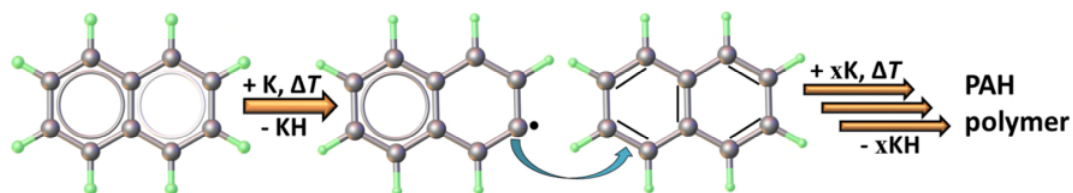
Figure 11: A schematic representation of naphthalene radical formation upon abstraction of hydrogen atom by potassium metal, followed by attack of radical on double bond in neighbouring naphthalene molecule resulting in a naphthalene polymer. Colour code: C grey and H pale green.

Due to issues associated with high-temperature synthesis of alkali-metal reduced PAHs, which do not result in phase-pure and crystalline materials, some groups in this scientific community made a U-turn and started exploring new less destructive synthesis routes. The group of K. Tanigaki in Japan optimised the solid-state route by performing reactions at near room temperature, yielding fairly crystalline materials exhibiting low-dimensional magnetism [101, 102, 103, 104]. Furthermore, the group of M. J. Rosseinsky in the UK changed the reducing agent, swapping potassium with potassium hydride, in this way decreasing the redox potential of the reducing agent and pushing the equilibrium away from hydride formation [105].

1.3 Our Aims and Objectives

In contrast to the groups that decided to optimise the solid-state synthesis routes, we resorted to organometallic chemistry, utilising the reduction in aprotic coordinating organic solvent, the method proven to yield well defined polycrystalline and single-crystalline materials. Our strategy was divided into two stages. The first stage was the synthesis of phase-pure materials, preferably, in single crystal form, followed by detailed analysis by single crystal X-ray diffraction, powder X-ray diffraction, magnetometry, Raman and infrared spectroscopy, and EPR spectroscopy. In the second stage we planned to heat-treat phase-pure materials under mild conditions in order to remove solvent molecules preserving the integrity of the PAH anion – solvent molecules are in most of the cases inevitably incorporated into the crystal structure when reduction is carried out in coordinating solvents. This strategy should afford phase-pure solvent-free superconducting materials, our ultimate aim of this project.

We choose phenanthrene, because superconductivity was reported in potassium, rubidium, strontium, barium and samarium doped phenanthrene [77, 80, 81], and because most calculations were performed on these superconducting materials. This is in contrast to organometallic chemistry where none of the alkali and alkaline earth metal reduced phenanthrene has been isolated in the solid state. Thus, the exploration of the family of solvent containing phenanthrides is an interesting topic to pursue. Phenanthrene (**3**, $C_{14}H_{10}$) is one of the smallest phenacene, consisting of three benzene rings fused in the arm-chair configuration, with molecular mass of 178.23 g/mol, the melting point of 101 ^{o}C and it is highly soluble in organic solvents including aprotic coordination solvents. It crystallises in a monoclinic $P2_1$ space group with lattice parameters of a = 8.441(2) Å, b =6.140(1) Å, c = 9.438(1) Å, β = 97.96(1)^{o} and V = 484.4(1) Å^3 at 295 K [106], and adopts the herringbone structure as shown in Figure 12.
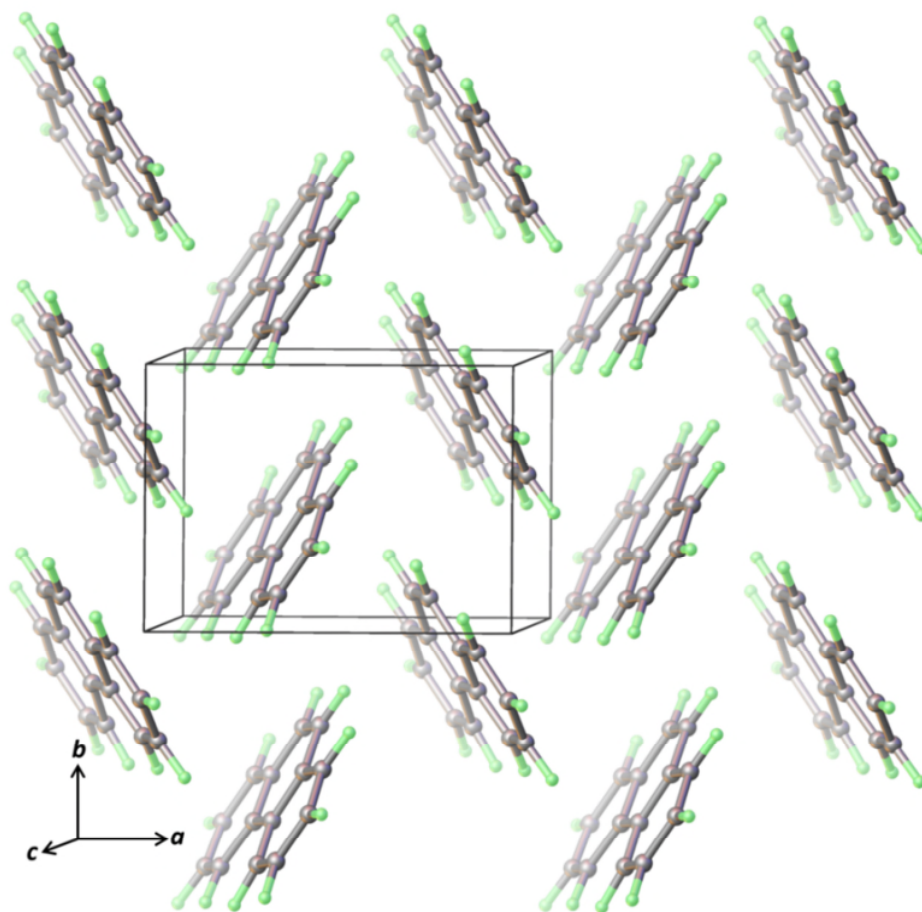
Figure 12: Depiction of the structure of phenanthrene showing a herringbone packing motif. Colour code: C grey and H pale green.

2 Chapter 2 – Methods

2.1 General synthetic procedure

Salts of alkali-metal reduced PAHs are highly air-sensitive (they immediately react with traces of oxygen or water), thereby all syntheses and handling of the products were carried out in anaerobic conditions, either in vacuum utilizing Schlenk techniques or under an argon atmosphere by using a glove box (MBraun, MB200B) with O_2 and H_2O levels kept below 0.1 ppm.

Phenanthrene (Acros Organics, 98+%) was sublimed at 110 ^{o}C in vacuum by using a custom-made 'cold finger' glass Schlenk vessel, equipped with high vacuum J. Young tap. Sublimed phenanthrene was afterwards stored in the glove box in air-tight vials.

Potassium (Sigma-Aldrich, ≥99.95%), rubidium (Sigma-Aldrich, 99.6%) and caesium (Sigma-Aldrich, ≥99.95%) ingots were transferred into glove box and stored in air-tight vials.

Tetrahydrofuran - THF (Fisher Scientific, laboratory reagent grade), *n*-pentane (Acros Organics, >99%) and *n*-hexane (Fisher Scientific, HPLC grade) were stored under Na/benzophenone mixture in a glass Schlenk vessels equipped with J. Young tap. The solution of the THF was deep purple while solutions of *n*-pentane and *n*-hexane were dark green confirming that solvents were oxygen and water free.

Solution reactions were carried out in custom-made and custom-designed Schlenk reaction vessels (Figure 13). Each vessel consists of two glass reaction parts (*ca*. 60 ml of available volume in each) equipped with J. Young taps. Both parts are connected with a glass tube containing a filtering disc and another J. Young tap. This special design allows solution manipulation (filtration, condensation, decantation, *etc*.) in vacuum or under argon atmosphere without exposing the solution or solids to air. Reaction vessels were cleaned in base (KOH/EtOH) and afterwards in an acid bath (10% HCl), dried in an oven at 90°C overnight, evacuated on the Schlenk line to $5×10^{-4}$ mbar, transferred into the glove-box and left open in the glove box (Ar atmosphere) overnight, prior to use.

In a typical run a stoichiometric amount of alkali metal and phenanthrene were placed on the bottom of the left hand side of the reaction vessel. Afterwards the reaction vessel was transferred out of the glove box and placed on the Schlenk line, evacuated and *ca.* 20 to 30 ml of THF were condensed on top of phenanthrene and alkali metal. Solutions were stirred from 24 to 72 hours at room temperature to ensure complete reaction. Radical anion solutions were filtered, concentrated and layered with *n*-hexane or *n*-pentane (*ca*. 30 ml). Crystallization was typically carried for four days at room temperature. The obtained crystals/polycrystalline powder was washed several times with a new portion of *n*-hexane or *n*-pentane and dried in dynamic vacuum for at least 2h. Products were transferred into the glove box and stored in air-tight containers.
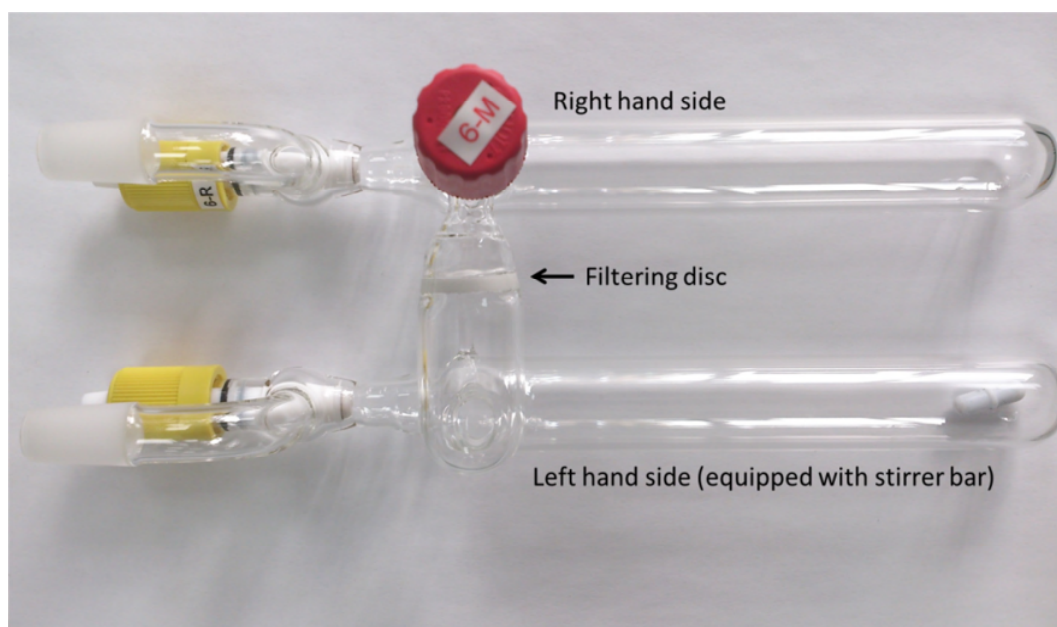
Figure 13: Representative example of a custom-made and custom-designed Schlenk reaction vessel.

2.2 Structural characterization – X-ray diffraction

2.2.1 Introduction

The determination of the structure of crystalline solids could be achieved by the diffraction of photons, neutrons and electrons on the crystal. X-ray (high energy photons) diffraction is the most frequently and most widely used technique for determination of crystal structure of solids.

In 1895 Wilhelm Conrad Röntgen discovered X-rays, a new type of electromagnetic radiation. Shortly after (1912) the discovery of X-rays, W. C. Röntgen and Max von Laue showed that X-rays can be diffracted by crystals. A year later (1913) William Lawrence Bragg used X-ray diffraction for the determination of the three-dimensional arrangement of atoms in a crystal of sodium chloride. Later on in 1928 Kathleen Lonsdale showed that the benzene ring, the basic building block of PAHs, is flat, by utilizing an X-ray diffraction technique [107].

For most of the diffraction studies, X-rays are generated either by X-ray tubes (Figure 14a) or by bending/wiggling electrons in synchrotrons (Figure 14b). In X-ray tubes, used in laboratory sources, electrons are accelerated between cathode and anode in vacuum by applying high voltage 30-60 kV. When electrons hit the anode most of the energy is released in the form of heat, hence the anode needs to be water cooled. The anode or target is a flat plate made of high-purity metal (most commonly Cu, Mo and Ag) and when accelerated electrons stop in the target material they expel electrons from the K-shell of atoms. When the electron falls from the L-shell into the vacancy in the K-shell a photon (X-ray), also called K_α radiation, with well-defined wavelength is emitted. Electrons coming from various L orbitals lead to $K_{\alpha 1}$, $K_{\alpha 2}$ radiation and in reality besides these, K_β radiation from upper orbitals and "white" Brehmsstrahlung radiation are also produced. For high-resolution X-ray diffraction measurements monochromatic light is needed, therefore the generated X-rays are passed either through filters (Ni foil for Cu-radiation and Zr foil for Mo-radiation) or monochromators (graphite or bent quartz/germanium crystals) in order to produce monochromatic light. A higher flux of photons can be achieved by using a rotating

anode, but those X-ray tubes are more expensive and require more maintenance [108]. X-rays with intensity 100-10000 times higher than those produced in X-ray tubes can be produced in synchrotrons. They are produced when electrons move at relativistic speed (near the speed of light) in a near-circular path and this near-circular path is achieved by using magnets. Here electrons are steered with a bending magnet and ultra-bright quasi-monochromatic radiation is produced. Later on a particular wavelength can be selected by using crystal monochromators [109, 110]. The high-brilliance of synchrotron X-rays allows the collection of a high-resolution diffraction profile in minutes. Therefore in situ reactions and transitions upon heating and cooling can be followed with X-ray diffraction.
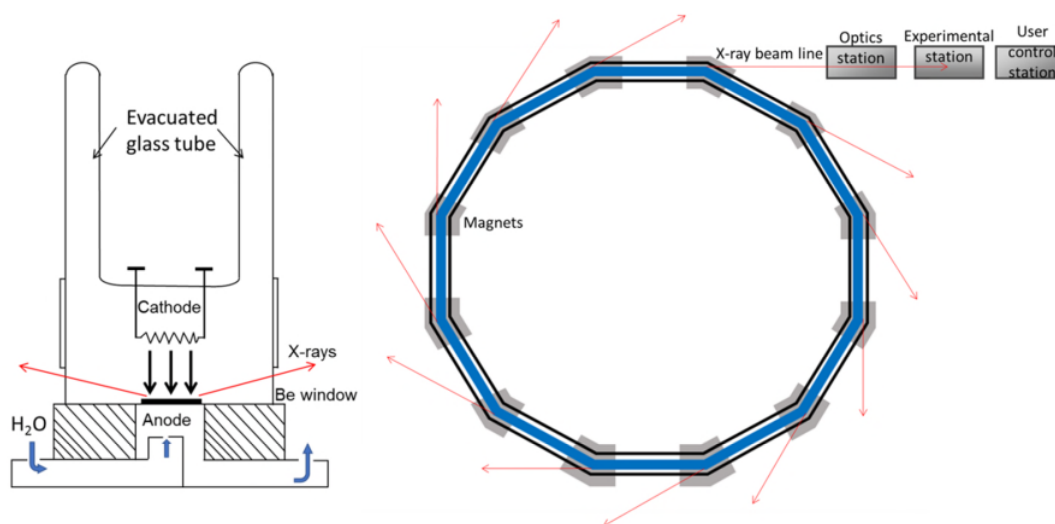
Figure 14: Figure on the left shows the schematic representation of an X-ray tube, where X-rays are generated when electrons accelerated from the cathode hit the metal target (anode) [108]. The scheme of a synchrotron and generation of X-rays upon bending the electrons with strong magnets is depicted on the right.

When the generated X-rays interact with the sample they are scattered by the electrons surrounding atoms and through constructive and destructive interference produce a diffraction pattern, from which the electron density and consequentially the accurate positions of atoms in the crystalline material can be determined. Once the positions of atoms are known the interatomic distances, bond angles, molecular geometry, angles between planes and conformation angles around bonds can be calculated. Moreover, packing motifs, orientations of molecules, symmetry and charge

distribution shed light on interactions between molecules, electronic structure and magnetism.

From a practical crystallographic perspective, atoms and molecules in the solid state can be classified in three categories. The first is an amorphous state, where the atoms and molecules are randomly oriented without any long-range order between them. The scattering of X-rays by a solid can be considered equal in all directions, yielding a broad hump in diffraction profile. The polycrystalline solids are the second class of solids, with atoms and/or molecules exhibiting a long-range order, but crystallites are small (between nano and several micron regimes). The grains of these solids are too small to enable the isolation of single crystals, but they can be studied with powder x-ray diffraction. The third class of solids are single crystals. A material can be classified as single crystal, if its atoms and/or molecules are repeated throughout the space and form long-range order and if the crystallites are big enough to be isolated. Single crystals from several microns up millimetre sizes are investigated by single crystal X-ray diffraction. Moreover, crystals grown in the earth crust can be several meters big.

Atoms and/or molecules exhibiting long-range order can be described using a crystal lattice. By mathematical definition a lattice is an array of points, related with the lattice translation operator $\mathbf{T} = u_1\mathbf{a}_1 + u_2\mathbf{a}_2 + u_3\mathbf{a}_3$, where u_1, u_2 and u_3 are integers and $\mathbf{a}_1$, $\mathbf{a}_2$ and $\mathbf{a}_3$ represent the axes of the crystal. The crystal is formed if an identical basis comprising of s atoms at the $\mathbf{r}_j = x_j\mathbf{a}_1 + y_j\mathbf{a}_2 + z_j\mathbf{a}_3$ (where j = 1, … s) positions is associated with each lattice point. In crystallography values between 0 and 1 for x, y and z are usually chosen and are called fractional coordinates [107, 111]. If we have crystal lattice and structural motif, then a crystal structure can be constructed as shown in Figure 15.
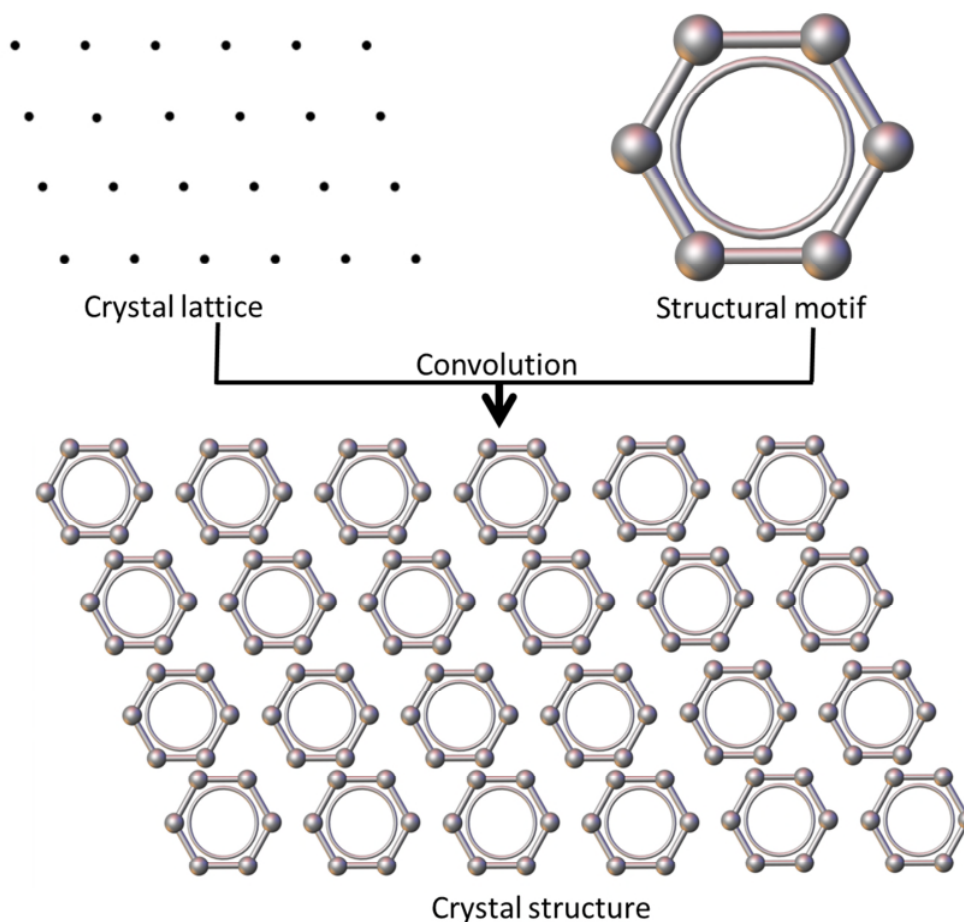
Figure 15: The construction of an imaginary crystal structure by convoluting the crystal lattice and structural motif, in our case a benzene ring.

Each crystal lattice point can be positioned in a primitive unit cell, the replication of which will fill all the space by applying appropriate translation operations. The smallest part of the unit cell is the asymmetric unit cell or asymmetric unit, where atoms and/or molecules are not related with any symmetry operation, so the constituents of asymmetric unit cell are crystallographically independent. By applying symmetry elements; translations, mirror planes, proper and improper rotation axes including inversion centre, screw axes and glide planes, to the asymmetric unit a unit cell is built. The presence of certain symmetry elements in the crystal structure causes the absence of specific reflections, called systematic absences, in the diffraction profile which is vital for identifying the symmetry in the material.

The unit cell is comprised of one or many lattice points belonging to a lattice point group and is described by the lattice parameters *a, b, c, α, β, γ* (Figure 16). In three

dimensions there are 14 unique lattice types, so called Bravais lattices. These lattice types are derived by combining seven cell types/crystal systems; triclinic, monoclinic, orthorhombic, tetragonal, trigonal, hexagonal and cubic, with lattice centering; primitive, body-centered and face-centered. Furthermore, combining symmetry elements with lattice types yield 230 unique space groups. The basic characteristics of crystal systems, which define three-dimensional unit cells, are gathered in Table 3 [112].
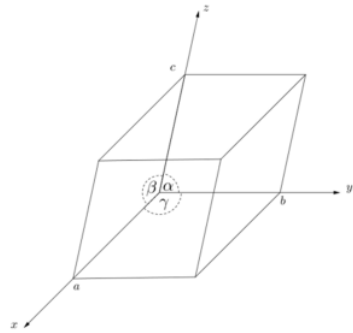
Figure 16: A three-dimensional unit cell defined by three axial lengths (*a*, *b*, and *c*) and angles between them (α, β and γ).

Table 3: The basic characteristics of crystal systems [112].

Crystal system	Essential symmetry element	Restriction on unit cell parameters
Triclinic	none	none
Monoclinic	one twofold rotation and/or mirror plane	α=γ=90°
Orthorhombic	three twofold rotations and/or mirror planes	α=β=γ=90°
Tetragonal	one fourfold rotation	a=b; α=β=γ=90°
Trigonal	one threefold rotation	a=b; α=β=90°; γ=120°
Hexagonal	one sixfold rotation	a=b; α=β=90°; γ=120°
Cubic	four threefold rotations	a=b=c; α=β=γ=90°

As stated above, X-rays scatter from electrons orbiting the nuclei and diffracted waves form constructive or destructive interference. Constructive interference enhances the scattering in specific directions and the magnitude of enhancement depends on the number of repeating lattice planes, shown as black lines intersecting the atoms in Figure 17. The occurrence of constructive interference is described by the Bragg Law:

$$n\lambda = 2d\ sin\theta$$

Equation 2.1

Where *n* is an integer, representing order of diffraction, λ is the wavelength of X-ray radiation, *d* is the distance between two parallel lattice planes and θ is the angle defined by incident X-ray and lattice plane. A graphical representation of the Bragg Law is in Figure 17.

In three dimensions repeating lattice planes are indexed with so-called Miller indices, denoted as *h*, *k*, *l*. The interplanar spacing is related to Miller indices and lattice constants. For example, in the orthorhombic system [108]:

$$\frac{1}{{d_{hkl}}^2} = \frac{h^2}{a^2} + \frac{k^2}{b^2} + \frac{l^2}{c^2}$$

<div align="right">Equation 2.2</div>

Each observed reflection can then be labelled with Miller indices (*hkl*), and appears in the powder diffractogram as a peak with intensity at a position in 2θ, corresponding to the scattering of monochromatic X-rays on electrons surrounding atoms in the crystalline solid.
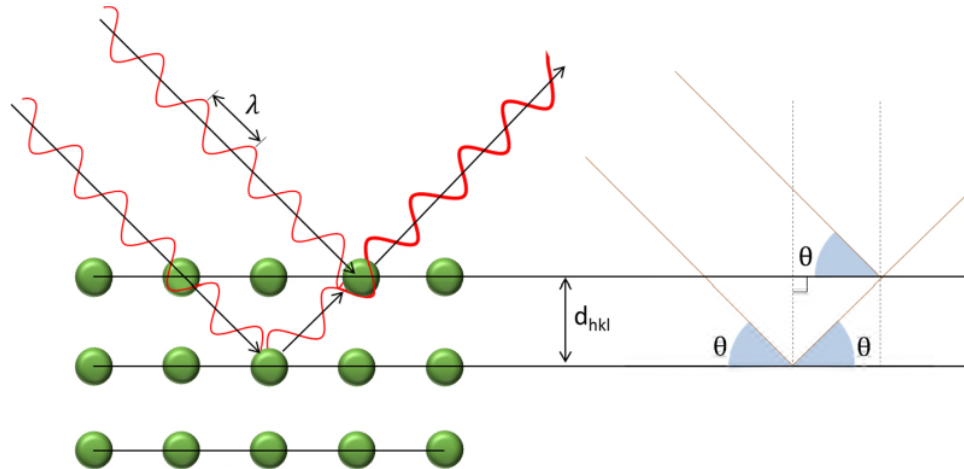
Figure 17: A graphical representation of constructive interference on two planes of atoms within the single crystal on the left and graphical derivation of the Bragg Law on the right side.

Diffraction of X-rays by single crystals results in pattern of beams in space which are usually recorder electronically as spots or, so-called, frames. By collecting a sufficient amount of frames at different positions and covering high-angle reflections, the accurate reconstruction of electron density in a single crystal can be achieved. The electron density is the Fourier transform of the diffraction pattern and *vice versa*. A structural model is determined, which corresponds to the actual position of the atoms with the level of agreement between the diffraction pattern calculated from the model and that observed defined by *R* factors.

In the case of powder X-ray diffraction, randomly orientated crystallites are measured, yielding a pattern of rings instead of individual spots as in the case of single crystals. Therefore, the three-dimensional information is compressed into one dimension, resulting in a loss of information. This loss of information makes the accurate determination of the structural model much more difficult, in some cases impossible, to achieve, and these models are in general less accurate than models obtained from single crystal X-ray diffraction. Despite this drawback, powder X-ray diffraction is an extremely powerful analytical tool to investigate the crystal structure and on many occasions, where single crystals cannot be grown, the only tool to determine the crystal structure.

In general, the powder X-ray diffraction measurement is performed in such a way that only a narrow stripe of the rings containing the diffraction pattern is collected. This results in the diffraction pattern consisting of peaks with well-defined intensities, widths and 2θ values. A variety of structural information can be extracted from the diffraction profile. By applying the Le Bail whole powder pattern decomposition method [113] the lattice constants can be determined. Rietveld refinement [114, 115] enables the determination of unit cell parameters, positions of atoms in the unit cell, their occupancy and thermal displacement parameters of both phase-pure and multiphase samples by refining the initial structure model to the whole diffraction pattern using a least-squares method. Commonly, scale factor, lattice constants, fractional positions of atoms, atomic displacement parameters, peak shape (sample and instrument contributions), preferred orientation and zero-shift are refined in the course of Rietveld refinement. The quality of refinement, agreement between observed and calculated diffraction pattern can be validated by R_{wp} and R_{exp} agreement factors and/or goodness-of-fit (χ^2). These are defined with the following equations:

$$R_{wp}{}^2 = \frac{\sum_i w_i [y_i(obs) - y_i(calc)]^2}{\sum_i w_i [y_i(obs)]^2}$$

Equation 2.3

$$R_{exp}{}^2 = \frac{(n-p)}{\sum_i w_i [y_i(obs)]^2}$$

Equation 2.4

$$\chi^2 = \left[\frac{R_{wp}}{R_{exp}}\right]^2$$

Equation 2.5

Where $y(\text{obs})$ and $y(\text{calc})$ are observed and calculated intensities at a given 2θ value and the summation runs through these 2θ values, n is number of observed peaks, p is number of parameters and w_i a weighting factor [110].

The crystal structures of solvent-free $Cs(C_{14}H_{10})$ and $Cs_2(C_{14}H_{10})$ materials were determined from polycrystalline powder by using direct-space simulated annealing global optimisation technique [116]. In this method selected fragments (atoms or molecules) are allowed to move inside the unit cell, and at each step a new diffraction profile is calculated and compared with the experimentally observed one. These moves are allowed to be larger at the beginning and then they are gradually decreased until the global minimum is reached (best agreement with calculated and observed diffraction profile). Usually, several runs (10 runs) with different starting positions of fragments are done in order to confirm the correct structural model and reduce the probability of finding a structural model in a local, instead of global, minimum. The success of obtaining the structural model by the simulated annealing technique strongly depends on the amount of pre-existing information about the studied material and how this information relates to the crystal structure. For instance the determination of a structural model where lots of degrees of freedom are used will most likely be unsuccessful. Therefore, in the case of $Cs(C_{14}H_{10})$ and $Cs_2(C_{14}H_{10})$ crystal structure determination, we used the following procedure: based on the unit cell parameters, the determined space group and its symmetry elements, and the ratio between caesium atoms and phenanthrene molecules obtained from elemental analysis the appropriate number of fragments were used in the simulated annealing process. Phenanthrene moieties were treated as rigid bodies without any internal degrees of freedom. The *x, y* and *z* translations and rotation of phenanthrene moieties and translations for caesium cations were used as external degrees of freedom. The structural model obtained from the simulated annealing was then refined with Rietveld refinement for $Cs(C_{14}H_{10})$ and $Cs_2(C_{14}H_{10})$.

After the refinement of the structural model a manifold of structural information is obtained. The coordination interactions between alkali cations and the phenanthrene radical anion play an important role for describing the structure and the structure-magnetism relationship. Therefore, a detailed description of cation location in respect to the benzene ring plane is needed in order to elucidate these interactions. While, in

the literature [69, 70], the cut-off for cation-radical ion coordination interactions is not exactly defined, we decided to take into account the distance and the angle between cation and benzene ring plane, where the interaction between cation and electrons in π cloud is still feasible. The optimal interaction is achieved when the cation is positioned at the middle and above/below the benzene ring plane. However, this ideal position is rarely observed due to steric crowding by the constituents of the crystal structure (in our case solvent molecules and neighbouring phenanthride units). The cation can move in three ways; vertical translation, horizontal translation and rotation around the centre of the benzene ring plane (so called ring plane centroid) as shown in Figure 18. Usually, the movement of the cation comprises all three possible movements. The length cut-off values were defined as a sum of the ionic radius of the alkali-metal cation and the Van der Waals radius of carbon, yielding values of 3.48, 3.67 and 3.72 Å for potassium, rubidium and caesium cations respectively. The angle, φ, smaller than 50° was also chosen as a cut-off value, because the overlap between cation σ-orbital and carbon π-orbitals is considered to be weak. The φ angle, later in the text denoted as cation projection on the ring plane angle, is defined as an angle between the cation (violet circle), ring plane centroid (orange circle) and cation projection to the ring plane (red circle) as shown in Figure 18.
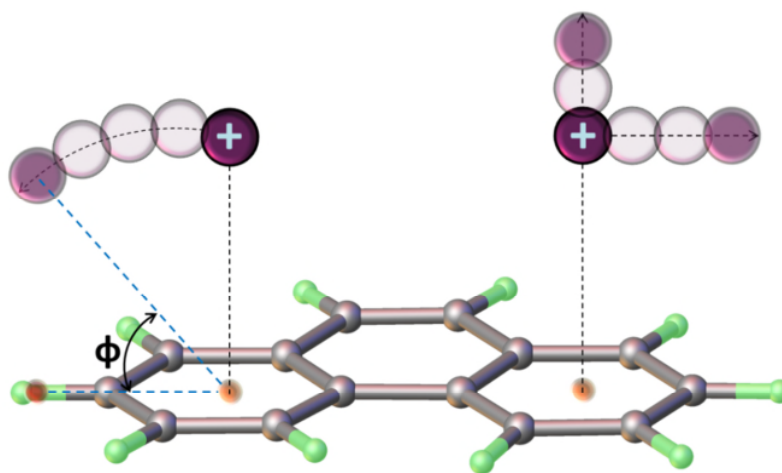
Figure 18: The three possible ways of cation movement due to steric crowding, vertical and horizontal translation (right), and rotation around ring plane centroid (left). The definition of the φ angle between the cation, ring plane centroid and the cation projection to the ring plane is depicted on the left side. Colour code: C grey, cation violet, H pale green, benzene ring plane centroid orange and cation projection to the ring plane red.

2.2.2 Experimental details of single crystal diffraction measurements

All synthesised samples are extremely air-sensitive, and therefore handling in oxygen- and moisture- free atmosphere was required. To protect samples from oxidation the following process was applied: a small amount of single crystals stored in an airtight container inside the glove box were transferred on an objective glass and covered with degassed and dried perfluorodecalin oil (Acros Organics, 95 %). Single crystals with well-defined facets were separated from damaged crystals and powder by using a stainless-steel needle and afterwards inserted into 20 mm long and 0.7 mm wide capillaries. The capillaries were sealed with wax and then additionally with UV-curing glue, and stored in an airtight container. These prepared capillaries were kept inside the glove box and taken out only immediately prior to the measurement.

The measurements were performed by Dr. Dmitry S. Yufit either on a Bruker D8 Venture diffractometer (IμS microsource λMoK_α, λ =0.71073 Å, focusing mirrors, Photon 100 CMOS detector,) shown in Figure 18 or on a Bruker SMART 6000 diffractometer (fine-focus tube, λMoK_α radiation, λ = 0.71073 Å, graphite monochromator, Monocap optics), both equipped with a Cryostream (Oxford Cryosystems) open-flow nitrogen cryostat. Data of $Rb_2(C_{14}H_{10})_2(THF)$, $Cs_2(C_{14}H_{10})_2(THF)$, $K_4(C_{14}H_{10})_3(THF)_4$ and $Rb_4(C_{14}H_{10})_3(THF)_4$ compounds were collected at 120 K (in the case of $Rb_2(C_{14}H_{10})_2(THF)$ an additional set of data was collected at 290 K). The structures were solved by direct methods and refined by full-matrix least squares on square of structure factors (F^2) for all data using Olex2 [117] and SHELXTL [118] software. All non-disordered non-hydrogen atoms were refined anisotropically, and disordered atoms of THF molecules and phenanthrides (one phenanthride unit in $K_4(C_{14}H_{10})_3(THF)_4$ and $Rb_4(C_{14}H_{10})_3(THF)_4$ compounds) were refined isotropically with fixed site occupancy factor (SOF) to 0.5. All hydrogen atoms were placed in the calculated positions and refined in riding mode with isotropic displacement parameter (U_{iso}) equaling 1.2 of equivalent isotropic displacement parameter (U_{eq}).
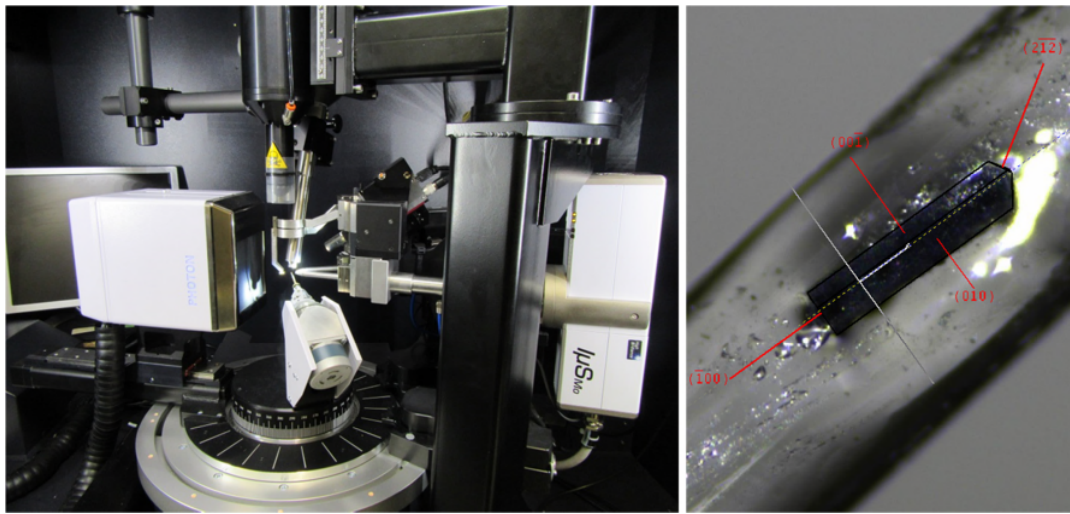
Figure 19: Photos of the Bruker D8 Venture diffractometer and a single crystal in an airtight-closed silica capillary with measured crystallographic directions are shown on the left and the right respectively.

2.2.3 Experimental details of powder diffraction measurements

A small amount of representative sample (containing crystals and powder if present) was thoroughly ground in an agate mortar. Due to the high air-sensitivity of the synthesised materials, an agate mortar was dried for several days in an oven (100 $^{\circ}$C), transferred into the glove box while still hot and left in the glove box over the night, in order to prevent sample oxidation with oxygen and water molecules, which can be absorbed on the surface of agate. The powder was tightly packed into 0.5 mm Special Glass capillaries (Capillary Tube Supplies Ltd). The prepared capillaries were sealed with silicone grease, transferred from the glove box and immediately flame sealed.

Data sets were collected on a laboratory Bruker D8 Advance powder diffractometers equipped with molybdenum source (Mo-K$_\alpha$ radiation, λ = 0.7093 Å), LYNXEYE XE-T point detector and Cryostream (Oxford Cryosystems) (Figure 20), and on a Rigaku SmartLab (9 kW rotating anode, Cu Kα radiation, λ = 1.54056 Å) diffractometer equipped with a linear D/teX Ultra point detector, both operating in transmission mode (Figure 20). Synchrotron data were collected with the high-resolution multi-detector diffractometer on ID31 (λ = 0.399959 and 0.399846 Å) and on ID22 (λ = 0.35420 Å) beamlines at the European Synchrotron Radiation Facility (ESRF), Grenoble. The diffraction of $Cs(C_{14}H_{10})$ on ID22 beamline was performed by Prof. Prassides' group. All Le Bail fitting and Rietveld refinement were performed with the EXPO2014 suite of programs [119] except the two-phase refinement of $Cs_2(C_{14}H_{10})_2(THF)$ sample, which was performed in TOPAS-Academic version 6 program suite [120]. The crystal structure determination of $Cs(C_{14}H_{10})$ and $Cs_2(C_{14}H_{10})$ compound was achieved by preforming the simulated annealing technique, initially determined by Dr. A. Johan C. Buurma, in the EXPO2014 program suite and in the course of this process the diffraction profiles were indexed with DICVOL [121] and N-TREOR [122] programs.
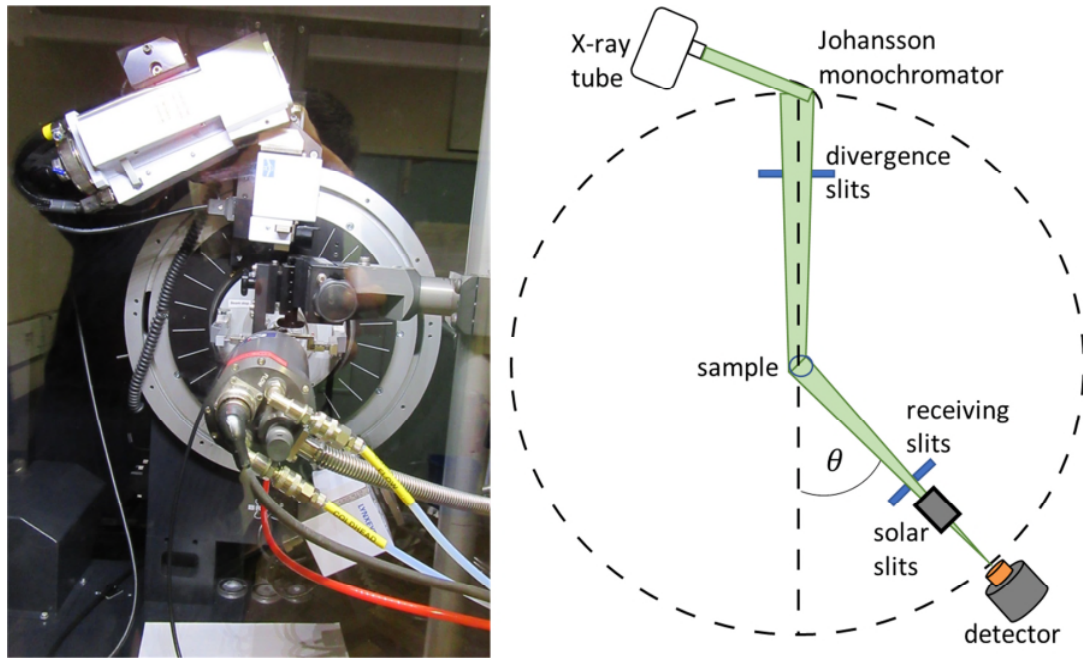
Figure 20: Photo of the Bruker D8 Advance diffractometer on the left and schematic representation of powder X-ray diffractometer operating in transmission mode (Debye-Scherrer geometry).

2.3 Investigation of magnetism – magnetometry

2.3.1 Introduction

A certain type of magnetism can be found in all materials, because the orbiting of electron gives rise to a magnetic moment ($d\mu$):

$$d\mu = IdS \qquad \text{Equation 2.6}$$

Where, the size of the magnetic moment, $d\mu$, depends on the magnitude of the current, I, in an elementary loop with the area, dS.

The magnetic moment, μ, of the single electron orbiting the hydrogen nucleus, with charge $-e$, mass m_e, velocity v, and angular momentum $m_e vr = \hbar$ can be calculated:

$$|\mu_e| = \pi r^2 I = -\frac{e\hbar}{2m_e} = -\mu_B = -9.274 \times 10^{-24} \ Am^2 \qquad \text{Equation 2.7}$$

The value of -9.274×10^{-24} Am^2 represents one Bohr magneton, μ_B, in SI units.

The magnetic spins present in materials can be measured by the application of an external magnetic field, B. The response of the material, the magnetisation, M, is proportional to the magnetic susceptibility, χ, of the material:

$$\chi = \frac{M}{B}\mu_0 \qquad \text{Equation 2.8}$$

Where μ_B ($4\pi\times10^{-7}$ Hm^{-1}) is magnetic permeability of free space.

In general materials can be divided into those which are exhibiting diamagnetism and those exhibiting paramagnetism. Diamagnetism is associated with materials with paired electrons, so called closed-shell systems, where a weak repulsive force, μ, which opposes the external B, is induced in applied field. The measured magnetic susceptibility, χ, is less than 0 and usually in the range of -1×10^{-6} emu/mol in CGS units. This small diamagnetic response originating from paired core electrons should not be confused with a very strong diamagnetic response induced with the Meissner effect, observed in superconducting materials.

Paramagnetism is observed in atoms, molecules and solids containing unpaired electrons and these unpaired electrons give rise to a magnetic dipole moment. The

34

measured χ of a paramagnetic material is larger than 0 and usually in the range of 1×10^{-4} emu/mol. The paramagnetic state resembles the gaseous state of matter, when no external field is applied, where spins do not interact with each other and can adopt any possible orientation at any time as shown in Figure 22a. If a magnetic field is applied the energy of the spin states split due to the Zeeman effect according to the alignment of spins with the direction of the external field. The energy of the resulting states are $-\mu_B B$ and $\mu_B B$ for the S = ½ spin system. This splitting of spin states leads to a Boltzmann distribution of populated states:

$$\frac{N_1}{N} = \frac{e^{\mu_B B/k_B T}}{e^{\mu_B B/k_B T}+e^{-\mu_B B/k_B T}} \text{ and } \frac{N_2}{N} = \frac{e^{-\mu_B B/k_B T}}{e^{\mu_B B/k_B T}+e^{-\mu_B B/k_B T}} \qquad \text{Equation 2.9}$$

Where N_1 and N_2 are populations of the lower and upper energy levels respectively, N is the total number of spins ($N = N_1 + N_2$) and k_B is the Boltzmann constant (of 1.381×10^{-23} J/K). The difference in the population of states in finite field leads to finite magnetization, M:

$$M = (N_1 - N_2)\mu_B = N\mu_B \frac{e^{\mu_B B/k_B T}-e^{-\mu_B B/k_B T}}{e^{\mu_B B/k_B T}+e^{-\mu_B B/k_B T}} = N\mu_B \tanh(e^{\mu_B B/k_B T}) \quad \text{Equation 2.10}$$

In the high-temperature and low-field limit, the expression for magnetic susceptibility (if the magnetic momentum of only spins is present) can be written as [111, 123]:

$$\chi = \frac{M}{B} \approx \frac{NS(S+1)g_L^2\mu_B^2}{3k_B T} = \frac{C}{T} \qquad \text{Equation 2.11}$$

Where g_L is the Landé factor and for free electron, $g_L \approx 2.0023$, and C is the Curie constant, defined as $C = \frac{N\mu_{\text{eff}}^2}{3k_B}$ and $\mu_{\text{eff}} = g_L\sqrt{S(S+1)}\mu_B$. According to these equations the calculated μ_{eff} and C for the S = ½ system are 1.734 μ_B and 0.3759 emu K/mol respectively [124]. The Equation 2.11 is also known as Curie's law. In most of the cases some interaction between spins does exist, therefore the correction term, known as Weiss temperature (θ_W), needs to be used. The addition of the the Weiss temperature leads to the Curie-Weiss law termed as:

$$\chi = \frac{C}{T-\theta_W} \text{ or } \chi^{-1} = \frac{T-\theta_W}{C} \qquad \text{Equation 2.12}$$

By plotting χ^{-1} *vs. T* the curve of the 'true' paramagnetic material will be linear with a zero intercept, while in materials where spins interact with each other the curve will

intercept at positive values, if interactions are ferromagnetic, or negative values, if interaction are antiferromagnetic, as shown in Figure 21. Additionally, from this plot the Curie constant and Weiss temperatures can be obtained.
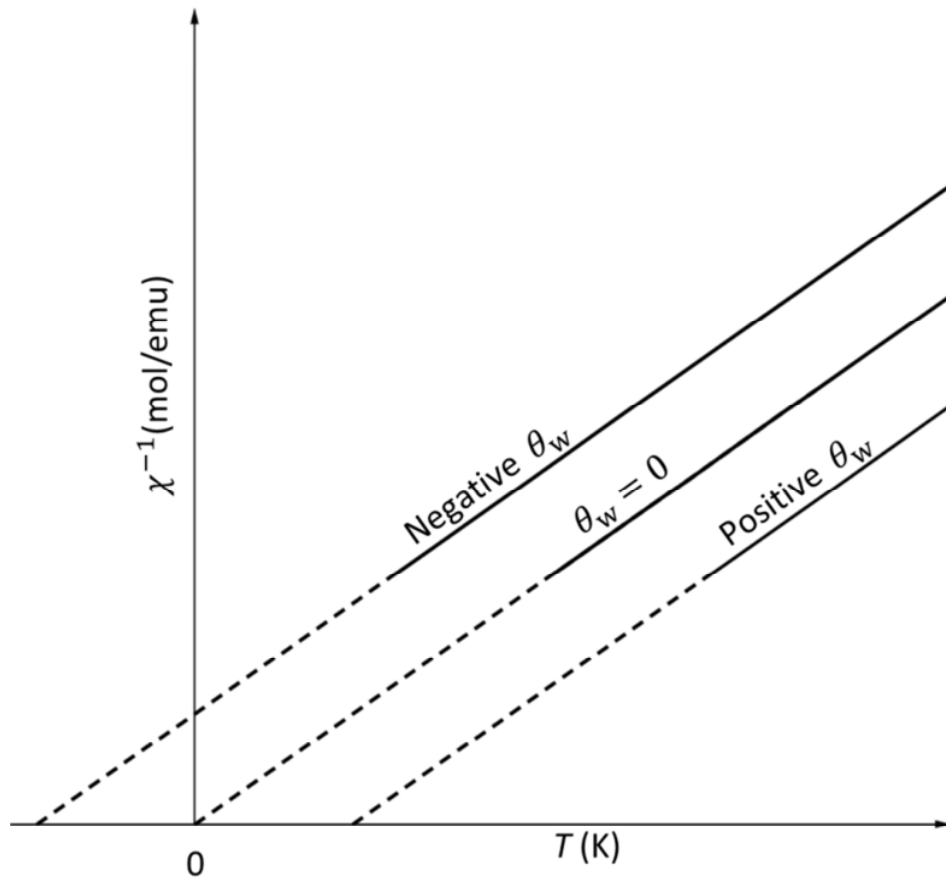
Figure 21: The χ^{-1} vs. T plot of the Curie-Weiss law. A Weiss temperature of 0 is expected for paramagnetic materials, while negative and positive values are expected for materials where spins are interacting in an antiferromagnetic and a ferromagnetic manner respectively.

The magnitude of the Weiss temperature, either extracted from fitting the magnetic susceptibility to the Curie-Weiss law or from the χ^{-1} vs. T plot, reflects the strength of spin interactions, and it is also a good indication of how the system is going to order in its ground state. Normally, the interactions become stronger when the materials are cooled down, because electrons are less excited. Therefore, thermal fluctuation will no longer prevail and the materials can undergo a long-range magnetic ordering upon cooling. The most widely observed ordered magnetic ground states are

ferromagnetism, antiferromagnetism and ferrimagnetism where spins align in the presence of an external magnetic field, as shown in Figure 22.
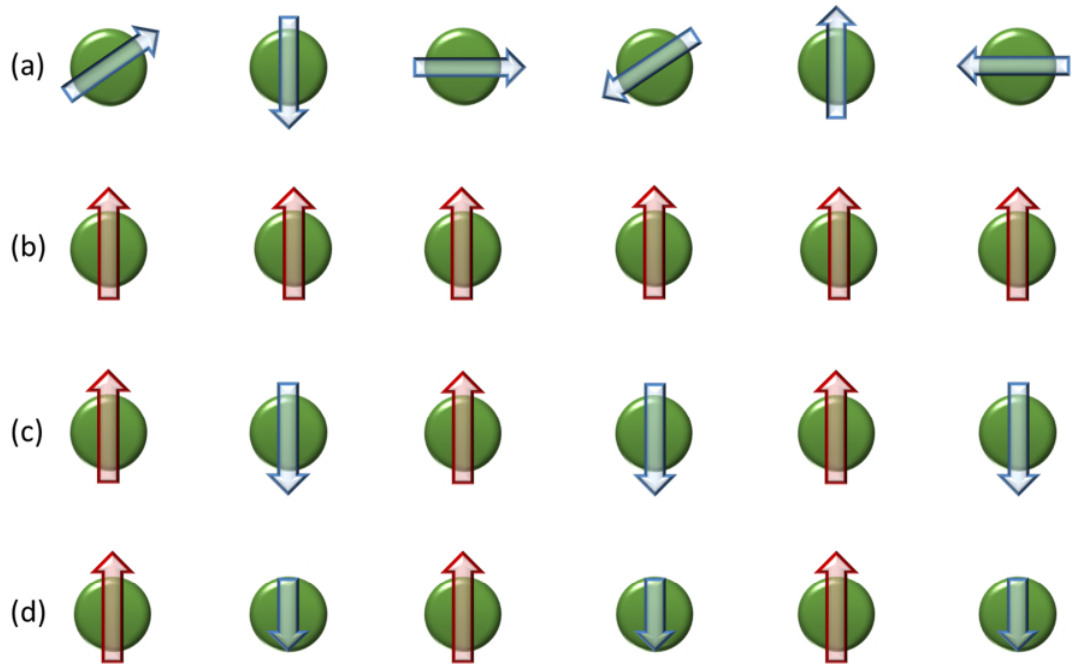
Figure 22: a) A paramagnetic state; b) ferromagnetic ground state, where all spins are aligned parallel; c) antiferromagnetic ground state, where every neighbouring spin is in antiparallel position; d) ferrimagnetic ground state, where neighbouring spins are aligned in antiparallel fashion with unequal magnetic moments.

In a ferromagnetic ground state, all neighbouring spins are aligned parallel (Figure 22b) inducing a net magnetisation. This causes a sharp increase of the susceptibility curve below the transition temperature, T_C (Curie temperature). In the case of an antiferromagnetic ground state neighbouring spins prefer an antiparallel orientation (Figure 22c). It can be viewed as two magnetic sub-lattices composed of two equally strong magnetic moments, which cancel each other forming a zero net magnetisation. This results in a sharp increase followed by sharp decrease in the susceptibility curve at the transition temperature, T_N (Néel temperature). The ferrimagnetic ground state is composed of two magnetic sub-lattices with unequal magnetic moments and where every second magnetic moment is orientated antiparallel to the others (Figure 22d). The susceptibility curve is similar to that observed in ferromagnetic materials (positive θ_W), but the net magnetisation is smaller [111, 123].

Some magnetic materials do not undergo long-range magnetic ordering despite having large positive or negative Weiss temperature. In these materials the geometry of the magnetically active constituents is such that it is impossible to align all spins of the lattice simultaneously. In these frustrated systems a long-range magnetic ordering is hindered. Such lattices - consisting of triangles - are shown in Figure 23. κ-(BEDT-TTF)$_2$Cu$_2$(CN)$_3$ [125] and Ba$_3$CuSb$_2$O$_9$ [126] are representatives of triangular lattice and ZnCu$_3$(OD)$_6$Cl$_2$ [127] and BaCu$_3$V$_2$O$_8$(OH)$_2$ [128] are representatives of the kagomé lattice, where exotic physical properties such as quantum spin liquid ground state were observed.
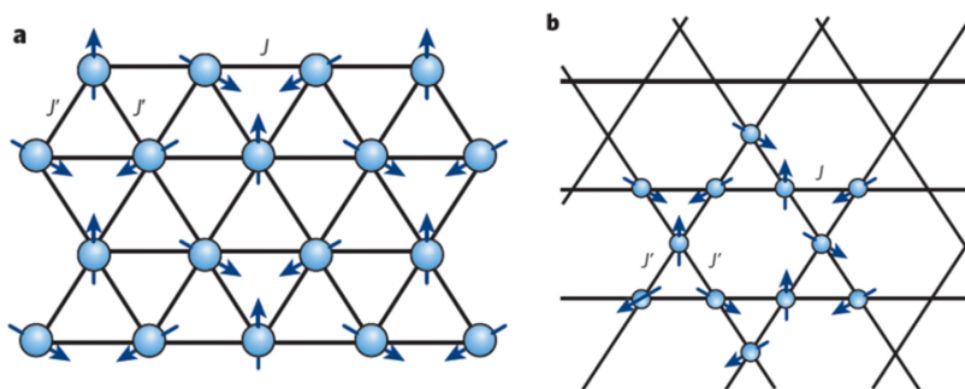
Figure 23: Two types of frustrated 2D lattices: a triangular lattice (a) and kagomé lattice (b) [129].

Another type of magnetism where long-range magnetic ordering is hindered is low-dimensional magnetism, where magnetically active species interact with each other in one- or two-dimensions, but they are unable to interact in the third-dimension because they are too far apart. The most basic low-dimensional magnet is composed of isolated dimers as shown in Figure 24a and a frequently occurring one is the one-dimensional uniform spin chain (Figure 24b). The interactions in one dimension can be divided in two groups. The first is known as a Heisenberg chain of spins, where the strength of magnetic exchange interaction (J) between spins is the same in all three directions, *i.e.* the interactions are isotropic. When the strength of interactions is not the same (anisotropy is present), the interactions between the spins can be described with Ising and with XY models. Two of the most widely used models where the magnetic lattice is quasi-one-dimensional are the alternating chain and spin ladder

models. In the alternating chain model the interactions between neighbouring and next-neighbouring spins are not the same and usually the strength of the weaker interactions can be described as a fraction (αJ) of the strength of the stronger interaction (J) as shown in Figure 24b. Here $\alpha = 1$ the system can be described as a uniform Heisenberg chain of spins, and when $\alpha = 0$ the system is composed of isolated dimers. The system where two parallel chains (two-leg ladder) are interacting with each other is described by the strong rung/rail ladder model. If the interactions along the rail (J_{rail}) are stronger, then strong rail model is used, and when the interactions along the rung are stronger (J_{rung}) the strong rung model is used (Figure 24c). By lowering the J_{rung} to zero the system becomes a 1D Heisenberg chain of spins. When infinite numbers of chains are interacting with each other 2D systems are obtained. The system with isotropic interactions forms a square magnetic lattice, while a system with anisotropic interactions forms a rectangular magnetic lattice, as shown in Figure 24d [123, 124]. Low-dimensional magnetism is generally quite rare, however, in several special organic systems it was frequently found. By far, most low-dimensional organic/organometallic magnets were found in the family of coordination polymers, where magnetically active cations of transition metals are connected/interacting with each other via bridging or terminal ligands. The second large groups are Fabre-, Bechgaard- and ET-salts, where the structure is composed of layers of S or Se containing heteroaromatic radical cations divided by layers of magnetically inactive monoanions. Similarly to frustrated systems low-dimensional magnets can exhibit intriguing ground states, such as spin liquid states. Therefore, these materials were/are extensively studied [124, 130, 131, 132].
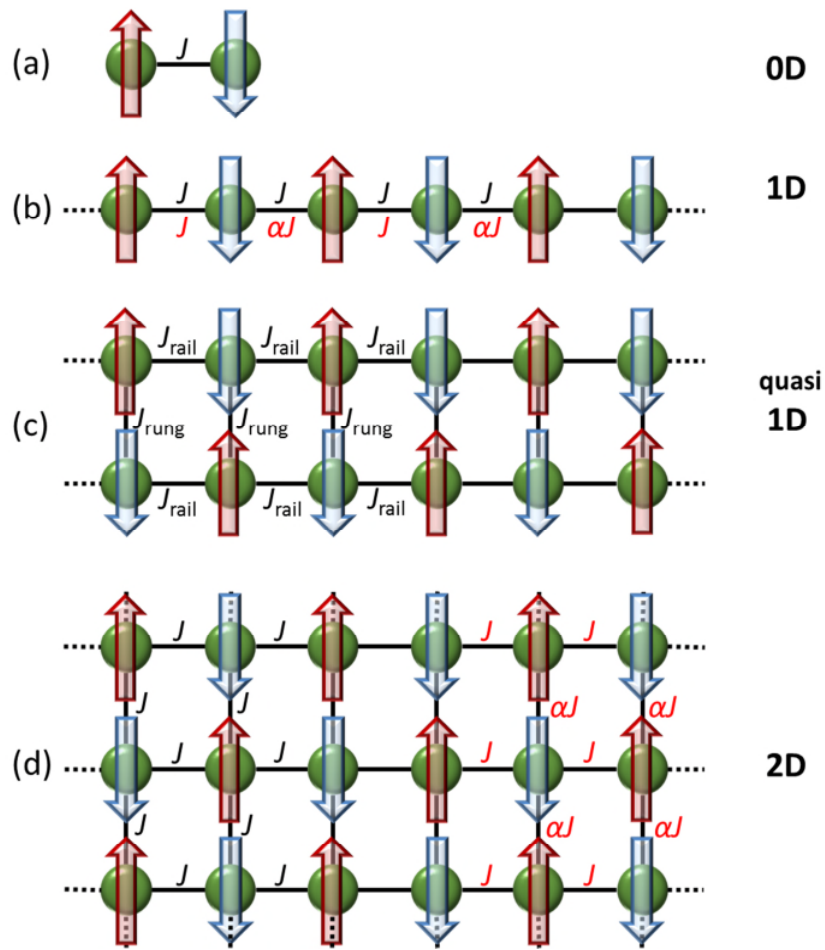
Figure 24: A schematic presentation of spin interactions in low-dimensional magnets: a) isolated dimers, 0 D system, b) 1D uniform Heisenberg chain of spins (black characters) and alternating chain model (red characters), c) two-leg spin ladders, a quasi-1D anisotropic system described with strong rail/rung model, d) 2D magnetic lattice, where systems with isotropic and anisotropic interactions are described as 2D square (black characters) and 2D rectangular (red characters) lattice. Only systems with antiferromagnetic spin interactions are shown in figure.

A hallmark of low-dimensional magnets is the broad maximum in susceptibility and heat capacity measurements recorded *vs. T*. This broad hump is known as the Schottky anomaly and it is associated with short-range magnetic ordering. At the temperature of the maximum the thermal excitation between two different states of the system is possible. When the temperature of the system is sufficiently low the excitation of the ground state is not possible because the system does not have enough energy. Therefore, spins are aligned with applied field. While, at high temperatures it is very difficult to change the energy of the system because both states are equally populated. The maximum of the broad hump is in between these two states [123].

2.3.2 Experimental details of magnetic measurements

The magnetism of all samples was investigated at ambient pressure with Superconducting Quantum Interference Device (SQUID) magnetometry. The Magnetic Property Measurement System (MPMS XL, Quantum Design) SQUID magnetometer equipped with an EverCool® system, capable of performing measurements in the temperature range between 1.8 and 400 K, and for a range of applied fields between 0 and 5 T with a specified lower detection limit of 1×10^{-8} emu, was used (Figure 25).
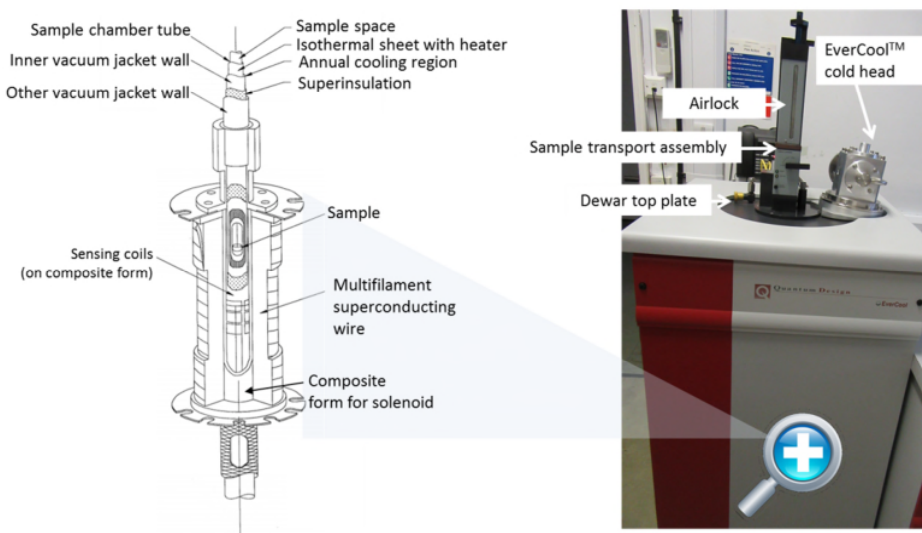
Figure 25: The MPMS XL SQUID magnetometer, equipped with an EverCool® system, on right, and a schematic representation of the MPMS magnet, sample space and sensing components [133].

An accurate amount ($\approx$ 30 mg) of unground sample was placed into a custom-made quartz tube (5 mm, diameter, thin walled, Suprasil high-grade SiO_2 glass). The tube was fitted with Swagelok Ultra-Torr fitting equipped with J-Young tap in order to keep the sample under Ar atmosphere, while transferring it from the glove box to the high-vacuum Schlenk line. Afterwards the sample was evacuated (5×10^{-5} mbar), backfilled with 300-500 mbar of pure He gas and flame (CH_3/O_2 mixture) sealed. Measurements of χ *vs. T* at various magnetic fields (B), using both zero-field (ZFC) and field cooled (FC) protocols, and *M vs. B* at various temperatures were performed on the samples. Temperature dependent measurements of magnetic susceptibility (χ) at 0.5-5 mT and low-temperature, to investigate the ground states, and at 1 T, to extract effective

moment (μ_{eff}) and Weiss temperature (θ_W) by fitting the data to the Curie-Weiss law, were performed on all samples. In $Cs(C_{14}H_{10})$ a broad hump in χ vs. T was observed, associated with low-dimensional magnetism. According to the structural motifs the curve was fitted to S = ½ 1D Ising chain and quasi 1D alternating chain models. The magnetic susceptibility data was fitted to the Bonner-Fisher expression of a finite chain in the Ising limit [134,124] (Equation 2.13), with the help of Dr. Hiroyuki Okazaki.

$$\chi(T) = \frac{C}{T} e^{-\frac{J}{k_B T}} \left[\frac{1-\left\{-\tanh\left(\frac{J}{2k_B T}\right)\right\}^N}{1+\left\{-\tanh\left(\frac{J}{2k_B T}\right)\right\}^N} \right] \qquad \text{Equation 2.13}$$

Where C is Curie constant, J the intrachain exchange constant and N ($\rightarrow\infty$) the chain length. The fitting to a S = ½ Heisenberg quasi 1D alternating chain [135] model was performed by colleagues in the Prof. Prassides' group.

2.3.3 Experimental details of electron paramagnetic resonance (EPR) spectroscopy measurements.

$Rb_2(C_{14}H_{10})_2(THF)$, $Cs(C_{14}H_{10})$, $Cs_2(C_{14}H_{10})$ compounds were sent to Prof. Denis Arčon at Jožef Stefan Institute (Ljubljana, Slovenia) to perform EPR spectroscopy measurements, in order to further investigate magnetism in these materials.

The samples were thoroughly ground in an agate mortar and accurate amounts ($\approx$ 10 mg) of materials were placed into Suprasil quartz tubes, evacuated under dynamic vacuum and flame-sealed.

The X-band (Larmor frequency~9.6 GHz) EPR experiments were performed on cooling with a home-built spectrometer equipped with a Varian E-101 microwave bridge and TEM104 dual-cavity resonator and an Oxford Instruments ESR900 cryostat with ITC503 temperature controller (stability, ±0.05 K). In all experiments, the microwave power was 1 mW.

2.4 Experimental details of infrared (IR) and Raman spectroscopy measurements.

IR measurements of KBr pellets containing a small amount of sample were prepared and measured by Dr. Gyöngyi Klupp inside the Ar-filled glove box and measured with a Bruker Alpha spectrometer operating in transition with a resolution of 2 cm^{-1}.

Raman spectra were collected by Dr. Gyöngyi Klupp in backscattering geometry on samples sealed in glass capillaries (same capillaries as used for powder X-ray diffraction experiments). A Horiba Jobin Yvon LabRAM HR spectrometer equipped with a confocal microscope was used with either a 633 nm (0.37 mW power) or a 532 nm (0.09 mW power) laser focused to a spot of ~1 µm in diameter. It has to be noted that higher laser power led to laser-induced irreversible changes.
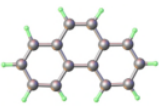
2.5 Experimental details of CHN elemental analysis

An Exeter CE-440 Elemental Analyzer was used to determine the amount of carbon, hydrogen and nitrogen in each synthesized sample. Small tin capsules were pre-weighed on a very accurate analytical balance (±1 µg) and placed into small vials to prevent contamination. Small vials containing tin capsules were, along with sealing tools, transferred into the glove-box (evacuating them and the tools overnight in the glove-box antechamber). Next day a small amount of sample (2-2.5 mg) was placed into three tin capsules, sealed and placed back into the small vials. Additionally, one blank tin capsule was sealed in order to determine accurate masses of the samples in the sealed tin capsules (the density of argon being higher than the density of air). All the vials containing tin capsules were submitted to Durham University elemental analysis service.

3 Chapter 3 – Results

Compounds with a composition of $K_2(C_{14}H_{10})_2(THF)$, $Rb_2(C_{14}H_{10})_2(THF)$, $Cs_2(C_{14}H_{10})_2(THF)$, $Cs(C_{14}H_{10})$, $K_4(C_{14}H_{10})_3(THF)_4$, $Rb_4(C_{14}H_{10})_3(THF)_4$ and $Cs_2(C_{14}H_{10})$ were successfully isolated and characterised. The basic structural and magnetic properties are gathered in Table 4, and these compounds will be described in detail in the Chapter 3.

Table 4: The basic properties of alkali-metal phenanthrides: chemical composition, crystal structure space group and magnetism.

	Potassium	*Rubidium*	*Caesium*	*A : ($C_{14}H_{10}$)*
Phenanthrene	**$K_2(C_{14}H_{10})_2(THF)$** *Fdd*2 Canted antiferromagnet T_N = 2 K (chapter 3.2)	**$Rb_2(C_{14}H_{10})_2(THF)$** *Fdd*2 Canted antiferromagnet T_N = 3.4 K (chapter 3.1)	**$Cs_2(C_{14}H_{10})_2(THF)$** *Cc* Canted antiferromagnet T_N = 9.9 K (chapter 3.3)	**1:1**
	Mixed phase samples obtained	*Mixed phase samples obtained*	**$Cs(C_{14}H_{10})$** $P2_12_12_1$ Low-dimensional antiferromagnet (chapter 3.4)	**1:1**
	$K_4(C_{14}H_{10})_3(THF)_4$ $P\bar{1}$ Localized mixed valence -/2- (chapter 3.5)	**$Rb_4(C_{14}H_{10})_3(THF)_4$** $P\bar{1}$ Localized mixed valence -/2- (chapter 3.6)	*Not formed/ isolated*	**4:3**
	Did not try	*Did not try*	**$Cs_2(C_{14}H_{10})$** $P2_1/a$ Diamagnet (chapter 3.7)	**2:1**

3.1 $Rb_2(C_{14}H_{10})_2(THF)$

3.1.1 Synthesis and crystal growth

Sublimed phenanthrene (159.0 mg, 0.892 mmol) and rubidium metal (77.0 mg, 0.910 mmol, 1wt% excess) were placed on the bottom of the left hand side of a reaction vessel (Figure 13) inside a glove box. Afterwards the reaction vessel was transferred out of the glove-box and placed on a Schlenk line, evacuated and THF (15 ml) was condensed on top of the phenanthrene and potassium. The solution turned olive green and the reaction was left to continue under vigorous stirring for 48 hours, to ensure complete reaction (rubidium metal dissolved/reacted). Then the solution was filtered into the right hand side of the reaction vessel and concentrated, by removing 7 ml of THF. The concentrated solution was layered with oxygen- and water-free n-hexane (30 ml). Crystallisation was carried out for the first five days at room temperature and then for an additional five days at 30°C. The obtained dark green/grey bipyramidal crystals (Figure 26) with purple lustre were washed three times with a new portion of n-hexane and dried under dynamic vacuum for 2 hours. Yield 221.8 mg (77 %). Elemental analysis, calculated (%) for $C_{32}H_{28}ORb_2$ are C 64.13, H 4.67; found C 63.89, H 4.71. Observed average values correspond to $Rb_{1.02}$-Phenanthrene-$THF_{0.54}$ formula.
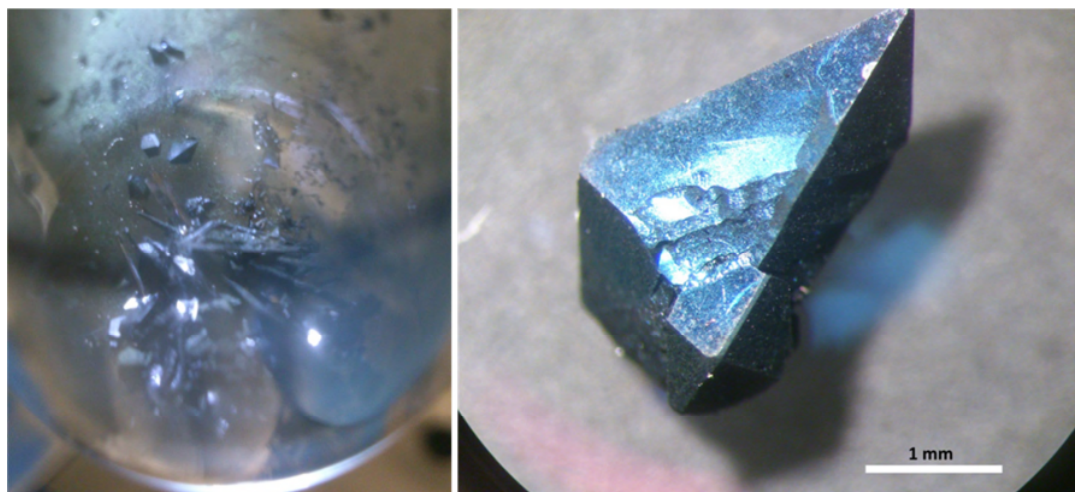
Figure 26: The isolated product in reaction vessel (left panel) and single crystals of $Rb_2(C_{14}H_{10})_2(THF)$ under 40× magnification (right panel). Thick white line represents 1mm length.

3.1.2 Single crystal structural analysis

The $Rb_2(C_{14}H_{10})_2$(THF) compound crystallizes in the orthorhombic *Fdd*2 space group with lattice parameters of a = 17.3215(13) Å, b =26.4735(19) Å and c = 11.1807(9) Å at 120 K. The asymmetric unit cell consists of one phenanthrene radical anion, one rubidium cation and half of the THF molecule. By replicating parts of the asymmetric unit cell, the coordination environment of Rb^+ cations is revealed (Figure 27). The Rb^+ interacts with phenanthride through η^3, η^4 and η^5 coordination modes. The η^3 coordination is between Rb^+ and the rim consisting of C1, C10 and C11 atoms (I and II planes) with distances of 3.100(7)- 3.282(8) Å in length. The η^4 coordination is between Rb^+ and the central benzene ring plane II (C9, C10, C11 and C12) with bond distances ranging from 3.167(8) to 3.432(5) Å. The Rb^+ to plane centroid distance is 3.132(3) Å and cation projection on the ring plane at an angle of 76°. The third η^5 coordination is between Rb^+ and peripheral benzene ring plane III (C5, C6, C7, C8 and C13 atoms) with bond distances of 3.167(7)- 3.621(6) Å in length. The Rb^+ to plane centroid distance is 3.166(3) Å and the angle of Rb^+ projection on the ring plane is 77°. All $Rb^+\cdots C$ and $Rb^+\cdots O$ coordination bond distances are gathered in Table 5 and they are comparable to those reported in rubidium-reduced rubrene, coronene, cyclopentadiene, indene, fluorene and corannulene (Table 6).

The THF located on a two-fold rotation axis is disordered between two orientations in a 50:50 ratio and its oxygen atom is a bridging ligand coordinated to Rb^+ through μ^2 coordination mode. The $Rb^+\cdots O$ distance is 2.873(3) Å and the Rb-O-Rb angle is 111.2 $(2)^o$, which is comparable to those reported in rubidium-reduced rubrene and fluorene (Table 7). The basic parameters obtained from refinement, fractional atomic coordinates, atom to atom bond distances and bond angles for crystal structures obtained from data sets collected at 120 and 290 K are gathered in the Appendix (6.1, 6.3).
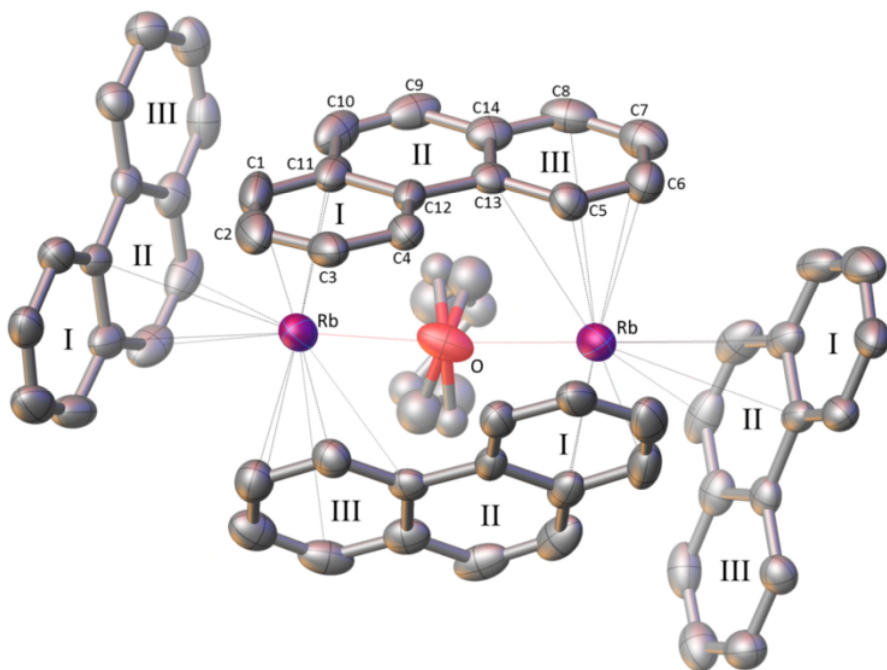
Figure 27: Coordination environment of Rb$^+$ ions in Rb$_2$(C$_{14}$H$_{10}$)$_2$(THF) compound. The two outer benzene ring planes are labelled as I, III, and the central plane as II. Black dotted lines and red dotted lines represent Rb$^+$···C and Rb$^+$···O coordination interactions respectively. Colour code: Rb violet; O red and C grey. Hydrogen atoms are omitted for clarity. Thermal ellipsoids are shown with 50% probability level and the occupancy of carbon atoms in THF molecule were fixed to 0.5. Depicted structure was obtained from data collected at 120 K.

Table 5: Coordination modes and coordination bond distances between rubidium cation and carbon/oxygen atoms extracted from structure obtained at 120 and 290 K.

Coordination mode	Rb$^+$ to C or O bond	Distance (Å) at 120 K	Distance (Å) at 290 K
η^3/ η^4	Rb-C11	3.100(7)	3.090(11)
	Rb-C10	3.266(8)	3.259(14)
	Rb-C1	3.282(8)	3.316(15)
	Rb-C12		3.625(8)
η^4	Rb-C10	3.167(8)	3.217(13)
	Rb-C11	3.172(6)	3.196(10)
	Rb-C9	3.409(8)	3.492(14)
	Rb-C12	3.432(5)	3.487(6)
η^5/ η^4	Rb-C6	3.167(7)	3.190(10)
	Rb-C5	3.263(6)	3.279(9)
	Rb-C7	3.339(7)	3.405(13)
	Rb-C13	3.589(5)	3.655(6)
	Rb-C8	3.621(6)	
μ^2	Rb-O	2.873(3)	2.915(5)

The structure of $Rb_2(C_{14}H_{10})_2(THF)$ can be described as having a triangle-like motif, where two phenanthride molecules (the two molecules in the middle of Figure 27) under an angle of 60.1(2)° with respect to each other and the THF molecule (behind) are forming this motif. Rb^+ cations are encapsulated in this triangle, but also interact with two side phenanthride molecules (left and right) through η^4 coordination mode and thereby forming the 3D polymeric network displayed in Figure 28. A very similar triangle-like motif was reported in potassium-reduced anthracene [72] and fluorene [156]. Moreover, the potassium-fluorenyl, $K_2(C_{10}H_9)_2(THF)$ is isostructural to that of $Rb_2(C_{14}H_{10})_2(THF)$.
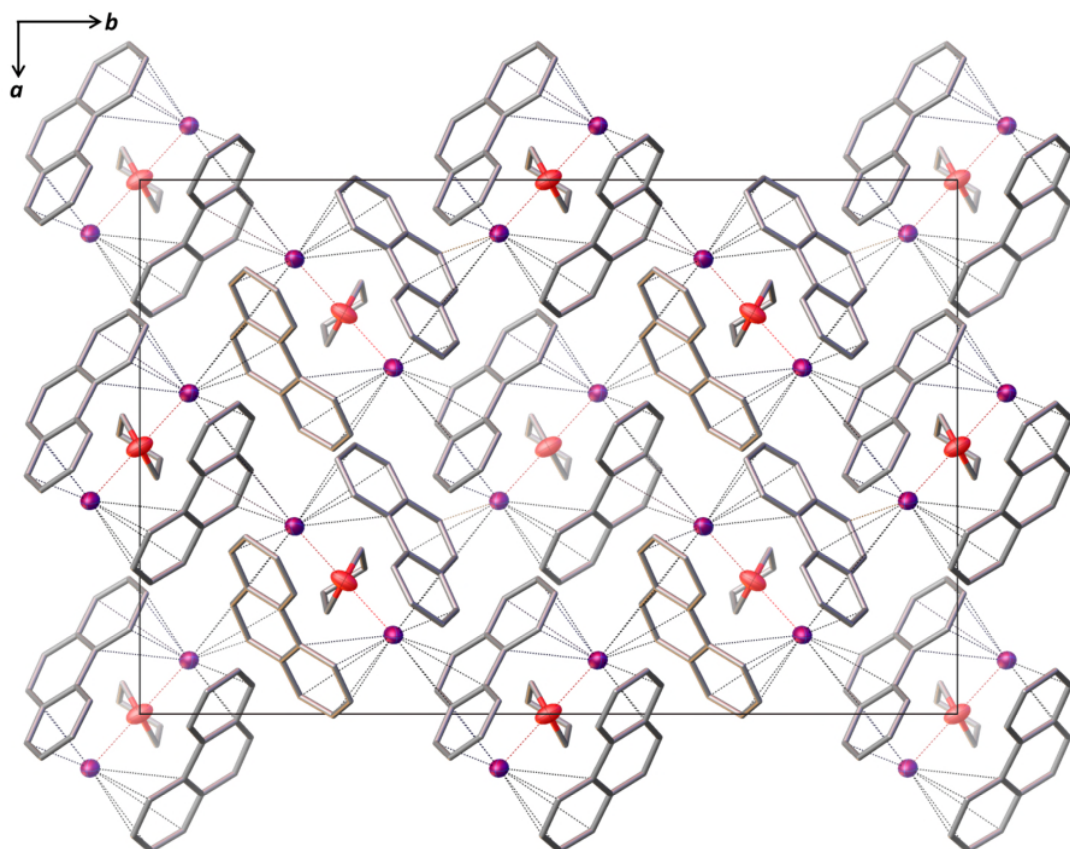
Figure 28: Projection of the $Rb_2(C_{14}H_{10})_2(THF)$ structure along the [001] direction showing the 3D polymeric network of $Rb^+\cdots C$ interaction (black dotted lines) between alkali metal ions and the phenanthride radical anions. One half of disordered THF molecule and hydrogen atoms are omitted for clarity. Colour code: Rb violet; O red and C grey, red dotted lines represent $Rb^+\cdots O$ coordination. Carbon-carbon bonds are depicted as tubes for clarity.

Table 6: Rubidium salts of selected PAHs, observed η coordination modes and Rb^{+}···C distances.

PAH	Compound	Coord.	Distance range (Å)
Rubrene[136]	[{Rb$^+_4$(THF)$_5$}(C$_{42}$H$_{28}$$^{4-}$)]	η^2	3.238(3) − 3.315(3)
		η^4	3.158(3) − 3.586(3)
		η^6	3.101(3) − 3.602(3)
Coronene[137]	[Rb$^+$(18-crown-6)(C$_{24}$H$_{12}$)]	η^3	3.312(8) − 3.545(8)
Cyclopentadiene[138]	[{Rb$^+$(18-crown-6)}(C$_5$H$_5$)]	η^5	3.116(8) − 3.26(1)
Indene[139]	[{Rb$^+$(18-crown-6) }(C$_9$H$_7$)]	η^5	3.178(4) − 3.209(4)
Fluorene	[{Rb$^+$(diglyme)}(C$_{13}$H$_9$$^-$)][140]	η^2	3.301(8) − 3.451(7)
		η^3	3.313(7) − 3.565(7)
		η^5	3.198(8) − 3.311(8)
	[{Rb$^+$(PMDTA)}(C$_{13}$H$_9$$^-$)][141]	η^3	3.156(1) − 3.508(2)
		η^5	3.213(1) − 3.411(2)
	[{Rb$^+$(18-crown-6)(THF)}(C$_{13}$H$_9$$^-$)][139]	η^5	3.24(1) − 3.58(3)
Corannulene[142]	[{Rb$^+$(18-crown-6)}(C$_{20}$H$_{10}$$^-$)]	η^4	3.273(3) − 3.479(3)

Table 7: Rubidium salts of selected PAHs and their Rb^{+}···O distances.

PAH	Compound	Coord.	Distance range (Å)
Rubrene[136]	[{Rb$^+_4$(THF)$_5$}(C$_{42}$H$_{28}$$^{4-}$)]	terminal	2.813(3) − 2.931(3)
		bridging	2.830(3) − 2.987(3)
Fluorene	[{Rb$^+$(18-crown-6)(THF)}(C$_{13}$H$_9$$^-$)][139]	terminal	3.45(1)

The temperature dependence of the unit cell parameters obtained from single crystal diffraction, shown in Figure 29 and 30, reveal a subtle contraction of *a* upon heating, while *b* and *c* follow a normal thermal expansion. Since the contraction of lattice parameter *a* is small, the volume still exhibits a normal thermal expansion. The comparison of coordination bond distances between Rb^{+}···C and Rb^{+}···O in the structures obtained at 120 and 290 K are gathered in Table 5. It was observed that Rb^{+}···C10 and Rb^{+}···C11 bond distances, which are part of an η^3 bonding of Rb^{+} to the outer rim of benzene ring plane II, marginally contract (almost staying the same) upon heating. All other Rb^{+}···C and Rb^{+}···O bond distances follow normal thermal expansion.

The combination of the marginal shortening of Rb^{+}···C10 and Rb^{+}···C11 bond distances and elongation of Rb^{+}···C5, Rb^{+}···C6, Rb^{+}···C7 and Rb^{+}···C13 bond distances result in the rotation of phenanthride along the C_2 axis (running through the oxygen atoms) as shown in Figure 31. The observed retention of Rb^{+}···C10 and Rb^{+}···C11 bond distances takes place in both phenanthrene radical anions in the Rb$_2$(C$_{14}$H$_{10}$)$_2$(THF) dimer unit, and this rigid rotational motion facilitates the rotation of the neighbouring dimers

connected to the first molecules. Furthermore, this structure can be viewed as an orthorhombically distorted zinc-blende-type structure, which is known to support negative thermal expansion [143, 144, 145], built of $Rb_2(C_{14}H_{10})_2(THF)$ dimers. A presentation of a pseudotetrahedron consisting of $Rb_2(C_{14}H_{10})_2(THF)$ dimers, for instance a dimer **T** at (¼, ¼, ¼) has four nearest neighbours: **O** at (0, 0, 0), **AC** at (½, 0, ½), **AB** at (½, ½, 0) and **BC** at (0, ½, ½), and the observed rotations of dimers are depicted in Figure 31. The movement of dimers is such that upon heating the **O**-**AC** interdimer separation remains practically unchanged, while all others expand.
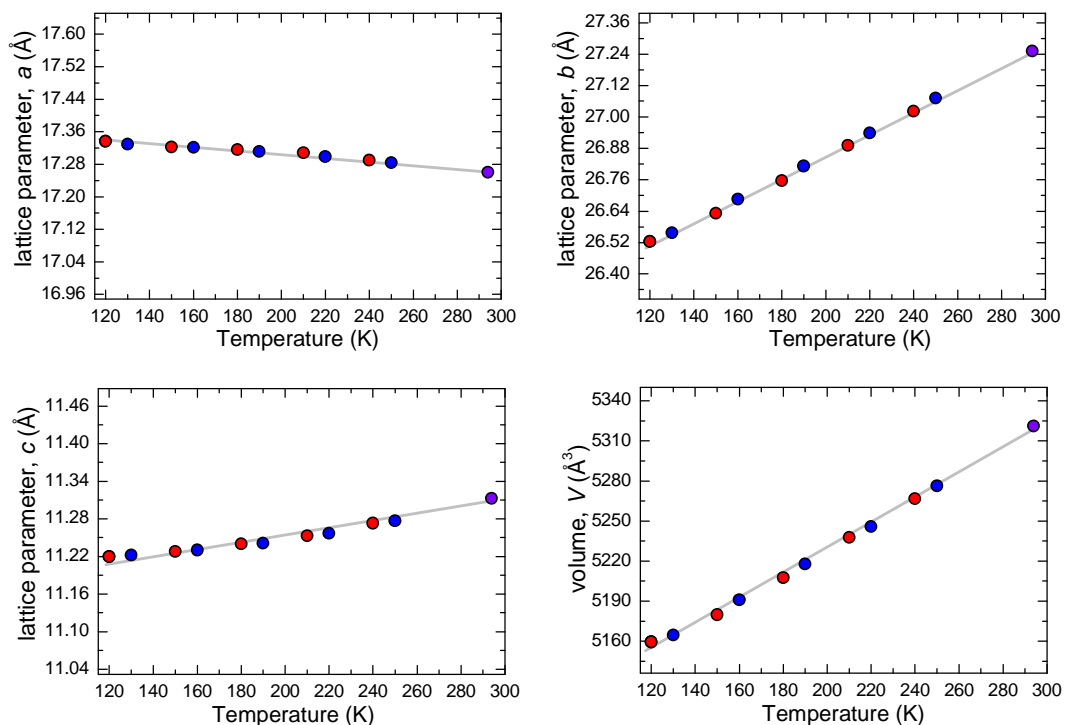
Figure 29: The temperature dependence of the lattice parameters *a*, *b*, *c* and volume (*V*). Blue and red circles represent values obtained upon cooling and heating respectively. Violet circles correspond to parameters obtained from Rietveld refinement of diffraction profile collected at 294 K. Grey lines are guides to the eye.
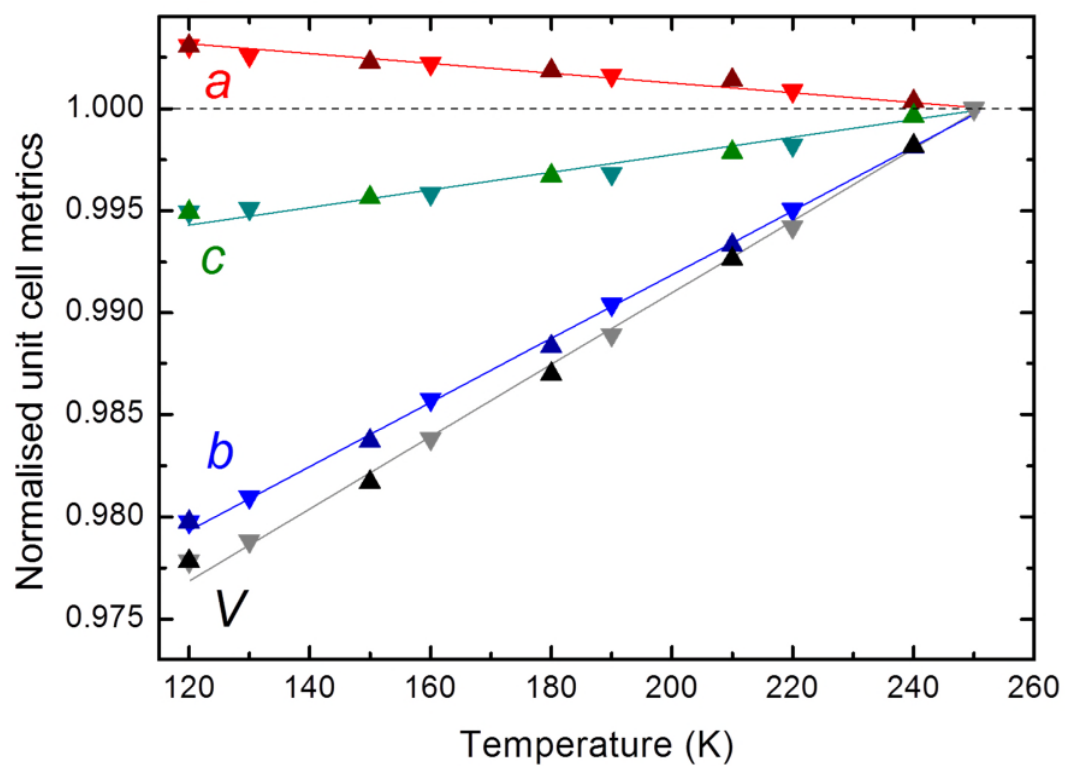
Figure 30: The temperature dependence of the unit cell parameters normalised to those at 250 K. The upside-down and upward facing triangles represent parameters obtained upon cooling and heating respectively. Lines are guides to the eye.
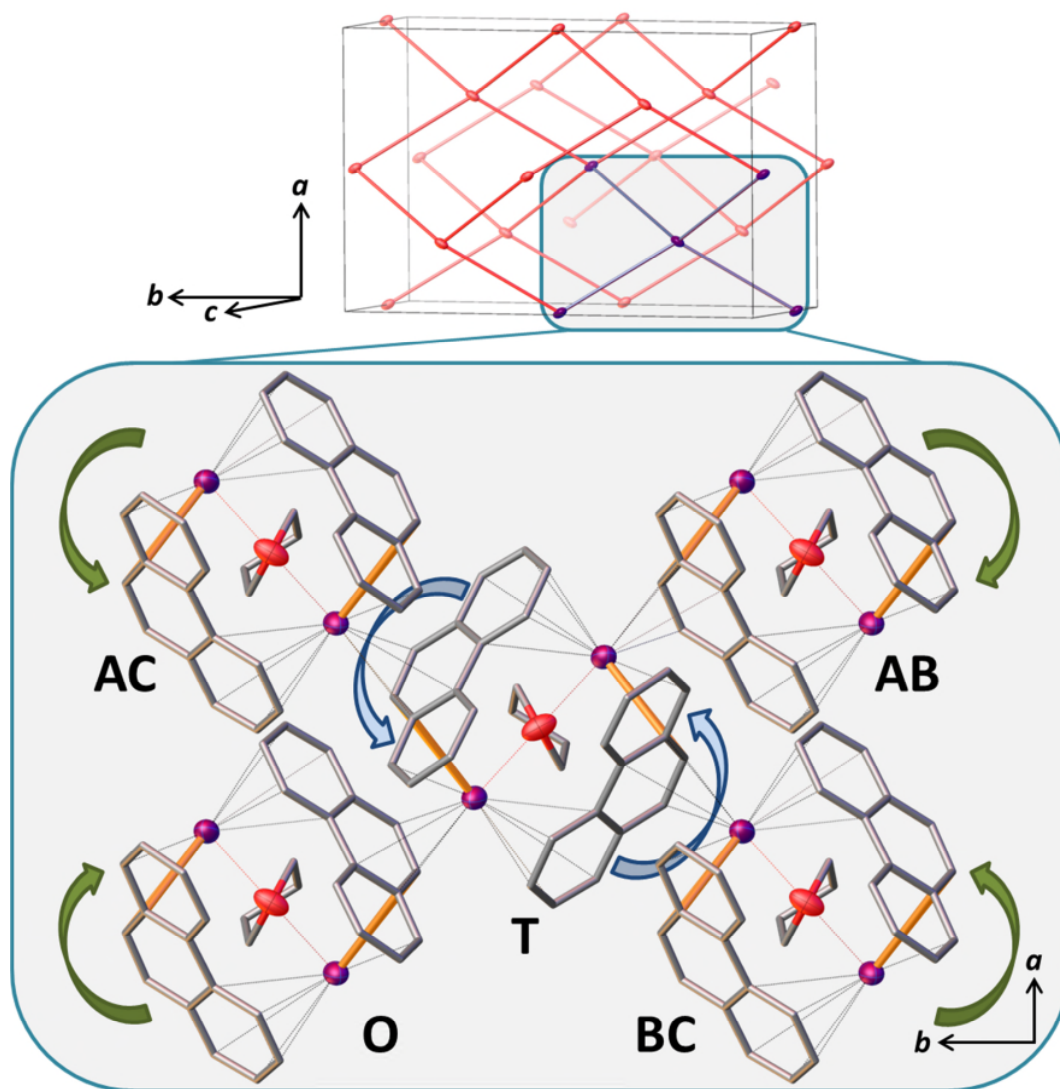
Figure 31: Top; the $Rb_2(C_{14}H_{10})_2(THF)$ dimers arranged in an orthorhombically distorted zinc blende lattice. Only oxygen atoms of the THF molecules are shown for clarity. Bottom; the pseudotetrahedron formed by the nearest neighbour dimers projected along [001] crystallographic direction. Blue arrows represent the thermal movement of phenanthrene radical ions in dimer T and green arrows the movement of dimers relative to dimer T, the direction of the subtle contraction of $Rb^+ \cdots (C_{14}H_{10})^{\bullet -}$ distances is shown in orange. The rotational motion is in balance with the normal thermal expansion and thereby, the **O-AC** distance remains practically constant. The dimers are labelled according to their position in the lattice (see text). Hydrogen atoms are omitted and C-C bonds are depicted as tubes for clarity.

3.1.3 Powder X-ray diffraction

The structural models obtained from single crystal analysis at 120 and 290 K were refined (Rietveld refinement) using the EXPO2014 program suite on the powder diffraction profile collected at 294 K on a laboratory source (λ = 0.7093 Å). The extracted lattice parameters are a = 17.2527(9) Å, b = 27.2386(13) Å and c = 11.3081(6) Å, and a = 17.2606(8) Å, b = 27.2515(12) Å and c = 11.3129(6) Å for structural models obtained at 120 and 290 K respectively. The unit cell parameters are very similar and the a slightly contracts upon heating, giving rise to subtle negative thermal expansion as described in section 3.1.2. Results of the Rietveld refinement for the structural model obtained at 290 K are shown in Figure 32.
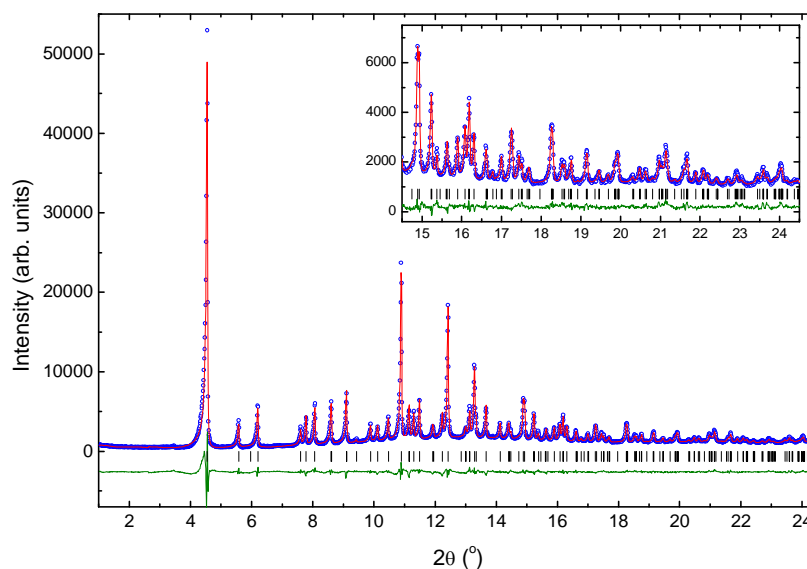
Figure 32: Powder diffraction of the rubidium phenanthride sample. The experimentally obtained diffraction profile (λ = 0.7093 Å, Mo Kα) at 294 K (blue open circles), the calculated profile (red solid line), difference (olive green solid line) and predicted peak position (black tick marks). The inset shows high 2θ region. The weight profile and expected R factors are R_{wp} = 7.606% and R_{exp} = 2.334%.

An excellent agreement between observed and calculated diffraction profiles indicates a phase-pure sample in the bulk. Additionally, elemental analysis (CHN) confirmed the phase-purity of the sample.

3.1.4 Vibrational Spectroscopy

Infrared (IR) and Raman vibrational spectroscopies were used for following the charge transfer from rubidium metal to the phenanthrene molecule. The vibrational peaks of the phenanthrene radical anion are red-shifted in comparison to those observed in neural phenanthrene, indicating the softening of the modes upon reduction as shown in Figure 33. Similar behaviour was found in other alkali metal reduced carbon based systems such as intercalated graphite [146] and fullerenes [147]. Donation of the electron into an anti-bonding orbital is reflected in subtle elongation of the bond distances in phenanthride, which were observed by X-ray diffraction and are related to the lowering of vibrational frequencies. The tentative assignment of vibrational peaks is gathered in Table 50 and 51 (Appendix 6.9). The vibrational modes of THF were not detected in the Raman spectra, despite unambiguous confirmation of THF presence by X-ray diffraction and CNH analysis, due to the expected considerably larger Raman cross section of the conjugated π-electron system in comparison to that of aliphatic organic molecules [148, 149].
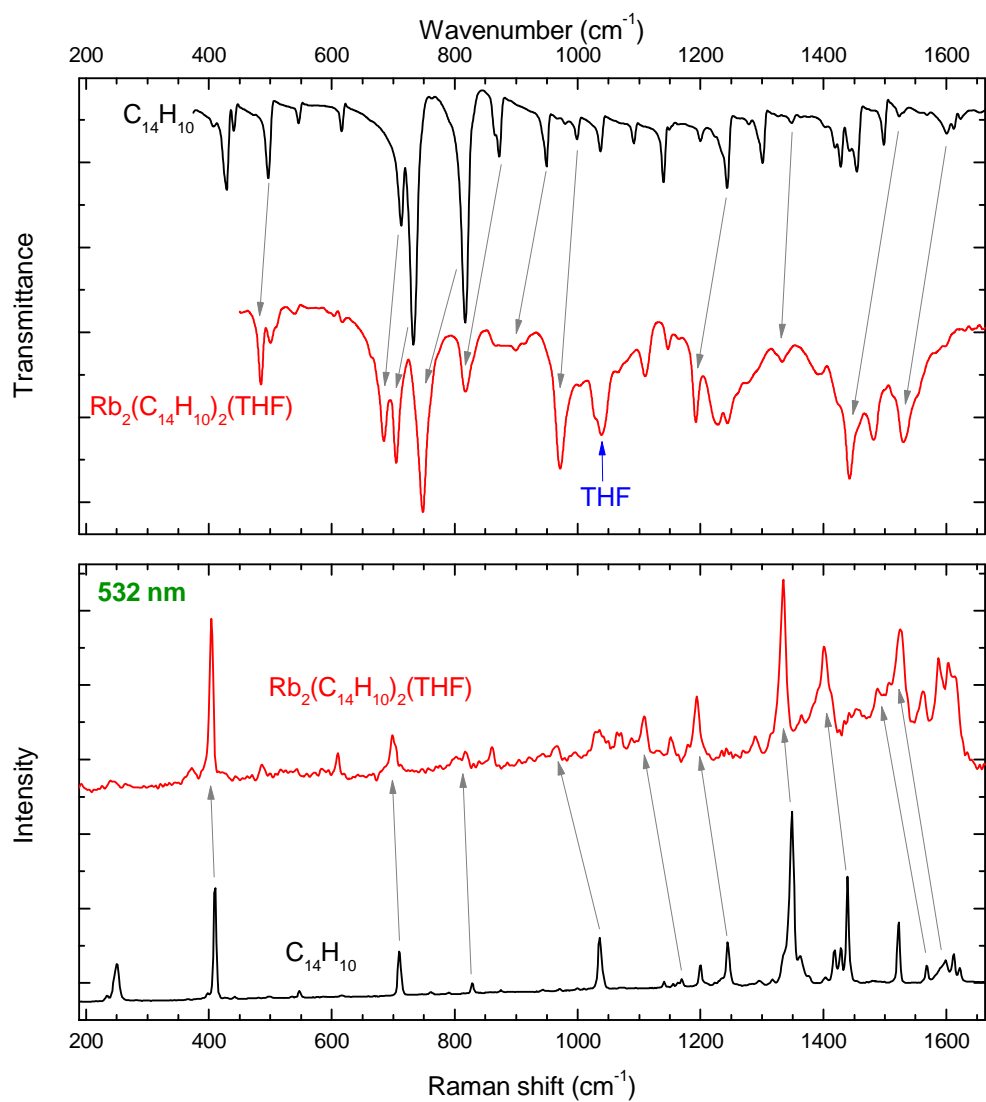
Figure 33: The infrared (top panel) and Raman (bottom panel) spectra of $Rb_2(C_{14}H_{10})_2(THF)$ (red solid line) and pristine phenanthrene (black solid line). Grey arrows represent a tentative red-shift of some peaks and the blue arrow represents the peak corresponding to C-O stretching mode in THF molecule. Raman spectrum was taken using a 532 nm excitation wavelength.

3.1.5 Magnetic Properties

The temperature dependence of magnetic susceptibility (χ) and $1/\chi$ of $Rb_2(C_{14}H_{10})_2$(THF) in an applied magnetic field of 1 T along with a Curie-Weiss fit and linear fit are shown in Figure 34.

In the high temperature region, above 90 K, the magnetic susceptibility follows the Curie-Weiss law, however, at lower temperature the susceptibility increases much faster than the law predicts. By fitting the data to a Curie-Weiss law in the temperature region between 90 and 300 K, an effective magnetic moment, μ_{eff} = 1.867(4) μ_B and negative Weiss temperature, Θ = -68.1(3) K were obtained (a linear fit to $1/\chi$ vs. T curve yielded almost identical values). The effective moment of 1.867(1) μ_B is in good agreement with the value of 1.73 μ_B expected for a spin ½ state, confirming the presence of a single unpaired electron per phenanthrene molecule in the $Rb_2(C_{14}H_{10})_2$(THF) compound. The negative Weiss temperature of -68.1(3) K indicates the presence of antiferromagnetic (AFM) exchange interactions.
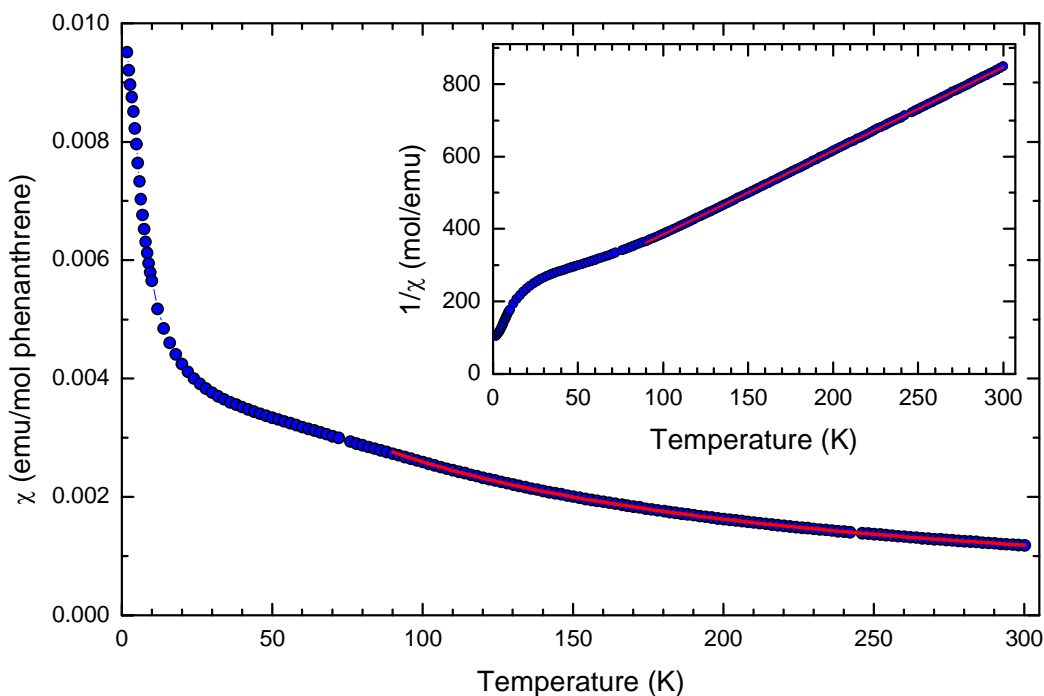
Figure 34: The temperature dependence of molecular susceptibility (χ vs. T) of the $Rb_2(C_{14}H_{10})_2$(THF) compound at an applied field of 1 T (blue circles) along with fit to Curie-Weiss law in temperature region between 90 and 300 K (red curve). Inset shows the $1/\chi$ vs. T plot (blue circles), with a corresponding linear fit in 90 to 300 K temperature region. Data collected in a field-cooled (FC) protocol upon heating.

The temperature dependence of field-cooled (FC) and zero-field-cooled (ZFC) magnetization measurements at various applied fields (0.5, 1, 10 and 100 mT) are plotted in Figure 35.

A well-defined cusp at low temperatures, observed in all measurements signals the onset of long-range AFM ordering with a Neel temperature (T_N) of 3.5 K. Moreover, an irreversible bifurcation of ZFC and FC curves below 3.8 K, at a small applied field of 0.5 and 1 mT, indicates the presence of a weak ferromagnetic component arising from canted spins. Therefore, this material can be classified as a canted antiferromagnet. The splitting between the ZFC and FC curves decreases with increasing applied field and completely vanishes at fields higher than 0.1 T. Likewise, the intensity of the cusp is suppressed with applied field and at high-fields such as 1 T it can no longer be observed.

The detection of the onset of long-range magnetic ordering below 3.8 K is consistent with the observed hysteretic behaviour of the field dependence measurements of the magnetization, *M vs. B*, below the ordering temperature as depicted in Figure 36.
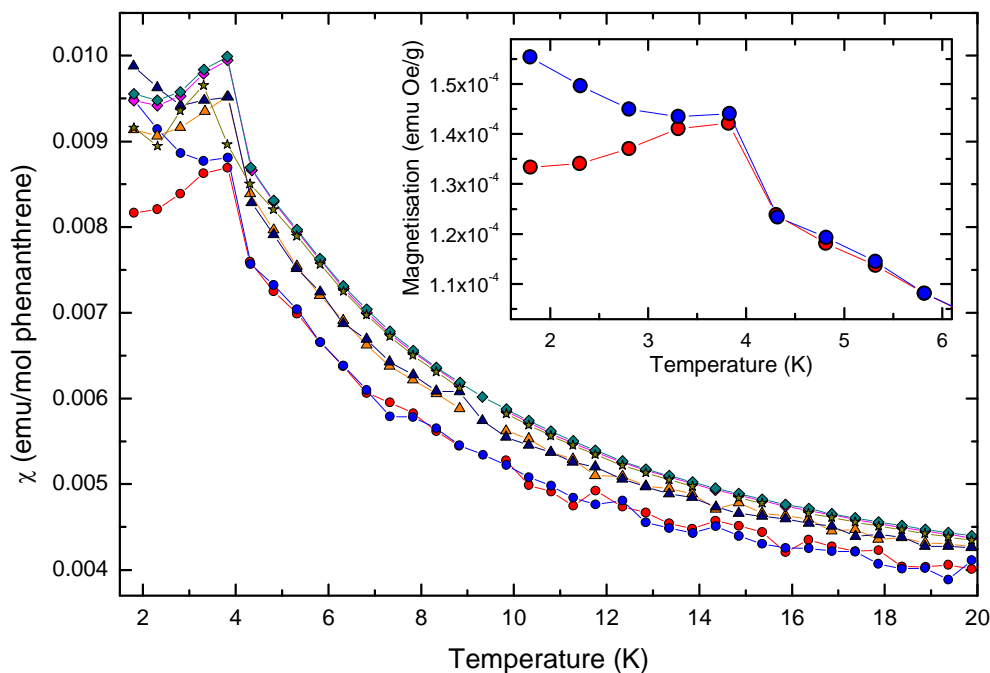
Figure 35: The temperature dependence of molecular susceptibility (χ) of Rb$_2$(C$_{14}$H$_{10}$)$_2$(THF) at *B* = 0.5 mT (ZFC red and FC blue circles), 1 mT (ZFC orange and FC navy blue triangles), 10 mT (ZFC magenta and FC cyan blue rectangles) and 0.1 T (ZFC dark yellow stars). Inset: temperature dependence of magnetisation, *M vs. T* at *B* = 0.5 mT in ZFC (red circles) and FC (blue circles) measuring protocol upon heating.
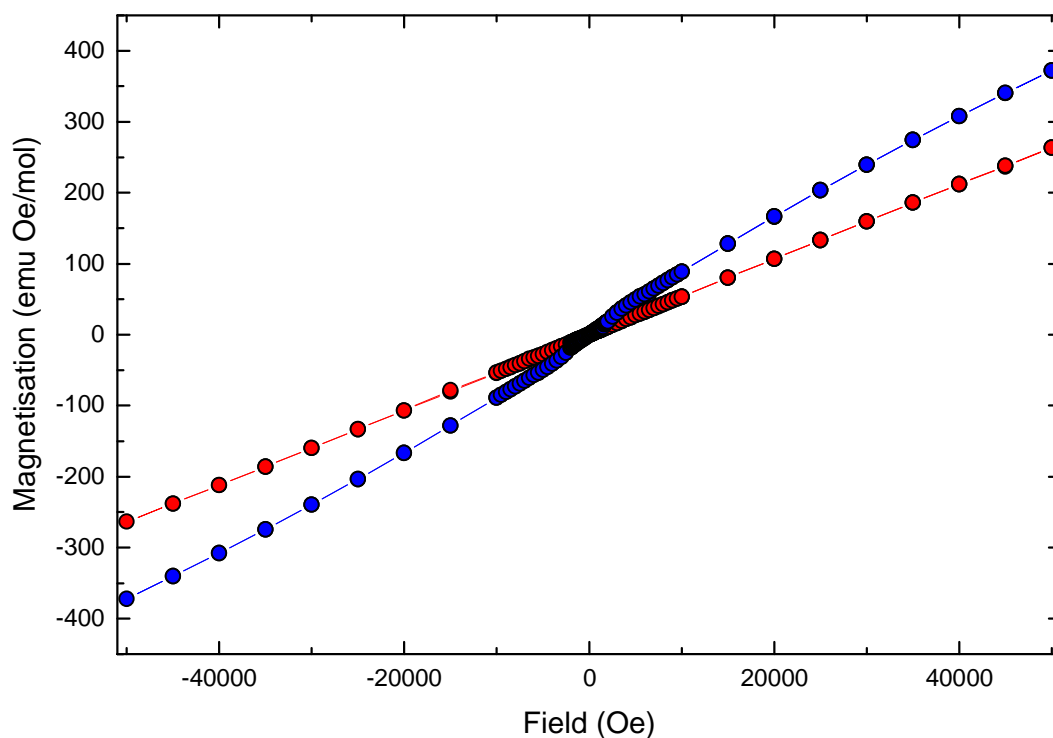
Figure 36: The isothermal magnetic field dependence of magnetisation of Rb$_2$(C$_{14}$H$_{10}$)$_2$(THF) compound (*M vs. H*) at 1.8 K (blue circles) and at 10 K (red circles).

For additional investigation of magnetism in this compound by EPR spectroscopy, the sample was sent to Prof. Denis Arčon at Jožef Stefan Institute (Ljubljana, Slovenia). The loss of the paramagnetic signal and appearance of a new resonance at a lower magnetic field at 3.4 K observed by antiferromagnetic resonance EPR spectroscopy confirmed the onset of long-range AFM ordering [150].

3.1.6 Summary of $Rb_2(C_{14}H_{10})_2$(THF) compound

Reducing phenanthrene with an equimolar amount of rubidium metal in THF at room temperature, followed by crystallisation at 30 ^{o}C, yielded a single-crystalline phase-pure monoanion containing a salt of phenanthrene. Single crystal X-ray diffraction analysis revealed the bipyramidal crystals to be $Rb_2(C_{14}H_{10})_2$(THF), whose asymmetric unit-cell comprises one phenanthrene radical anion, one rubidium cation and half of a THF molecule. Two phenanthride and one THF molecule form a triangle-like motif, encapsulating two rubidium cations. The coordination sphere of rubidium cations is completed with interactions with an additional phenanthride unit at each site of the triangle-like arrangement. These additional coordinating interactions establish a 3D polymeric network. The determination of the crystal structure at 120 and 290 K, and consequent unit cell determination at intermediate temperatures, revealed a subtle negative thermal expansion of the lattice parameter a. The rest of the lattice parameters follow normal thermal expansion.

Vibrational infrared and Raman spectroscopies confirmed the charge transfer from rubidium metal to the phenanthrene molecule. The red-shift of vibrational bands of phenanthride in $Rb_2(C_{14}H_{10})_2$(THF) indicates the softening of the vibrational modes which reflects the subtle elongation of the bond distances in the phenanthride ion.

Fitting of the temperature-dependent magnetic susceptibility data to a Curie-Weiss law yielded an effective magnetic moment of 1.867(1) μ_B and negative Weiss temperature of -68.1(3) K. The obtained values are in good agreement with S = ½ spin state per phenanthrene and the relatively large negative Weiss temperature signals an antiferromagnetic exchange interactions. The magnetisation measurements at low applied field, 0.5 to 10 mT, revealed a bifurcation between the ZFC and FC curves below 3.8 K, indicating the presence of a weak ferromagnetic component that could be associated with the onset of long-range magnetic ordering. The observation of antiferromagnetic resonance unambiguously confirmed the long-range magnetic ordering.

3.2 $K_2(C_{14}H_{10})_2(THF)$

3.2.1 Synthesis and isolation

Sublimed phenanthrene (117.3 mg, 0.658 mmol) and potassium metal (25.7 mg, 0.657 mmol) were placed on the bottom of the left hand side of a reaction vessel inside a glove box. Afterwards the reaction vessel was transferred out of the glove-box and placed on a Schlenk line, evacuated and THF (32 ml) was condensed on top of the phenanthrene and potassium. The solution turned olive green and the reaction was left to continue under vigorous stirring for 24 hours, ensuring the reaction to complete (all potassium metal dissolved/reacted). Then the solution was filtered and concentrated, by removing all THF. The polymeric-like slurry was layered with oxygen- and water-free n-hexane (27 ml). In the course of 2 days the slurry turned into a dark green/grey crystalline-like solid (Figure 37). The product was washed with a new portion of n-hexane and dried under dynamic vacuum for 5 hours. Yield 130.6 mg (78%). Elemental analysis, calculated (%) for $C_{32}H_{28}K_2O$: C 75.84, H 5.57; found C 72.71, H 5.24. Observed values correspond to $K_{1.28}$-Phenanthrene-$THF_{0.47}$ formula.
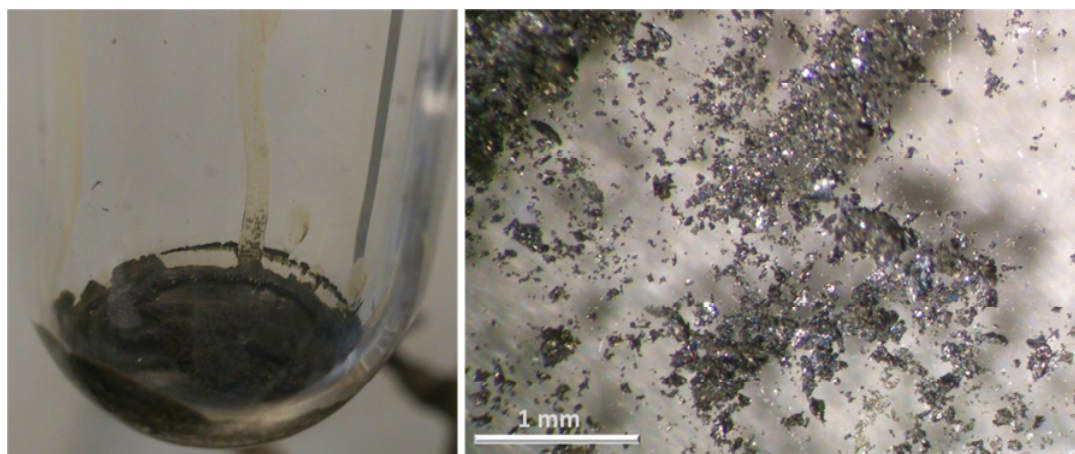
Figure 37: The isolated product in reaction vessel (left panel) and polycrystalline-like solid of $K_2(C_{14}H_{10})_2(THF)$ under 40× magnification (right panel). Thick white line represents 1mm length.

3.2.2 Structural analysis based on powder X-ray diffraction

We were unsuccessful to crystallise and isolate single crystals despite several attempts. However, an obvious similarity between diffraction profiles of $K_2(C_{14}H_{10})_2(THF)$ and $Rb_2(C_{14}H_{10})_2(THF)$ compounds (Figure 38) indicated that these two compounds could be isostructural, and indeed, the Le Bail fitting confirmed this. According to these findings the rubidium atoms were exchanged with potassiums in the structural model of $Rb_2(C_{14}H_{10})_2(THF)$ obtained from data collected at 290 K and this model was afterwards refined to the powder diffraction profile collected at 295 K on a synchrotron source (λ = 0.399959(4) Å). The extracted lattice parameters are a = 16.9460(3) Å, b = 27.2106(3) Å and c = 11.1257(2) Å. Results of Rietveld refinement are shown in Figure 39 and the obtained structural model was further used for analysis of the structure. Excellent agreements between observed and calculated diffraction profiles along with the CHN analysis indicate a phase-pure sample in the bulk.
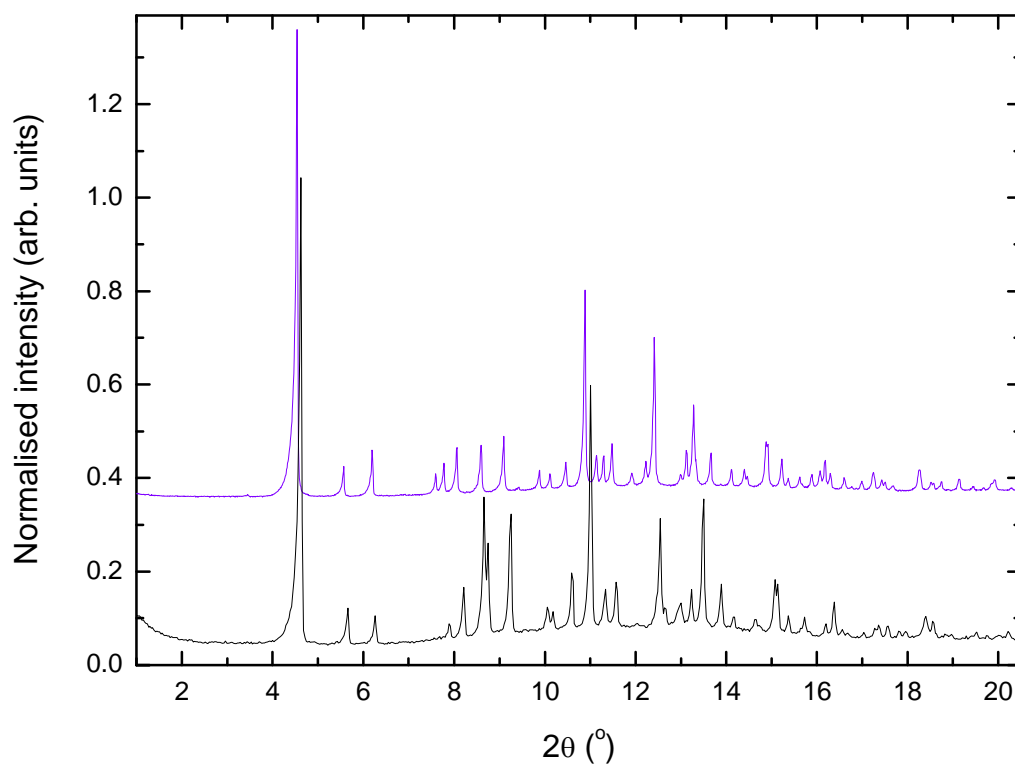
Figure 38: Diffraction profiles of $K_2(C_{14}H_{10})_2(THF)$ (black solid line) and $Rb_2(C_{14}H_{10})_2(THF)$ (violet solid line). The data were collected on a laboratory source (λ = 0.7093 Å, Mo Kα) at 294 K.
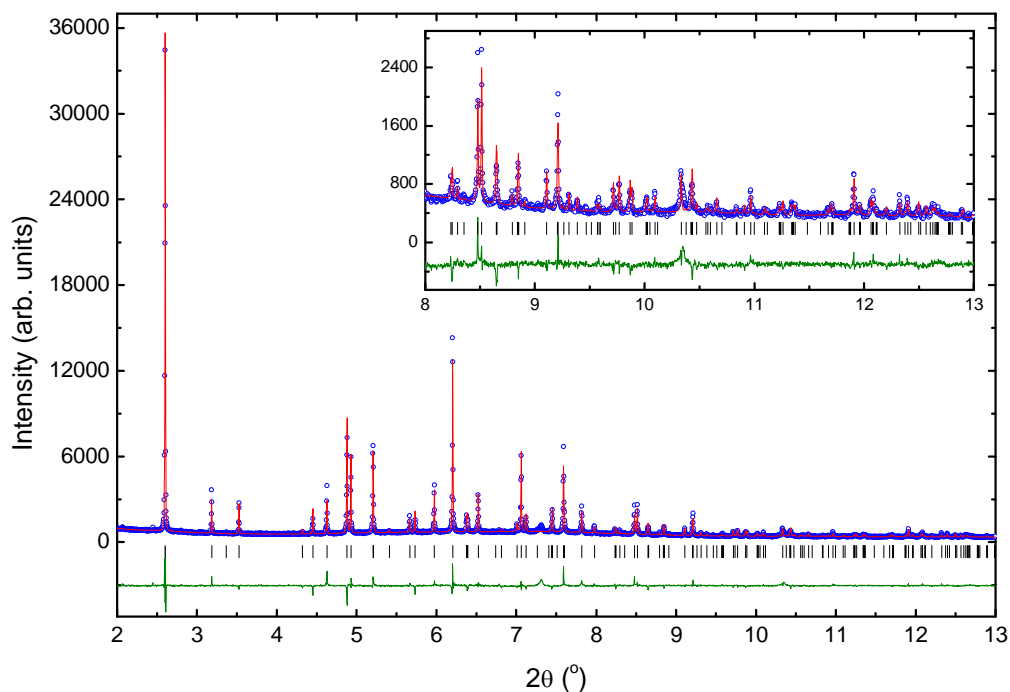
Figure 39: Powder diffraction of the $K_2(C_{14}H_{10})_2$(THF). The experimentally obtained diffraction profile (λ = 0.399959(4) Å) at 295 K (blue open circles), the calculated profile (red solid line), difference (olive green solid line) and predicted peak position (black tick marks). The inset shows high 2θ region. The weight profile and expected R factors are R_{wp} = 7.649% and R_{exp} = 3.757%.

As in the case of the $Rb_2(C_{14}H_{10})_2$(THF) compound, the asymmetric unit cell consists of one phenanthrene radical anion, one potassium cation and half of a THF molecule. The coordination environment of K cations is shown in Figure 40. The potassium cation interacts with phenanthride through two η^3 and one η^4 coordination modes. The first η^3 coordination is between K^+ and the peripheral benzene ring plane III (C5, C6 and C7) with bond distances ranging from 3.243(4) to 3.478(5) Å. The K^+ to plane centroid distance is 3.315(5)Å and the angle of K^+ projection to the ring plane is 74°. The second η^3 coordination is between K^+ and the rim consisting of C1, C10 and C11 atoms (I and II planes) with distances of 2.969(4)- 3.223(4) Å in length. The η^4 coordination is between K^+ and central benzene ring plane II (C9, C10, C11 and C12) with the bond distances ranging from 3.177(5) to 3.448(5) Å. The K^+ to plane centroid distance is 3.168(5) Å and cation projection on the ring plane at an angle of 76°. All $K^+\cdots C$ and $K^+\cdots O$ coordination bond distances are gathered in Table 8 and they are comparable to those reported in potassium-reduced naphthalene, anthracene, tetracene, perylene, coronene,

62

cyclopentadiene, indene, fluorene, bisfluorene, Cp-phenanthrene, corannulene, sumanene, decacyclene and [8]CPP (Table 9).

The oxygen atom in the disordered THF molecule (located on a two-fold rotation axis) is a bridging ligand coordinated to K^+ through a μ^2 coordination mode, as also observed in the rubidium analogue. The $K^+\cdots O$ distance is 2.888(4) Å and the K-O-K angle is 109.2 (1)°, comparable to those reported in potassium-reduced naphthalene, anthracene, perylene, coronene, fluorene, Cp-phenanthrene, sumanene and [8]CPP (Table 10). The basic parameters obtained from refinement, fractional atomic coordinates, atom to atom bond distances and bond angles of the $K_2(C_{14}H_{10})_2$(THF) crystal structure are gathered in the Appendix (6.3).
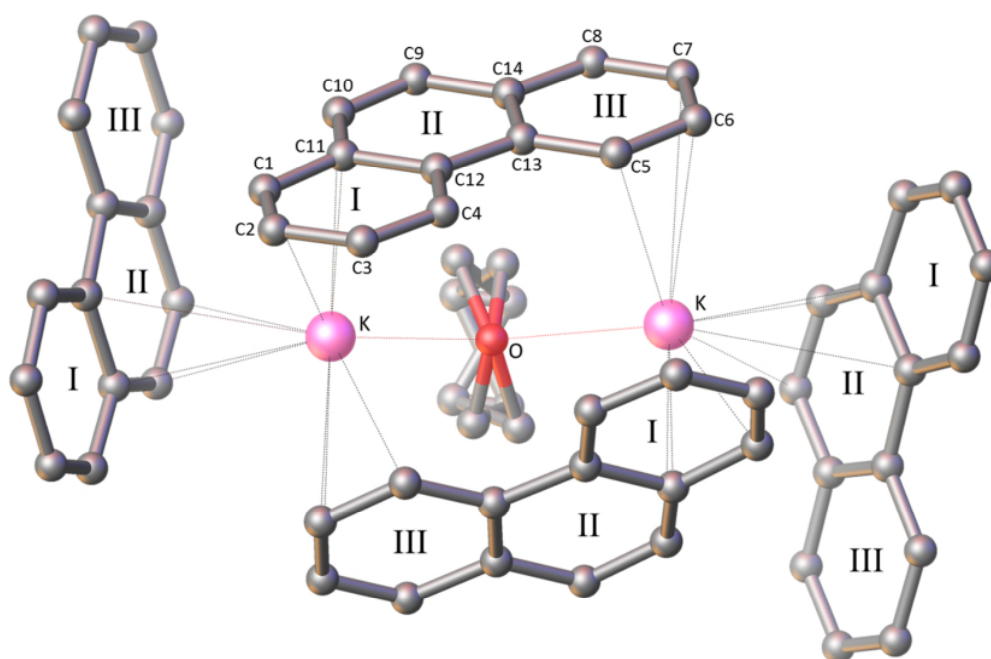
Figure 40: Coordination environment of K^+ ions in $K_2(C_{14}H_{10})_2$(THF) compound. The two peripheral benzene ring planes are labelled as I, III, and central plane as II. Black dotted lines and red dotted lines represent $K^+\cdots C$ and $K^+\cdots O$ coordination interactions respectively. Colour code: K lilac; O red and C grey. Hydrogen atoms are omitted for clarity. The occupancy of carbon atoms in THF molecule were fixed to 0.5 and depicted structure was obtained from data collected at 295 K.

Table 8: Coordination modes and coordination bond distances between potassium cation and carbon/oxygen atoms extracted from structure obtained at 295 K.

Coordination mode	K⁺ to C or O bond	Distance (Å)
η^3	K-C6	3.243(4)
	K-C5	3.324(4)
	K-C7	3.478(5)
η^3	K-C11	2.969(4)
	K-C10	3.122(5)
	K-C1	3.223(4)
η^4	K-C11	3.117(5)
	K-C10	3.189(4)
	K-C9	3.432(3)
	K-C12	3.448(5)
μ^2	Rb-O	2.888(4)

Similarly as in the rubidium analogue, the structure of $K_2(C_{14}H_{10})_2$(THF) could be described as consisting of triangle-like motifs, which are formed by two phenanthride molecules (the middle ones depicted in Figure 40) under an angle of $61.4(1)^o$ $(61.1(3)^o$ in Rb analogue at 290 K) with respect to each other and a THF molecule (behind). The encapsulation of potassium cations is achieved with this triangle and two side phenanthride molecules (left and right) interacting through a η^4 coordination mode. This arrangement of molecules and the K^+ ions is a 3D polymeric network depicted in Figure 41. The observed triangle motif is very similar to that reported in potassium-reduced anthracene [72] and fluorene [156]. The lattice of the former, $K_2(C_{10}H_9)_2$(THF), is isostructural to that of $K_2(C_{14}H_{10})_2$(THF).
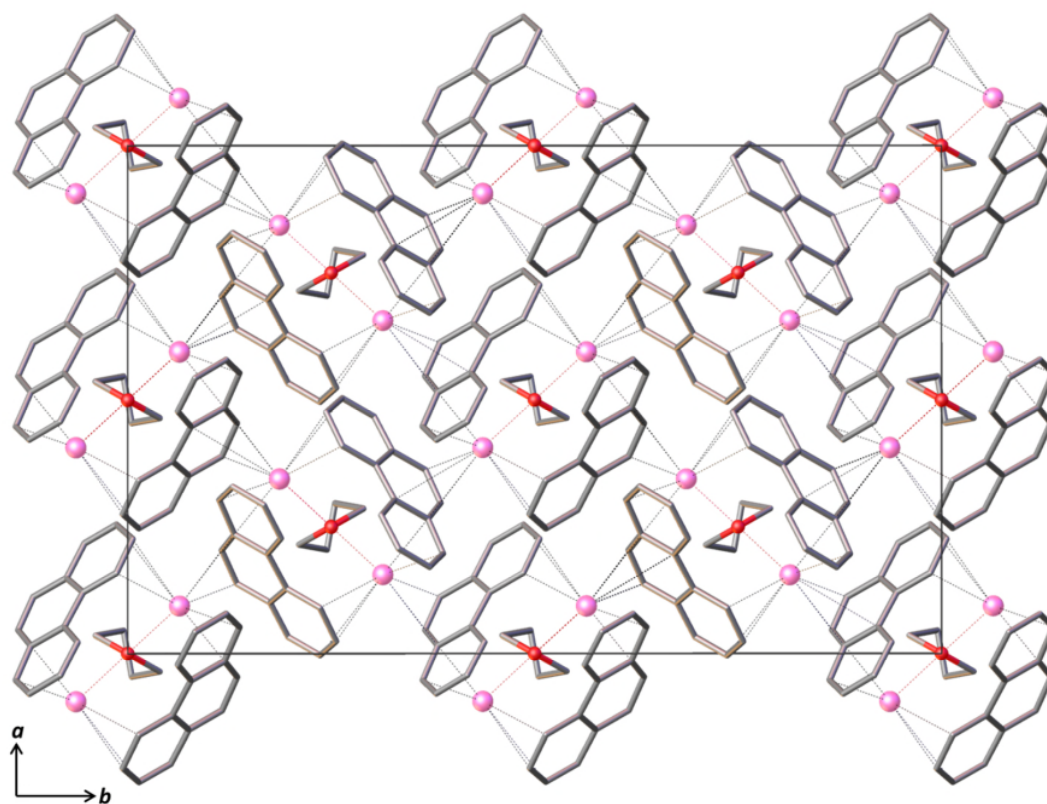
Figure 41: Projection of the $K_2(C_{14}H_{10})_2(THF)$ structure along the [001] direction showing the 3D polymeric network of $K^+\cdots C$ interaction (black dotted lines) between alkali metal ions and the phenanthride radical anions. One half of disordered THF molecule and hydrogen atoms are omitted, and carbon-carbon bonds are depicted as tubes for clarity. Colour code: K lilac; O red and C grey, red dotted lines represent $K^+\cdots O$ coordination.

Table 9: Potassium salts of selected PAHs, observed η coordination modes and $K^+\cdots C$ distances.

PAH	Compound	Coord.	Distance range (Å)
Naphthalene[71]	$[\{K^+_2(THF)\}(C_{10}H_8^-)_2]$	η^6	2.995(3) – 3.523(2)
		η^2	3.095(3) – 3.533(4)
Anthracene[72]	$[K^+_2(THF)_3(C_{14}H_{10}^-)_2]$	η^6	3.066(3) – 3.190(4)
		η^4	3.027(3) – 3.213(4)
	$[K^+_4(THF)_6(C_{14}H_{10}^-)_2(C_{14}H_{10}^{2-})]$	η^6	2.988(2) – 3.191(3)
		η^4	3.136(2) – 3.245(2)
Tetracene[151]	$[\{K^+(tetraglyme)\}_2(C_{18}H_{12}^{2-})]$	η^6	3.044(2) – 3.182(2)
Perylene[152]	$[\{K^+(DME)_2\}_2(C_{20}H_{12}^{2-})]$	η^6	2.994(2) – 3.521(2)
Coronene[153]	$[\{K^+(TMEDA)(THF)_2\}(C_{24}H_{12}^-)$	η^6	3.185(3) – 3.455(4)
		η^5	3.232(4) – 3.467(3)
Cyclopentadiene	$[\{K^+(Et_2O)\}(C_5H_5^-)]$[154]	η^5	2.992(3) – 3.030(2)
	$[\{K^+(18\text{-crown-6})\}(C_5H_5^-)]$[138]	η^5	2.970(7) – 3.130(6)
Indene	$[\{K^+(NH_3)_2\}(C_9H_7^-)\}$[155]	η^5	3.026(1) – 3.255(1)
	$[\{K^+(18\text{-crown-6})\}(C_9H_7^-)\}$[138]	η^5	3.065(3) – 3.153(3)
	$[\{K^+(TMEDA)\}(C_9H_7^-)\}$[154]	η^5	3.046(2) – 3.113(2)
	$[\{K^+(PMDETA)\}(C_9H_7^-)\}$[154]	η^5	3.074(7) – 3.156(9)
		η^3	3.195(2) – 3.305(2)
Fluorene	$[\{K^+(THF)_{0.5}\}(C_{13}H_9^-)]$[156]	η^6	3.083(3) – 3.443(2)
		η^4	3.001(3) – 3.411(3)
		η^3	3.022(3) – 3.480(2)
	$[\{K^+(TMEDA)\}(C_{13}H_9^-)]$[157]	η^5	3.044(3) – 3.424(5)
		η^3	3.074(3) – 3.35(1)
	$[\{K^+(diglyme)\}(C_{13}H_9^-)]$[140]	η^6	3.092(3) – 3.414(4)
		η^5	3.143(3) – 3.370(3)
		η^5	3.041(3) – 3.538(3)
		η^2	3.191(4) – 3.248(4)
	$[\{K^+(18\text{-crown-6})\}(C_{13}H_9^-)]$[138]	η^6	3.239(2) – 3.371(2)
		η^5	3.234(4) – 3.530(4)
		η^3	3.148(7) – 3.349(8)
	$[\{K^+(18\text{-crown-6})(THF)\}(C_{13}H_9^-)]$[139]	η^5	3.234(4) – 3.530(4)
	$[\{K^+(18\text{-crown-6})(DME)\}(C_{13}H_9^-)]$[139]	η^5	3.234(4) – 3.530(4)
Bisfluorene	$[\{K^+(Et_2O)\}_2(C_{26}H_{16}^-)]$[158]	η^5	3.009(5) – 3.149(5)
		η^4	3.132(6) – 3.208(5)
CpPhenanthrene	$[\{K^+(THF)_2\}(C_{17}H_{11}^-]$[159]	η^5	2.986(3) – 3.168(2)
Corannulene[160]	$[\{K^+(18\text{-crown-6})\}(C_{20}H_{10}^-)]$	η^2	3.142(3) – 3.289(2)
	$[\{K^+(18\text{-crown-6})\}_2(C_{20}H_{10}^{2-})]$	η^6	3.052(4) – 3.378(4)
		η^2	3.068(4) – 3.269(4)
		η^5	3.05(2) – 3.29(1)
		η^3	3.15(1) – 3.43(2)
Sumanene[161]	$[\{K^+_7(THF)_8\}(C_{21}H_{10}^{2-})_2(C_{21}H_{10}^{3-})]$	η^6	3.141(5) – 3.343(5)
		η^5	2.967(5) – 3.275(5)
Decacyclene[151]	$[\{K^+(diglyme)\}_4(C_{36}H_{18})]$	η^6	2.865(3) – 3.286(3)
[8]CPP[162]	$[\{K_4^+(18\text{-crown-6})_2(THF)_3\}(C_{46}H_{32}^{4-})]$	η^6	2.942(6) – 3.248(6)
		η^5	3.196(6) – 3.461(6)
		η^4	2.984(6) – 3.086(6)
		η^3	2.903(6) – 3.303(6)
		η^2	3.097(7) – 3.424(7)

Table 10: Potassium salts of selected PAHs and their $K^+ \cdots O$ distances.

PAH	Compound	Coord.	Distance range (Å)
Naphthalene[71]	$[\{K^+_2(THF)\}(C_{10}H_8^-)_2]$	bridging	2.795(2)
Anthracene[72]	$[K^+_2(THF)_3(C_{14}H_{10}^-)_2]$	terminal	2.650(3)
		bridging	2.794(2)
	$[K^+_4(THF)_6(C_{14}H_{10}^-)_2(C_{14}H_{10}^{2-})]$	terminal	2.646(2) − 2.651(2)
		bridging	2.828(2) − 2.855(2)
Perylene[152]	$[\{K^+(DME)_2\}_2(C_{20}H_{12}^{2-})]$	terminal	2.693(2) − 2.922(2)
		bridging	2.861(2) − 2.994(2)
Coronene[153]	$[\{K^+(TMEDA)(THF)_2\}(C_{24}H_{12}^-)$	terminal	2.656(4) − 2.697(3)
Fluorene	$[\{K^+(THF)_{0.5}\}(C_{13}H_9^-)]$[156]	bridging	2.766(2)
	$[\{K^+(18\text{-crown-}6)(THF)\}(C_{13}H_9^-)]$[139]	terminal	3.020(7)
	$[\{K^+(18\text{-crown-}6)(DME)\}(C_{13}H_9^-)]$[139]	terminal	2.889(4)
CpPhenanthrene	$[\{K^+(THF)_2\}(C_{17}H_{11}^-]$[159]	terminal	2.63(3) − 2.79(1)
Sumanene[161]	$[\{K^+_7(THF)_8\}(C_{21}H_{10}^{2-})_2(C_{21}H_{10}^{3-})]$	terminal	2.57(2) − 2.88(2)
		bridging	2.76(3) − 3.04(4)
[8]CPP[162]	$[\{K_4^+(18\text{-crown-}6)_2(THF)_3\}(C_{46}H_{32}^{4-})]$	terminal	2.643(5) − 2.758(7)

A temperature-dependent powder X-ray diffraction experiment, performed on a synchrotron source by using a hot-air blower, revealed that the $K_2(C_{14}H_{10})_2(THF)$ phase is stable up to 80^oC and above that temperature it undergoes a structural phase transition or a transition into a new crystalline material (Figure 42). On the basis of obvious differences between diffraction profiles and because of the volatility of THF at elevated temperatures the latter process seems more plausible. This new crystalline phase is stable in the temperature range between 100 and *ca.* 200^oC and above that temperature the sample became amorphous. The large number of diffraction peaks and peaks at lower 2θ indicate that the new crystalline phase crystallises in a lower-symmetry space group and/or the lattice parameters are considerable larger than in the $K_2(C_{14}H_{10})_2(THF)$ phase. It is plausible to assume that the higher temperature is sufficiently high to trigger the formation of phenanthrene radicals which polymerise further and this polymer or other decomposition products are most likely amorphous. The diffraction profiles obtained during the temperature-dependent powder X-ray experiment are shown in Figure 42.
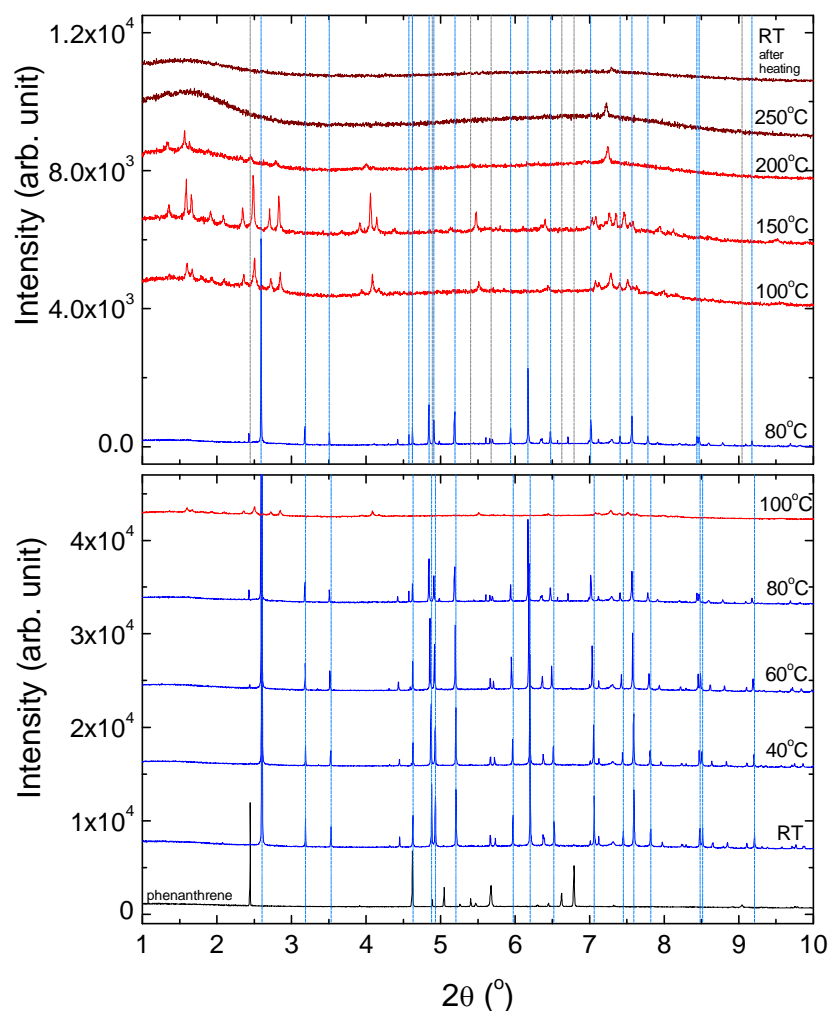
Figure 42: Temperature-dependent powder diffractograms (λ = 0.399959(4) Å). Diffraction profiles of pristine phenanthrene at room temperature (black solid line), $K_2(C_{14}H_{10})_2(THF)$ phase (blue solid line, at 20, 40, 60 and 80°C), newly formed crystalline phase (red solid line, at 100, 150 and 200°C) and temperature degraded amorphous phase (wine red solid line, at 250°C and back at room temperature after heating. The intensities in the upper panel are expanded for clarity. Light blue and grey dotted lines represents positions of the most intense peaks in the $K_2(C_{14}H_{10})_2(THF)$ phase and pristine phenanthrene respectively.

The Le Bail decomposition method was used to extract the unit cell parameters at 22 (room temperature), 40, 60 and 80°C to follow the thermal expansion. The temperature dependence of the unit cell parameters obtained from powder diffraction are gathered in Table 11 and shown in Figure 43.

Table 11: The unit cell parameters obtained from diffraction profiles taken on a synchrotron source, by using Le Bail decomposition method.

Cell parameters	22°C	40°C	60°C	80°C
a (Å)	16.9462(2)	16.9438(5)	16.9454(2)	16.9503(4)
b (Å)	27.2106(3)	27.2774(7)	27.3729(3)	27.4591(5)
c (Å)	11.1258(2)	11.1411(4)	11.1688(2)	11.1960(4)
V (Å³)	5130.3(1)	5149.2(3)	5180.6(1)	5211.0(2)
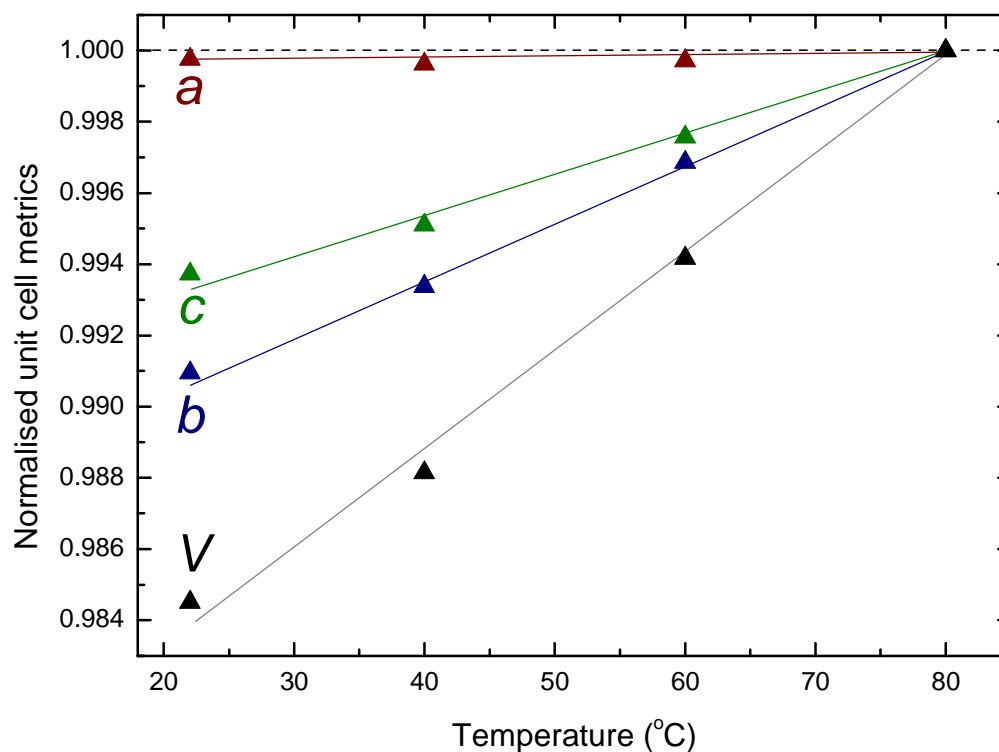
Figure 43: The temperature dependence of the unit cell parameters normalised to those at 80°C. The upward facing triangles represent parameters obtained upon heating. Lines are for eye guidance.

The obtained results indicate a very similar thermal expansion of the unit cell parameters as was observed in the $Rb_2(C_{14}H_{10})_2(THF)$ compound. The lattice parameter a stays the same, while b, c and V follow normal thermal expansion upon heating. However, in contrast to rubidium analogue where the a parameter exhibits a subtle negative thermal expansion, the a parameter in $K_2(C_{14}H_{10})_2(THF)$ exhibits a subtle positive thermal expansion, implying less pronounced rotation of the dimers (described in Figure 31) around the two-fold axis running through oxygen atoms in the THF molecules.

3.2.3 Vibrational Spectroscopy

The charge transfer from the potassium atom to the phenanthrene molecule was followed using infrared and Raman vibrational spectroscopies. A similar red-shift of vibrational peaks in the potassium-reduced phenanthrene radical anion was observed to that in the rubidium analogue, indicating the softening of the modes upon reduction (Figure 44). The tentative assignment of vibrational peaks is gathered in Table 50 and 51 (Appendix 6.9).
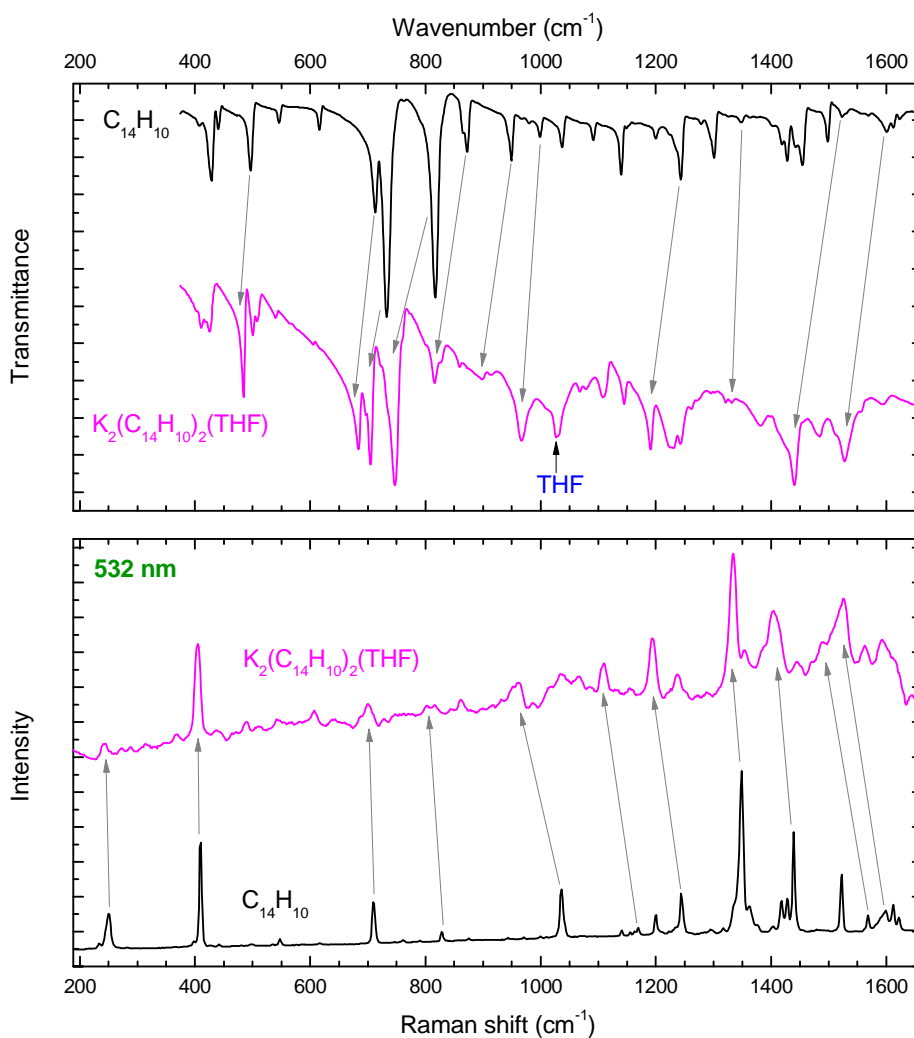
Figure 44: The infrared (top panel) and Raman (bottom panel) spectra of the $K_2(C_{14}H_{10})_2$(THF) (magenta solid line) and pristine phenanthrene (black solid line). Grey arrows represent a tentative red-shift of some peaks and the blue arrow represents the peak corresponding to C-O stretching mode in THF molecule. Raman spectrum was taken using a 532 nm excitation wavelength.

3.2.4 Magnetic Properties

The temperature dependence of the magnetic susceptibility (χ) along with a Curie-Weiss fit and the temperature dependence of the magnetisation (inset) of $K_2(C_{14}H_{10})_2$(THF) in an applied magnetic field of 1 T and 1 mT respectively are shown in Figure 45.
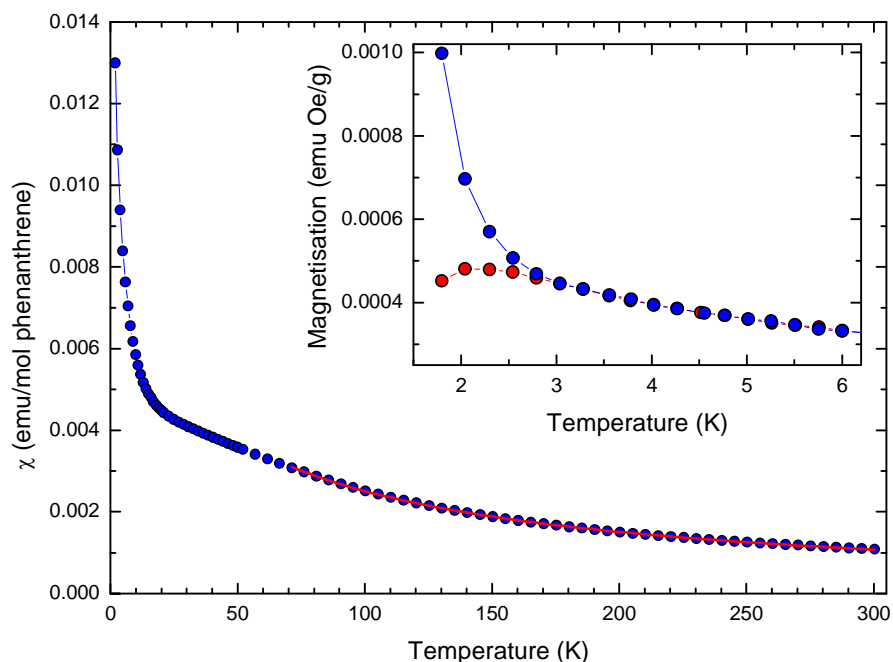
Figure 45: The temperature dependence of molecular susceptibility (χ *vs. T*) of the $K_2(C_{14}H_{10})_2$(THF) compound at an applied field of 1 T (blue circles, FC) along with fit to Curie-Weiss law in temperature region between 70 and 300 K (red curve). Inset shows the temperature dependence of magnetisation *M vs. T* at *B* = 1 mT in ZFC (red circles) and FC (blue circles) measuring protocol. All measurements were collected upon heating.

By fitting the magnetic susceptibility in the high temperature region (70 to 300 K) to a Curie-Weiss law an effective magnetic moment, μ_{eff} = 1.739(1) μ_B and negative Weiss temperature, Θ = -50.7(3) K were obtained. The effective moment of 1.739(1) μ_B is in good agreement with the value of 1.73 μ_B expected for a spin ½ state, confirming the presence of a single unpaired electron per phenanthrene molecule in the $K_2(C_{14}H_{10})_2$(THF) compound. The negative Weiss temperature of -50.7(3) K indicates the presence of antiferromagnetic (AFM) exchange interactions, however, the value is smaller than that observed, -68.1(3) K, in $Rb_2(C_{14}H_{10})_2$(THF).

The irreversible bifurcation of the ZFC and FC curves obtained from the magnetisation measurement at low applied field appears below 2.8 K (in contrast to 3.8 K in the case of the rubidium analogue) and can be associated with a structural rearrangement. A closer investigation of the crystal structure revealed subtle changes in the bond distances between phenanthride dimers in comparison to those in the $Rb_2(C_{14}H_{10})_2(THF)$ phase . The middle phenanthrides in Figure 40 move towards the potassium cations to compensate the difference in cation size and consequently, due to steric crowding, and phenanthrides on the left and right side move away from the potassium cations. The subtle change in the separation of spins can have a profound effect on the magnetic exchange interactions and lower the ordering temperature. The Néel temperature (T_N) of 2.8 K (extracted from the ZFC curve) and the splitting between the ZFC and FC curves indicate the onset of long-range AFM ordering and the presence of a weak ferromagnetic component. Therefore, this material can be classified as a canted antiferromagnet.

3.2.5 Summary of $K_2(C_{14}H_{10})_2(THF)$ compound

The polycrystalline phase-pure $K_2(C_{14}H_{10})_2(THF)$ salt was obtained by reducing phenanthrene with potassium metal in THF at room temperature. In contrast to the rubidium analogue, the crystallisation at slightly elevated temperatures did not yield single crystals. A structural model based on the $Rb_2(C_{14}H_{10})_2(THF)$ structure was built and refined to synchrotron data and the resulting model was used for structural analysis. While the potassium and rubidium analogues are isostructural, almost identical arrangement of the constituents and structural motifs as those found in the $Rb_2(C_{14}H_{10})_2(THF)$ structure were observed. The $K_2(C_{14}H_{10})_2(THF)$ structure exhibits no negative thermal expansion, as the lattice parameter a stays practically the same upon cooling/ heating. Based on a temperature-dependent powder diffraction X-ray experiment performed on the synchrotron, $K_2(C_{14}H_{10})_2(THF)$ undergoes a structural phase transition in the temperature range between 80 and 100 ^{o}C. The newly formed crystalline phase has lower crystal symmetry and/or larger lattice parameters. This phase is stable up to 200 ^{o}C and above this temperature it transforms into another, amorphous phase or decomposes.

By fitting the temperature-dependent magnetic susceptibility data to a Curie-Weiss law, an effective magnetic moment, μ_{eff}, of 1.739(1) μ_B and negative Weiss temperature, Θ, of -50.7(3) K were obtained. The obtained effective magnetic moment is in perfect agreement with S = ½ spin state, where there is one unpaired electron per phenanthrene unit. The Weiss temperature is slightly less negative than observed in the rubidium analogue, however it still indicates fairly strong antiferromagnetic exchange interactions. The same irreversible bifurcation between ZFC and FC curves was observed in the magnetisation data at an applied field of 1 mT, which classifies this material as a canted antiferromagnet. In contrast to the T_N of 3.8 K in the $Rb_2(C_{14}H_{10})_2(THF)$ compound, the T_N in the $K_2(C_{14}H_{10})_2(THF)$ compound is 2.8 K. Lower Néel temperature implies slightly lower antiferromagnetic exchange interactions, which could be a reflection of subtle structural differences between the potassium and the rubidium analogue.

3.3 Cs$_2$(C$_{14}$H$_{10}$)$_2$(THF)

3.3.1 Synthesis and crystal growth

Sublimed phenanthrene (142.4 mg, 0.799 mmol) and caesium metal (107.3 mg, 0.807 mmol, 1wt% excess) were placed on the bottom of the reaction vessel in a glove box. Afterwards the reaction vessel was transferred out of the glove-box and placed on a Schlenk line, evacuated and THF (38 ml) were condensed on top of the phenanthrene and potassium. The olive green solution was vigorous stirred for 45hours, ensuring the reaction to complete (all caesium metal dissolved/reacted); a small amount of dark-green powder was observed on the bottom of the reaction vessel. Then the solution was filtered into the right hand side of the reaction vessel and concentrated, by removing 24 ml of THF. The solution was layered with oxygen- and water-free *n*-hexane (25 ml) and crystallisation was carried out for 3 days. The obtained dark green/grey truncated-pyramid-like crystals (Figure 46) with purple lustre, covered with green powder, were washed twice with a new portion of *n*-hexane and dried under dynamic vacuum for 2.5 hours. Yield 205.1 mg (74 %). Elemental analysis, calculated (%) for C$_{32}$H$_{28}$Cs$_2$O: C 55.35, H 4.06; average found C 52.94, H 3.39. Observed values correspond to a Cs$_{1.12}$-Phenanthrene-THF$_{0.15}$ formula, indicating the multiphase nature of this particular sample. Several syntheses yielded samples with different degrees of phase purity, however, none of the samples was phase-pure (more details are presented in the section on the Powder X-ray Diffraction of this material below) because of the presence of the green powder, here denoted as Phase B.
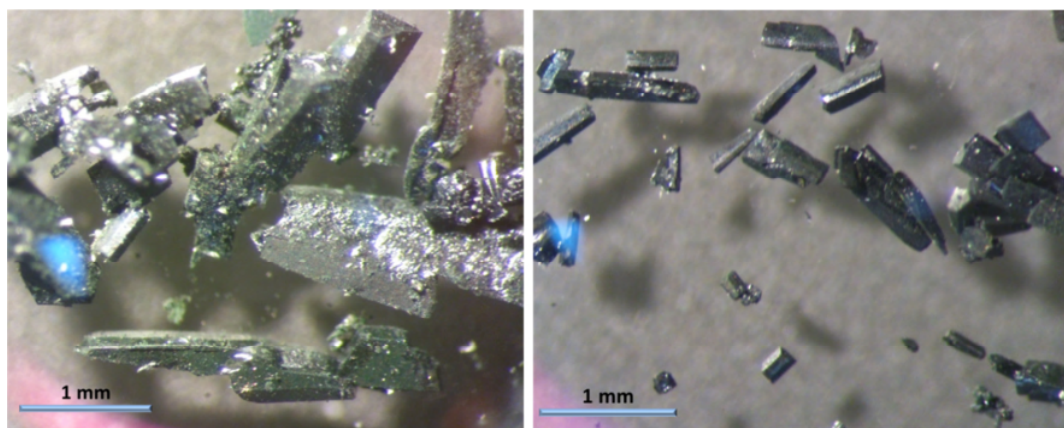
Figure 46: Single crystals of $Cs_2(C_{14}H_{10})_2$(THF) under 40× magnification. Left and right panels present two different samples with different phase purity. On the left panel the coating of single crystals with green powder can be observed. Thick blue line represents 1mm length.

3.3.2 Single crystal structural analysis

The truncated-pyramid-like crystals were identified as $Cs_2(C_{14}H_{10})_2(THF)$, which in contrast to the *Fdd2* structure of rubidium and potassium analogues crystallises in the monoclinic *Cc* space group with lattice parameters of a = 10.6212(7) Å, b =25.0224(15) Å, c = 20.1555(12) Å and β = 92.284(2)° at 120 K. The asymmetric unit consists of four phenanthrene radical anions, four caesium cations and two THF molecules as depicted in Figure 47. For convenient explanation of the coordination environments of Cs^+ cations the constituents of the crystal structure are presented in a way to separately describe the coordination environment of Cs1 and Cs2 (Figure 48), and Cs3 and Cs4 (Figure 49) cations.
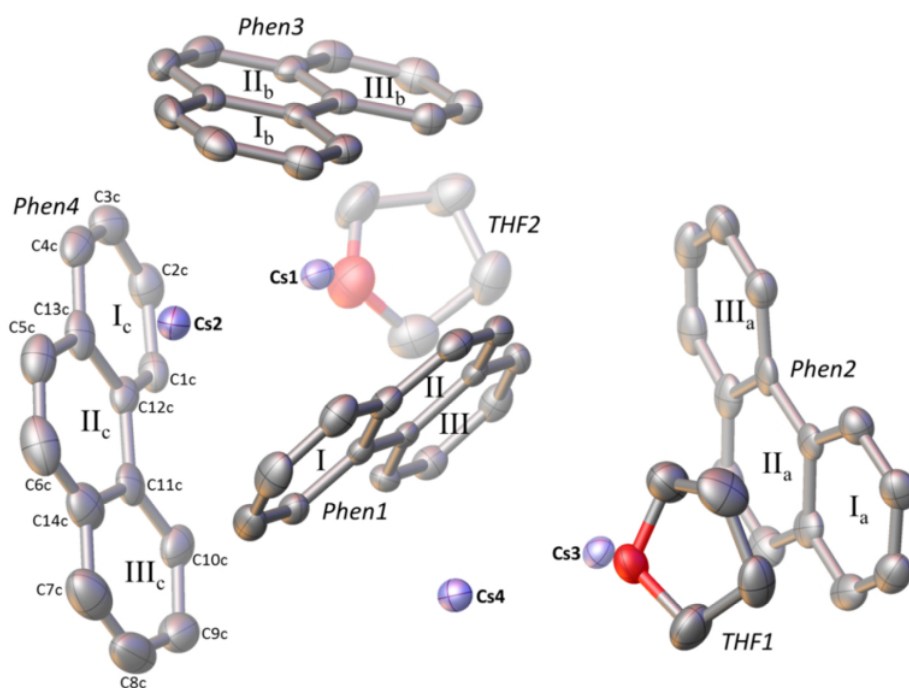
Figure 47: The asymmetric unit cell of $Cs_2(C_{14}H_{10})_2(THF)$ consisting of four crystallographically independent phenanthrides denoted as *Phen1*, *Phen2*, *Phen3* and *Phen4*, four caesium cations denoted as Cs1, Cs2, Cs3 and Cs4, and two THF molecules denoted as *THF1* and *THF2*. The peripheral benzene ring planes are labelled as I, III, I_a, III_a, I_b, III_b, I_c, III_c, and central planes as II, II_a, II_b, II_c. Colour code: Cs purple; O red and C grey. Hydrogen atoms are omitted for clarity and the numbering of *Phen1*, *Phen2* and *Phen3* can be followed by the depicted benzene ring planes.
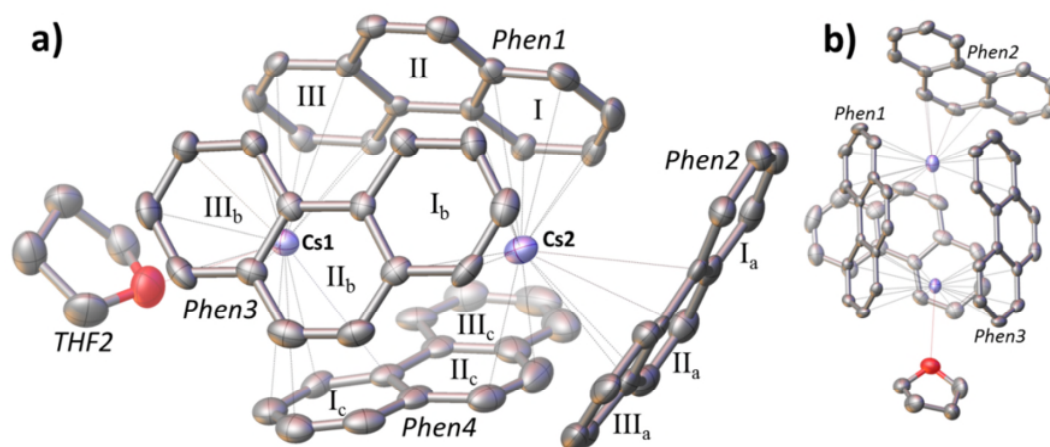
Figure 48: a) and b) represent two perspectives of coordination environments of $Cs1^+$ and $Cs2^+$ ions in $Cs_2(C_{14}H_{10})_2(THF)$ compound. Four crystallographically independent phenanthrene radical ions are denoted as *Phen1*, *Phen2*, *Phen3* and *Phen4*. The peripheral benzene ring planes are labelled as I, III, I_a, III_a, I_b, III_b, I_c, III_c, and central planes as II, II_a, II_b, II_c. Black dotted lines and red dotted lines represent $Cs^+\cdots C$ and $Cs^+\cdots O$ coordination interactions respectively. Colour code: Cs purple; O red and C grey. Thermal ellipsoids are shown with 50% probability level, hydrogen atoms are omitted for clarity and depicted structure was obtained from data collected at 120 K.

The $Cs1^+$ interacts with phenanthrides through η^4 and two η^6 coordination modes. The η^4 coordination is between $Cs1^+$ and the peripheral benzene plane I_c (C1c, C2c, C3c and C12c) of *Phen4* with distances of 3.351(4)- 3.564(5) Å in length. The $Cs1^+$ to plane centroid distance is 3.294(2) Å and the angle of $Cs1^+$ projection on the ring plane of 78°. The first η^6 coordination is between $Cs1^+$ and the peripheral benzene ring plane III (C7, C8, C9, C10, C11 and C14) of *Phen1* with bond distances ranging from 3.414(4) to 3.584(4) Å, the $Cs1^+$ to plane centroid distance is 3.196(2) Å and cation projection on the ring plane at an angle of 86°. The second η^6 coordination is between $Cs1^+$ and peripheral benzene ring plane III_b (C7b, C8b, C9b, C10b, C11b and C13b atoms) of *Phen3* with bond distances of 3.341(4)- 3.514(5) Å in length. The Cs^+ to plane centroid distance is 3.130(2) Å and the angle of Cs^+ projection on the ring plane is 85°. The local binding of $Cs1^+$ cation is shown in Figure 48.

The oxygen atom in the *THF2* molecule is coordinated to $Cs1^+$ as a terminal ligand through a μ^1 coordination mode, with the $Cs1^+\cdots O$ bond distance of 3.153(4) Å (Figure 48).

The second cation, $Cs2^+$, interacts with the phenanthrene radical ions through η^2, η^3, η^4 and η^6 coordination modes. The η^2 coordination is between $Cs2^+$ and the rim of benzene plane II_c (C5c, C6c) of *Phen4* with bond distances ranging from 3.261(4) to 3.450(5) Å. The $Cs2^+$ to plane centroid distance is 3.786(2) Å and cation projection on the ring plane at an angle of 56°. The η^3 coordination is between $Cs2^+$ and the rim of benzene plane II_a (C5a, C6a and C13a) of *Phen2* with distances of 3.351(4)- 3.564(5) Å in length, the $Cs2^+$ to plane centroid distance is 3.444(2) Å and the angle of Cs^+ projection on the ring plane is 74°. The η^4 coordination is between $Cs2^+$ and the peripheral benzene ring plane I_b (C2b, C3b, C4b and C13b) of *Phen3* with bond distances ranging from 3.286(5) to 3.618(4) Å. The $Cs2^+$ to plane centroid distance is 3.287(2) Å and cation projection on the ring plane at an angle of 77°. The last η^6 coordination is between $Cs2^+$ and the peripheral benzene ring plane I (C1, C2, C3, C4, C12 and C13 atoms) of *Phen* with bond distances of 3.350(6)- 3.590(4) Å in length. The $Cs2^+$ to plane centroid distance is 3.173(2) Å and the angle of Cs^+ projection on the ring plane is 85°. The local binding of $Cs2^+$ cation is shown in Figure 48.

The $Cs3^+$ interacts with phenanthrides through one η^3 and two η^6 coordination modes. The η^3 coordination is between $Cs3^+$ and the central benzene plane II_a (C5a, C6a and C13a) of *Phen2* with distances of 3.247(5)- 3.506(5) Å in length. The $Cs3^+$ to plane centroid distance is 3.330(2) Å and the angle of $Cs3^+$ projection on the ring plane of 74°. The first η^6 coordination is between $Cs3^+$ and the peripheral benzene ring plane III (C7, C8, C9, C10, C11 and C14) of *Phen1* with bond distances ranging from 3.362(4) to 3.582(4) Å. The $Cs3^+$ to plane centroid distance is 3.177(2) Å and cation projection on the ring plane at an angle of 85°. The second η^6 coordination is between $Cs2^+$ and peripheral benzene ring plane III_b (C7b, C8b, C9b, C10b, C11b and C14b atoms) of *Phen3* with bond distances of 3.392(4)- 3.513(4) Å in length. The $Cs3^+$ to plane centroid distance is 3.177(2) Å and the angle of $Cs3^+$ projection on the ring plane of 87°. The local binding of $Cs3^+$ cation is shown in Figure 49.
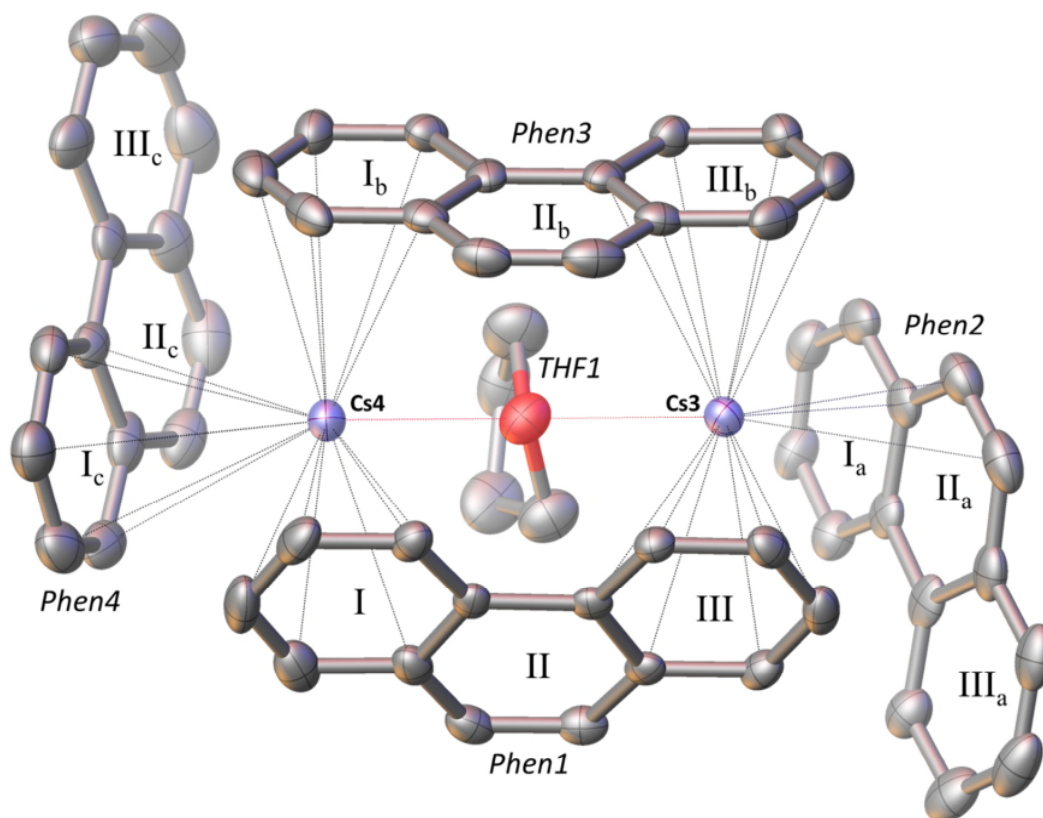
Figure 49: The coordination environment of $Cs3^+$ and $Cs4^+$ ions in $Cs_2(C_{14}H_{10})_2(THF)$ compound. Four crystallographically independent phenanthrene radical ions are denoted as *Phen1*, *Phen2*, *Phen3* and *Phen4*. The peripheral benzene ring planes are labelled as I, III, I_a, III_a, I_b, III_b, I_c, III_c, and central planes as II, II_a, II_b, II_c. Black dotted lines and red dotted lines represent $Cs^+ \cdots C$ and $Cs^+ \cdots O$ coordination interactions respectively. Colour code: Cs purple; O red and C grey. Hydrogen atoms are omitted for clarity and depicted structure was obtained from data collected at 120 K.

The $Cs4^+$ interacts with phenanthrene radical ions through one η^5 and two η^6 coordination modes. The η^5 coordination is between $Cs4^+$ and the peripheral benzene plane I_b (C1b, C2b, C3b, C4b and C13b) of *Phen3* with bond distances ranging from 3.326(5) to 3.721(4) Å. The $Cs4^+$ to plane centroid distance is 3.250(2) Å and the angle of $Cs4^+$ projection on the ring plane of 80°. The first η^6 coordination is between $Cs4^+$ and the peripheral benzene plane I (C1, C2, C3, C4, C12 and C13) atoms) of *Phen* with bond distances of 3.340(5)- 3.683(4) Å in length. The $Cs4^+$ to plane centroid distance is 3.225(2) Å and the angle of $Cs4^+$ projection on the ring plane is 82°. The second η^6 coordination is between $Cs4^+$ and the peripheral benzene ring plane I_c (C1c, C2c, C3c, C4c, C12c and C13c) of *Phen4* with bond distances ranging from 3.355(4) to 3.638(5) Å.

The Cs4$^+$ to plane centroid distance is 3.226(2) Å and cation projection on the ring plane at an angle of 83°. The local binding of Cs4$^+$ cation is shown in Figure 49.

The oxygen atom in *THF1* molecule is as a bridging ligand coordinated to Cs3$^+$ and Cs4$^+$ through a µ^2 coordination mode. The Cs3$^+$···O and Cs4$^+$···O distances are 3.087(3) and 3.047(4) Å respectively. The Cs3-O-Cs4 angle is 105.16(9)^o.

All Cs$^+$···C and Cs$^+$···O coordination bond distances are gathered in Table 12 and they are comparable to those reported in caesium-reduced 2,5,8-tri-tBu-phenalene, rubrene, cyclopentadiene, indene, fluorene and corannulene (Table 13 and 14). The basic parameters obtained from refinement, fractional atomic coordinates, atom to atom bond distances and bond angles for crystal structures obtained from data sets collected at 120 K are gathered in the Appendix (6.4).

Table 12: Coordination modes and coordination bond distances between caesium cations and carbon/oxygen atoms extracted from structure obtained at 120 K.

Coordination mode	*Cs$^+$ to C or O bond*	*Distance (Å)*
η^2	Cs2-C5c	3.261(4)
	Cs2-C6c	3.450(5)
η^3	Cs2-C5a	3.394(5)
	Cs2-C6a	3.433(5)
	Cs2-C13a	3.678(5)
η^3	Cs3-C5a	3.247(5)
	Cs3-C13a	3.368(5)
	Cs3-C6a	3.506(5)
η^4	Cs1-C2c	3.351(4)
	Cs1-C1c	3.357(4)
	Cs1-C3c	3.550(5)
	Cs1-C12c	3.564(5)
η^4	Cs2-C3b	3.286(5)
	Cs2-C4b	3.330(4)
	Cs2-C2b	3.517(4)
	Cs2-C13b	3.618(4)
η^5	Cs4-C3b	3.326(5)
	Cs4-C4b	3.337(4)
	Cs4-C2b	3.530(4)
	Cs4-C13b	3.554(4)
	Cs4-C1b	3.721(4)
	Cs1-C11b	3.341(4)
	Cs1-C14b	3.345(4)

η^6	Cs1-C10b	3.430(4)
	Cs1-C7b	3.436(4)
	Cs1-C9b	3.504(5)
	Cs1-C8b	3.514(5)
η^6	Cs1-C9	3.414(4)
	Cs1-C8	3.421(5)
	Cs1-C10	3.471(4)
	Cs1-C7	3.481(4)
	Cs1-C11	3.565(4)
	Cs1-C14	3.584(4)
η^6	Cs2-C3	3.350(6)
	Cs2-C2	3.399(5)
	Cs2-C4	3.409(5)
	Cs2-C1	3.490(4)
	Cs2-C13	3.566(5)
	Cs2-C12	3.590(4)
η^6	Cs3-C7	3.362(4)
	Cs3-C8	3.384(4)
	Cs3-C14	3.449(4)
	Cs3-C9	3.491(4)
	Cs3-C11	3.561(4)
	Cs3-C10	3.582(4)
η^6	Cs3-C14b	3.392(4)
	Cs3-C7b	3.394(4)
	Cs3-C11b	3.467(4)
	Cs3-C8b	3.473(4)
	Cs3-C10b	3.495(4)
	Cs3-C9b	3.513(4)
η^6	Cs4-C4	3.340(5)
	Cs4-C3	3.394(5)
	Cs4-C13	3.442(4)
	Cs4-C2	3.576(6)
	Cs4-C12	3.646(4)
	Cs4-C1	3.683(4)
η^6	Cs4-C13c	3.355(4)
	Cs4-C12c	3.427(4)
	Cs4-C4c	3.516(4)
	Cs4-C1c	3.520(5)
	Cs4-C2c	3.632(5)
	Cs4-C3c	3.638(5)
μ^2	Cs4-O$_{THF1}$	3.047(4)
	Cs3-O$_{THF1}$	3.087(3)
μ^1	Cs1- O$_{THF2}$	3.153(4)

The arrangement of phenanthrene radical ions and the *THF1* molecule coordinated to Cs3$^+$ and Cs4$^+$ is very similar to that observed in Rb$_2$(C$_{14}$H$_{10}$)$_2$(THF) and K$_2$(C$_{14}$H$_{10}$)$_2$(THF): a triangle-like motif comprising *Phen1*, *Phen3* and *THF1*, along with additional coordination of caesium cations to *Phen2* and *Phen4*, finishing the encapsulation of Cs3$^+$ and Cs4$^+$. Also, *Phen1* and *Phen3* form a dimer at an angle of 62.77(8)^o with respect to each other, which is comparable to the angle in the rubidium and potassium analogues.

In contrast to the familiar arrangement of constituents coordinated to Cs3$^+$ and Cs4$^+$ cations, the arrangement of phenanthrides and *THF2* coordinated to Cs1$^+$ and Cs2$^+$ is considerably different. The *THF2* is no longer a bridging ligand forming a triangle-like motif, but its position is effectively exchanged with *Phen4*, which becomes part of the triangle-like motif as shown in Figure 48b. However, the arrangement of *Phen1*, *Phen2* and *Phen3* around Cs1$^+$ and Cs2$^+$ remains similar. Moreover, a closer inspection of the *Phen1* and *Phen3* dimer arrangements reveal noticeable differences in comparison to the rubidium and potassium analogues, despite similar angle of *Phen1* and *Phen3* and the angles observed in Rb$_2$(C$_{14}$H$_{10}$)$_2$(THF) and K$_2$(C$_{14}$H$_{10}$)$_2$(THF). The coordination to caesium cations is solely to the peripheral benzene rings (Figure 48 and 49), and the rotation angle of 2.8(3)^o between *Phen1* and *Phen3* is considerably smaller than that observed in the potassium (52°) and rubidium (50°) analogues. These two effects are most likely cation size driven.

The two different coordination environments around Cs1$^+$ and Cs2$^+$, and Cs3$^+$ and Cs4$^+$, alternate along [100] and form a channel-like arrangement of constituents shown in Figure 50. All four crystallographically independent caesium cations along with *Phen1* and *Phen3* form a zig-zag chain running along the crystallographic *a* direction as depicted in Figure 51a, while *Phen2* and *Phen4* along with *THF1* and *THF2* form a cage around the chain. In contrast to practically planar *Phen1* and *Phen3* (multihapto coordination to peripheral benzene rings), the *Phen2* and *Phen4* are visibly distorted. In the case of *Phen2*, Cs2$^+$ and Cs3$^+$ coordinate to the central benzene ring plane II$_a$ via two η^3 coordination modes, allowing the peripheral benzene ring planes I$_a$ and III$_a$ to twist and fold in order to minimize intramolecular steric crowding of bay Hs as shown in Figure 51b. The distortion of *Phen4* seems to originate from uneven coordination of

Cs1$^+$ (η^4) and Cs4$^+$ (η^6) to peripheral benzene ring plane I$_c$, and Cs2$^+$ (η^2) to the central benzene ring plane III$_c$ (Figure 51c).
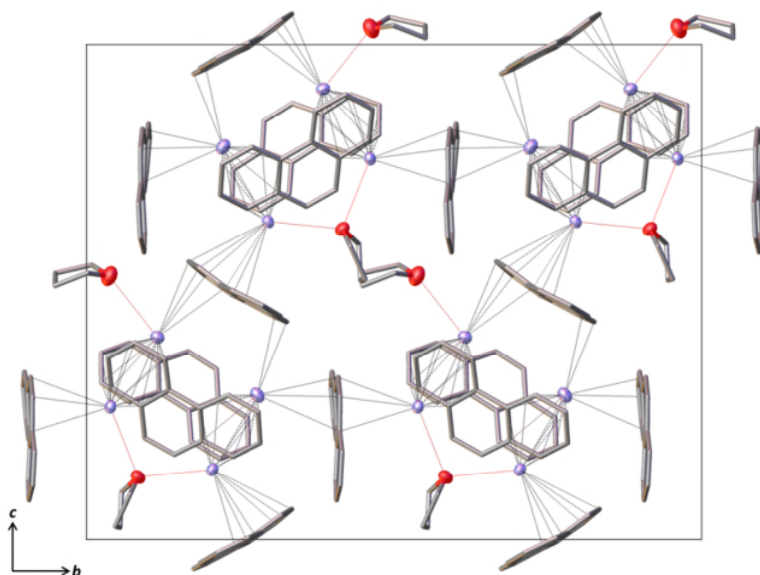
Figure 50: Projection of the Cs$_2$(C$_{14}$H$_{10}$)$_2$(THF) structure along the [100] direction showing four channel-like motifs forming a 3D polymeric network of Cs$^+$···C interaction (black dotted lines) between alkali metal ions and the phenanthride radical anions. Hydrogen atoms are omitted, and carbon-carbon bonds are depicted as tubes for clarity. Colour code: Cs purple; O red and C grey, red dotted lines represent Cs$^+$···O coordination.
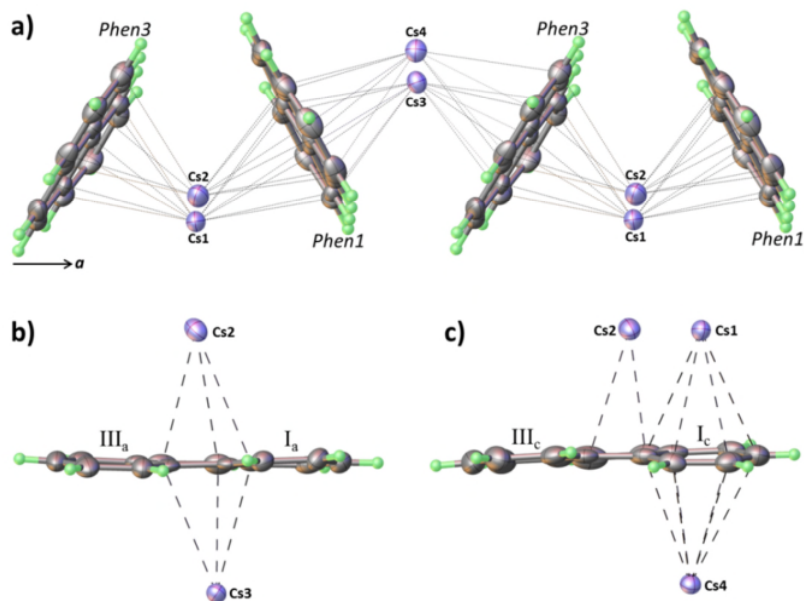
Figure 51: a) A zig-zag chain running along the crystallographic *a* direction comprised of *Phen1*, *Phen3*, Cs1$^+$, Cs2$^+$, Cs3$^+$ and Cs4$^+$. b) and c) represent distortion of *Phen2* and *Phen4* respectively. Colour code: Cs purple; O red, C grey and H light green, and Cs$^+$···C black dotted lines.

Table 13: Caesium salts of selected PAHs, observed η coordination modes and $Cs^+\cdots C$ distances.

PAH	Compound	Coord.	Distance range (Å)
2,5,8-tri-*tBu*-phenalene[163]	$[\{Cs^+(THF)_2\}\{C_{16}H_6(^tBu)_3^-\}]$	η^6	3.38(1) − 3.63(1)
Rubrene[136]	$[\{Cs^+(THF)\}(C_{42}H_{28}^-)]$	η^6	3.277(3) − 3.628(3)
		η^3	3.436(3) − 3.852(3)
	$[\{Cs^+_2(C_{42}H_{28}^{2-})\}(DME)]$	η^6	3.392(4) − 3.689(3)
		η^2	3.535(3) − 3.717(3)
Cyclopentadiene[138]	$[\{Cs^+(18\text{-crown-}6)\}(C_5H_5^-)]$	η^5	3.298(8) − 3.495(5)
Indene[139]	$[\{Cs^+(18\text{-crown-}6)\}(C_9H_7^-)]$	η^5	3.393(2) − 3.437(2)
Fluorene	$[\{Cs^+(THF)_{0.5}\}(C_{13}H_9^-)]$[156]	η^5	3.214(7) − 3.578(8)
		η^4	3.32(2) − 3.67(2)
	$[\{Cs^+(diglyme)\}(C_{13}H_9^-)]$[140]	η^5	3.26(2) − 3.61(3)
		η^3	3.22(2) − 3.59(3)
	$[\{Cs^+(18\text{-crown-}6)\}(C_{13}H_9^-)]$[139]	η^2	3.247(8) − 3.355(8)
		η^4	3.14(1) − 3.58(1)
Corannulene	$[\{Cs^+(18\text{-crown-}6)\}(C_{20}H_{10}^-)]$[142]	η^5	3.424(3) − 3.573(3)
	$[\{Cs^+(diglyme)\}(C_{20}H_{10}^-)]$[164]	η^5	3.35(2) − 3.43(2)
		η^3	3.40(2) − 3.55(5)

Table 14: Caesium salts of selected PAHs and their $Cs^+\cdots O$ distances.

PAH	Compound	Coord.	Distance range (Å)
2,5,8-tri-*tBu*-phenalene[163]	$[\{Cs^+(THF)_2\}\{C_{16}H_6(^tBu)_3^-\}]$	terminal	2.98(1) − 3.13(2)
Rubrene[136]	$[\{Cs^+(THF)\}(C_{42}H_{28}^-)]$	terminal	2.996(3)
	$[\{Cs^+_2(C_{42}H_{28}^{2-})\}(DME)]$	terminal	3.085(3) − 3.194(3)
Fluorene	$[\{Cs^+(THF)_{0.5}\}(C_{13}H_9^-)]$[156]	bridging	3.094(3)

3.3.3 Powder X-ray diffraction

Despite several attempts to synthesise and isolate a phase-pure $Cs_2(C_{14}H_{10})_2(THF)$, only mixed-phase materials with different ratios of $Cs_2(C_{14}H_{10})_2(THF)$ were obtained as shown in Figure 52.
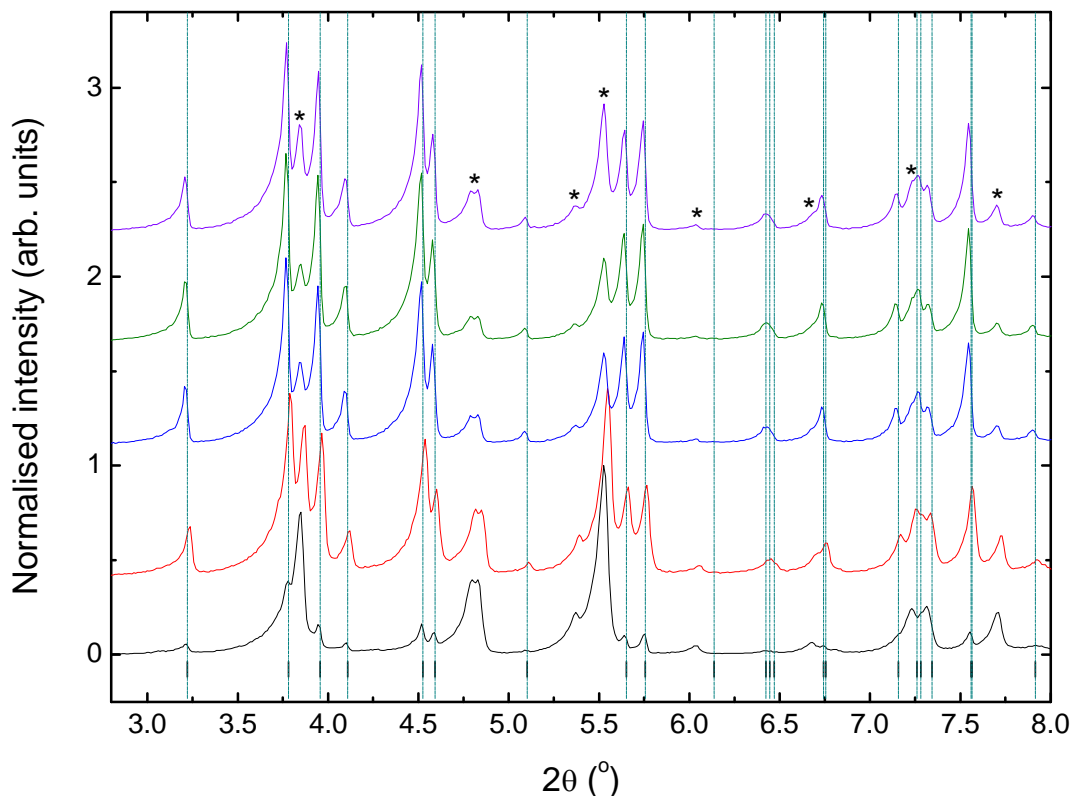
Figure 52: Powder X-ray diffraction profiles of several samples (black, red, blue, olive-green and violet curves) along with predicted peak positions for $Cs_2(C_{14}H_{10})_2(THF)$ phase from single crystal diffraction (black ticks, cyan-blue lines are for eye guidance). The black asterisks correspond to unknown well-crystalline Phase B. The data were collected on a laboratory source (λ = 0.7093 Å, Mo Kα) at 294 K.

An unknown highly-crystalline Phase B was afterwards indexed as an orthorhombic $P2_12_12_1$ phase. The simultaneous Rietveld refinement of structural models obtained from single crystal analysis and the additional orthorhombic phase to the powder diffraction profile (red curve in Figure 52) collected at 294 K was performed by Prof. John S. O. Evans in TOPAS-Academic (version 6). The extracted lattice parameters are a = 10.7696(7) Å, b = 25.2498(18) Å, c = 20.5689(17) Å and β = 91.156(6)°, and a = 14.7082(12) Å, b = 15.1247(13) Å and c = 10.2293(8) Å for the $Cs_2(C_{14}H_{10})_2(THF)$ and the

orthorhombic phase respectively. The weight percentage of the monoclinic phase is 60.1(3)% and the orthorhombic phase is 39.9(3)%. In contrast to the potassium and rubidium analogues the unit cell parameters of $Cs_2(C_{14}H_{10})_2(THF)$ phase follow a normal thermal expansion. Results of the Rietveld refinement are shown in Figure 53.
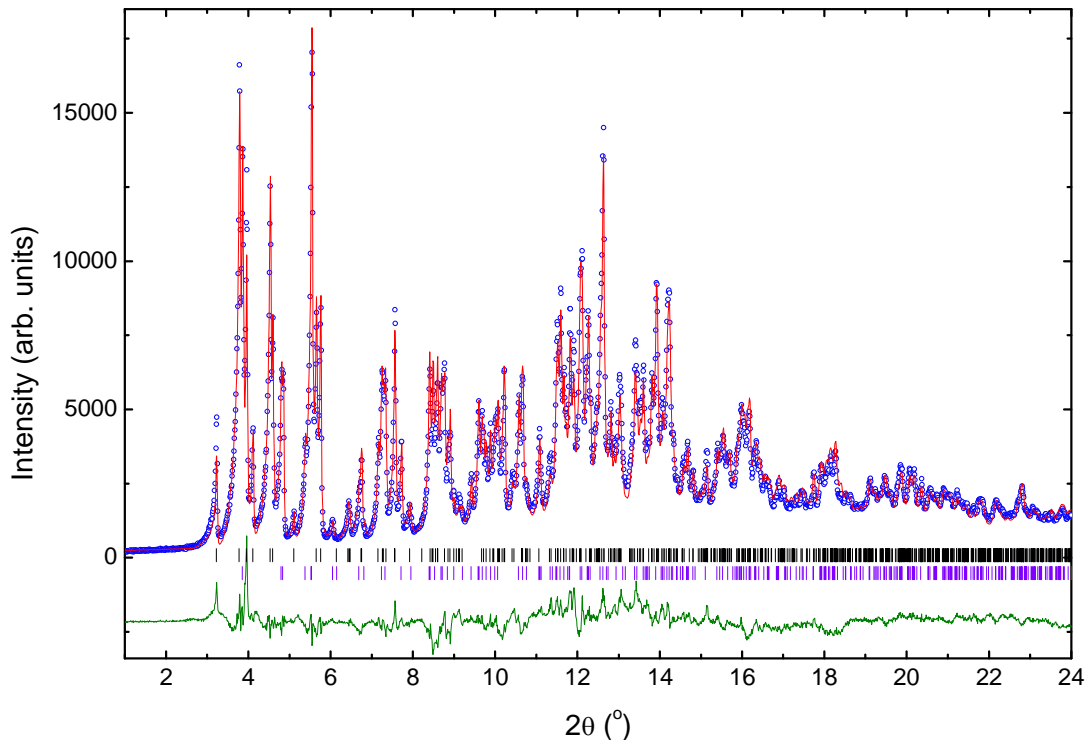
Figure 53: Two-phase Rietveld refinement of sample containing $Cs_2(C_{14}H_{10})_2(THF)$ (60.1%) and orthorhombic (39.9%) phase. The experimentally obtained diffraction profile (λ = 0.7093 Å) at 294 K (blue open circles), the calculated profile (red solid line), difference (olive green solid line) and predicted peak position for monoclinic (black tick marks) and orthorhombic (violet tick marks) phase. The weight profile and expected R factors are R_{wp} = 8.725% and R_{exp} = 1.898%.

A temperature-dependent powder X-ray diffraction experiment, performed on a laboratory source (λ = 0.7093 Å) by using an Oxford 500 cryostream in a temperature range between 27 and 167°C (300-440 K), revealed that the amount of the $Cs_2(C_{14}H_{10})_2(THF)$ phase diminishes and the orthorhombic Phase B increases upon heating. The monoclinic phase is relatively stable up to *ca.* 107°C and above this temperature it starts rapidly converting into the orthorhombic phase as shown in Figure 54. Moreover, the orthorhombic phase starts to degrade and eventually vanishes upon further heating, and the sample becomes amorphous. By combining the results obtained from the temperature-dependent powder X-ray diffraction

experiment and elemental analysis, we obtain the formula for one sample (black curve in Figure 52) of $Cs_{1.12}$-Phenanthrene-$THF_{0.15}$. We concluded that the $Cs_2(C_{14}H_{10})_2(THF)$ phase is metastable with a tendency to lose solvent (THF) molecules and it transforms into the highly-crystalline solvent-free orthorhombic Phase B. This finding opened up a path towards a new synthetic approach which enabled the synthesis of solvent-free Cs-phenanthride described in Section 3.4.
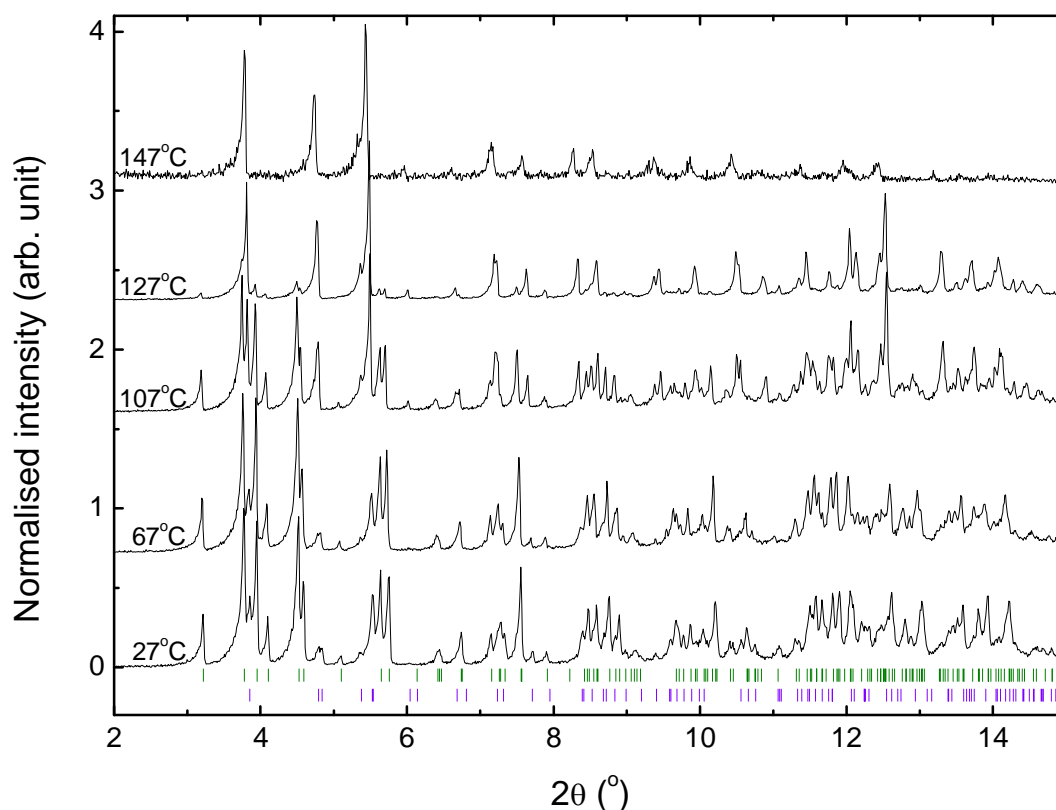
Figure 54: Temperature-dependent powder diffraction experiment (λ = 0.7093 Å). Diffraction profiles of mixed-phase sample containing $Cs_2(C_{14}H_{10})_2(THF)$ and orthorhombic phase at 27, 67, 107, 127 and 147°C (black solid lines). The predicted peak position for monoclinic and orthorhombic (violet tick marks) phase are shown as olive-green and violet tick marks respectively.

3.3.4 Vibrational Spectroscopy

As in the case of the potassium and rubidium analogues, a charge transfer from the caesium atom to the phenanthrene molecule was followed by infrared and Raman vibrational spectroscopies. A similar red-shift of vibrational peaks in the caesium-reduced phenanthrene radical anion was observed, indicating the softening of modes upon reduction (Figure 31). The similarity between the IR and Raman spectra of $Cs_2(C_{14}H_{10})_2(THF)$ and both the potassium and rubidium analogues confirms that all vibrational modes present in the phenanthrene radial anions are preserved. Therefore, the coexistence of the solvent-containing and solvent-free phases is a feasible explanation. The tentative assignment of vibrational peaks is gathered in Table 50 and 51 (Appendix 6.9).
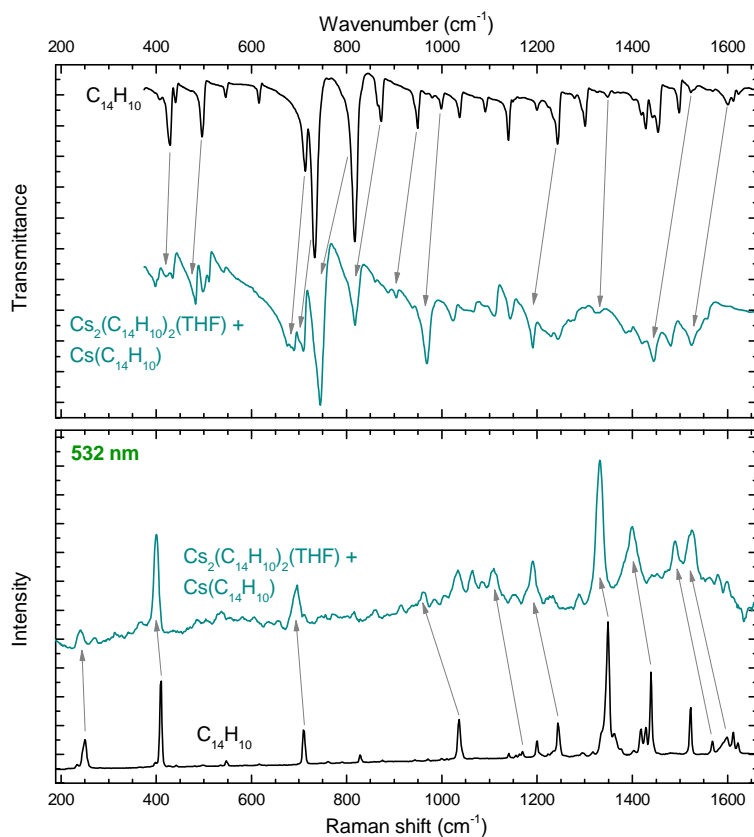
Figure 55: The infrared (top panel) and Raman (bottom panel) spectra of sample containing $Cs_2(C_{14}H_{10})_2(THF)$ phase (dark cyan solid line) and pristine phenanthrene (black solid line). Grey arrows represent a tentative red-shift of some peaks and the orange circle represents the peak, which is by intensity, position and shape different to that observed in potassium and rubidium analogues. Raman spectrum was taken using a 532 nm excitation wavelength.

3.3.5 Magnetic Properties

The temperature dependence of the magnetic susceptibility (χ) along with a Curie-Weiss fit of a sample containing *ca*. 30% $Cs_2(C_{14}H_{10})_2(THF)$ and 70% of Phase B at applied field of 1 T is shown in Figure 56. The inset represents the temperature dependence of the magnetisation of a sample containing 60% of $Cs_2(C_{14}H_{10})_2(THF)$ phase and 40% Phase B in an applied field of 10 mT. The magnetic behaviour in these two samples is different. A broad hump around 35 K can be observed in the susceptibility curve of the sample containing only 30% of $Cs_2(C_{14}H_{10})_2(THF)$ phase. In contrast to this, a bifurcation between the ZFC and FC curves with a small local maximum at 10 K is observed in the magnetisation measurement in the sample containing 60% of $Cs_2(C_{14}H_{10})_2(THF)$ phase.
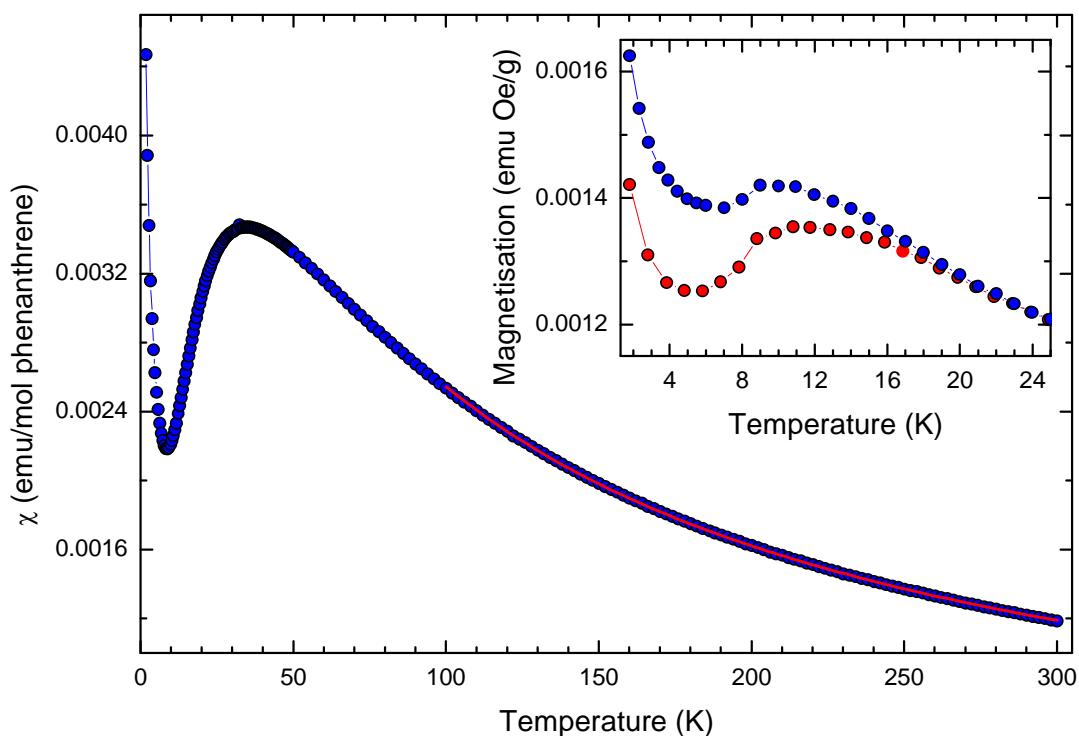
Figure 56: The temperature dependence of molecular susceptibility (χ *vs. T*) of sample containing 30% of $Cs_2(C_{14}H_{10})_2(THF)$ phase at applied field of 1 T (blue circles, FC) along with fit to Curie-Weiss law in temperature region between 100 and 300 K (red curve). Inset shows the temperature dependence of magnetisation *M vs. T* of sample containing 60% of $Cs_2(C_{14}H_{10})_2(THF)$ phase at *B* = 10 mT in ZFC (red circles) and FC (blue circles) measuring protocol. All measurements were collected upon heating.

Fitting of the magnetic susceptibility in the high temperature region (100 to 300 K) to a Curie-Weiss law yielded the effective magnetic moment, μ_{eff} = 1.8898(6) μ_B and

negative Weiss temperature, Θ = -75.4(2) K. This effective moment is similar to that found in $Rb_2(C_{14}H_{10})_2(THF)$, (1.867(1) μ_B) and it is in good agreement with the value of 1.73 μ_B expected for spin S=½ state, confirming the presence of a single unpaired electron per phenanthrene molecule in the sample containing 30% of the $Cs_2(C_{14}H_{10})_2(THF)$ phase. The good agreement of the effective moment with a spin ½ state signals that both $Cs_2(C_{14}H_{10})_2(THF)$ and the orthorhombic Phase B should consist of phenanthride molecules containing one unpaired electron. This is an additional indication that the orthorhombic Phase B is most likely solvent-free $Cs(C_{14}H_{10})$ compound. The negative Weiss temperature of -75.4(2) K indicates the presence of strong antiferromagnetic (AFM) exchange interactions, and its absolute value is larger than the one observed (-68.1(3) K) in $Rb_2(C_{14}H_{10})_2(THF)$.

A well-defined splitting of the ZFC and FC curves below 18 K at low applied field in magnetisation measurements, signals the onset of long-range AFM ordering with Néel temperature (T_N) of 9.9 K, which is considerably higher than the 3.8 K observed in $Rb_2(C_{14}H_{10})_2(THF)$. Moreover, an irreversible bifurcation of ZFC and FC indicates the presence of a weak ferromagnetic component. Therefore, the $Cs_2(C_{14}H_{10})_2(THF)$ phase can be classified as a canted antiferromagnet.

A closer investigation of the magnetisation curves of the two samples containing 60% and 30% of the $Cs_2(C_{14}H_{10})_2(THF)$ phase, collected in both ZFC and FC measuring protocols in an applied field of 10 mT, revealed a staggering difference, undoubtedly confirming that each phase possesses different magnetic behaviour, as shown in Figure 57. In the sample where the $Cs_2(C_{14}H_{10})_2(THF)$ phase is dominating (60%) the bifurcation between ZFC and FC curves indicates canted antiferromagnetism. Meanwhile, in the sample where the orthorhombic Phase B dominates (70%) the broad hump in magnetization with a maximum at 35 K and the superimposition of ZFC and FC curves indicates the presence of low-dimensional magnetism. Therefore, on the basis of elemental analysis, powder X-ray diffraction and magnetisation measurements it can be concluded that the orthorhombic Phase B present in all samples is most likely solvent-free caesium phenanthride and it is a low-dimensional magnet. This conclusion initiated a search for other solvent-free alkali metal phenanthrides.
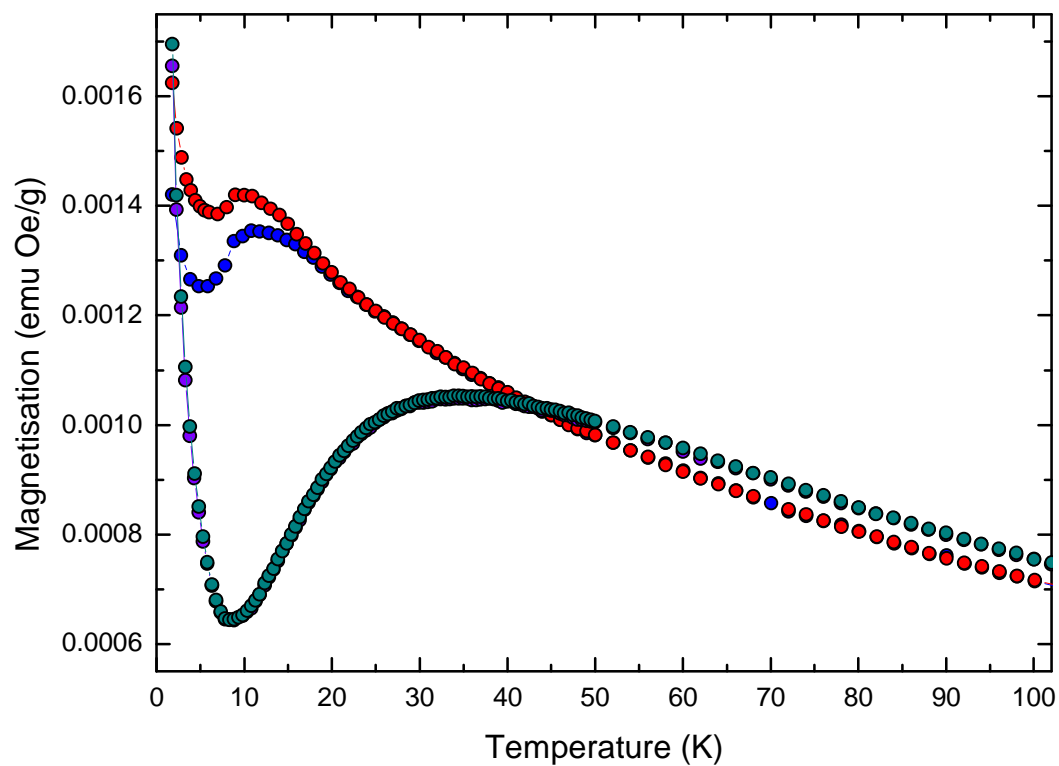
Figure 57: The temperature dependence of magnetisation *M vs. T* at applied field of 10 mT of samples containing 60% and 30% of $Cs_2(C_{14}H_{10})_2(THF)$ phase in ZFC (red circles) and FC (blue circles), and ZFC (violet circles) and FC (dark cyan circles) measuring protocols respectively. All measurements were collected upon heating.

3.3.6 Summary of $Cs_2(C_{14}H_{10})_2(THF)$ compound

Truncated-pyramid-like crystals and olive-green powder were obtained upon reduction of equimolar amounts of caesium metal and phenanthrene in THF. Based on single crystal X-ray diffraction analysis, the truncated-pyramid-like crystals were identified as $Cs_2(C_{14}H_{10})_2(THF)$. In contrast to the orthorhombic structure of $Rb_2(C_{14}H_{10})_2(THF)$ and $K_2(C_{14}H_{10})_2(THF)$ compounds, the $Cs_2(C_{14}H_{10})_2(THF)$ material crystallises in a monoclinic Cc space group. The asymmetric unit cell consists of four phenanthride ions, four caesium cations and two THF molecules. The coordination environment of $Cs3^+$ and $Cs4^+$ cations is very similar to that observed in the potassium and rubidium compounds. However, the coordination environment of $Cs1^+$ and $Cs2^+$, where the position of one phenanthride unit and a THF molecule is swapped, is entirely different. The two different coordination environments of the caesium cation pairs, the appearance of which is most likely cation size driven, builds up a channel-like structural motif running along the crystallographic a direction. Two phenanthride units form a zig-zag chain, while other phenanthrides and THF molecules form a cage encapsulating the chain. The phenanthrides forming a cage are, in contrast to those forming a chain, asymmetrically coordinated to caesium cations, and therefore distorted.

The $Cs_{1.12}$-Phenanthrene-$THF_{0.15}$ formula obtained from elemental analysis of a specific sample signals its multiphase nature. The powder X-ray diffraction analysis of several synthesised samples revealed that they contain two different crystalline phases in different ratios. The first corresponds to the crystal structure of truncated-pyramid-like crystals and second corresponds to olive-green powder that crystallises in an orthorhombic $P2_12_12_1$ space group. On the basis of a temperature-dependent powder X-ray diffraction experiment, the monoclinic phase irreversibly converts into the orthorhombic upon heating. The elemental analysis and the irreversible conversion to another crystalline phase upon heating indicated that this orthorhombic phase could correspond to a solvent free phase. This assumption was later confirmed and olive-green powder was identified as a $Cs(C_{14}H_{10})$ phase (Section 3.4).

Molecular susceptibility measurements of two of the samples containing 60% and 30% of $Cs_2(C_{14}H_{10})_2(THF)$ phase revealed two different magnetic behaviours. In the sample

containing 60% of the $Cs_2(C_{14}H_{10})_2$(THF) phase, an irreversible bifurcation between ZFC and FC curves was observed. This splitting of ZFC and FC curves confirms, similarly to the potassium and rubidium phases, canted antiferromagnetism. The onset of long-range AFM ordering occurs at T_N = 9.9 K, significantly higher than that observed in the $Rb_2(C_{14}H_{10})_2$(THF) compound. In the sample containing $Cs(C_{14}H_{10})$ as the majority phase, a broad hump was observed. The observation of the broad hump in magnetic susceptibility is usually associated with low-dimensional magnetism. The values μ_{eff} = 1.8898(6) μ_B and Θ = -75.4(2) K from the Curie-Weiss fit in the high temperature region are in good agreement with spin S = ½ state and indicate strong AFM interactions between spins located on phenanthrides.

3.4 Cs(C$_{14}$H$_{10}$)

3.4.1 Synthesis and isolation

Caesium metal (120.3 mg, 0.905 mmol) and sublimed phenanthrene (166.3 mg, 0.933 mmol, 3 wt% excess) were placed in the bottom of the left hand side of the reaction vessel inside a glove box. Afterwards, the reaction vessel was transferred out of the glove-box and placed on a Schlenk line, evacuated, and THF (35 ml) was condensed on top of the phenanthrene and caesium. The mixture was ultrasonicated for 8 h at 50°C. The solution turned olive green, and the reaction was left to continue under vigorous stirring for 24 hours at room temperature, ensuring the reaction reached completion (all caesium metal dissolved/reacted). Then the solution, containing a small amount of insoluble green powder, was filtered into the right hand side of the reaction vessel and concentrated, by removing 22 ml of THF. Oxygen- and water-free *n*-hexane (36 ml) was condensed into the left hand side of the reaction vessel. The reaction vessel was inserted into a circulating bath, heated to 64°C, allowing THF to diffuse into the hexane-containing part. After 24 h a dry dark-olive green crystalline powder with purple lustre upon illumination was obtained (Figure 58). The material was washed with a fresh portion of *n*-hexane and dried under dynamic vacuum for 6 hours. Yield 200.3 mg (71%). Elemental analysis, calculated (%) for C$_{14}$H$_{10}$Cs: C 54.04, H 3.24; found C 54.12, H 3.28. The observed values correspond to Cs$_{0.999}$-Phenanthrene-THF$_{0.04}$ formula.
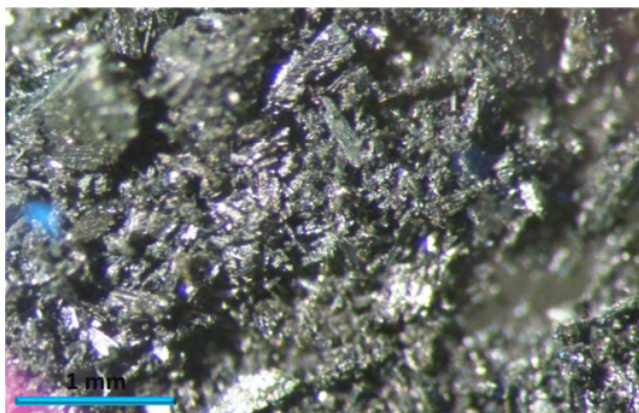
Figure 58: Polycrystalline solid of Cs(C$_{14}$H$_{10}$) under 40× magnification, a thick blue line represents 1 mm length.

3.4.2 Structural analysis based on powder X-ray diffraction

The powder X-ray diffraction profile of $Cs(C_{14}H_{10})$ collected on a laboratory source (λ = 1.54056 Å) at 295 K was used for determination of the structure using the EXPO2014 software suite. Based on the Le Bail decomposition method all observed Bragg reflections obey the extinction rules of the primitive orthorhombic $P2_12_12_1$ space group with lattice parameters a = 14.71 Å, b = 15.13 Å, a = 10.23 Å. According to the multiplicity for this space group and calculated volume per non-hydrogen atom (19.448 $Å^3$) two crystallographically independent Cs cations and two phenanthrene molecules, modelled as rigid bodies without internal degrees of freedom, were used in a direct-space simulated annealing global optimisation technique to obtain the initial structural model. The Rietveld refinement of the obtained structural model to the above described powder diffraction (Figure 59), yielded the lattice parameters a = 14.69611(17) Å, b = 15.11696(17) Å and c = 10.22026(11) Å.
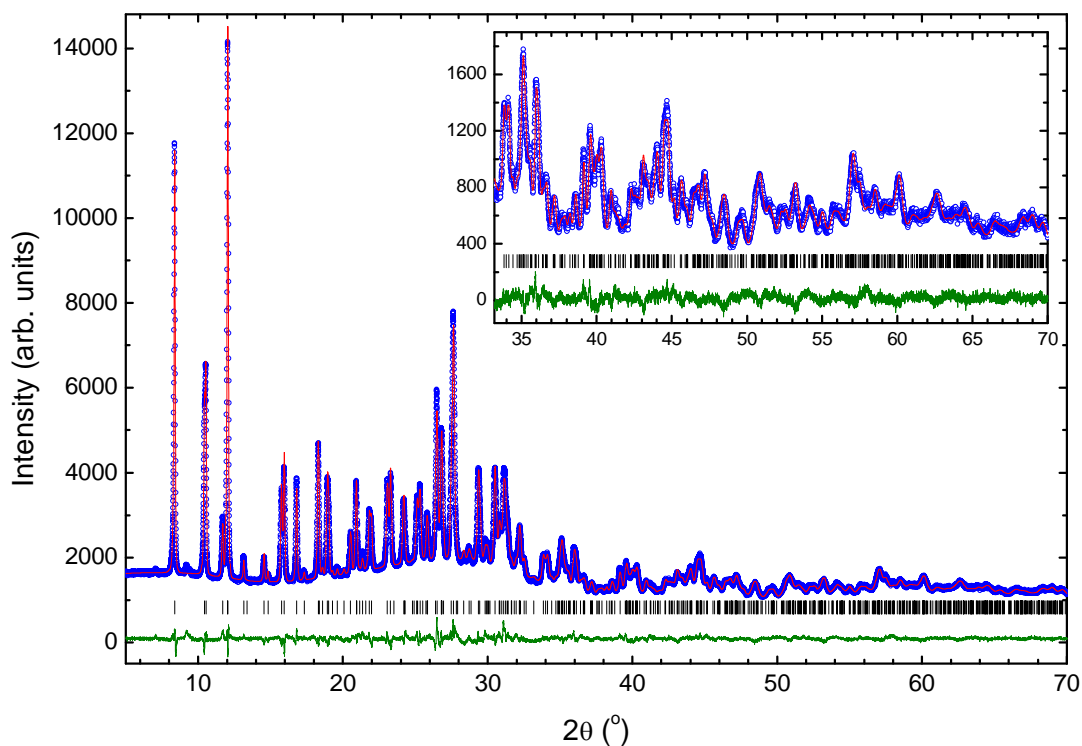
Figure 59: Powder diffraction of the caesium phenanthride, $Cs(C_{14}H_{10})$, sample. The experimentally obtained diffraction profile (λ = 1.54056 Å, Cu Kα) at 295 K (blue open circles), the calculated profile (red solid line), difference (olive green solid line) and predicted peak position (black tick marks). The inset shows the high 2θ region. The weighted profile and expected R factors are R_{wp} = 2.569% and R_{exp} = 2.397%.

The asymmetric unit cell consists of two phenanthrene radical anions and two caesium cations. By replicating parts of the asymmetric unit cell the coordination environment of Cs1$^+$ and Cs2$^+$ can be presented as shown in Figure 60.

The Cs1$^+$ interacts with phenanthrides through η^3, η^4 and η^5 coordination modes. The η^3 coordination is between Cs1$^+$ and the rim consisting of C1b, C10b and C11b (I$_b$ and II$_b$ planes) of *Phen2* with distances ranging from 3.3049(13) to 3.5640(12) Å. The η^4 coordination is between Cs1$^+$ and peripheral benzene ring plane III (C5, C6, C7 and C13) of *Phen1* with bond distances of 3.1009(13)- 3.7194(12) Å in length. The Cs1$^+$ to plane centroid distance is 3.2436(12)Å and the angle of Cs1$^+$ projection to the ring plane is 71°. The η^5 coordination is between Cs1$^+$ and shared benzene ring planes II and III (C8, C9, C10, C13 and C14) of *Phen1* with the bond distances ranging from 3.0698(13) to 3.5893(12) Å. The Cs1$^+$ to plane II centroid distance is 3.2318(13) Å and cation projection on the ring plane II at an angle of 68°. There is another short bond distance, 3.5467(13) Å, between Cs1$^+$ and C8b (*Phen2* on the right side of Figure 60), but it was not considered as a coordination bond due to the off-centred position between the cation and peripheral benzene ring plane III$_b$ (the Cs1$^+$ projection on the ring plane III$_b$ at an angle of 42°).

The Cs2$^+$ interacts with phenanthrides through η^3, η^5 and η^6 coordination modes. The η^3 coordination is between Cs2$^+$ and the central benzene plane II (C9, C10 and C11) of *Phen1* with distances of 3.3295(12)- 3.6912(12) Å in length. The Cs2$^+$ to plane centroid distance is 3.4530(13) Å and the angle of Cs2$^+$ projection on the ring plane is 71°. The η^5 coordination is between Cs2$^+$ and the peripheral benzene ring plane III$_b$ (C5b, C6b, C7b, C8b and C13b) of *Phen2* with bond distances ranging from 3.3194(12) to 3.6653(11) Å. The Cs2$^+$ to plane centroid distance is 3.2519(11) Å and cation projection on the ring plane at an angle of 81°. The η^6 coordination is between Cs2$^+$ and the peripheral benzene ring plane I$_b$ (C1b, C2b, C3b, C4b, C11b and C12b) of *Phen2* with bond distances of 3.4407(12)- 3.6818(11) Å in length. The Cs2$^+$ to plane centroid distance is 3.2682(11) Å and the angle of Cs2$^+$ projection on the ring plane is 85°. Likewise in the case of Cs1$^+$, the short bond distance, 3.5400(13) Å, between Cs2$^+$ and C7 was not considered as a coordination bond due to the off-centred position between cation and peripheral benzene ring plane III (the Cs2$^+$ projection on the ring plane III at an angle of 51°).
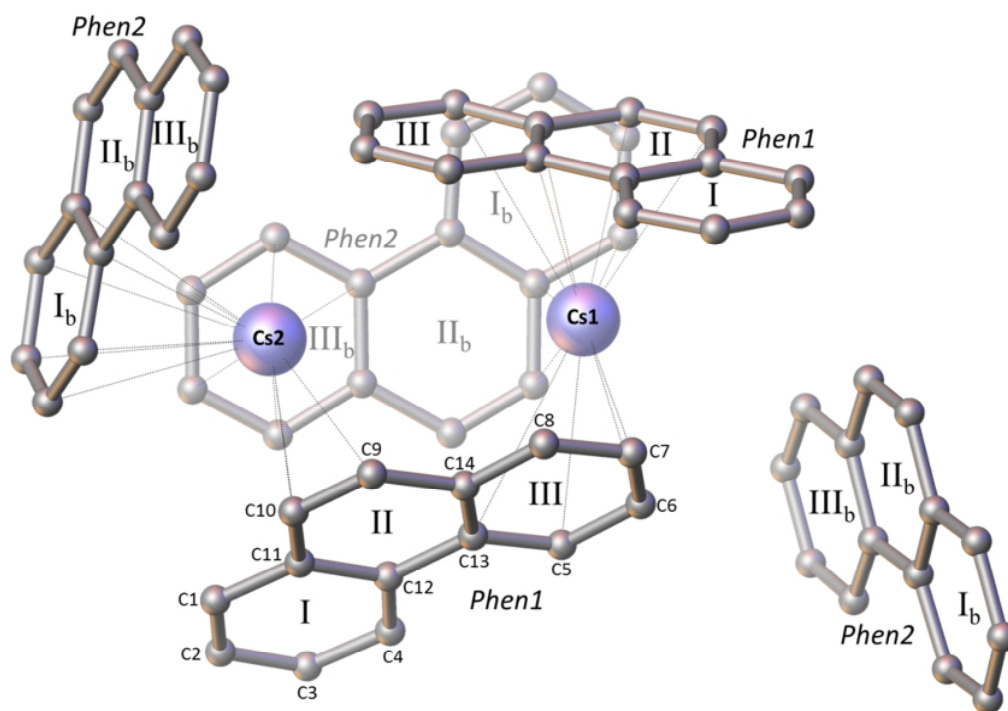
Figure 60: The coordination environment of $Cs1^+$ and $Cs2^+$ ions in $Cs(C_{14}H_{10})$ compound. Two crystallographically independent phenanthrene radical ions are denoted as *Phen1* and *Phen2*. The peripheral benzene ring planes are labelled as I, III, I_b, III_b and central planes as II, II_b. Black dotted lines represent $Cs^+\cdots C$ coordination interactions. Colour code: Cs purple and C grey. Hydrogen atoms are omitted for clarity and depicted structure was obtained from powder X-ray data collected at 295 K.

All $Cs^+\cdots C$ coordination bond distances are gathered in Table 15 and they are comparable to those reported in caesium-reduced 2,5,8-tri-tBu-phenalene, rubrene, cyclopentadiene, indene, fluorene and corannulene (Table 13 and 14). The basic parameters obtained from refinement, fractional atomic coordinates and atom to atom bond distances for crystal structures obtained from data sets collected at 295 K are gathered in the Appendix (6.5).

Table 15: Coordination modes and coordination bond distances between caesium cations and carbon atoms extracted from structure obtained at 295 K

Coordination mode	Cs$^+$ to C bond	Distance (Å)
η^3	Cs2-C10	3.3295(12)
	Cs2-C11	3.3474(12)
	Cs2-C9	3.6912(12)
η^3	Cs1-C11b	3.3049(13)
	Cs1-C10b	3.4822(13)
	Cs1-C1b	3.5640(12)
η^4	Cs1-C6	3.1009(13)
	Cs1-C5	3.3132(12)
	Cs1-C7	3.3287(13)
	Cs1-C13	3.7194(12)
η^5	Cs1-C9	3.0698(13)
	Cs1-C14	3.1015(12)
	Cs1-C10	3.4861(14)
	Cs1-C13	3.5772(12)
	Cs1-C8	3.5893(12)
η^5	Cs2-C6b	3.3194(12)
	Cs2-C7b	3.4301(12)
	Cs2-C5b	3.4586(11)
	Cs2-C8b	3.6210(11)
	Cs2-C13b	3.6653(11)
η^6	Cs2-C1b	3.4407(12)
	Cs2-C2b	3.4660(12)
	Cs2-C11b	3.5201(12)
	Cs2-C3b	3.5867(12)
	Cs2-C12b	3.6405(11)
	Cs2-C4b	3.6818(11)

The structure of $Cs(C_{14}H_{10})$ can be described as channel-like, where *Phen1* radical ions, under an angle of 52° in respect to each other, along with caesium cations form a chain along the crystallographic *c* direction, and *Phen2* form a cage around the chain, as shown in Figure 61. An alternative representation of the $Cs(C_{14}H_{10})$ structure would be a network of chains running along all three crystallographic directions. As described above, the chain running along the direction *c* consists of *Phen1*, while chains running along the *a* and *b* directions consist of *Phen2*. The angle between *Phen2* along the *a* direction is 106° and along the *b* direction is 78°. The position (spatial dislocation) of the *Phen2* along the *a* direction and the angle between radical ions prevent a strong interaction with Cs1$^+$. In contrast, the strong interaction between *Phen2* and Cs2$^+$ can be observed in the chain running along the crystallographic *b* direction (Figure 61).

The crystal structure of $Cs(C_{14}H_{10})$, according to temperature-dependent experiments performed at ESRF by Prof. Prassides' group, exhibits normal thermal contraction upon cooling. Values, a = 14.4388(2) Å, b = 15.0250(2) Å and b = 10.0842(1) Å, extracted from the diffraction profile at 30 K, show 1.8, 0.6 and 1.3% contraction of a, b, and c lattice parameters respectively, in comparison to lattice parameters obtained from the diffraction profile collected at ambient temperature (295 K) [165].
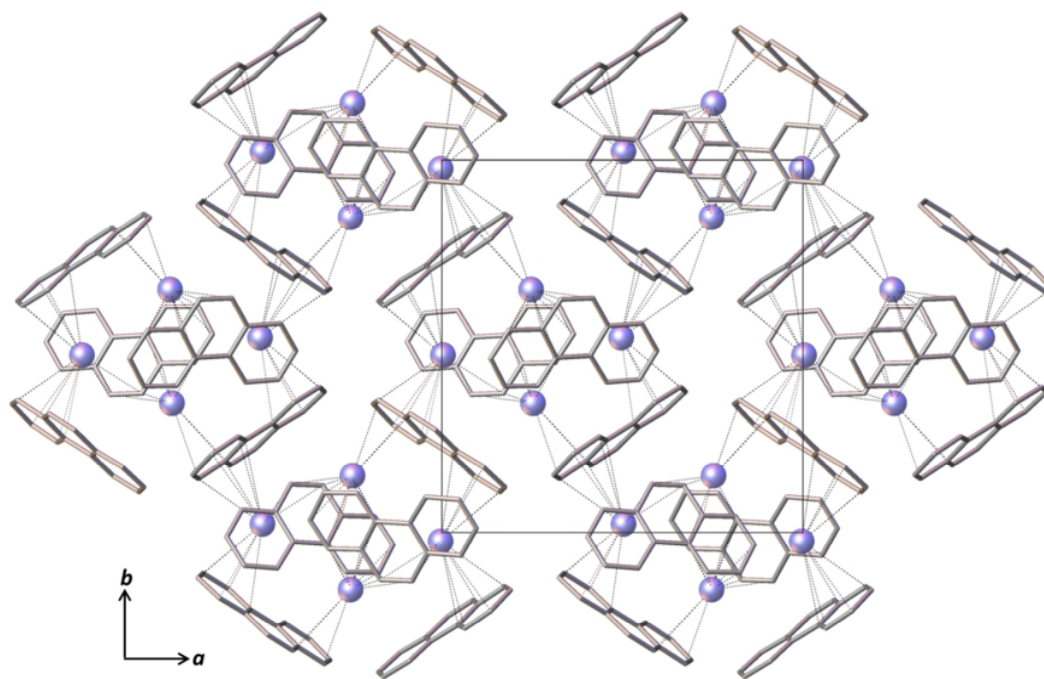
Figure 61: Projection of the $Cs(C_{14}H_{10})$ structure along the [001] direction showing a channel-like motif forming a 3D polymeric network of $Cs^+ \cdots C$ interaction (black dotted lines) between alkali metal ions and the phenanthride radical anions. Hydrogen atoms are omitted, and carbon-carbon bonds are depicted as tubes, for clarity. Colour code: Cs purple and C grey.

An obvious resemblance between $Cs_2(C_{14}H_{10})_2(THF)$ and solvent-free $Cs(C_{14}H_{10})$ indicates a subtle structural rearrangement during the solvent-loss process. Here we propose a mechanism for this structural rearrangement. It can be described as dissociation of THF molecules from Cs cations (red arrows), through the channels present in the a direction of the crystal structure. This is followed by clockwise/anticlockwise rotation of channels (purple arrow) and phenanthrene radical ions forming a cage (blue arrows), along with the translation (green arrows) and out of plane rotation (orange arrow) of the chain forming phenanthrides, as shown in Figure

62. Within this structural rearrangement, the voids after solvent dissociation became occupied and optimal Cs$^+$···π interactions are established.
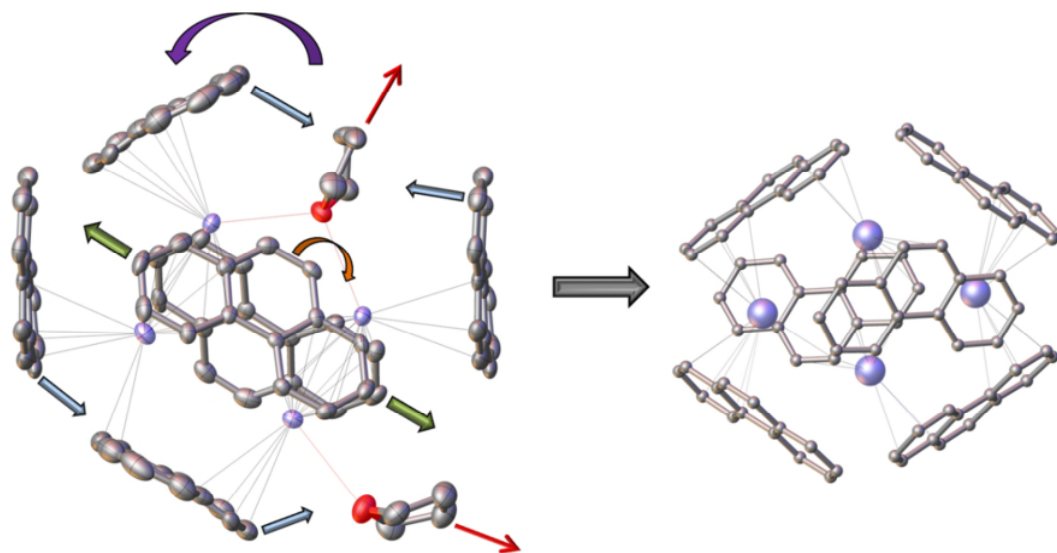
Figure 62: Projection of the Cs$_2$(C$_{14}$H$_{10}$)$_2$THF (left side) and Cs$_2$(C$_{14}$H$_{10}$) (right side) channel along the [001] direction. Red arrows represent the dissociation of molecules, purple the rotation of channel, blue the rotation of cage forming phenanthrides, and green and orange a translation and rotation of chain forming phenanthrides. Hydrogen atoms are omitted for clarity. Colour code: Cs purple O red and C grey.

3.4.3 Vibrational Spectroscopy

The charge transfer from caesium atom to phenanthrene molecule was investigated using Raman and IR vibrational spectroscopies. A red-shift of the vibrational peaks in the solvent-free caesium-reduced phenanthrene radical anion is the same as in the solvent-containing analogue, indicating the softening of the modes upon reduction (Figure 63). Moreover, the IR and Raman spectra of $Cs(C_{14}H_{10})$ and $Cs_2(C_{14}H_{10})_2THF$ are nearly identical, confirming a solvent loss. The tentative assignment of vibrational peaks is gathered in Table 50 and 51 (Appendix 6.9).
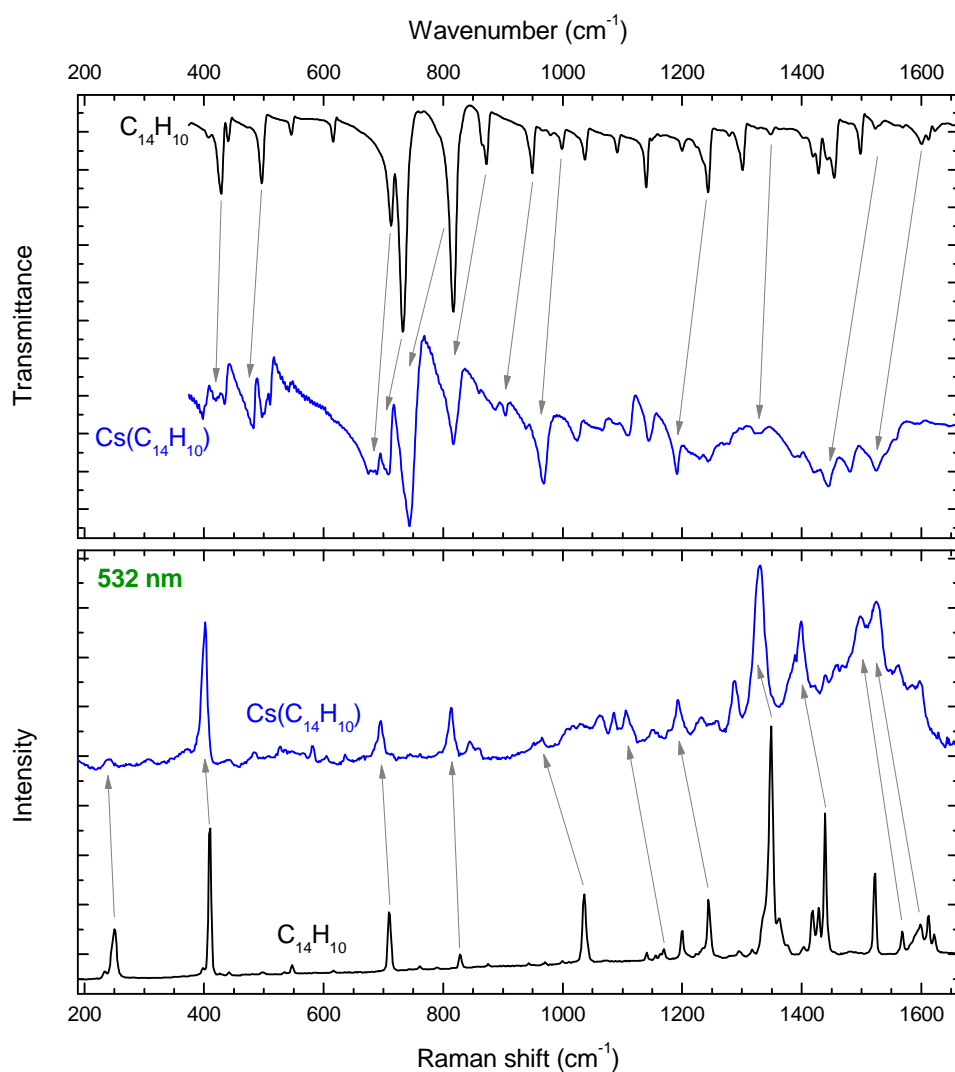
Figure 63: The infrared (top panel) and Raman (bottom panel) spectra of sample containing $Cs(C_{14}H_{10})$ phase (blue solid line) and pristine phenanthrene (black solid line). Grey arrows represent a tentative red-shift of some peaks. Raman spectrum was taken using a 532 nm excitation wavelength.

3.4.4 Magnetic Properties

The temperature dependence of the magnetic susceptibility (χ) of Cs(C$_{14}$H$_{10}$) in an applied magnetic field of 1 T and a Curie-Weiss fit in a temperature range between 150 and 300 K are shown in Figure 64.
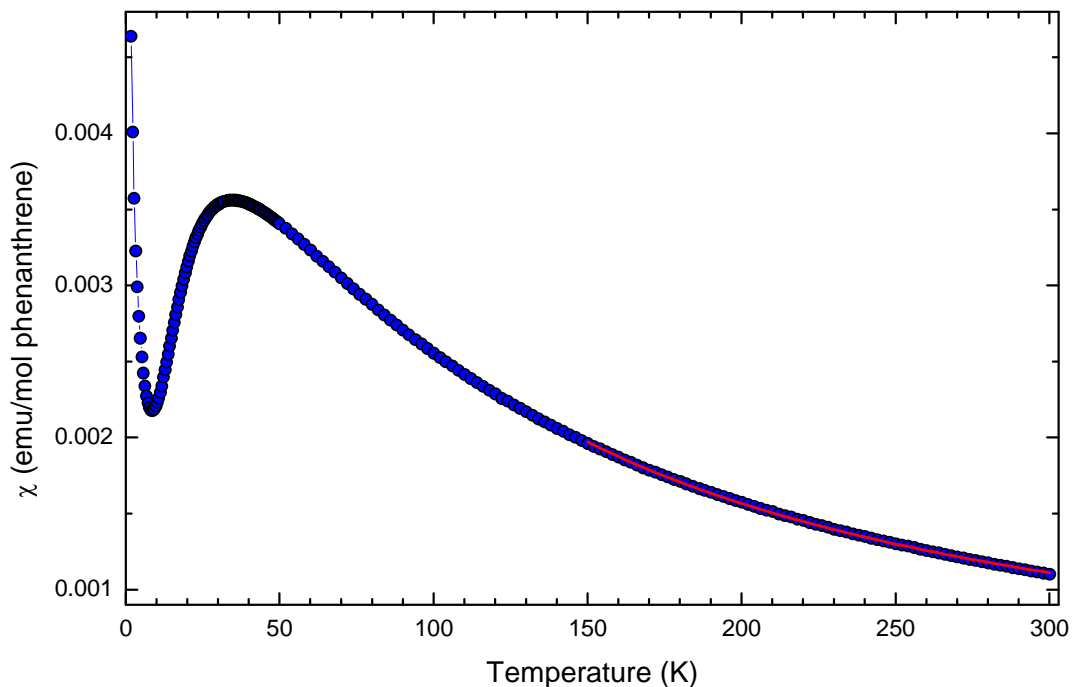
Figure 64: The temperature dependence of molecular susceptibility (χ *vs. T*) of Cs(C$_{14}$H$_{10}$) compound at applied field of 1 T (blue circles) along with fit to Curie-Weiss law in temperature region between 150 and 300 K (red curve). Data was collected in field-cooled (FC) protocol upon heating.

A broad hump with maximum T_{max} ~40 K can be observed in the χ *vs. T* curve, often associated with low-dimensional magnetism, followed by a sharp upturn at low temperatures arising from (we presume) impurity spin contributions. The susceptibility follows the Curie-Weiss law above 150 K yielding the effective magnetic moment μ_{eff} = 1.747(2) μ_B and negative Weiss temperature, Θ = -43.4(6) K. Extracted values are in excellent agreement with S = ½ state (one unpaired electron per phenanthrene molecule) and the large negative Weiss temperature indicates strong antiferromagnetic exchange interactions. The robustness of the broad hump feature was confirmed by performing magnetisation measurements (*M vs. T*) in the field range

between 5 mT and 1T, where no shift of the maximum, or splitting between ZFC and FC curves, was detected.

In order to investigate the magnetism in more detail the samples were sent to Prof. Denis Arčon for EPR analysis. The results were published [165]. Two coexisting components are observed in the X-band EPR spectrum at room temperature and both components show a Lorentzian lineshape. The temperature evolution of the X-band EPR signal is shown in Figure 65. The EPR intensity of the majority component (blue line in Figure 65) increases with decreasing temperature down to ~40 K where it reaches its maximum. Afterwards the intensity starts to decrease and at 6 K the signal for this component completely vanishes. The g value of 2.0007(3) of the majority component is in very good agreement with the g value for a free-electron, g_e = 2.0023, indicating the presence of the electronically-active phenanthride radical anion and confirming the complete electron transfer from caesium metal to the phenanthrene molecule. At low temperatures the EPR intensity of the minor component (green line in Figure 65) becomes dominant and increases with decreasing temperature. This minority component follows a Curie-like temperature dependence and corresponds to ca. 5% of spins in this material. These spin impurities can be associated with unpaired spins at the end of the chains and defects in the polycrystalline material. No additional line was observed in a wider field sweep at low temperature, which could be associated with antiferromagnetic resonance and therefore evidenced the absence of long range magnetic ordering. As stated above, both components follow a Lorentzian lineshape and, based on the absence of the Dyson lineshape asymmetry, which would provide a fingerprint for a metallic state, we can conclude that $Cs(C_{14}H_{10})$ is an insulator.
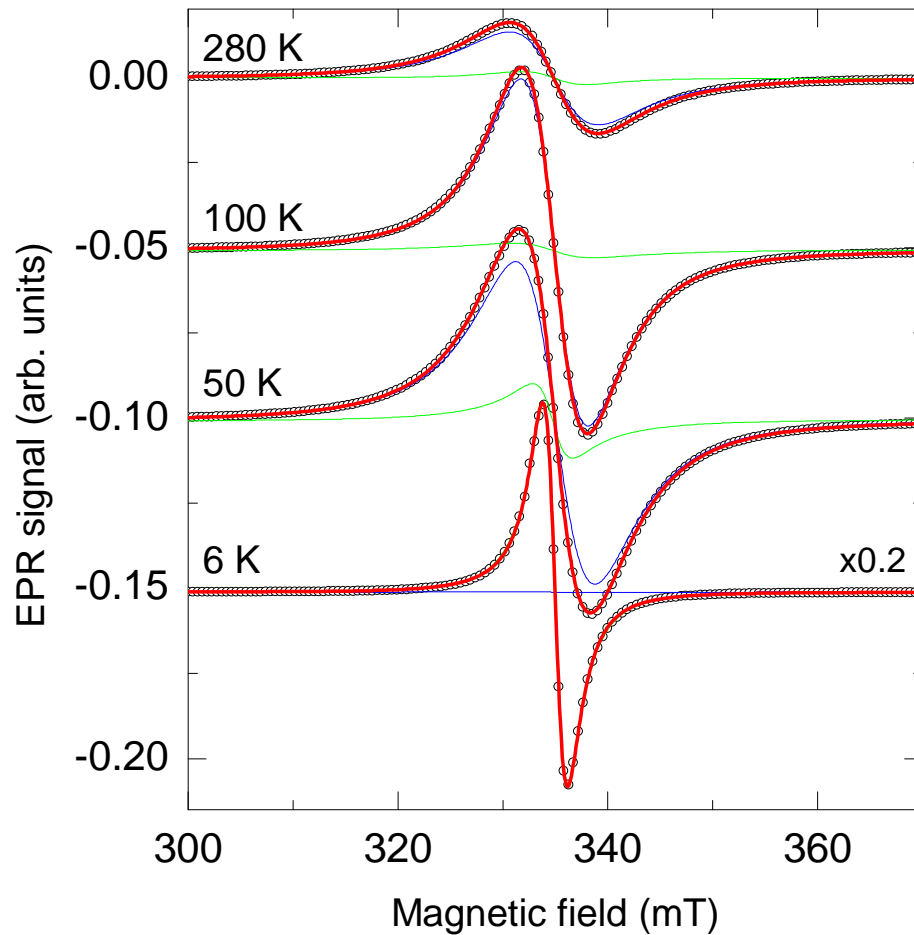
Figure 65: A temperature evolution of the X-band EPR spectra of Cs(C$_{14}$H$_{10}$) sample (open circles). The red solid line represents a combined fit of two overlapping components, which are following the Lorentzian lineshape. Blue and green solid lines are the fits of majority and minority component respectively [165].

The temperature-dependent SQUID and EPR magnetic susceptibility curves were fitted to several low-dimensional magnetic models explaining the exchange interaction in one or two dimensions. Both S = ½ 1D Ising uniform chain and quasi 1D Heisenberg alternating chain models gave equally good fits, and since these models can be explained and visualised with observed structural motifs, we present both of them.

Based on high-resolution EPR spectroscopy, the deconvolution of the EPR magnetic susceptibility into the majority low-dimensional and minority paramagnetic component was achieved. This permitted the subtraction of the impurity paramagnetic phase from the low-dimensional phase in the SQUID data (Figure 66). The fit of subtracted SQUID magnetic susceptibility data to the S = ½ 1D Ising chain model [134,

124] yields an intrachain exchange constant, J/k_B, of 88.6(2) K and a Curie constant, C, of 0.315(1) emuK/mol (μ_{eff} = 1.587(3) μ_B), consistent with S = ½ per phenanthrene molecule (grey solid line in Figure 66). A Curie constant of 0.0177(2) emuK/mol (μ_{eff} = 0.376(2) μ_B), corresponding to ca. 5% spins and Weiss temperature of -2(1) K were obtained after fitting the EPR minority magnetic susceptibility component to the Curie-Weiss law (purple dashed line in Figure 66).
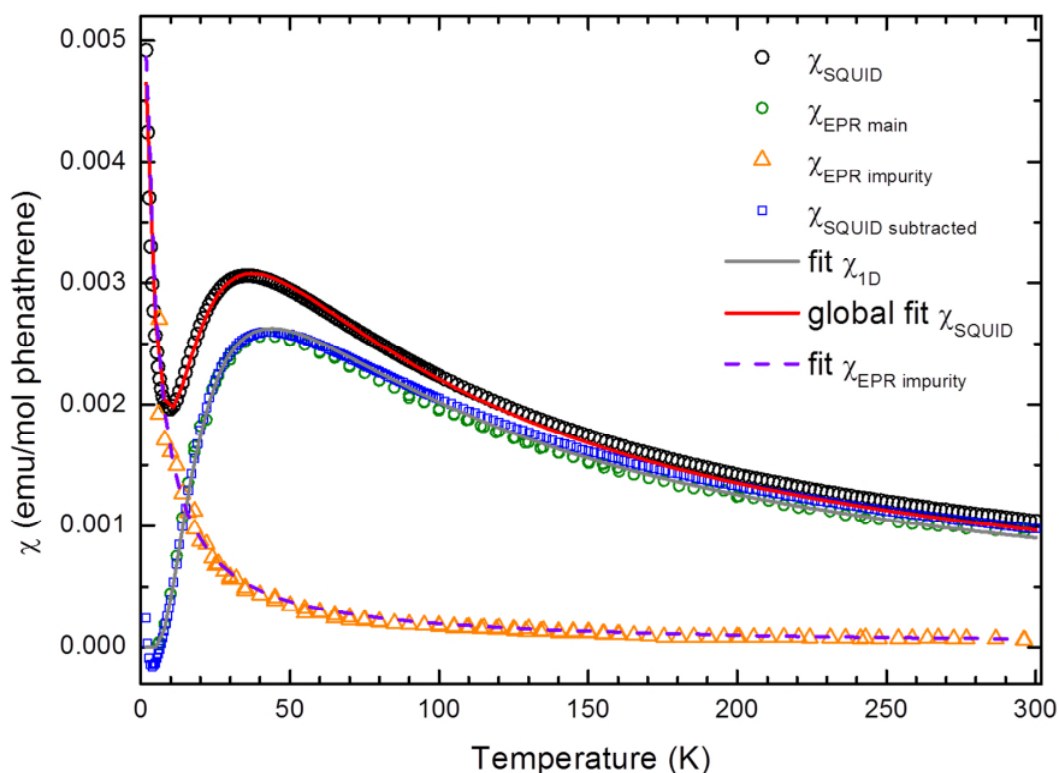
Figure 66: Magnetic susceptibility of Cs($C_{14}H_{10}$). The open black circles, open blue squares, open green circles and open triangles represent the temperature dependence of magnetic SQUID susceptibility, low-dimensional component after subtracting the impurity phase from SQUID data, temperature dependence of EPR susceptibility of majority low-dimensional component and minority paramagnetic component respectively. Solid red, solid grey and dotted purple lines correspond to global fit of SQUID data over the whole temperature range, fit of subtracted SQUID data to low-dimensional component and fit of de-convoluted EPR data to paramagnetic impurity phase.

According to structural motifs, the S = ½ uniform Ising 1D chain model can be described with antiferromagnetic superexchange interactions between phenanthride ions mediated through caesium cations. The chain consisting of *Phen1* − Cs1 − *Phen1* units runs along the c direction and the chain consisting of *Phen2* − Cs2 − *Phen2* units

runs along the *b* crystallographic direction, practically perpendicular in respect to each other. The angles between the II – Cs1 – III in *Phen1*, and the I_b – Cs2 – III_b in *Phen2* radical ions are 77.5^o and 64.2^o respectively, as depicted in Figure 67. On the basis of the extracted intrachain exchange constant, J/k_B, the strength of the superexchange interactions, J_1 and J_2, in the above-described chains (pale blue and red) needs to be similar in order to agree with the magnetic model. The interplay of those chains induces a frustration, and therefore prevents a long range magnetic ordering.
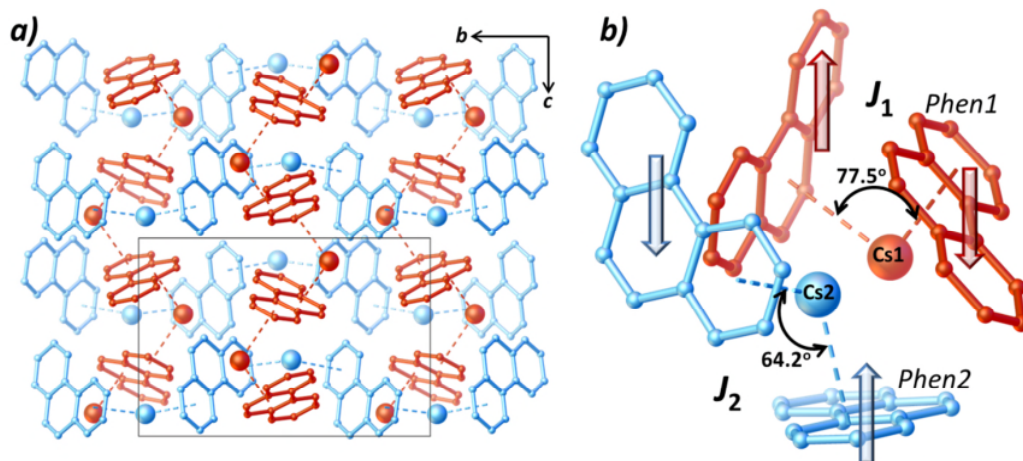
Figure 67: a) A representation of two chains consisting of phenanthride anions and Cs cations running along the crystallographic *c* and *b* directions, providing potential routes for superexchange interactions. b) The *Phen1* – Cs1 – *Phen1* and *Phen2* – Cs2 – *Phen2* units with corresponding angles.

The second low-dimensional magnetic model that describes the SQUID and EPR magnetic susceptibility data is a S = ½ Heisenberg quasi 1D alternating chain [135] model. Note: this fitting was performed by colleagues of the Prof. Prassides' group and is published in [165]. The fit of subtracted SQUID data to this model yields an intrachain exchange constant, J/k_B, of 77.9(3) K, an alternation parameter, α, of 0.687(5) and a Curie constant, *C*, of 0.301(1) emuK/mol (μ_{eff} = 1.552(3) μ_B), consistent with S = ½ per phenanthrene molecule (red solid line in Figure 68). As in the case of the above-described 1D chain model, the fit of the EPR minority magnetic susceptibility component to a Curie-Weiss law (solid green line in Figure 68) resulted in a Curie constant of 0.0177(2) emuK/mol (μ_{eff} = 0.376(2) μ_B), and Weiss temperature of -2(1) K.
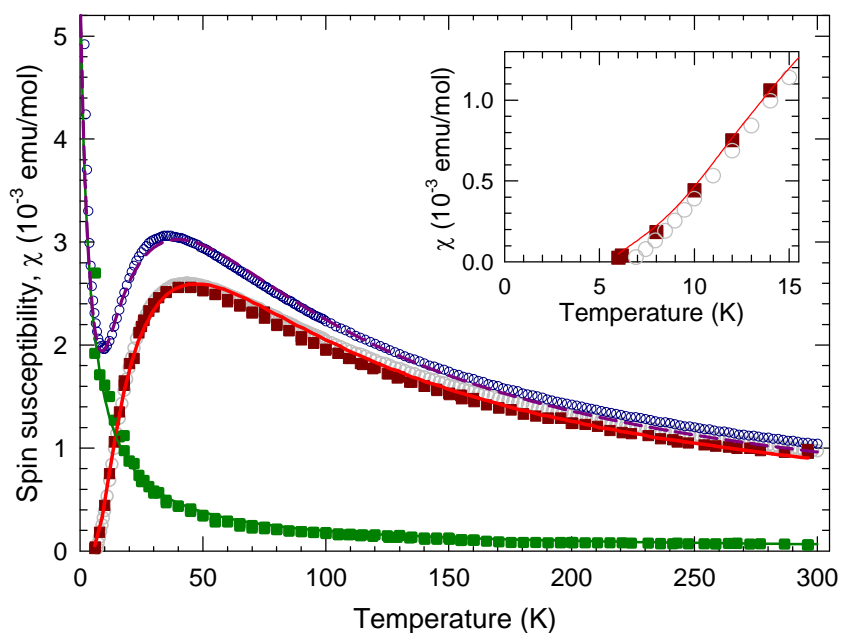
Figure 68: Temperature-dependent of main (dark red squares) and minority (green squares) EPR susceptibility data. The temperature dependence SQUID data (open blue circles) and, after Curie-like minority phase, subtracted SQUID data (open grey circles). The global fit of SQUID data over the whole temperature range, fit of subtracted SQUID data to low-dimensional component and fit of de-convoluted EPR data to paramagnetic impurity phase are shown with dotted purple, solid red and solid green lines respectively. The inset represents the spin susceptibility at low temperature [165].

The S = ½ Heisenberg quasi 1D alternating chain model consists, can be rationalised based on the structural motif, of direct exchange interactions between unpaired electrons localised on phenanthride anions. The structure can be represented as an array of chains comprising of *Phen1* and *Phen2* radical ions running along the crystallographic *c* direction, as depicted in Figure 69a. The spins interact in an antiferromagnetic manner where *J* with a value of 77.9(3) K and α*J* with a value of 53.5(2) K represent stronger and weaker intrachain exchange interactions as shown in Figure 69b. The close proximity of *Phen2'* and *Phen2''* radical ions in neighbouring delta chains should provide interactions in all three dimensions and long-range magnetic ordering should occur. However, the geometry of those channels prevents the antiferromagnetic interactions between spins on *Phen1*, *Phen2*, *Phen2'* and *Phen2''* (as presented in Figure 69c), and therefore, frustration needs to be taken into account.
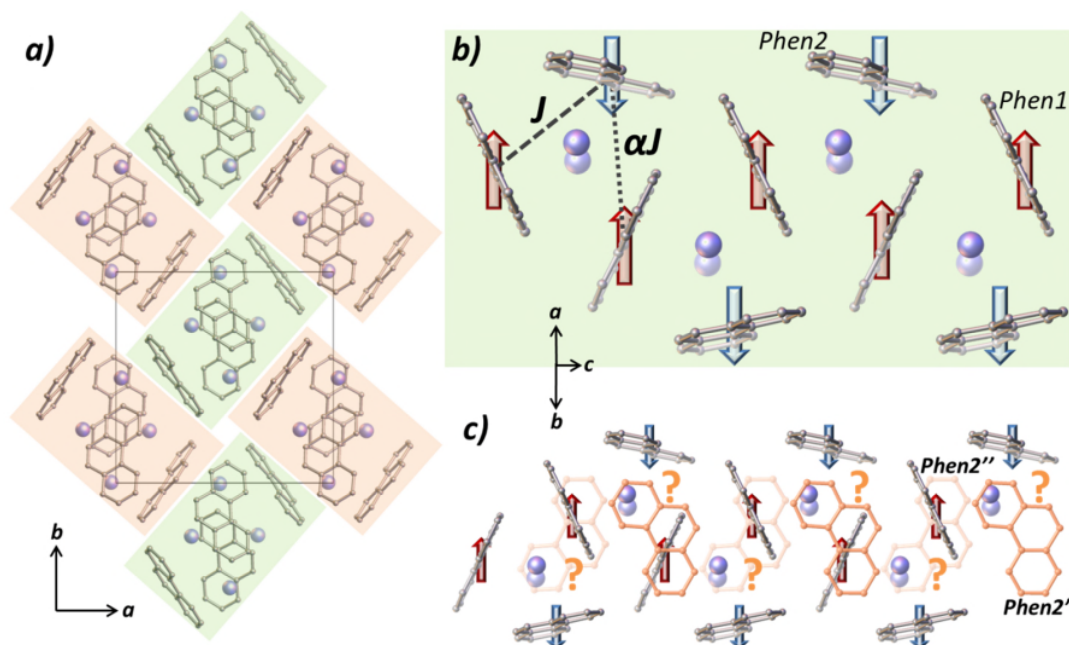
Figure 69: a) The presentation of chains with two different orientations comprising of *Phen1* and *Phen2* radical ions, pale green and pale red squares. b) A chain running along the crystallographic *c* direction with depicted stronger, *J*, and weaker, α*J*, intrachain magnetic exchange interactions (dotted grey lines) and spins (red and blue arrows) on *Phen1* and *Phen2* ions interacting in antiferromagnetic manner. c) The geometry induced frustration, for alternating chain magnetic model, preventing a long-range magnetic ordering via *Phen2'* and *Phen2''* radical ions (orange phenanthrene molecules). Colour code: Cs$^+$ purple, C grey.

Comprehensive first-principles Density functional theory (DFT), Density functional theory + Dynamical mean field theory (DFT + DMFT) and Quantum Monte Carlo calculations were performed by Prof. Ryotaro Arita's group in RIKEN, Center for Emergent Matter Science, Japan. These calculations provide further information about the magnetism in this material and linking the S = ½ Heisenberg quasi 1D alternating chain magnetic model to the determined crystal structure and measured magnetic data. The calculations are described in the literature [165] and this material is considered as a quantum spin liquid candidate.

3.4.5 Summary on $Cs(C_{14}H_{10})$ compound

The reduction of phenanthrene with caesium metal in THF followed by crystallisation at slightly elevated temperature yielded the highly crystalline solvent-free Cs salt of phenanthrene for the first time. The complete charge transfer was indicated by Raman and IR spectroscopy. The crystal structure of $Cs(C_{14}H_{10})$ was solved from data obtained on a powder X-ray diffractometer at room temperature using the simulated annealing technique. Two crystallographically independent phenanthrides (*Phen1* and *Phen2*) are with various η coordination bonds interacting with two crystallographically independent caesium cations (Cs1 and Cs2). The structural motif of $Cs(C_{14}H_{10})$ resembles that observed in the $Cs_2(C_{14}H_{10})_2(THF)$ compound and the structural rearrangement from $Cs_2(C_{14}H_{10})_2(THF)$ to $Cs(C_{14}H_{10})$ can be rationalised by rotation and translation of phenanthride units along with diffusion of THF molecules from the $Cs_2(C_{14}H_{10})_2(THF)$ crystal structure. The arrangement of constituents is such that *Phen1*, along with Cs1 and Cs2, form a chain along the crystallographic *c* direction and *Phen2* form a cage around the chain, all together effectively establishing a one dimensional structure.

The hallmark of the presence of low-dimensional magnetism, a broad hump in the temperature dependent SQUID magnetic susceptibility, was found. Based on EPR spectroscopy the separation of a majority low-dimensional component from the minor paramagnetic component following the Curie-Weiss law, originating from spin impurities in the sample, was achieved. After subtraction of the minor paramagnetic component, the SQUID susceptibility data was fitted to low-dimensional magnetic models. The S = ½ 1D Ising uniform chain and quasi 1D Heisenberg alternating chain models both yielded excellent fits. The S = ½ 1D Ising chain model relies on superexchange interactions, while the S = ½ Heisenberg quasi 1D alternating chain on direct exchange interactions. The structural geometry induces frustration, and therefore prevents long-range magnetic order, the absence of which down to low temperature renders $Cs(C_{14}H_{10})$ as a prominent candidate for a quantum spin liquid. More details about this compound, especially the description of magnetic properties based on the calculations can be found in the published article [165].

3.5 $K_4(C_{14}H_{10})_3(THF)_4$

3.5.1 Synthesis and crystal growth

Sublimed phenanthrene (167.8 mg, 0.941 mmol) and potassium metal (36.8 mg, 0.941 mmol) were placed on the bottom in the left hand side of the reaction vessel inside a glove box. Afterwards the reaction vessel was transferred out of the glove-box and placed on a Schlenk line, evacuated and THF (32 ml) were condensed on top of the phenanthrene and potassium. The olive green solution was vigorously stirred for 44 hours, ensuring the reaction completed (all potassium metal dissolved/reacted). Then the solution was filtered in to the right hand side of the reaction vessel and concentrated, by removing 25 ml of THF. The solution was layered with oxygen- and water-free n-hexane at -20 ^{o}C and crystallisation was carried out for 4 days at room temperature. The dark green/grey prism-like crystals (Figure 70) with purple lustre were washed twice with a new portion of n-hexane and dried under dynamic vacuum for 3 hours. A noticeable amount of white material, presumably pristine phenanthrene, was observed in the left hand side of the reaction vessel after washing the crystals grown in the right hand side part of the vessel. Beside single crystals, a small amount of olive green powder was observed in the right hand side of the reaction vessel. Yield 190.0 mg (82 %). Elemental analysis, calculated (%) for $C_{58}H_{62}K_4O_4$: C 71.12, H 6.38; found C 70.527, H 6.39. Observed values correspond to $K_{4.2}$-Phenanthrene$_3$-THF$_{4.3}$.
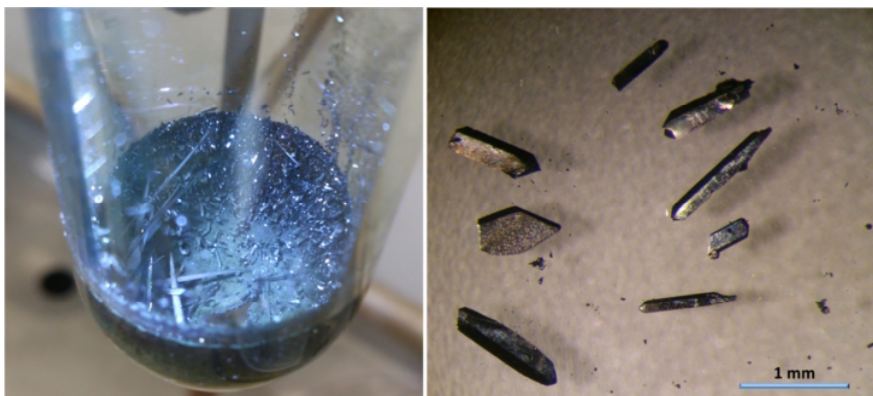
Figure 70: Isolated product in the reaction vessel (left panel) and single crystals of $K_4(C_{14}H_{10})_3(THF)_4$ under 40× magnification (right panel). Thick pale blue line represents 1mm length.

3.5.2 Single crystal structural analysis

Based on single crystal X-ray diffraction, collected using a synchrotron (λ = 0.688900 Å) at 120 K, the prism-like crystals were identified as $K_4(C_{14}H_{10})_3(THF)_4$. This compound crystallises in the triclinic $P\bar{1}$ space group with lattice parameters of a = 12.271(3) Å, b =13.346(3) Å, c = 15.1555(12) Å, α = 89.455(3)$^{\circ}$, β = 85.581(2)$^{\circ}$ and γ = 86.965(3)$^{\circ}$ at 120 K. The asymmetric unit cell consists of three phenanthrene radical anions (*Phen1, Phen2* and *Phen3*), four potassium cations (K1, K2, K3 andK4) and four THF molecules (*THF1*, *THF2*, *THF3* and *THF4*) as depicted in Figure 71. Moreover, two THF (*THF2* and *THF4*) molecules and one phenanthride (*Phen3*) are disordered, in the case of *Phen3*, because it is sitting on a centre of inversion. The occupancy of these three constituents was fixed to 0.5 during the refinement of the structural model. In Figure 71 both halves of the disordered phenanthrene radical ion, *Phen3*, are presented and shown as *Phen3'* and *Phen3''*.
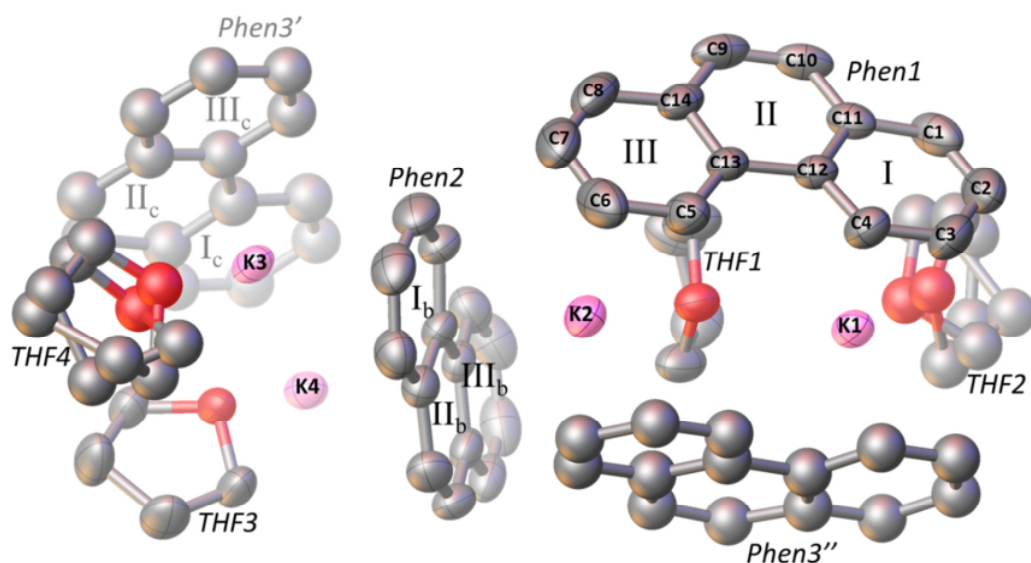
Figure 71: The asymmetric unit of $K_4(C_{14}H_{10})_3(THF)_4$ consisting of three crystallographically independent phenanthrides denoted *Phen1*, *Phen2* and *Phen3* (both parts of a disordered *Phen3* are presented as *Phen3'* and *Phen3''*) four potassium cations denoted as K1, K2, K3 and K4, and four THF molecules denoted as *THF1*, *THF2*, *THF3* and *THF4*. The peripheral benzene ring planes are labelled as I, III, I_b, III_b, I_c, III_c, and central planes as II, II_b, II_c. The pale green and grey phenanthrides at *Phen3''* position represent two different orientations in neighbouring unit cells, labels of the benzene ring planes of *Phen3''* are omitted for clarity. Colour code: K lilac; O red and C grey. Hydrogen atoms are omitted for clarity, and the carbon atom numbering of phenanthrene radical anions can be followed by labels of benzene ring planes.

To simplify the coordination environments of potassium cations the constituents of the crystal structure are presented by separately describing the coordination environment of K1 and K2 (Figure 72), and K3 and K4 (Figure 73) cations.

The $K1^+$ interacts with phenanthrides, *Phen1* and *Phen3''*, through two η^6 coordination modes. The first η^6 coordination is between $K1^+$ and the peripheral benzene plane I (C1, C2, C3, C4, C11 and C12) of *Phen1* with distances of 3.049(4)- 3.460(4) Å in length, the $K1^+$ to plane centroid distance is 2.952(2) Å and the angle of $K1^+$ projection on the ring plane of 80°. The second η^6 coordination is between $K1^+$ and the peripheral benzene ring plane III_c (C65, C66, C67, C68, C73 and C74) of *Phen3''* with bond distances ranging from 2.965(5) to 3.294(6) Å, the $K1^+$ to plane centroid distance is 2.809(3) Å and cation projection on the ring plane at an angle of 82°. The local binding of the $K1^+$ cation is shown in Figure 72.

The oxygen atom in *THF1* molecule is coordinated as a bridging ligand to $K1^+$ and $K2^+$ through μ^2 coordination mode. The $K1^+ \cdots O1$ and $K2^+ \cdots O1$ distances are 2.781(3) and 2.748(3) Å respectively and the K1-O1-K2 angle is 106.71(9)^o. The oxygen atoms in the *THF2* molecule (two oxygen atoms are depicted, because of the disordered *THF2* molecule) are as a terminal ligand coordinated to $K1^+$ through a μ^1 coordination mode, with the $K1^+ \cdots O2a/O2b$ bond distances of 2.602(6) and 2.698(6) Å (Figure 72).

The second cation, $K2^+$, interacts with the phenanthrene radical ions (*Phen1*, *Phen2* and *Phen3''*) through η^3, η^4 and η^6 coordination modes. The η^3 coordination is between $K2^+$ and the peripheral benzene ring plane III (C5, C6 and C7) of *Phen1* with bond distances ranging from 3.054(5) to 3.320(6) Å. The $K2^+$ to plane centroid distance is 3.149(2) Å and the angle of $K2^+$ projection on the ring plane is 73°. The η^4 coordination is between $K2^+$ and the peripheral benzene ring plane I_c (C62, C63, C64 and C72) of *Phen3''* with distances of 3.054(5)- 3.408(4) Å in length. The $K2^+$ to plane centroid distance is 3.050(2) Å and cation projection on the ring plane at an angle of 76°. The η^6 coordination is between $K2^+$ and the peripheral benzene ring plane I_b (C21, C22, C23, C24, C31 and C32) of *Phen2* with bond distances ranging from 3.134(4) to 3.462(4) Å. The $K2^+$ to plane centroid distance is 2.992(2) Å and cation projection on the ring plane at an angle of 82°. The local binding of $K2^+$ cation is shown in Figure 72.
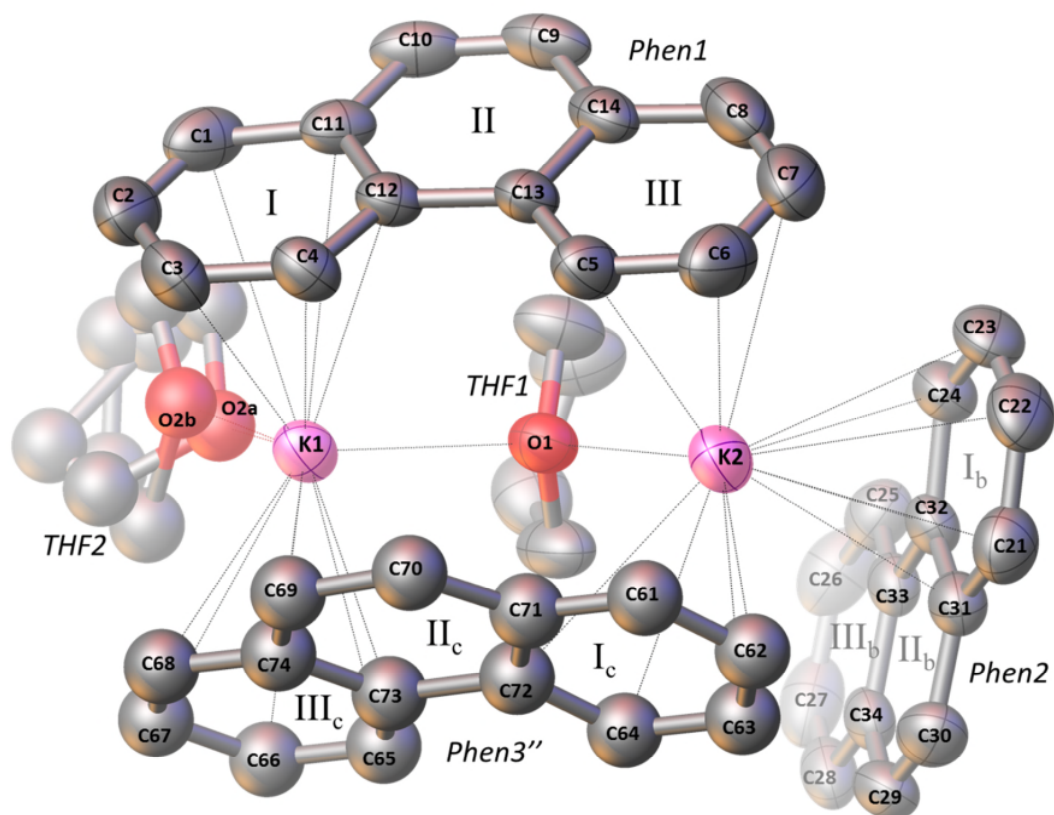
Figure 72: Representation of coordination environment of $K1^+$ and $K2^+$ ions in the $K_4(C_{14}H_{10})_3(THF)_4$ compound. Three crystallographically independent phenanthrene radical ions are denoted *Phen1*, *Phen2* and *Phen3''*. The peripheral benzene ring planes are labelled I, III, I_b, III_b, I_c, III_c, and central planes II, II_b, II_c. Black dotted lines and red dotted lines represent $K^+ \cdots C$ and $K^+ \cdots O$ coordination. Colour code: K lilac; O red and C grey. Thermal ellipsoids are shown with 50% probability level (except in the disordered molecules), hydrogen atoms are omitted for clarity and the depicted structure was obtained from data collected at 120 K.

The $K3^+$ interacts with phenanthrides (*Phen2* and *Phen3'*) through η^4 and η^6 coordination modes. The η^4 coordination is between $K3^+$ and the peripheral benzene plane I_b (C22, C23, C24 and C32) of *Phen2* with distances of 3.041(4)- 3.402(5) Å in length. The $K3^+$ to plane centroid distance is 3.008(2) Å and the angle of $K3^+$ projection on the ring plane is 78°. The η^6 coordination is between $K3^+$ and the peripheral benzene ring plane III_c (C45, C46, C47, C48, C53 and C54) of *Phen3'* with bond distances ranging from 2.983(5) to 3.243(6) Å. The $K3^+$ to plane centroid distance is 2.788(2) Å and cation projection on the ring plane at an angle of 84°. The local binding of $K3^+$ cation is shown in Figure 73.

113
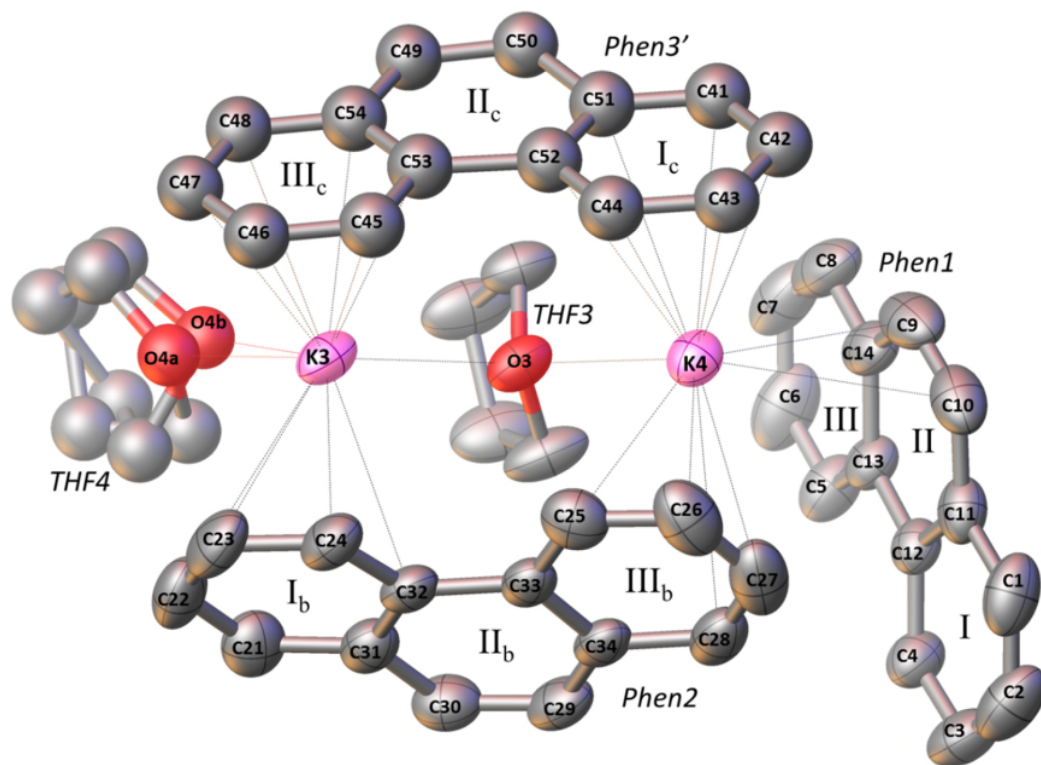
Figure 73: The coordination environment of K3$^+$ and K4$^+$ ions in the K$_4$(C$_{14}$H$_{10}$)$_3$(THF)$_4$ compound. Three crystallographically independent phenanthrene radical ions are denoted *Phen1*, *Phen2* and *Phen3'*. The peripheral benzene ring planes are labelled I, III, I$_b$, III$_b$, I$_c$, III$_c$, and central planes II, II$_b$, II$_c$. Black dotted lines and red dotted lines represent K$^+$···C and K$^+$···O coordination. Colour code: K lilac; O red and C grey. Thermal ellipsoids are shown with 50% probability level (except in the disordered molecules), hydrogen atoms are omitted for clarity and the depicted structure was obtained from data collected at 120 K.

The coordination interactions between K4$^+$ and the phenanthrene radical ions (*Phen1*, *Phen2* and *Phen3'*) are through η^2, η^4 and η^6 coordination modes. The η^2 coordination is between K4$^+$ and the rim of benzene plane II (C9 and C10) of *Phen1* with bond distances of 3.047(4) to 3.278(5) Å the K4$^+$ to plane centroid distance is 3.384(2) Å and the angle of K4$^+$ projection on the ring plane of 64°. The η^4 coordination is between K4$^+$ and the peripheral benzene plane III$_b$ (C25, C26, C27 and C28 atoms) of *Phen2* with bond distances of 3.116(4)- 3.413(4) Å in length, the K4$^+$ to plane centroid distance is 3.063(2) Å and the angle of K4$^+$ projection on the ring plane is 79°. The η^6 coordination is between K4$^+$ and the peripheral benzene ring plane I$_c$ (C41, C42, C43, C44, C51 and C52) of *Phen3'* with bond distances ranging from 3.069(5) to 3.283(4) Å. The K4$^+$ to

114

plane centroid distance is 2.857(2) Å and the cation projection on the ring plane at an angle of 85°. The local binding of K4$^+$ cation is shown in Figure 73.

Similarly as in the local coordination environment of K1 and K2 cations, the oxygen atom in the *THF3* molecule is as a bridging ligand coordinated to K3$^+$ and K4$^+$ through a μ^2 coordination mode. The K3$^+\cdots$O and K4$^+\cdots$O distances are 2.798(3) and 2.787(3) Å respectively and the K3-O-K4 angle is 105.30(8)^o. The oxygen atoms in the *THF4* molecule (two oxygen atoms are depicted, because of the disordered *THF4* molecule) act as a terminal ligand coordinated to K3$^+$ through a μ^1 coordination mode, with the K3$^+\cdots$O4a/O4b bond distances of 2.659(5) and 2.694(5) Å (Figure 73).

All K$^+\cdots$C and K$^+\cdots$O coordination bond distances are gathered in Table 16 and they are comparable to those reported in potassium-reduced naphthalene, anthracene, tetracene, perylene, coronene, cyclopentadiene, indene, fluorene, bisfluorene, Cp-phenanthrene, corannulene, sumanene, decacyclene and [8]CPP materials (Table 9 and 10). The basic parameters obtained from refinement, fractional atomic coordinates, atom to atom bond distances and bond angles for crystal structures obtained from data sets collected at 120 K are gathered in the Appendix (6.6).

Table 16: Coordination modes and coordination bond distances between potassium cations and carbon/oxygen atoms extracted from structure obtained at 120 K.

Coordination mode	K$^+$ to C or O bond	Distance (Å)
η^2	K4-C9	3.047(4)
	K4-C10	3.278(5)
η^3	K2-C6	3.054(5)
	K2-C5	3.172(4)
	K2-C7	3.320(6)
η^4	K2-C63	3.054(5)
	K2-C64	3.117(5)
	K2-C62	3.295(5)
	K2-C72	3.408(4)
η^4	K3-C24	3.041(4)
	K3-C23	3.166(4)
	K3-C32	3.193(4)
	K3-C22	3.402(5)
η^4	K4-C26	3.116(4)
	K4-C27	3.193(5)
	K4-C25	3.274(4)

	K4-C28	3.413(4)
η⁶	K1-C4	3.049(4)
	K1-C3	3.107(5)
	K1-C12	3.206(4)
	K1-C2	3.301(6)
	K1-C1	3.454(4)
	K1-C11	3.460(4)
η⁶	K1-C74	2.965(5)
	K1-C73	3.042(5)
	K1-C68	3.061(6)
	K1-C65	3.206(5)
	K1-C67	3.224(5)
	K1-C66	3.294(6)
η⁶	K2-C21	3.134(4)
	K2-C22	3.192(5)
	K2-C31	3.246(4)
	K2-C23	3.331(5)
	K2-C24	3.451(4)
	K2-C32	3.462(4)
η⁶	K3-C54	2.983(5)
	K3-C48	3.043(4)
	K3-C53	3.056(5)
	K3-C47	3.172(6)
	K3-C45	3.186(6)
	K3-C46	3.243(6)
η⁶	K4-C43	3.069(5)
	K4-C42	3.081(5)
	K4-C44	3.164(5)
	K4-C41	3.190(6)
	K4-C52	3.271(4)
	K4-C51	3.283(4)
μ²	K1-O$_{THF1}$	2.781(3)
	K2-O$_{THF1}$	2.748(3)
μ¹	K1-O2a$_{THF2}$	2.602(6)
	K1-O2b$_{THF2}$	2.698(6)
μ²	K3-O$_{THF3}$	2.798(3)
	K4-O$_{THF3}$	2.787(3)
μ¹	K3-O4a$_{THF4}$	2.659(5)
	K3-O4b$_{THF4}$	2.694(5)

The coordination environment of potassium cations pairs, $K1^+/K2^+$ and $K3^+/K4^+$, are practically identical. In the first case *Phen1*, *Phen3''* and *THF1* form a triangle-like motif around $K1^+$ and $K2^+$ cations, and *Phen2* and *THF2* make the coordination sphere of

potassium cations complete, and thereby encapsulate them. In the second case the coordination is very similar: *Phen2*, *Phen3'* and *THF3* form a triangle-like motif, and *Phen1* and *THF4* finish off the encapsulation of the $K3^+$ and $K4^+$ cations. Even the angles between *Phen1* and *Phen3''*, and *Phen2* and *Phen3'* dimers are almost the same, $69.738(6)^o$ and $68.034(6)^o$ respectively. This arrangement of phenanthrene radical ions and THF molecules around potassium ions is reminiscent of the arrangement observed in $Rb_2(C_{14}H_{10})_2(THF)$, $K_2(C_{14}H_{10})_2(THF)$ and $Cs_2(C_{14}H_{10})_2(THF)$ compounds, with the exception that the second THF molecule completes the coordination sphere of $K1^+/K3^+$, instead of a phenanthride unit.
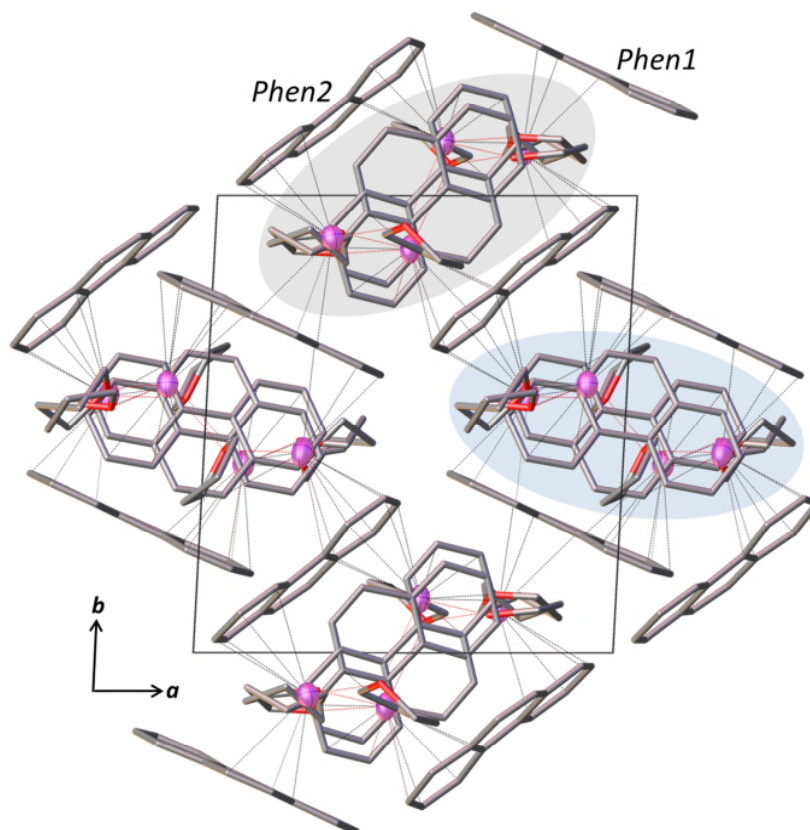
Figure 74: Projection of $K_4(C_{14}H_{10})_3(THF)_4$ structure along the [001] direction showing four channel-like motifs forming a 3D polymeric network of $K^+ \cdots C$ interaction (black dotted lines) between alkali metal ions and the phenanthride radical anions. The pale grey and the pale blue ellipses present chains comprised of *Phen3'*, *THF3*, *THF4*, $K3^+$ and $K4^+$, and *Phen3''*, *THF1*, *THF2*, $K1^+$ and $K2^+$ respectively. Hydrogen atoms are omitted, and carbon-carbon and carbon-oxygen bonds are depicted as tubes for clarity. Colour code: K lilac; O red and C grey, red dotted lines represent $K^+ \cdots O$ coordination.

By repeating the asymmetric parts of the unit cell throughout the space, a 3D structural motif, presented in Figure 74, is observed.

An examination of this structural motif reveals a channel-like arrangement of constituents, where *Phen3'*, K3$^+$, K4$^+$, *THF3* and *THF4* form the first type (grey ellipse) and *Phen3''*, K1$^+$, K2$^+$, *THF1* and *THF2* form the second type of chains running along the crystallographic *c* direction. *Phen1* and *Phen2* surround those chains and form a cage around them. A similar packing motif was also observed in $Cs_2(C_{14}H_{10})_2(THF)$ and $Cs(C_{14}H_{10})$. However, under a closer investigation, a very profound difference can be observed. The THF molecules orientated in a specific way form channels, running along the crystallographic *b* direction, and thus effectively prevent any interactions between *Phen3'* or *Phen3''* along the *c* direction as shown in Figure 75 and 76. Moreover, the *Phen3'* or *Phen3''* are coordinated to four potassium cations, in contrast to Phen1 and Phen2, suggesting that these two phenanthride units are dianions, which is in agreement with the formula extracted from single crystal X-ray diffraction analysis.
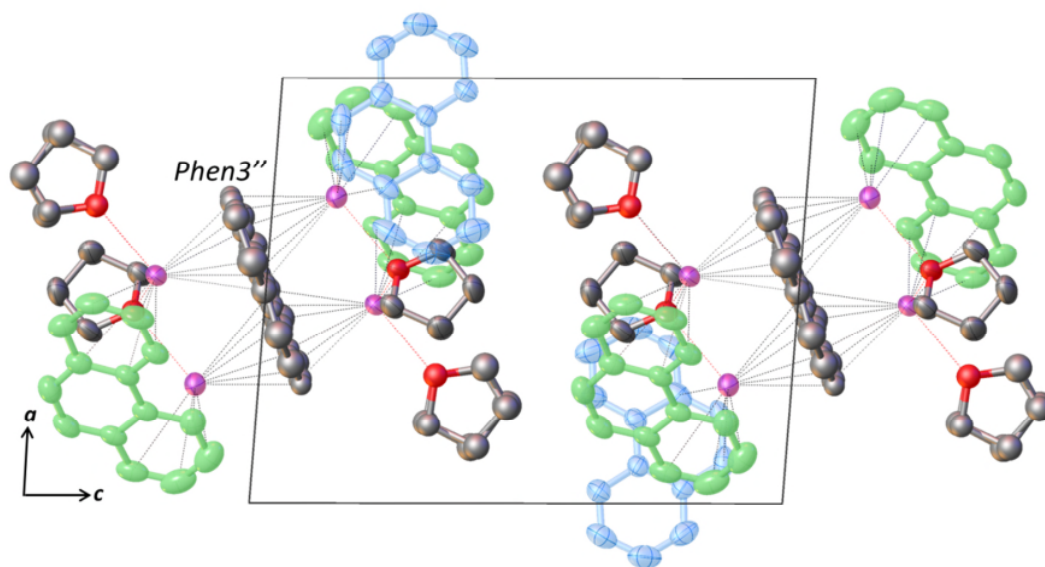
Figure 75: A channel-like arrangement projected along the [010] direction, disclosing the disconnection in coordination between *Phen3'* units along the crystallographic *c* direction due to the position and orientation of THF molecules. Pale blue and pale green phenanthrides represent *Phen1* and *Phen2* respectively. Colour code: K lilac; O red and C grey. Hydrogen atoms are omitted for clarity.
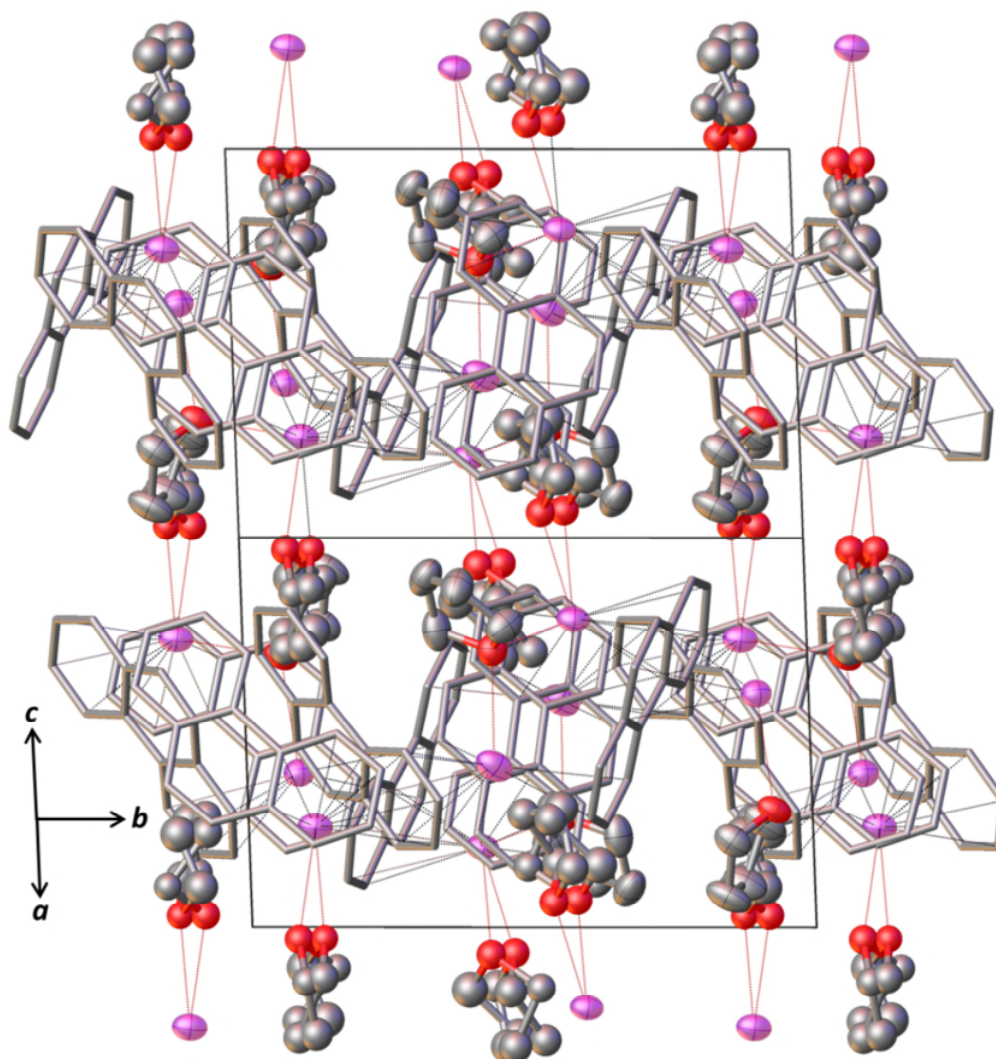
Figure 76: A projection along the [101] direction shows channels of THF molecules running along the crystallographic *b* direction. Carbon-carbon bonds in phenanthrides are depicted as tubes and hydrogen atoms are omitted for clarity. $K^+ \cdots C$ and $K^+ \cdots O$ interactions are represented with black dotted and red dotted lines respectively. Colour code: K lilac; O red and C grey.

3.5.3 Powder X-ray diffraction

The structural model obtained from single crystal analysis at 120 K was refined to the powder diffraction profile collected at 294 K using a laboratory source (λ = 0.7093 Å). The extracted lattice parameters are a = 12.3625(9) Å, b = 13.5529(9) Å, c = 15.4573(9) Å, α = 89.351(7)^o, β = 85.359(6)^o and γ = 87.400(5)^o. In contrast to $K_2(C_{14}H_{10})_2(THF)$, no negative thermal expansion of the lattice parameters was observed in this compound. Results of the Rietveld refinement are shown in Figure 77.
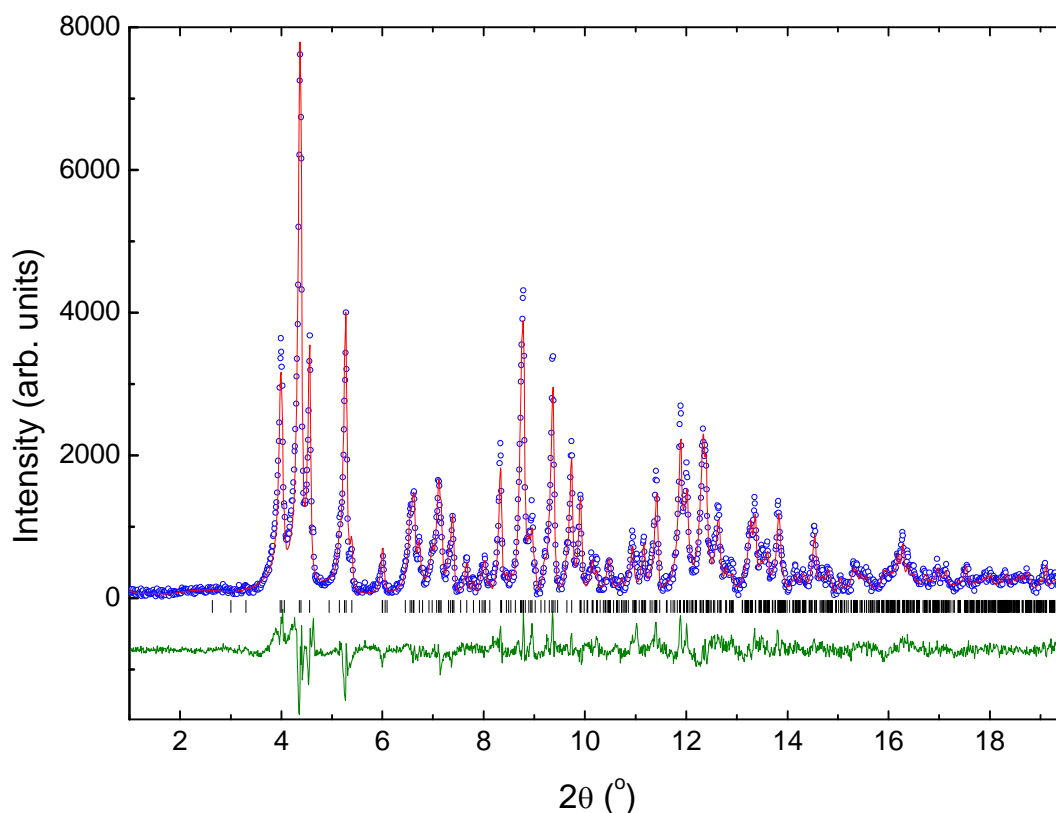
Figure 77: Powder diffraction of the $K_4(C_{14}H_{10})_3(THF)_4$ sample. The experimentally obtained diffraction profile (λ = 0.7093 Å, Mo Kα) at 294 K (blue open circles), the calculated profile (red solid line), difference (olive green solid line) and predicted peak position (black tick marks). The weight profile and expected R factors are R_{wp} = 18.97% and R_{exp} = 4.73%.

Based on a temperature-dependent powder X-ray diffraction experiment performed on a synchrotron source (λ = 0.399846(13) Å) using a hot-air blower, two structural transitions of the $K_4(C_{14}H_{10})_3(THF)_4$ were observed upon heating. It must be noted that

several months elapsed between synthesis of the material and the temperature-dependent experiment at the synchrotron and the diffraction profile taken at room temperature (20 ^{o}C), before the temperature-dependent experiment, shows the presence of the most intense peaks (denoted as blue asterisks) corresponding to $K_2(C_{14}H_{10})_2(THF)$. The presence of this peak signals a slow solvent loss at room temperature over a longer time period. The first transition on heating occurs between 60 and 70 ^{o}C and the second between 90 and 100 ^{o}C as shown in Figure 78. During the first transition the number of diffraction peaks decreases indicating that the new phase crystallises in crystallographic space group with higher symmetry than the parent one. The exact match between the diffraction profiles of $K_2(C_{14}H_{10})_2(THF)$ (orange curve) and the sample (blue curve) confirms that the $K_4(C_{14}H_{10})_3(THF)_4$ phase converts to $K_2(C_{14}H_{10})_2(THF)$ upon heating. The disproportionation process is not yet confirmed, but it seems that THF is labile enough to leave the structure, perhaps through the channels described in Figure 76, followed by rearrangement of the remaining constituents into a $K_2(C_{14}H_{10})_2(THF)$ phase. The second transition in the temperature range between 90 and 100 ^{o}C is the same as described in the Section 3.2.2.
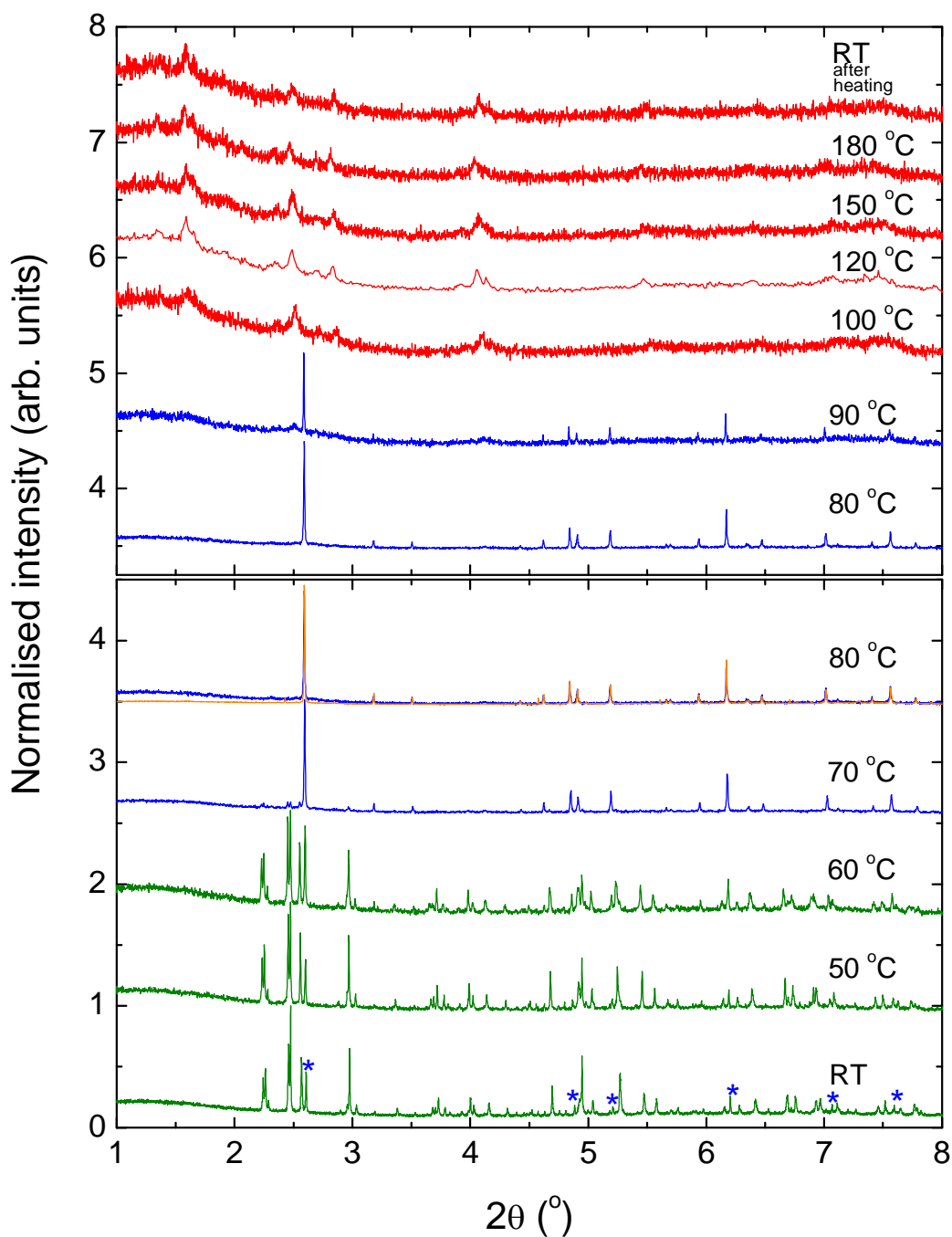
Figure 78: Temperature-dependent powder diffractograms (λ = 0.399846(13) Å). Diffraction profiles of $K_4(C_{14}H_{10})_3(THF)_4$ phase (olive green solid lines, at 20, 50 and 60 ^{o}C), $K_2(C_{14}H_{10})_2(THF)$ phase (blue solid lines, at 70, 80 and 90 ^{o}C) and newly formed poorly crystalline phase (red solid line, at 100, 120, 150 and 180°C). The asterisks indicate the presence of $K_2(C_{14}H_{10})_2(THF)$ phase in the starting material and the orange solid line is the diffraction profile of the phase-pure $K_2(C_{14}H_{10})_2(THF)$ sample taken at 80 ^{o}C.

3.5.4 Vibrational Spectroscopy

Raman and infrared vibrational spectroscopies were used to follow the charge transfer from the potassium atom to the phenanthrene molecule. The more numerous vibration bands found in the IR and Raman spectra of $K_4(C_{14}H_{10})_3(THF)_4$ compared to the spectra of $Rb_2(C_{14}H_{10})_2(THF)$, $K_2(C_{14}H_{10})_2(THF)$, $Cs_2(C_{14}H_{10})_2(THF)$ and $Cs(C_{14}H_{10})$ indicate the presence of either an additional phase or two differently charged phenanthride units. While peaks observed in monoanions were also found in this compound and additional peaks exhibit even larger red-shift, we concluded that this material contains, besides the monoanion (orange arrows), the dianion (dark blue arrows) as well, as shown in Figure 79. This conclusion was confirmed after the IR and Raman spectra of phase-pure $Cs_2(C_{14}H_{10})$ were obtained (Section 3.7.3). The intensity of the vibrational band associated with an O-C stretching mode in the THF molecule is higher than observed in the other alkali-metal phenanthrides, indicating a higher content of THF in this compound. The tentative assignment of vibrational peaks is gathered in Table 50 and 51 (Appendix 6.9).
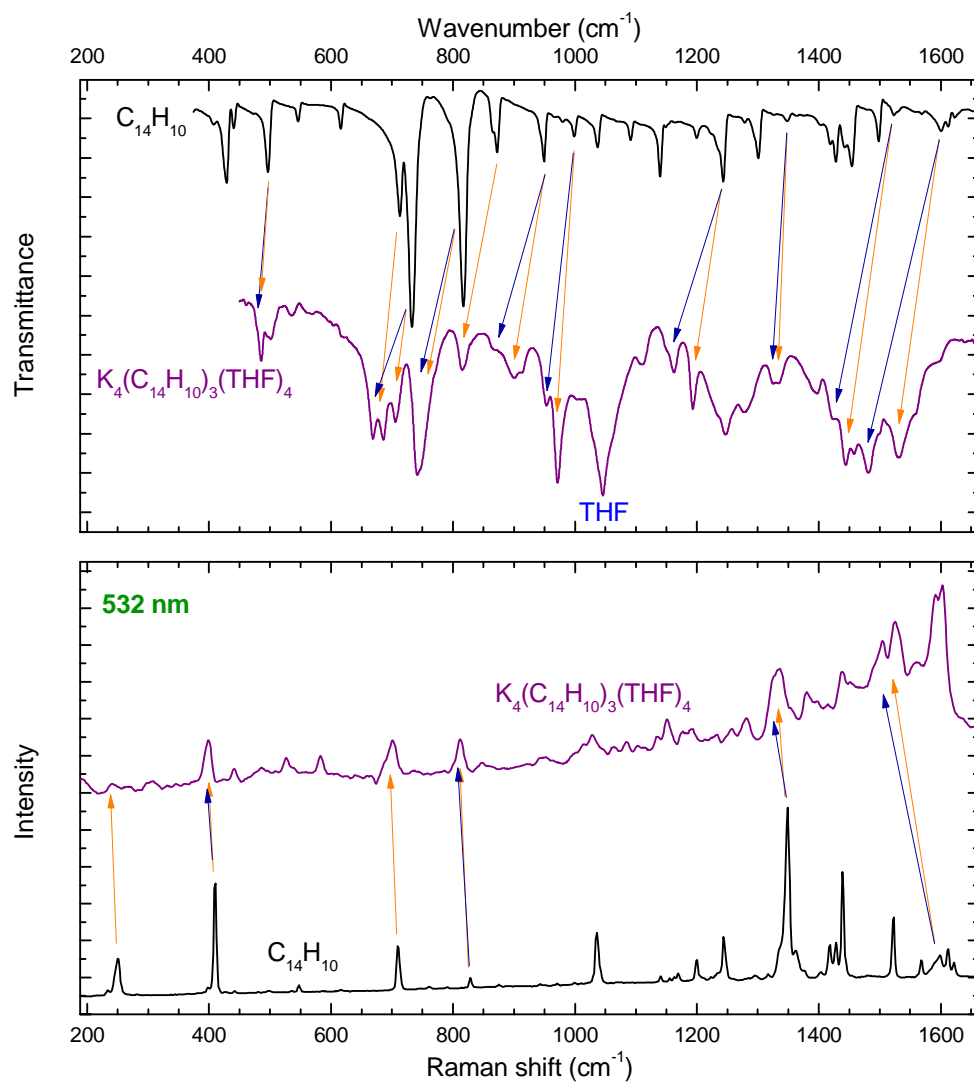
Figure 79: The infrared (top panel) and Raman (bottom panel) spectra of the sample containing the $K_4(C_{14}H_{10})_3(THF)_4$ phase (dark violet solid line) and pristine phenanthrene (black solid line). Orange and blue arrows represent the tentative red-shift of monoanion and dianion respectively. The Raman spectrum was taken using a 532 nm excitation wavelength.

3.5.5 Magnetic Properties

The temperature dependence of the magnetic susceptibility (χ) along with a Curie-Weiss fit and the temperature dependence of the magnetisation (inset) of $K_4(C_{14}H_{10})_3(THF)_4$ in applied magnetic fields of 1 T and 5 mT are shown in Figure 80.
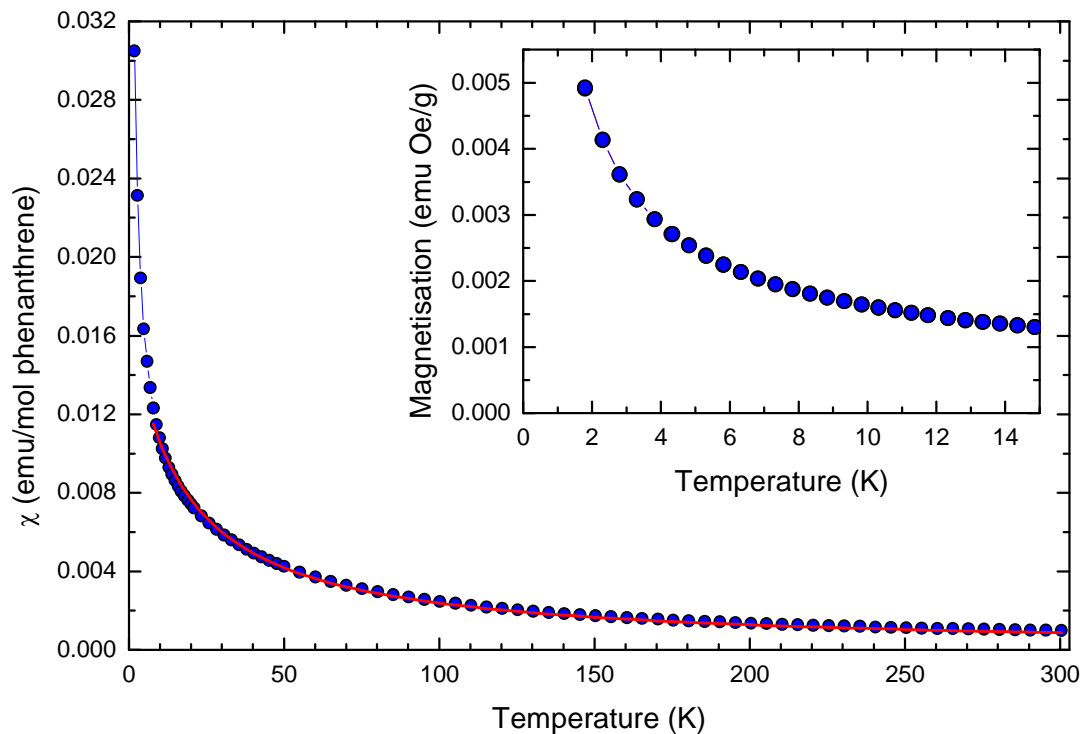
Figure 80: The temperature dependence of molecular susceptibility (χ *vs. T*) of the $K_4(C_{14}H_{10})_3(THF)_4$ compound in an applied field of 1 T (blue circles, FC) along with fit to Curie-Weiss law in the temperature region between 8 and 300 K (red curve). Inset shows the temperature dependence of magnetisation *M vs. T* at *B* = 5 mT in a ZFC (red circles) and FC (blue circles) measuring protocol. All measurements were collected upon heating.

Fitting of the magnetic susceptibility in the temperature region between 8 and 300 K to a Curie-Weiss law yielded the effective magnetic moment, μ_{eff} = 1.488(8) μ_B and a negative Weiss temperature, Θ = -16.2(4) K. The effective moment is considerably smaller than expected for spin ½ state (1.73 μ_B). However, the value of 1.488(8) μ_B is in good agreement with the value of 1.41 μ_B expected for a compound containing two unpaired spins and two spins in a singlet state. According to this datum, two phenanthrides are singly charged and one is doubly charged in $K_4(C_{14}H_{10})_3(THF)_4$, and

therefore, the accurate molecular formula for this compound is $[\{K(THF)\}_4(C_{14}H_{10})^{-}_{2}(C_{14}H_{10})^{2-}]$. The suggested formula is also in good agreement with findings based on single crystal analysis, where *Phen1* and *Phen2* seems to be singly charged (phenanthrene radical anion) and *Phen3* (combining *Phen3'* and *Phen3''* with chemical occupancy of 0.5) doubly charged (dianion). The presence of the dianion is also in good agreement with the observation of additional vibration bands in the infrared and Raman spectra. The observed negative Weiss temperature of -16.2(4) K indicates the presence of weak antiferromagnetic (AFM) exchange interactions. However, the value is much smaller than those observed in the other compounds described above. The superposition of ZFC and FC magnetic susceptibility curves at low applied field (inset of Figure 80), confirms the absence of long-range magnetic ordering.

3.5.6 Summary on $K_4(C_{14}H_{10})_3(THF)_4$ compound

A reduction of equivalent amounts of phenanthrene with potassium metal in THF followed by crystallisation, starting at -20 ^{o}C and continuing at room temperature, and then washing out excess neutral phenanthrene yielded prism-like crystals. According to single crystal X-ray diffraction analysis they were identified as $K_4(C_{14}H_{10})_3(THF)_4$. The asymmetric unit comprises three phenanthrene radical ions, *Phen1*, *Phen2* and *Phen3* (where *Phen3* is disordered, yielding *Phen3'* and *Phen3''* with chemical occupancy of 0.5), four potassium cations, $K1^+$, $K2^+$, $K3^+$ and $K4^+$ and four THF molecules, *THF1*, *THF2*, *THF3* and *THF4* (where *THF2* and *THF4* are disordered). The coordination environment of $K1^+$and $K2^+$ is very similar to that of $K3^+$ and $K4^+$, where one ordered and one disordered phenanthride ions along with one THF molecule (*THF1* or *THF2*, acting as a bridging ligand) form a triangle-like structural motif. The potassium coordination sphere is made complete through interaction with the remaining ordered phenanthride and one disordered THF molecules (acting as a terminal ligand). These two moieties are effectively encapsulating potassium cations inside the triangle-like motif. The evident difference between disordered *Phen3* and ordered *Phen1* and *Phen2* is in the η coordination bonds interactions, where four $η^6$ coordination modes per *Phen3* moiety strongly interact with cations. The temperature-dependent powder X-ray experiment, revealed two structural transitions upon heating the $K_4(C_{14}H_{10})_3(THF)_4$ compound. The first occurs in the temperature range between 60 and 70 ^{o}C and this phase was identified as the $K_2(C_{14}H_{10})_2(THF)$ phase, and the second between 90 and 100 ^{o}C, which remains unidentified and is identical to that obtained after heating $K_2(C_{14}H_{10})_2(THF)$ phase above 80 ^{o}C (see Section 3.2.2). The presence of additional vibrational bands, which are even more red-shifted than those observed in $Rb_2(C_{14}H_{10})_2(THF)$, $K_2(C_{14}H_{10})_2(THF)$, $Cs_2(C_{14}H_{10})_2(THF)$ and $Cs(C_{14}H_{10})$ compounds imply the presence of a dianion in the $K_4(C_{14}H_{10})_3(THF)_4$ compound. Fitting the temperature dependence of magnetic susceptibility to a Curie-Weiss law yielded the effective moment of 1.488(8) $μ_B$, which is in good agreement with predictions for a mixed valence spin system consisting of two unpaired spins and two paired spins in a singlet configuration, and additionally confirms the presence of a dianion in $K_4(C_{14}H_{10})_3(THF)_4$. Therefore, the precise formula of $K_4(C_{14}H_{10})_3(THF)_4$ compound is [{K(THF)}$_4$(C$_{14}$H$_{10}$)$^-$

$_2$(C$_{14}$H$_{10}$)$^{2-}$]. The relatively small negative Weiss temperature, -16.2(4) K, and superposition of the ZFC and FC curves at low applied field confirm the absence of long-range magnetic ordering in this compound.

3.6 Rb$_4$(C$_{14}$H$_{10}$)$_3$(THF)$_4$

3.6.1 Synthesis and crystal growth

Sublimed phenanthrene (151.5 mg, 0.850 mmol) and rubidium metal (73.4 mg, 0.859 mmol) were placed on the bottom in the left hand side of the reaction vessel. Afterwards the reaction vessel was transferred out of a glove-box and placed on a Schlenk line, evacuated and THF (36 ml) was condensed on top of the phenanthrene and rubidium. The olive green solution was vigorously stirred for 67 hours, ensuring the reaction was completed (all rubidium metal dissolved/reacted). Then the solution was filtered into the right side of the reaction vessel and concentrated by removing 28 ml of THF. The solution was layered with oxygen- and water-free *n*-hexane (35 ml) at -30 ^{o}C and crystallisation was carried out for 3 days at room temperature. The resulting dark green/grey prism-like crystals (Figure 81) with purple lustre were washed twice with a new portion of *n*-hexane and dried under dynamic vacuum for 1.5 hours. A noticeable amount of white material, presumably pristine phenanthrene, was observed in the left hand side of the reaction vessel after washing the crystals grown in the right hand side part of the vessel. Beside single crystals a small amount of olive green powder was observed in the right hand side of the reaction vessel. Yield 221.4 mg (67 %). Elemental analysis, calculated (%) for C$_{58}$H$_{62}$Rb$_4$O$_4$: C 59.8, H 5.36; found C 56.49, H 4.167. Observed values correspond to Rb$_{4.5}$-Phenanthrene$_3$-THF$_{2.2}$. The surplus of rubidium and deficiency of THF indicates that the obtained material is not phase-pure.
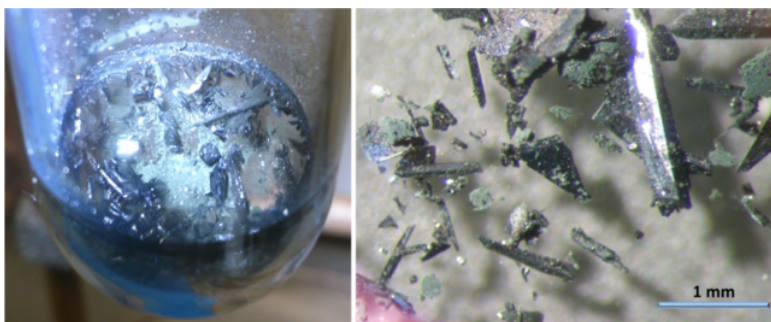
Figure 81: Isolated product in reaction vessel (left panel) and single crystals of Rb$_4$(C$_{14}$H$_{10}$)$_3$(THF)$_4$, along with some olive green powder under 40× magnification (right panel). Thick pale blue line represents 1mm length.

3.6.2 Single crystal structural analysis

The prism-like crystals were identified as $Rb_4(C_{14}H_{10})_3(THF)_4$ by single crystal X-ray diffraction. This compound is isostructural to $K_4(C_{14}H_{10})_3(THF)_4$, and crystallises in the triclinic $P\bar{1}$ space group with lattice parameters a = 12.3669(8)Å, b = 13.4681(9)Å, c = 15.4725(11)Å, α = 90.366(2)^o, β = 93.996(2)^o and γ = 93.795(2)^o at 120 K. Similar to the potassium analogue, the asymmetric unit cell consists of three phenanthrene radical anions (*Phen1, Phen2* and *Phen3*), four rubidium cations (K1, K2, K3 and K4) and four THF molecules (*THF1*, *THF2*, *THF3* and *THF4*) as depicted in Figure 82. Two THF (*THF3* and *THF4*) molecules and one phenanthride (*Phen3*) are disordered and the disorder of *Phen3* is symmetry related, because it is lying on the centre of inversion. The occupancy of all three disordered constituents is fixed to 0.5.
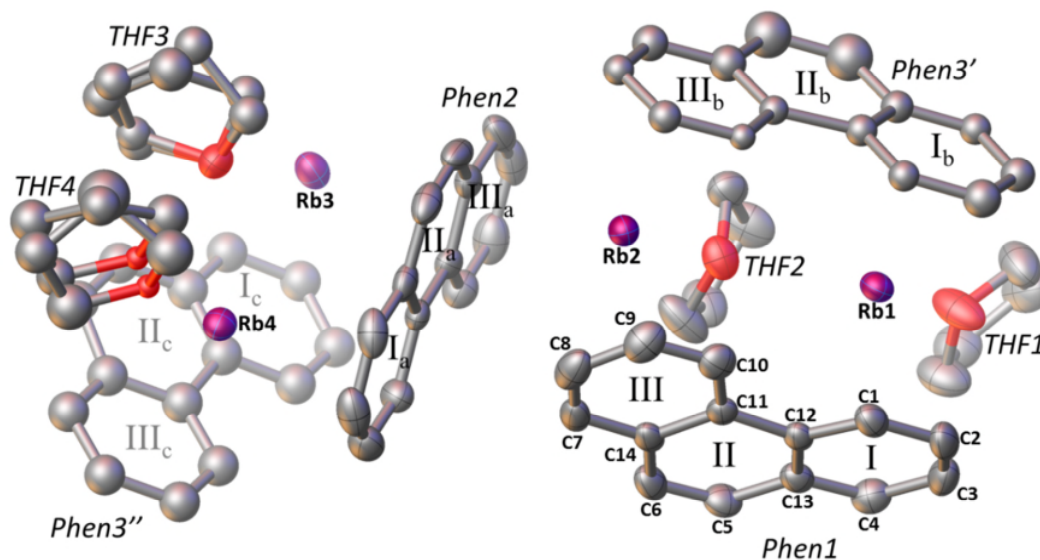
Figure 82: The asymmetric unit cell of the $Rb_4(C_{14}H_{10})_3(THF)_4$ consisting of three crystallographically independent phenanthrides denoted *Phen1*, *Phen2* and *Phen3* (both halves of disordered *Phen3* are shown as *Phen3'* and *Phen3''*), four rubidium cations denoted as Rb1, Rb2, Rb3 and Rb4, and four THF molecules denoted as *THF1*, *THF2*, *THF3* and *THF4* . The peripheral benzene ring planes are labelled as I, III, I_a, III_a, I_b, III_b, I_c, III_c, and central planes as II, II_a, II_b, II_c. Colour code: Rb violet; O red and C grey. Hydrogen atoms are omitted for clarity.

By analogy with the isostructural potassium compound, the coordination environments of rubidium cations are separated into a coordination environment of Rb1 and Rb2, and Rb3 and Rb4 actions, depicted in Figures 83 and 84 respectively.

The Rb1$^+$ interacts with phenanthrene radical ions (*Phen1* and *Phen3'*) through two η^6 coordination modes. The first η^6 coordination is between Rb1$^+$ and the peripheral benzene ring plane I (C1, C2, C3, C4, C12 and C13) of *Phen1* with bond distances ranging from 3.153(4) to 3.511(4) Å. The Rb1$^+$ to plane centroid distance is 3.0295(16) Å and the angle of Rb1$^+$ projection on the ring plane is 82°. The second η^6 coordination is between Rb1$^+$ and the peripheral benzene ring plane I$_b$ (C1b, C2b, C3b, C4b, C12b and C13b) of *Phen3'* with distances of 3.101(6)- 3.341(6) Å in length. The Rb1$^+$ to plane centroid distance is 2.908(3) Å and cation projection on the ring plane at an angle of 84°.The local binding of Rb1$^+$ cation is shown in Figure 83.

The second cation, Rb2$^+$, interacts with phenanthrides (*Phen1*, *Phen2* and *Phen3'*) through one η^3 and two η^6 coordination modes. The η^3 coordination is between Rb2$^+$ and the central benzene plane II$_a$ (C5a, C6a and C14a) of *Phen2* with distances of 3.169(4) - 3.450(4) Å in length. The Rb$^+$ to plane centroid distance is 3.3078(18) Å and the angle of Rb2$^+$ projection on the ring plane is 72°. The first η^6 coordination is between Rb2$^+$ and the peripheral benzene ring plane III (C7, C8, C9, C10, C11 and C14) of *Phen1* with bond distances ranging from 3.266(4) to 3.579(4) Å. The Rb$^+$ to plane centroid distance is 3.1053(17) Å and cation projection on the ring plane at an angle of 83°. The second η^6 coordination is between Rb2$^+$ and the peripheral benzene plane III$_b$ (C7b, C8b, C9b, C10b, C11b and C14b) of *Phen3'* with distances of 3.189(6) - 3.370(6) Å in length. The Rb$^+$ to plane centroid distance is 2.972(2) Å and the angle of Rb2$^+$ projection on the ring plane is 58°. The local binding of Rb2$^+$ cation is shown in Figure 83.

The oxygen atoms in the *THF1* molecule is as a terminal ligand coordinated to Rb1$^+$ through a μ^1 coordination mode, with a K1$^+$···O1 bond distance of 2.796(3) Å. The oxygen atom in the *THF2* molecule is as a bridging ligand coordinated to Rb1$^+$ and Rb2$^+$ through a μ^2 coordination mode. The Rb1$^+$···O2 and Rb2$^+$···O2 distances are 2.916(3) and 2.910(3) Å respectively and the Rb1-O2-Rb2 angle is 101.28(8)^o (Figure 83).
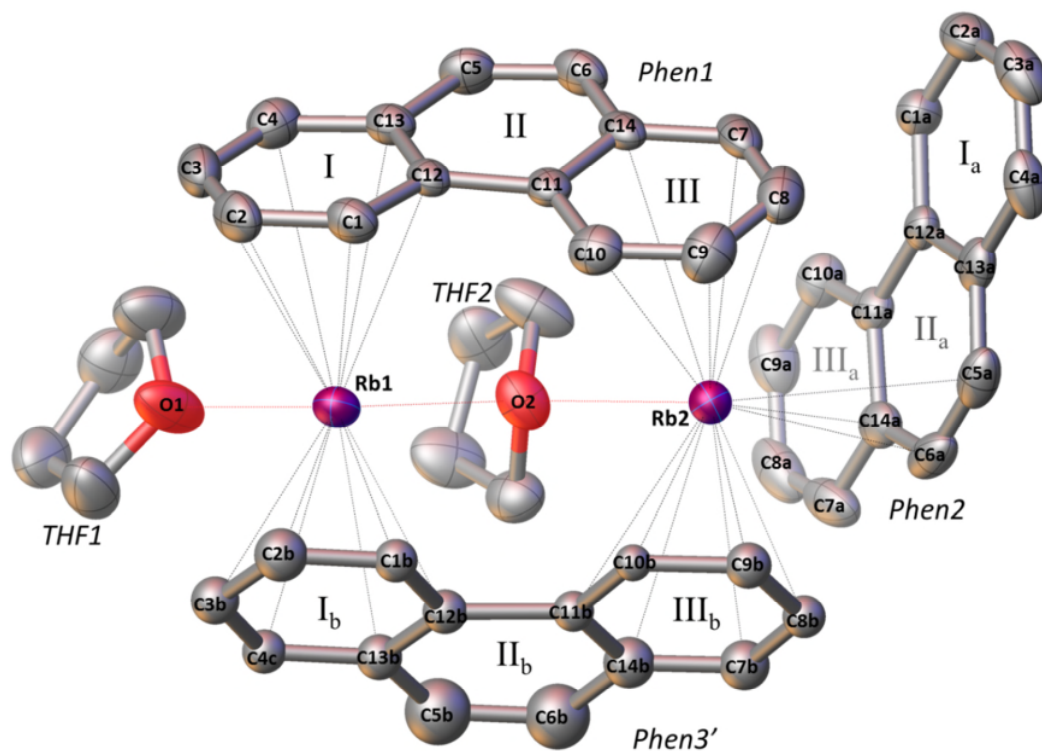
Figure 83: The coordination environment of Rb1$^+$ and Rb2$^+$ ions in Rb$_4$(C$_{14}$H$_{10}$)$_3$(THF)$_4$ compound. Three crystallographically independent phenanthrene radical ions are denoted as *Phen1*, *Phen2* and *Phen3'*. The peripheral benzene ring planes are labelled as I, III, I$_a$, III$_a$, I$_b$, III$_b$, and central planes as II, II$_a$, II$_b$. Black dotted lines and red dotted lines represent Rb$^+$···C and Rb$^+$···O coordination respectively. Colour code: Rb violet; O red and C grey. Thermal ellipsoids are shown with 50% probability level, except in the disordered *Phen3'*, hydrogen atoms are omitted for clarity and depicted structure was obtained from data collected at 120 K.

The interactions of Rb3$^+$ with phenanthrides (*Phen1*, *Phen2* and *Phen3''*) are through a η^5 and two η^6 coordination modes. The η^5 coordination is between Rb3$^+$ and the peripheral benzene plane I$_c$ (C2c, C3c C4c, C12c and C13c) of *Phen3''* with distances of 3.022(7) - 3.634(8) Å in length. The Rb3$^+$ to plane centroid distance is 3.095(3) Å and the angle of Rb3$^+$ projection on the ring plane is 73°. The first η^6 coordination is between Rb3$^+$ and the peripheral benzene ring plane I (C1, C2, C3, C4, C12 and C13) of *Phen1* with bond distances ranging from 3.249(9) to 3.614(4) Å. The Rb3$^+$ to plane centroid distance is 3.1178(17) Å and cation projection on the ring plane at an angle of 81°. The second η^6 coordination is between Rb3$^+$ and the peripheral benzene plane III$_a$ (C7a, C8a C9a, C10a, C11a and C14a) of *Phen2* with distances of 3.204(5) - 3.624(4) Å in length. The Rb3$^+$ to plane centroid distance is 3.1151(18) Å and the angle of Rb3$^+$

projection on the ring plane is 81°. The local binding of Rb3$^+$ cation is shown in Figure 84.

The Rb4$^+$ interacts with phenanthrene radical ions (*Phen2* and *Phen3''*) through two η^6 coordination modes. The first η^6 coordination is between Rb4$^+$ and the peripheral benzene plane I$_a$ (C1a, C2a, C3a, C4a, C12a and C13a) of *Phen2* with bond distances ranging from 3.209(4) to 3.407(4) Å. The Rb4$^+$ to plane centroid distance is 3.0130(17) Å and the angle of Rb4$^+$ projection on the ring plane of 85°. The second η^6 coordination is between Rb4$^+$ and the peripheral benzene plane III$_c$ (C7c, C8c, C9c, C10c C11c and C14c atoms) of *Phen3''* with bond distances of 3.113(8)- 3.231(7) Å in length. The Rb4$^+$ to plane centroid distance is 2.852(3) Å and the angle of Rb4$^+$ projection on the ring plane is 87°. The local binding of Rb4$^+$ cation is shown in Figure 84.
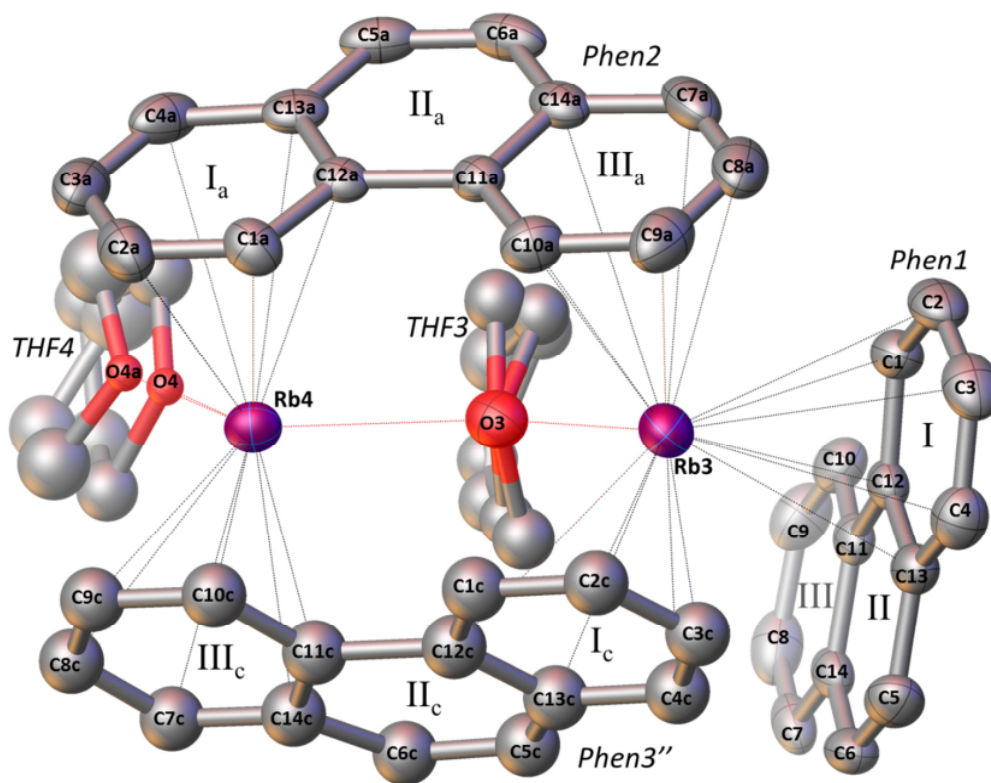
Figure 84: Representation of coordination environment of Rb3$^+$ and Rb4$^+$ ions in Rb$_4$(C$_{14}$H$_{10}$)$_3$(THF)$_4$ compound. Three crystallographically independent phenanthrene radical ions are denoted as *Phen1*, *Phen2* and *Phen3''*. The peripheral benzene ring planes are labelled as I, III, I$_a$, III$_a$, I$_c$, III$_c$, and central planes as II, II$_a$, II$_c$. Black dotted lines and red dotted lines represent Rb$^+$···C and Rb$^+$···O coordination respectively. Colour code: Rb violet; O red and C grey. Thermal ellipsoids are shown with 50% probability level (except in the disordered molecules), hydrogen atoms are omitted for clarity and depicted structure was obtained from data collected at 120 K.

The oxygen atom in the *THF3* molecule is coordinated as a bridging ligand to $Rb3^+$ and $Rb4^+$ through a μ^2 coordination mode. The $Rb3^+\cdots O$ and $Rb4^+\cdots O$ distances are 2.878(3) and 2.880(3) Å respectively and the Rb3-O-Rb4 angle is 101.47(8)°. The oxygen atoms in the *THF4* molecule (two oxygen atoms are depicted due to the disorder in the *THF4* molecule) are coordinated as a terminal ligand to $Rb4^+$ through a μ^1 coordination mode, with the $Rb4^+\cdots O4/O4a$ bond distances of 2.825(6) and 2.764(6) Å (Figure 84).

All $Rb^+\cdots C$ and $Rb^+\cdots O$ coordination bond distances are gathered in Table 17 and they are comparable to those reported in rubidium-reduced rubrene, coronene, cyclopentadiene, indene, fluorene and corannulene materials (Table 6 and 7). The basic parameters obtained from refinement, fractional atomic coordinates, atom to atom bond distances and bond angles for crystal structures obtained from data sets collected at 120 K are gathered in the Appendix (6.7).

Table 17: Coordination modes and coordination bond distances between rubidium cations and carbon/oxygen atoms extracted from structure obtained at 120 K.

Coordination mode	Rb^+ to C or O bond	Distance (Å)
η^3	Rb2-C6a	3.169(4)
	Rb2-C5a	3.328(5)
	Rb2-14a	3.450(4)
η^5	Rb3-C4c	3.022(7)
	Rb3-C13c	3.133(7)
	Rb3-C3c	3.291(8)
	Rb3- C12c	3.492(7)
	Rb3-C2c	3.634(8)
η^6	Rb1-C1	3.153(4)
	Rb1-C2	3.238(4)
	Rb1-C12	3.254(4)
	Rb1-C3	3.384(4)
	Rb1-C13	3.477(4)
	Rb1-C4	3.511(4)
η^6	Rb1-C13b	3.101(6)
	Rb1-C4b	3.135(4)
	Rb1-C12b	3.191(6)
	Rb1-C3b	3.255(6)
	Rb1-C1b	3.310(6)
	Rb1-C2b	3.341(6)
η^6	Rb2-C8	3.266(4)
	Rb2-C9	3.307(4)
	Rb2-C7	3.341(4)
	Rb2-C10	3.440(4)

	Rb2-C14	3.503(4)
	Rb2-C11	3.579(4)
η^6	Rb2-C8b	3.189(6)
	Rb2-C7b	3.223(6)
	Rb2-C9b	3.249(5)
	Rb2-C14b	3.314(6)
	Rb2-C10b	3.339(5)
	Rb2-C11b	3.370(6)
η^6	Rb3-C9a	3.204(5)
	Rb3-C10a	3.287(4)
	Rb3-C8a	3.336(5)
	Rb3-C7a	3.510(5)
	Rb3-C11a	3.513(4)
	Rb3-C14a	3.624(4)
η^6	Rb3-C4	3.249(4)
	Rb3-C3	3.259(4)
	Rb3-C2	3.394(4)
	Rb3-C13	3.416(4)
	Rb3-C1	3.566(4)
	Rb3-C12	3.614(4)
η^6	Rb4-C1a	3.209(4)
	Rb4-C2a	3.239(4)
	Rb4-C12a	3.313(4)
	Rb4-C3a	3.330(4)
	Rb4-C13a	3.422(4)
	Rb4-C4a	3.407(4)
η^6	Rb4-C11c	3.113(8)
	Rb4-C14c	3.135(7)
	Rb4-C10c	3.150(8)
	Rb4-C7c	3.195(7)
	Rb4-C9c	3.210(7)
	Rb4-C8c	3.231(7)
μ^1	Rb1-O$_{THF1}$	2.796(3)
μ^2	Rb1-O$_{THF2}$	2.916(3)
	Rb2-O$_{THF2}$	2.910(3)
μ^2	Rb3-O$_{THF3}$	2.878(3)
	Rb4-O$_{THF3}$	2.880(3)
μ^1	Rb4-O4$_{THF4}$	2.825(6)
	Rb4-O4a$_{THF4}$	2.764(6)

The coordination environment of the rubidium cations is genuinely similar to that found in $K_4(C_{14}H_{10})_3(THF)_4$. The *Phen1*, *Phen3'* and *THF2*, and *Phen2*, *Phen3''* and *THF3* molecular units are coordinated to Rb1$^+$/Rb2$^+$ and Rb3$^+$/Rb4$^+$ pairs, respectively, in a

135

triangle-like motif manner. The encapsulation of those two rubidium cations pairs is achieved by *Phen2* and *THF1* in the first case and *Phen1* and *THF4* in the second case. Nearly identical angles, 63.8(2)^o and 63.7(2)^o, were observed in the *Phen1/Phen3'* and *Phen2/Phen3''* dimers, and those angles are similar to those, 69.738(6)^o and 68.034(6)^o, found in the potassium analogue.

As a result of similar coordination interactions between $K_4(C_{14}H_{10})_3(THF)_4$ and $Rb_4(C_{14}H_{10})_3(THF)_4$, the same channel-like motif is observed when the asymmetric unit cell is repeated throughout the space and the structure is projected along the [001] direction as shown in Figure 85. *Phen3''*, $Rb3^+$, $Rb4^+$, *THF3* and *THF4*, and *Phen3'*, $Rb1^+$, $Rb2^+$, *THF1* and *THF2* form chains running along the crystallographic *c* direction, and are shown in pale orange and pale green ellipses, respectively. These chains are encapsulated with *Phen1* and *Phen2* ions, completing a channel-like motif. The same, discontinuation (Figure 75) of possible exchange interactions between *Phen3'* or *Phen3''*, due to the orientation of THF molecules, is observed in the $Rb_4(C_{14}H_{10})_3(THF)_4$ compound.
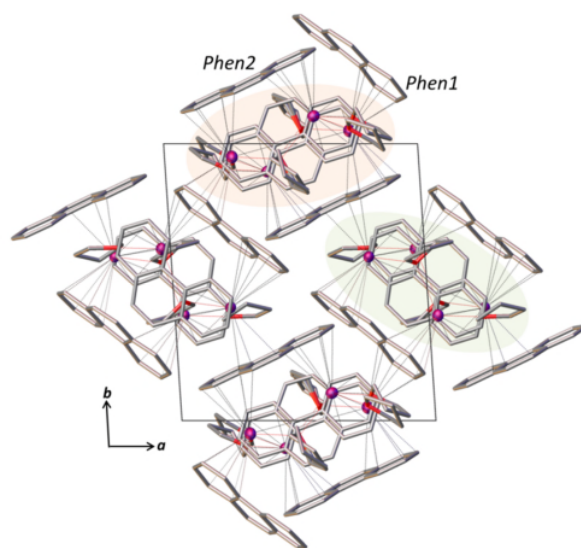
Figure 85: Projection of $Rb_4(C_{14}H_{10})_3(THF)_4$ structure along the [001] direction showing four channel-like motifs forming a 3D polymeric network of $Rb^+\cdots C$ interactions (black dotted lines) between alkali metal ions and the phenanthride radical anions. The pale orange and the pale green ellipses present chains comprised of *Phen3''*, *THF3*, *THF4*, $Rb3^+$ and $Rb4^+$, and *Phen3'*, *THF1*, *THF2*, $Rb1^+$ and $Rb2^+$ respectively. Hydrogen atoms are omitted, and carbon-carbon and carbon-oxygen bonds are depicted as tubes for clarity. Colour code: Rb violet; O red and C grey, red dotted lines represent $K^+\cdots O$ coordination.

3.6.3 Powder X-ray diffraction

The diffraction profile of a ground $Rb_4(C_{14}H_{10})_3(THF)_4$ sample collected at 295 K on a laboratory source ($\lambda = 0.7093$ Å) was compared with predicted diffraction profiles of the $Rb_4(C_{14}H_{10})_3(THF)_4$ and $Rb_2(C_{14}H_{10})_2(THF)$ structures, as shown in Figure 86. Simulations of diffraction profiles were performed in Mercury (version 3.5) software suite, by using structural models obtained from data collected on single crystals at 120 K. The comparison revealed that the diffraction profile of the ground $Rb_4(C_{14}H_{10})_3(THF)_4$ sample (black solid line) does not match with the $Rb_4(C_{14}H_{10})_3(THF)_4$ predicted diffraction profile (olive green solid line). However, it is in good agreement with the diffraction profile predicted from the $Rb_2(C_{14}H_{10})_2(THF)$ structural model (blue solid line). A slight discrepancy in peak positions originates from the temperature difference (295 *vs.* 120 K) and the corresponding thermal contractions/ expansion of the unit cell.
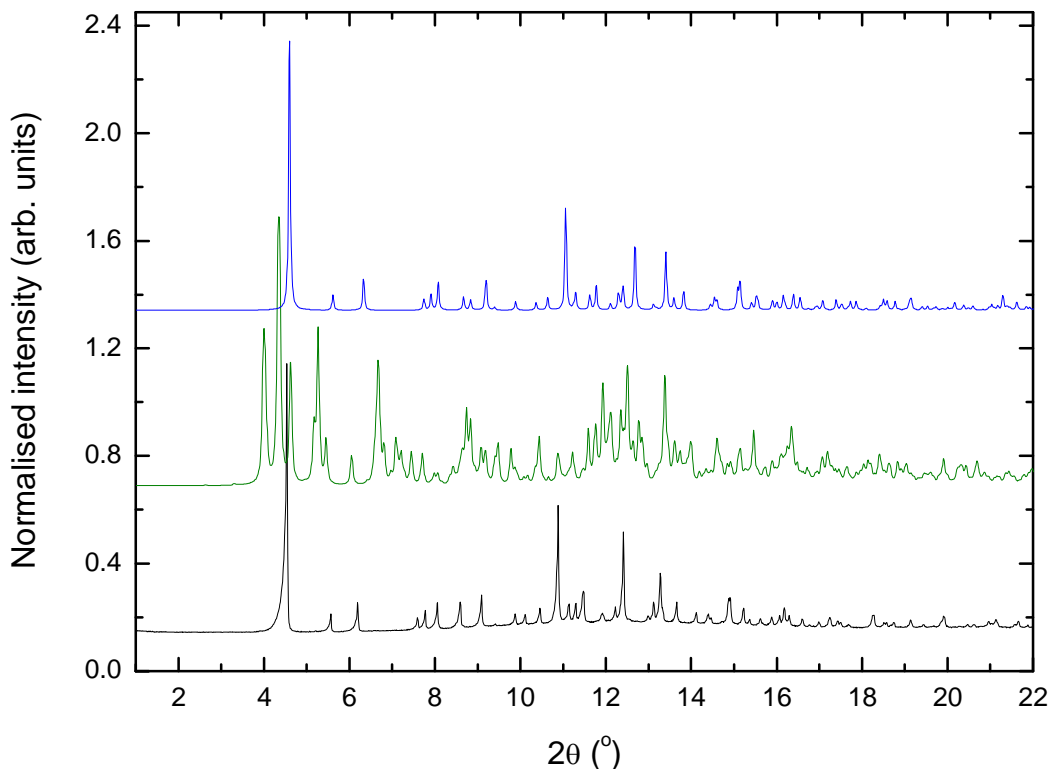
Figure 86: Comparison of the measured diffraction profile of the ground $Rb_4(C_{14}H_{10})_3(THF)_4$ sample (black solid line) with diffraction profiles of $Rb_4(C_{14}H_{10})_3(THF)_4$ (olive green solid line) and $Rb_2(C_{14}H_{10})_2(THF)$ (blue solid line) predicted from the structural models.

Based on these observations the structural model of $Rb_2(C_{14}H_{10})_2(THF)$, obtained from single crystal analysis at 290 K, was refined to the powder diffraction data from the ground $Rb_4(C_{14}H_{10})_3(THF)_4$ sample. The extracted lattice parameters are a = 17.2615(9) Å, b = 27.2556(13) Å and c = 11.3163(6) Å, which are in agreement to those, a = 17.2606(8) Å, b = 27.2515(12) Å and c = 11.3129(6) Å, obtained on the phase-pure $Rb_2(C_{14}H_{10})_2(THF)$ sample. This finding shows that complete conversion from $Rb_4(C_{14}H_{10})_3(THF)_4$ to $Rb_2(C_{14}H_{10})_2(THF)$ phase was achieved by grinding the sample. Results of the Rietveld refinement are shown in Figure 87.
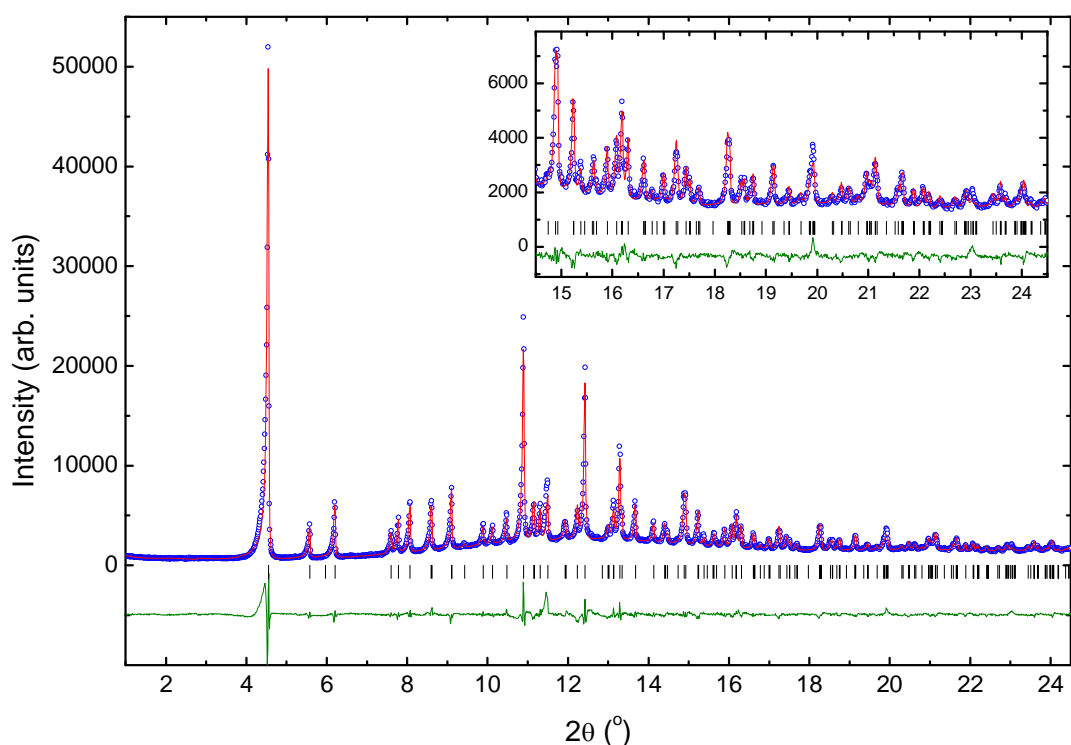
Figure 87: Powder diffraction of the ground $Rb_4(C_{14}H_{10})_3(THF)_4$ sample. The experimentally obtained diffraction profile (λ = 0.7093 Å, Mo Kα) at 295 K (blue open circles), the calculated profile (red solid line), difference (olive green solid line) and predicted peak position (black tick marks). The inset shows high 2θ region. The weight profile and expected R factors are R_{wp} = 7.889% and R_{exp} = 2.081%.

3.6.4 Magnetic Properties

The temperature dependence of the magnetic susceptibility of the sample, where molecular masses and diamagnetic corrections for $Rb_4(C_{14}H_{10})_3(THF)_4$ and $Rb_2(C_{14}H_{10})_2(THF)$ formulas were applied, along with corresponding Curie Weiss fits in an applied magnetic field of 1 T, are shown in Figure 88. The inset represents the temperature dependence of the magnetisation of the same sample in an applied magnetic field of 1 mT.
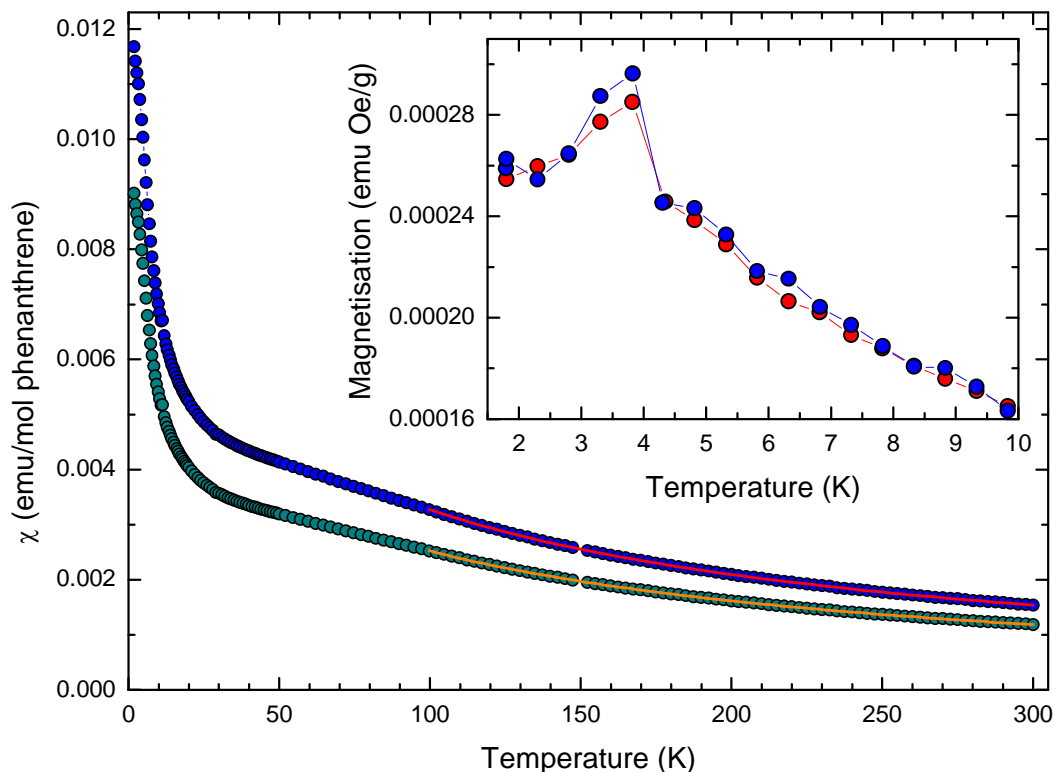
Figure 88: The temperature dependence of molecular susceptibility (χ *vs. T*) with applied molecular mass and diamagnetic correction for $Rb_4(C_{14}H_{10})_3(THF)_4$ and $Rb_2(C_{14}H_{10})_2(THF)$ phases at an applied field of 1 T along with fit to a Curie-Weiss law in the temperature region between 100 and 300 K are presented with blue circles and red curve, and cyan green circles and orange curve, respectively. Inset shows the temperature dependence of the magnetisation *M vs. T* at *B* = 5 mT using ZFC (red circles) and FC (blue circles) measuring protocols. All measurements were collected upon heating.

As we have seen, $Rb_4(C_{14}H_{10})_3(THF)_4$ readily transforms to $Rb_2(C_{14}H_{10})_2(THF)$ under mild conditions, e.g. upon grinding or over time, which is probably also reflected in the elemental analysis results. Thus, the temperature-dependent magnetic susceptibilities for both possible compounds were calculated and fitted with a Curie-Weiss law. The extracted effective magnetic moments and Weiss temperatures are μ_{eff} = 2.1569(6) μ_B and Θ = -77.8(1) K for $Rb_4(C_{14}H_{10})_3(THF)_4$ and μ_{eff} = 1.8939(4) μ_B and Θ = -77.6(1) K for $Rb_2(C_{14}H_{10})_2(THF)$. The effective magnetic moment of 2.1569(6) μ_B does not agree with the expected value of 1.41 μ_B for the mixed valence system observed in the potassium analogue, where two phenanthrides are singly charged and one doubly charged with the spins in a singlet state. However, the value is in good agreement with value of 1.99 μ_B expected for a mixed valence system where spins on the third phenanthride would be in a triplet state. The second, more plausible explanation is that $Rb_4(C_{14}H_{10})_3(THF)_4$ converted into $Rb_2(C_{14}H_{10})_2(THF)$ during the sample preparation, because UV radiation is produced upon sealing the quartz tube required for SQUID measurements. The magnetic effective moment of 1.8939(4) μ_B, and negative Weiss temperature of Θ = -77.6(1) K are nearly identical to those, μ_{eff} = 1.867(1) μ_B and Θ = -68.1(3) K, found for the phase-pure $Rb_2(C_{14}H_{10})_2(THF)$ compound, where the results were in good agreement with S = ½ spin state per phenanthride ion. Moreover, the observed cusp in the magnetisation measurement at low applied field (1 mT) occurs at the same temperature as in the phase-pure $Rb_2(C_{14}H_{10})_2(THF)$ material.

3.6.5 Summary on Rb$_4$(C$_{14}$H$_{10}$)$_3$(THF)$_4$ compound

The same synthesis and crystallisation procedure as in the case of K$_4$(C$_{14}$H$_{10}$)$_3$(THF)$_4$ yielded prism-like single crystals with the molecular formula of Rb$_4$(C$_{14}$H$_{10}$)$_3$(THF)$_4$. The rubidium compound crystallises in the same space group $P\bar{1}$ as the potassium one. Therefore those two compounds are isostructural, with the disorder of the THF molecules being slightly different. The channel-like arrangement of constituents along the crystallographic [001] direction is similar with only subtle changes. The strong coordination interaction between disordered *Phen3* (either *Phen3'* or *Phen3''*) and the four rubidium cations implies that *Phen3* is a dianion. The observation of the Rb$_2$(C$_{14}$H$_{10}$)$_2$(THF) phase in powder X-ray diffraction and SQUID magnetometry indicates that the transformation of the Rb$_4$(C$_{14}$H$_{10}$)$_3$(THF)$_4$ phase to Rb$_2$(C$_{14}$H$_{10}$)$_2$(THF) is very rapid and occurs either by grinding, heating, UV illumination or even by standing at room temperature for sufficient time. Therefore, this fast transformation is most likely the origin of the inaccuracy of elemental analysis and the values obtained from the Curie-Weiss fit of the magnetic susceptibility data, which are in good agreement with those obtained in the phase-pure Rb$_2$(C$_{14}$H$_{10}$)$_2$(THF) material.

3.7 $Cs_2(C_{14}H_{10})$

3.7.1 Synthesis and isolation

Caesium metal (224.1 mg, 1.686 mmol) and sublimed phenanthrene (150.2 mg, 0.843 mmol) were placed on the bottom of the left hand side of the reaction vessel. Afterwards, the reaction vessel was transferred out of a glove-box and placed on a Schlenk line, evacuated and THF (41 ml) was condensed on top of the phenanthrene and caesium. The mixture was vigorously stirred for 3 days at room temperature and additionally ultrasonicated for 5 h at $50^{o}C$ each day to ensure the reaction was complete. A black crystalline powder precipitated from the dark olive green solution, formed at the beginning, during the reaction. The dark green/ almost black solution was carefully, decanted into the right hand side of the reaction vessel, to avoid powder transfer. Then all THF was removed and the black crystalline powder (Figure 89) was washed three times with oxygen- and water-free n-pentane and dried under dynamic vacuum for 5 hours. Yield 311.2 mg (83%). Elemental analysis, calculated (%) for $C_{14}H_{10}Cs_2$: C 37.87, H 2.28; found C 37.36, H 2.30. These observed values correspond to the $Cs_{2.1}$-Phenanthrene-$THF_{0.07}$ formula.

Figure 89: Polycrystalline solid of $Cs_2(C_{14}H_{10})$ under 40× magnification, the thick blue line represents 1 mm length.

3.7.2 Structural analysis based on powder X-ray diffraction

Similar to the case of $Cs(C_{14}H_{10})$, a powder X-ray diffraction profile of $Cs_2(C_{14}H_{10})$ collected using a laboratory source (λ = 1.54056 Å) at 295 K was used for determination of the structure by using the Expo2014 software suite. The Le Bail decomposition method confirmed that all observed Bragg reflections obey the extinction rules of the primitive monoclinic $P2_1/a$ space group with lattice parameters a = 11.8 Å, b = 11.5 Å, c = 9.8 Å and β = 110.9°. According to the formula obtained from elemental analysis, the multiplicity for this space group (Z =4) and the calculated volume per non-hydrogen atom (19.43 Å^3), two crystallographically independent Cs cations and one phenanthrene molecule, modelled as a rigid bodies without internal degrees of freedom, were used in a direct-space simulated annealing global optimisation technique to obtain the initial structural model. The Rietveld refinement of the obtained structural model to the powder diffraction profile, yielded the lattice parameters a = 11.8123(2) Å, b = 11.4666(2) Å, c = 9.8263(2) Å and β = 110.891(1)°. Results of the Rietveld refinement are shown in Figure 90.
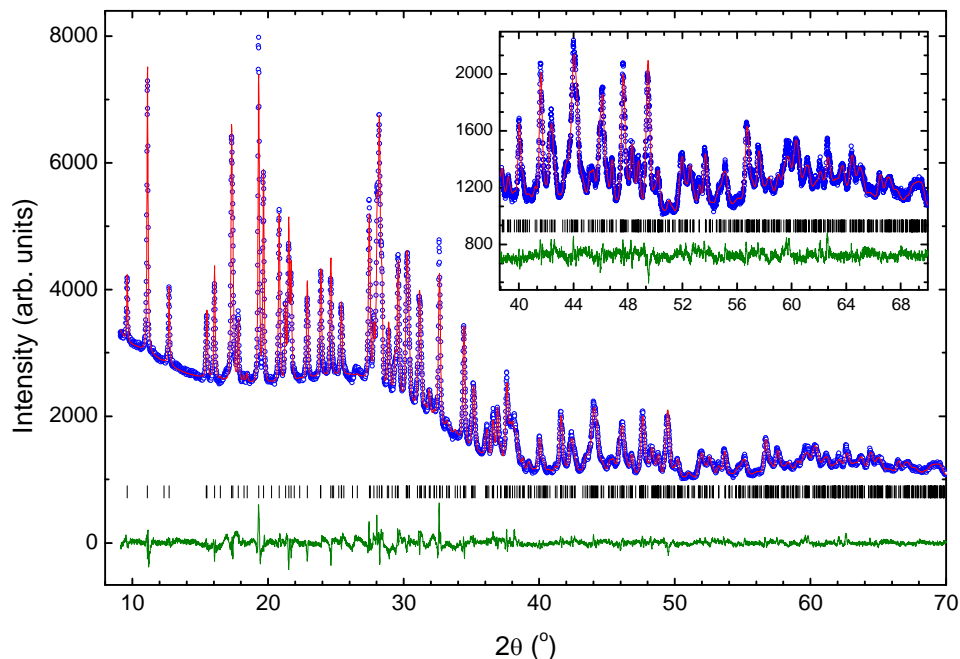
Figure 90: Powder diffraction of the dicaesium phenanthride, $Cs_2(C_{14}H_{10})$, sample. The experimentally obtained diffraction profile (λ = 1.54056 Å, Cu Kα) at 295 K (blue open circles), the calculated profile (red solid line), difference (olive green solid line) and predicted peak position (black tick marks). The inset shows high 2θ region. The weighted profile and expected R factors are R_{wp} = 2.085% and R_{exp} = 1.975%.

The asymmetric unit consists of one phenanthrene radical anion and two caesium cations. In order to explain the coordination environment of Cs1$^+$ and Cs2$^+$, the constituents of asymmetric unit were repeated as shown in Figure 91.

The Cs1$^+$ interacts with the phenanthride through η^3 and η^5 coordination modes. The η^3 coordination is between Cs1$^+$ and the peripheral benzene ring plane III (C5, C6 and C7) with distances ranging from 3.133(3) to 3.401(3) Å. The Cs1$^+$ to plane centroid distance is 3.357(3) Å and the angle of Cs1$^+$ projection on the ring plane is 69°. The η^5 coordination is between Cs1$^+$ and the peripheral benzene ring plane I (C1, C2, C3, C11 and C12) with bond distances of 3.109(3)- 3.715(3) Å in length. The Cs1$^+$ to plane I centroid distance is 3.207(3) Å and cation projection on the ring plane I at an angle of 73°. The bond distance, 3.457(13) Å, between Cs1$^+$ and C10 in the central benzene ring plane II was not considered as a coordinating bond due to its off-centred position between the cation and benzene ring plane (the Cs1$^+$ plane II centroid distance is 4.485(3) Å and projection on the ring plane II at an angle of 35°).
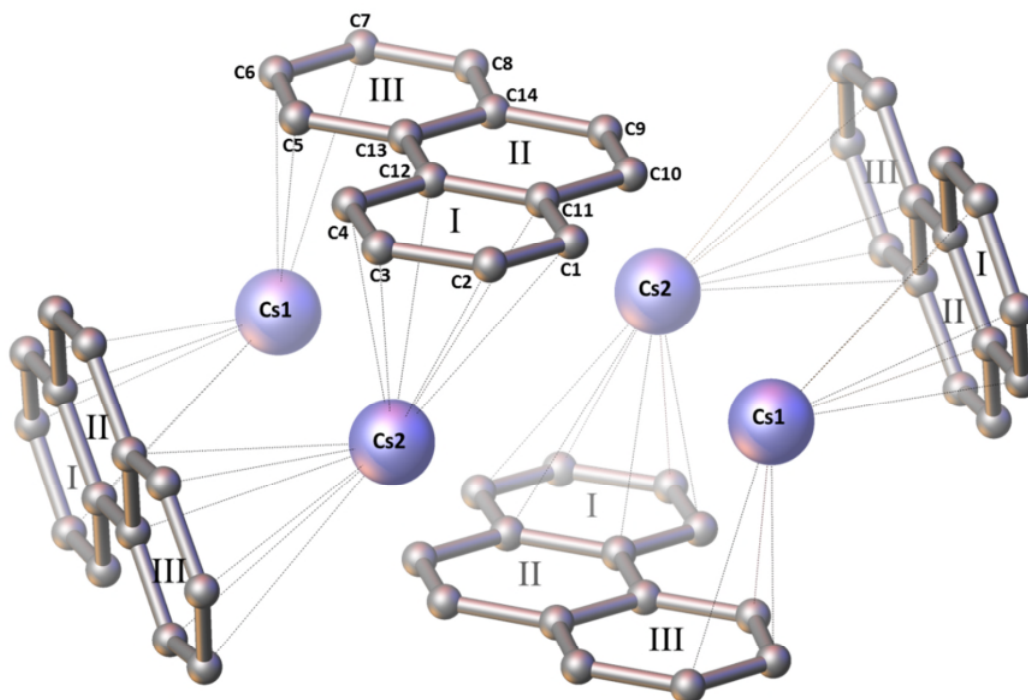
Figure 91: The coordination environment of Cs1$^+$ and Cs2$^+$ ions in Cs$_2$(C$_{14}$H$_{10}$) compound. The peripheral benzene ring planes are labelled as I and III, and central plane as II. Black dotted lines represent Cs$^+$···C coordination interactions. Colour code: Cs purple and C grey. Hydrogen atoms are omitted for clarity and depicted structure was obtained from powder X-ray data collected at 295 K. Benzene ring planes in other symmetry related phenanthrides are shown to keep track of atom numbers.

The Cs2$^+$ interacts with the phenanthride through two η^6 coordination modes. The first η^6 coordination is between Cs2$^+$ and the peripheral benzene plane I (C1, C2, C3, C4, C11 and C12) with distances of 3.136(3)- 3.721(3) Å in length. The Cs2$^+$ to plane centroid distance is 3.144(3) Å and the angle of Cs2$^+$ projection on the ring plane of 76°. The second η^6 coordination is between Cs2$^+$ and the peripheral benzene ring plane III (C5, C6, C7, C8, C13 and C14) with bond distances ranging from 3.198(3) to 3.633(3) Å. The Cs2$^+$ to plane centroid distance is 3.127(3) Å and cation projection on the ring plane angle is 78°. Like for the case of Cs1$^+$, the short bond distance of 3.254(3) Å, between Cs2$^+$ and C9 was not considered as a coordination bond due to the off-centred position between the cation and the central benzene ring plane II (the Cs2$^+$ projection on the ring plane at an angle of 40° and the cation to plane centroid distance is 4.170(2) Å).

All Cs$^+$···C coordination bond distances are gathered in Table 18 and they are comparable to those reported in caesium-reduced 2,5,8-tri-^{t}Bu-phenalene, rubrene, cyclopentadiene, indene, fluorene and corannulene materials (Table 13 and 14). The basic parameters obtained from refinement, fractional atomic coordinates and atom to atom bond distances for crystal structures obtained from data sets collected at 295 K are gathered in the Appendix (6.8).

Table 18: Coordination modes and coordination bond distances between caesium cations and carbon atoms extracted from structure obtained at 295 K

Coordination mode	Cs^+ to C bond	Distance (Å)
η^3	Cs1-C6	3.133(3)
	Cs1-C7	3.382(3)
	Cs1-C5	3.401(3)
η^5	Cs1-C1	3.109(3)
	Cs1-C11	3.268(3)
	Cs1-C2	3.344(3)
	Cs1-C12	3.640(3)
	Cs1-C3	3.715(3)
η^6	Cs2-C4	3.136(3)
	Cs2-C12	3.211(3)
	Cs2-C3	3.365(3)
	Cs2-C11	3.493(3)
	Cs2-C2	3.674(3)
	Cs2-C11	3.721(3)
η^6	Cs2-C14	3.198(3)
	Cs2-C8	3.224(3)
	Cs2-C13	3.412(3)
	Cs2-C7	3.439(3)
	Cs2-C5	3.633(3)
	Cs2-C6	3.633(3)

Strong and exclusive coordination interactions between each peripheral benzene ring plane (I and II) with both caesium cations ($Cs1^+$ and $Cs2^+$) are observed. The same coordination motif was also observed in the disordered *Phen3* ion in both the $K_4(C_{14}H_{10})_3(THF)_4$ and $Rb_4(C_{14}H_{10})_3(THF)_4$ compounds, where it was associated with a dianion. Based on this it can be concluded that disordered *Phen3* is indeed a dianion.

Furthermore, the $Cs_2(C_{14}H_{10})$ structure can be described as an array of chains running along the crystallographic *b* direction (Figure 92), where the phenanthrides lie at an angle of 74.863(1)° with respect to each other and every neighbouring phenanthrene radical ion is flipped for 180° and in this way the steric crowding is minimised . Those chains do not exhibit any interactions along either crystallographic *a* or *c* directions, and by projecting the structure along the [110] directions, a layer-like motif can be observed.
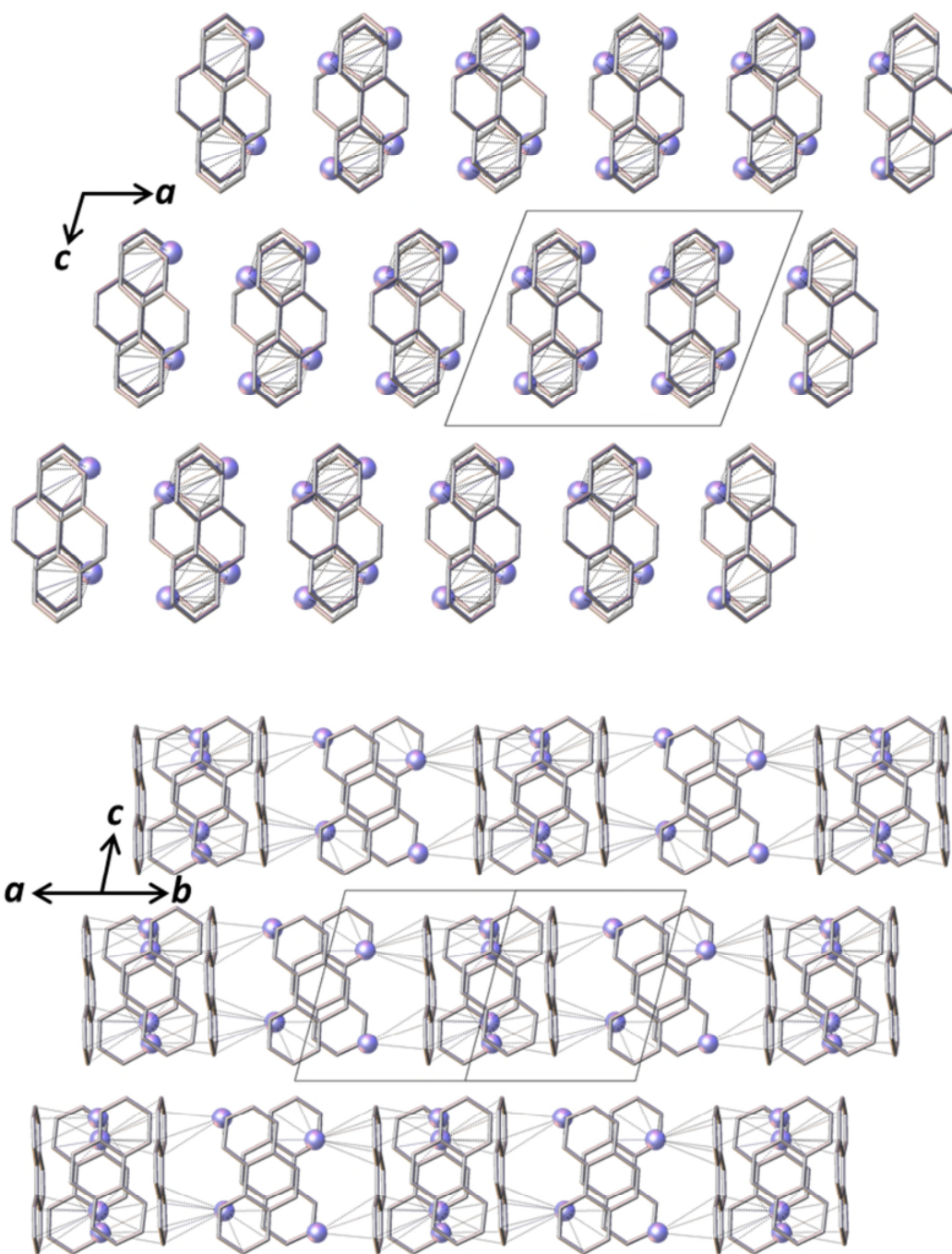
Figure 92: Projection of the $Cs_2(C_{14}H_{10})$ structure along the [010] (upper panel) and [110] (lower panel) direction showing a chain-like motif and layer-like motif respectively. $Cs^+ \cdots C$ represent interaction (black dotted lines) between alkali metal ions and the phenanthride radical anions. Hydrogen atoms are omitted, and carbon-carbon bonds are depicted as tubes, for clarity. Colour code: Cs purple and C grey.

3.7.3 Vibrational Spectroscopy

The charge transfer from the caesium atom to the phenanthrene molecule was followed by Raman and IR vibrational spectroscopies. A red-shift of vibrational bands in the caesium dianion is larger than that observed in $Cs(C_{14}H_{10})$ indicating further softening of the modes upon reduction of the radical ion to a dianion, as shown in Figure 93. The vibrational bands observed in $Cs_2(C_{14}H_{10})$ are also present in the $K_4(C_{14}H_{10})_3(THF)_4$ compound confirming that it contains a dianion as well. The tentative assignment of vibrational peaks is gathered in Table 50 and 51 (Appendix 6.9).
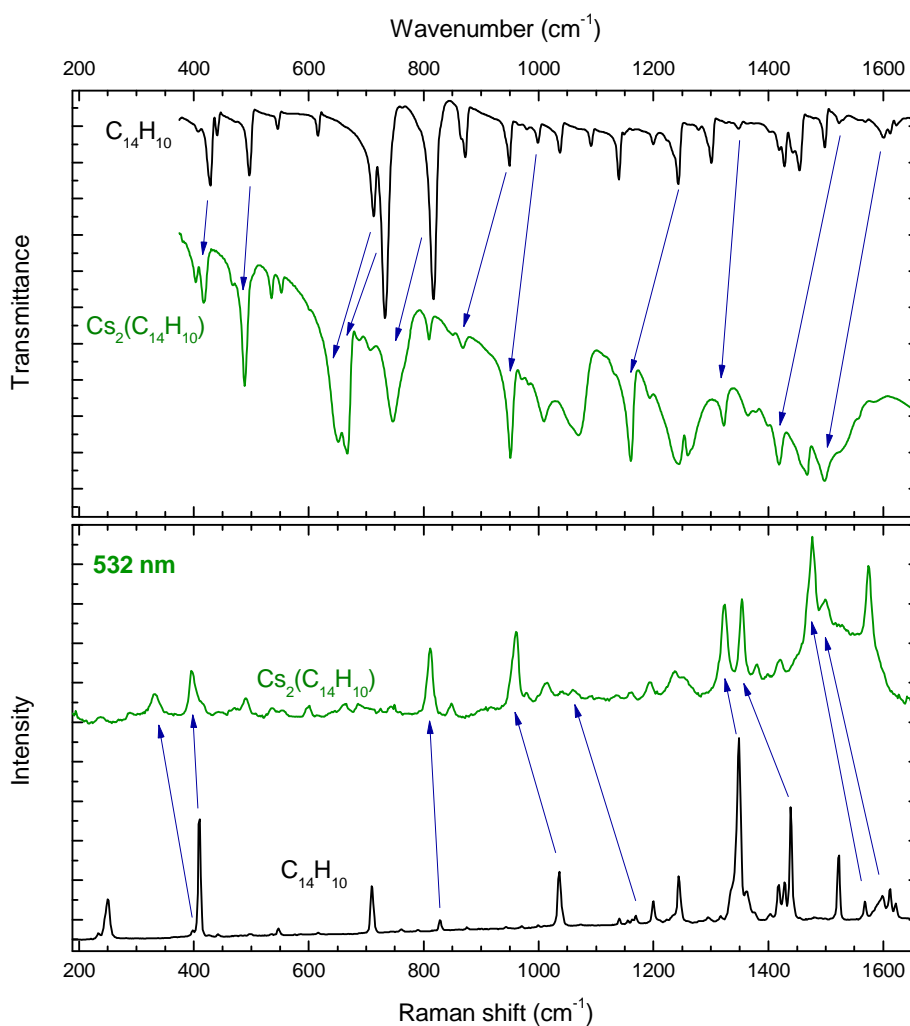
Figure 93: The infrared (top panel) and Raman (bottom panel) spectra of the sample containing $Cs_2(C_{14}H_{10})$ phase (olive green solid line) and pristine phenanthrene (black solid line). Dark blue arrows represent a tentative red-shift of some peaks. Raman spectrum was taken using a 532 nm excitation wavelength.

3.7.4 Magnetic Properties

The temperature dependence of the magnetic susceptibility (χ) of $Cs_2(C_{14}H_{10})$ in an applied magnetic field of 5 T and a Curie-Weiss fit over the whole temperature range are shown in Figure 94.
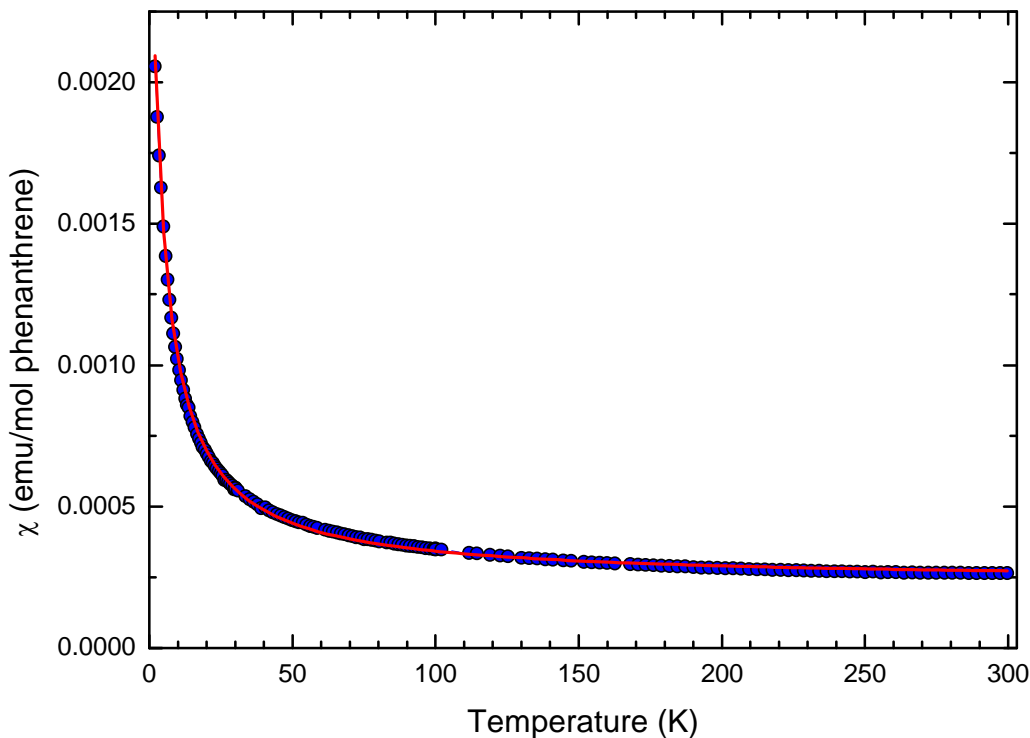
Figure 94: The temperature dependence of molecular susceptibility (χ *vs. T*) of $Cs_2(C_{14}H_{10})$ compound at applied field of 5 T (blue circles) along with fit to Curie-Weiss law in the whole temperature range (red curve). Data was collected using a field-cooled (FC) protocol upon heating.

Fitting the magnetic susceptibility to a Curie-Weiss law yielded a Curie constant of 0.01107(7) emu K/mol that equals to an effective magnetic moment, μ_{eff}, of 0.2976(8) a μ_B, small negative Weiss temperature, Θ = -4.06(5) K and a temperature independent term, χ_0, of $2.36(1)\times10^{-4}$ emu/mol. These values confirm that $Cs_2(C_{14}H_{10})$ is a closed shell system with two spins in a singlet state, giving rise to a weak diamagnetic response in the magnetometer. The obtained Curie constant value of 0.01107(7) emu K/mol corresponds to 3% paramagnetic impurities, which most likely originate from a $Cs(C_{14}H_{10})$ phase that can be formed when the dianion gets oxidised during the sample preparation.

3.7.5 Summary on $Cs_2(C_{14}H_{10})$ compound

The reduction of phenanthrene with two equivalents of caesium metal at near room temperature in THF yielded a highly crystalline solvent-free dianion salt of phenanthrene. In contrast to the synthesis of a solvent-free phenanthrene radical anion which can be achieved only at elevated temperatures, the dianion precipitated from the solution. Similar to the case of $Cs(C_{14}H_{10})$, the crystal structure of $Cs_2(C_{14}H_{10})$ was solved from data obtained on a powder X-ray diffractometer at room temperature by using a simulated annealing technique and confirmed by Rietveld refinement. Two crystallographically independent caesium cations (Cs1 and Cs2) are interacting with various η (mainly $η^6$) coordination bonds with each peripheral benzene ring plane (I and II) of the phenanthride dianion. The structure can be visualised as an array of chains comprising of phenanthrides and caesium cations running along the crystallographic b direction with no interactions along either the crystallographic a or c directions. By projecting the structure along [110] a layered motif can be observed. Except for the coordination interactions motif where two pairs of alkali cations interact with a single phenanthride unit (also present for *Phen3* in $K_4(C_{14}H_{10})_3(THF)_4$ and $Rb_4(C_{14}H_{10})_3(THF)_4$ compounds) none of the structural motifs (isolated zig-zag chains or layer-like structure) observed in $Cs_2(C_{14}H_{10})$ were found in other mono-reduced salts of phenanthrene. The charge transfer and presence of a doubly reduced phenathrene ion, $(C_{14}H_{10})^{2-}$, was confirmed by Raman and infrared spectroscopies, where vibrational bands are red-shifted in comparison to neutral phenanthrene, and the red-shift is larger than in the monoanion-containing compounds. Based on the small magnetisation observed in the temperature-dependent magnetic susceptibility data, it can be concluded that $Cs_2(C_{14}H_{10})$ is a closed-shell system, with spins in a singlet state.

4 Chapter 4 - Conclusions and Future directions

By reducing phenanthrene with alkali-metals (K, Rb and Cs) in the aprotic coordinating organic solvent, THF, at near room temperatures, highly crystalline (in most cases) phase-pure compounds $K_2(C_{14}H_{10})_2(THF)$, $K_4(C_{14}H_{10})_3(THF)_4$, $Rb_2(C_{14}H_{10})_2(THF)$, $Rb_4(C_{14}H_{10})_3(THF)_4$, $Cs_2(C_{14}H_{10})_2(THF)$, $Cs(C_{14}H_{10})$ and $Cs_2(C_{14}H_{10})$ were synthesised for the first time. These compounds exhibit a variety of interesting magnetic properties, spanning canted- antiferromagnetism, low-dimensional magnetism, mixed valence systems and low-spin diamagnetism.

4.1 Structural rearrangements upon reduction

The apparent difference between pristine phenanthrene and the alkali-metal phenanthrides is the rearrangement of phenanthrene units upon reduction. The variety of structures prepared is compared on Fig. 95 (for isostructural analogues only one compound is depicted).

In contrast to π-stacking in phenanthrene, driven by relatively weak $H^{\delta+}\cdots\pi^{\delta-}$ interactions as described in the Introduction, the $A^+\cdots\pi^-$ (A = K, Rb, Cs) and $A^+\cdots O^{\delta-}$ interactions are the dominate for the packing interactions in alkali-metal reduced phenanthrides. The phenanthride units rearrange in a way to optimise the interactions between the alkali metal and the π cloud on the phenanthride, and at the same time minimise the steric crowding. The flipping of each neighbouring phenanthrene by 180° seems to be the favourable reconstructive mechanism where strong $A^+\cdots\pi^-$ interactions between the alkali metal and the peripheral benzene ring planes are established and the steric crowding is minimised. This rearrangement is clearly observed in the $Cs_2(C_{14}H_{10})_2(THF)$ and $Cs_2(C_{14}H_{10})$ structures, where caesium atoms are positioned over the peripheral benzene ring planes of phenanthrene and are strongly interacting with them on both sides. The angles between neighbouring phenanthrides in $Cs_2(C_{14}H_{10})_2(THF)$ and $Cs_2(C_{14}H_{10})$ are 63.0 and 75° respectively. The flipping, accompanied with the translation and/ or rotation of phenanthride units was observed

in the $K_4(C_{14}H_{10})_3(THF)_4$, $Rb_4(C_{14}H_{10})_3(THF)_4$ and $Cs(C_{14}H_{10})$ structures. In the case of $K_4(C_{14}H_{10})_3(THF)_4$ the flipping is accompanied with anti-clockwise rotation (with respect to the slip-stack chain) of neighbouring phenanthride, opening an angle of 66.3^o between them. In addition to flipping and anti-clockwise rotation, the translation along the crystallographic a direction was observed in the $Cs(C_{14}H_{10})$ structure, and an angle of 52° is observed between neighbouring phenanthrides. In $K_2(C_{14}H_{10})_2(THF)$ and $Rb_2(C_{14}H_{10})_2(THF)$ only two types of rotation and no flipping were observed. The first type of rotation is anti-clockwise rotation, with respect to the slip-stack chain, opening an angle of 70.5^o between neighbouring phenanthride units. The second is an in-plane clockwise rotation of those units. Based on these findings it can be concluded that in the structures ($Cs_2(C_{14}H_{10})_2(THF)$ and $Cs_2(C_{14}H_{10})$) where only flipping of neighbouring phenanthrides takes place, the caesium cations strongly interact with both sides of the peripheral benzene ring planes in the phenanthride. In contrast to that, the interactions between one alkali-metal cation and one benzene ring plane (either the peripheral or central one) is observed along the slip-stack chains in the structures ($K_4(C_{14}H_{10})_3(THF)_4$, $K_2(C_{14}H_{10})_2(THF)$, $Rb_4(C_{14}H_{10})_3(THF)_4$, $Rb_2(C_{14}H_{10})_2(THF)$ and $Cs(C_{14}H_{10})$), where rotation and translation is taking place. We assume that the above-described rearrangements are strongly related to the size of the cation and the amount of solvent present in the structure, which determine the type of coordination and steric crowding.

The majority of neutral PAHs adopt a herringbone structure and these molecular units undergo similar, in some cases even identical, rearrangements upon reduction, as described in this work, in order to optimise the $A^+ \cdots \pi^-$ interactions. A detailed description of some alkali metal reduced PAHs is gathered in two review articles [69][70].
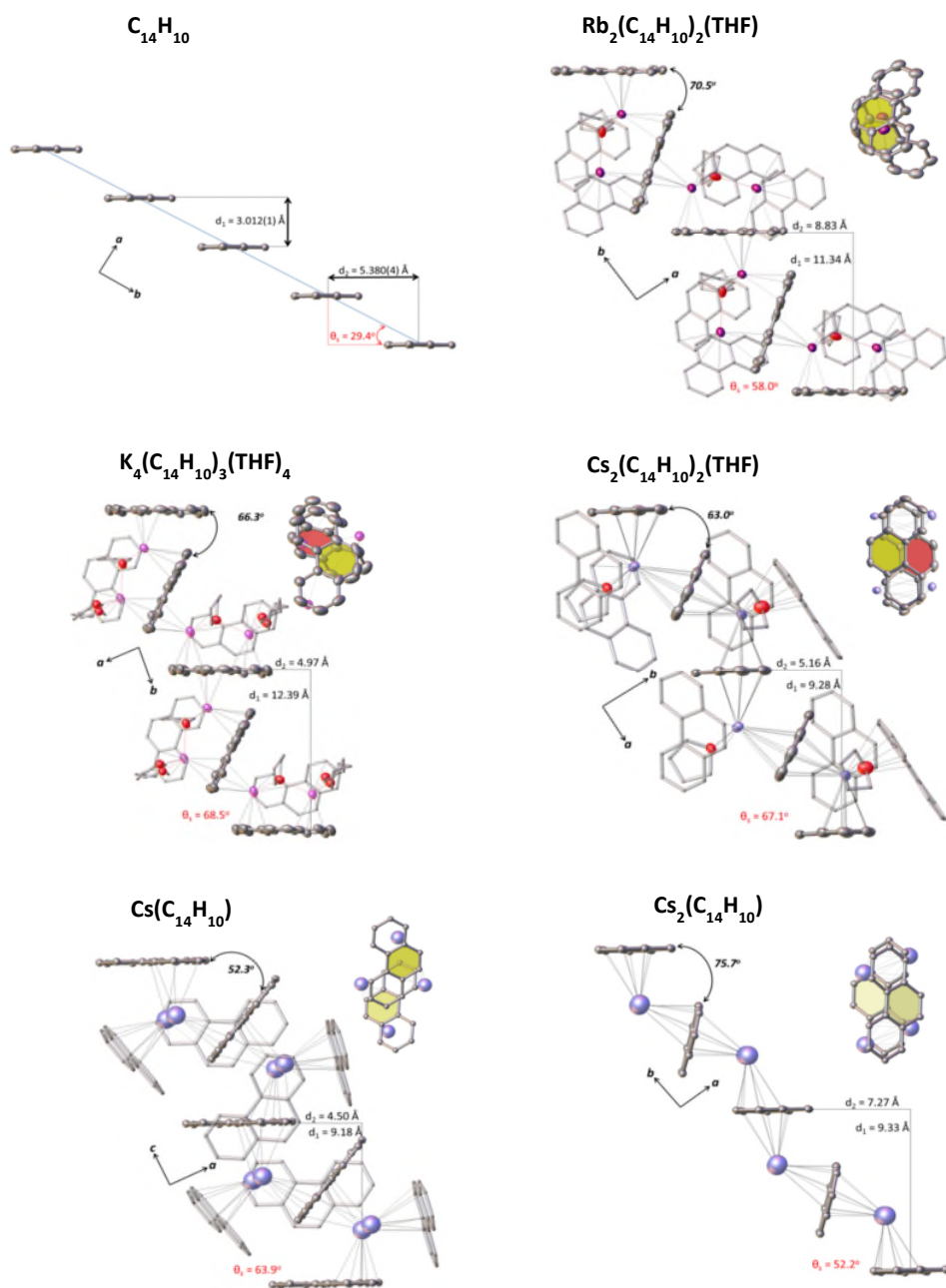
Figure 95: Molecular slip-stacking in pristine phenanthrene along *b*, $Rb_2(C_{14}H_{10})_2$(THF) along *b*, $K_4(C_{14}H_{10})_3$(THF)$_4$ along *b*, $Cs_2(C_{14}H_{10})_2$(THF) along *a*, $Cs(C_{14}H_{10})$ along *c* and $Cs_2(C_{14}H_{10})$ along *b* crystallographic directions. Smaller figures, next to molecular slip-stacking, show the in-plane projection of phenanthride units along the slip-stack chains. d_1, d_2 and θ_s represent the intrastack distance, the slipping distance and the slipping angle between parallel-oriented phenanthrene/ phenanthrides respectively. Depicted black double arrows correspond to the angle between neighbouring molecular planes. Colour code: Rb violet, K lilac, Cs purple, C grey and O red. Hydrogen atoms are omitted and the rest of molecular units (phenanthrides and THF), which are not involved in slip-stack chain are depicted as tubes and with 60% transparency level for clarity. Thermal ellipsoids are shown with 50% probability level, and the crystallographically independent central benzene ring planes are coloured in yellow and red.

153

There are numerous theoretical and gas-phase experimental studies of cation···π interactions, because those non-covalent interactions play an important role in biology, biochemistry and in pharmacy [166, 167, 168, 169, 170, 171, 172, 173]. The role of the cation's position with respect to the centre of the benzene ring plane is described in [174]. The authors of that work concluded, on the basis of calculations that the potential energy drops by moving the cation away from the centre of the benzene ring plane, as shown in Figure 96 (values are given in Table 19). The A^+-π interaction energy decreases with increasing θ, deviation from the centre of the benzene ring plane above the plane, and ɸ, the deviation of the in-plane angle.
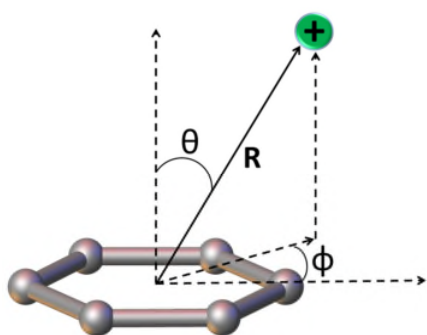
Figure 96: Geometries of cation-π system [174].

Table 19: Counterpoise Corrected Interaction Energies (E_{int}, kcal/mol) and Equilibrium Distances (R, Å) [174].

Cation	θ	ɸ	E_{int}	R
K	0	0	-16.5	2.9
	30	0	-12.1	3.4
	60	0	-5.1	4.4
	90	0	-1.5	5.2
	30	30	-12.1	3.4
	60	30	-6.6	4.1
	90	30	-3.0	4.5

Both experimental and theoretical studies confirm that A^+···$π^-$ interactions are strong, and therefore the phenanthrene molecular units need to undergo the rearrangements described above, to optimise the Coulomb-attraction between the cation and the electrons in the π orbitals of the phenanthride. In order to obtain this energetically more favourable state the herringbone structure needs to be collapsed.

By performing the reduction of phenanthrene with alkali metals in an aprotic coordinating organic solvent, in our case THF, the collapse of the herringbone structure and rearrangement of phenanthrides to establish strong A^+···$π^-$ interactions can be easily achieved, because pristine phenanthrene and phenanthrides are soluble in THF. In contrast to this, the rearrangement of the PAH units requires considerably more energy when reduction is performed by a solid-state reaction. We believe that in many PAH systems, the thermal energy needed to overcome these rearrangements

barriers is higher than the energy at which decomposition occurs. Perhaps this is the main reason why well-defined and phase-pure alkali-metal reduced PAHs are so notoriously difficult to synthesise utilising solid-state techniques.

The reports of superconductivity in alkali-metal reduced PAHs triggered the avalanche of research in this field, where many groups entered this research topic in order to synthesise new superconductors and understand their physical properties, as described in the Introduction. However, the lack of well crystalline and phase-pure samples, which are a precondition for detailed investigation of their physical properties, severely hampered the whole topic. Therefore, many of these groups diverted their effort into the crystal structure determination of these materials, either based on experimental data or by performing geometry optimisation calculations [78, 83, 85, 86, 87, 88, 89, 90, 91, 105]. The main assumption, used in those papers, was that the herringbone structure of PAHs is retained upon reduction. According to their results, the π-π stacking interactions remain, the structural changes are very subtle and cations occupy the interstices between PAH molecules. These findings are in total disagreement with our findings and those found in the literature [69, 70]. In two recent works [83][105] the crystal structures were solved from powder diffractograms containing only a small number (12-24) of well-resolved Bragg peaks, together with a considerable background hump. In this case the reliability of the obtained structures can be questioned.

4.2 The salt of the dianion and its similarities with pristine phenanthrene

As described above, the arrangement of phenanthrides in alkali-metal salts of phenanthrene is drastically different to that observed in pristine phenanthrene. However, the structures of $Cs_2(C_{14}H_{10})$ and the structure of phenanthrene do share similarities. By projecting both structures along the crystallographic b direction a chain of phenanthrene molecular units is found to run along that direction. In contrast to pristine phenanthrene, where all molecules are co-aligned along the b direction, every second phenanthride is flipped by 180° in the $Cs_2(C_{14}H_{10})$ compound. The projection along the [110] direction revealed a layer-like structural motif, where phenanthrene and phenanthride units running along a and b are well separated along the crystallographic c direction as shown in figure 97.
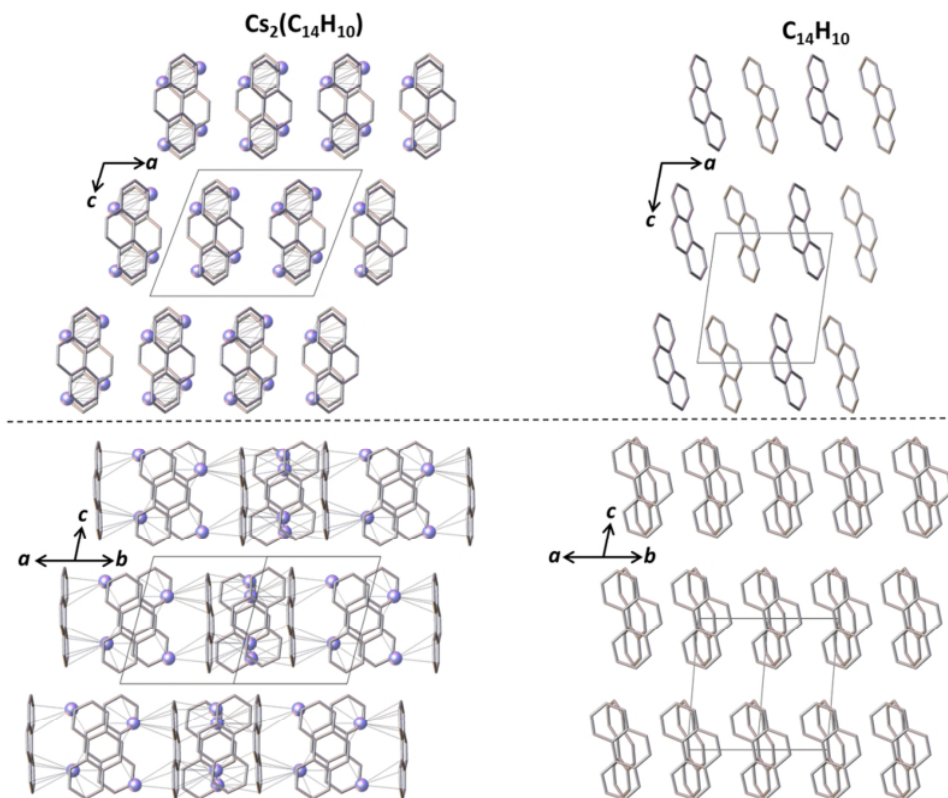
Figure 97: The projection of $Cs_2(C_{14}H_{10})$ and pristine phenanthrene structures along the [010] (upper panel) and [110] (lower panel) crystallographic directions. Colour code: Cs purple and C grey. Hydrogen atoms are omitted and phenanthrene/phenanthride units are depicted as tubes for clarity.

Similarly to the $Cs_2(C_{14}H_{10})$ compound, a chain-like structural motif was observed in solvent-free and diethyl ether (Et_2O) containing lithium-, sodium- and potassium-reduced cyclopentadienes (A-C_5H_5) [175, 176, 154]. Besides the alkali cyclopentadienyls, this motif was also reported in potassium-reduced indene [154] and sodium-reduced pyrene [152, 177]. Caesium-reduced rubrene, $Cs_4(C_{42}H_{28})_3(DME)_2(C_6H_{14})$, exhibits a layer-like structural motif and is one of the rare known dianions [136].

Taking into account that there is a small number of doubly-reduced PAHs known, the expansion of this family of compounds would be desirable. A reduction of phenanthrene with two equivalents of potassium and rubidium metal under similar conditions in order to produce $K_2(C_{14}H_{10})$ and $Rb_2(C_{14}H_{10})$ compounds should be undertaken. Based on our findings thus far, the caesium salts of phenanthrene adopt different structures to the potassium and rubidium ones. For instance, the $Cs_2(C_{14}H_{10})_2(THF)$ compound crystallises in a different space group and exhibits different structural motifs to the isostructural $K_2(C_{14}H_{10})_2(THF)$ and $Rb_2(C_{14}H_{10})_2(THF)$ compounds even though all of them contain the same constituents. Therefore, the crystallisation in different crystal systems and space groups is anticipated for potassium and rubidium dianions of phenanthrene. Additionally, these compounds could give us a valuable insight into how the size of the cation affects the solvent uptake into the crystal structure, and perhaps it would be possible to obtain solvent-containing salts of dianions.

4.3 The solvent-free $Cs(C_{14}H_{10})$ and the search for new low-dimensional molecular magnets

As depicted in Figure 95, all three caesium salts of phenanthrene, ($Cs_2(C_{14}H_{10})_2$(THF), $Cs(C_{14}H_{10})$ and $Cs_2(C_{14}H_{10})$) exhibit the same feature: the flipping of neighbouring phenanthride ions. The same flipping was also observed in potassium-reduced fluorene, $K(C_{13}H_9)$(TMEDA)$_2$, which has a layered structure [178] and potassium-reduced triphenylene, $K_2(C_{18}H_{12})_2$(DME) [179]. The latter shares a lot of similarities with the $Cs_2(C_{14}H_{10})_2$(THF) and $Cs(C_{14}H_{10})$ compounds, as shown in Figure 98.

The $K_2(C_{18}H_{12})_2$(DME) compound contains the same number of constituents as $Cs_2(C_{14}H_{10})_2$(THF), and by comparing them it can be seen that chains running along the crystallographic a directions are nearly identical if we forget about the extra benzene ring on the triphenylene molecule. Another clear observation is the difference in size of the solvent molecule and how the size of it has a major impact on the crystal structure. While the THF is bulkier, it is pushed on to the periphery of the chain and becomes part of the cage surrounding the chain. In contrast DME (a bidendate ligand) is effectively a smaller molecule than THF and becomes rather part of the chain, rather than the cage. Therefore, as a whole channel-like structure, it shares more resemblances to $Cs(C_{14}H_{10})$ than to the $Cs_2(C_{14}H_{10})_2$(THF) structure. Moreover, the $K_2(C_{18}H_{12})_2$(DME) compound crystallises in the same orthorhombic $P2_12_12_1$ space group as $Cs(C_{14}H_{10})$ and exhibits low-dimensional magnetism with exchange interactions three times stronger than those found in $Cs(C_{14}H_{10})$ [179].

These findings open up a very intriguing synthesis route for the future. By changing THF to a different aprotic solvent of appropriate size, we might be able to cause the solvent to become part of the chain, instead of the cage, and therefore force the system to adopt a different crystal structure. Perhaps it could even be possible to drive the system to the point where low-dimensional magnetism would appear. Nevertheless, it has to be noted that the size of the phenanthrene and caesium atoms might play a profound role and prevent this structural rearrangement. However some new form of magnetism could arise from the newly formed structures.
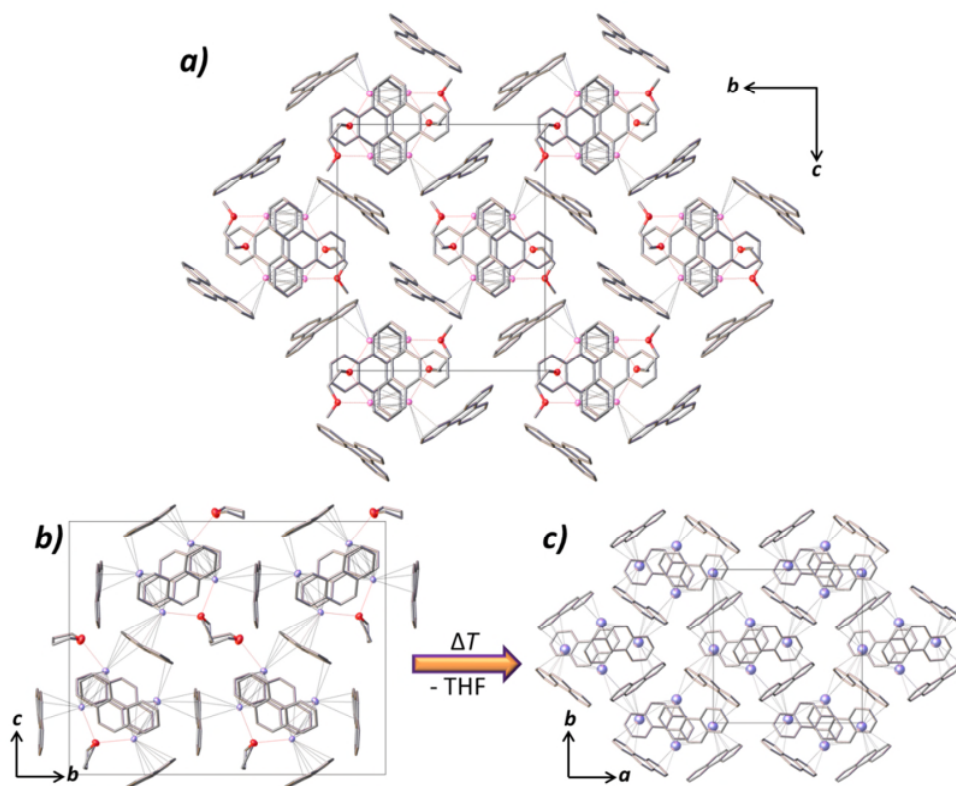
Figure 98: a) $K_2(C_{18}H_{12})_2(DME)$ structure, b) $Cs_2(C_{14}H_{10})_2(THF)$ structure projected along [100] and c) $Cs(C_{14}H_{10})$ structure projected along [001] crystallographic directions are representing the similarities between all three crystal structures. Colour code: K lilac, Cs purple and C grey. Hydrogen atoms are omitted and phenanthride/triphenylide units are depicted as tubes for clarity.

We would also like to propose the optimisation of the crystallisation procedure, to perform it at elevated temperatures, in order to obtain single crystals of $Cs(C_{14}H_{10})$, which would permit more accurate structure determination. The plausibility of the success of this synthesis procedure can be seen based on the morphology of the $Cs(C_{14}H_{10})$ powder, which contains small crystals (Figure 34). The structural model obtained from single crystal analysis would provide valuable information needed for better understanding of the intriguing low-dimensional magnetism found in this material. Besides the growth of single crystals, additional magnetic measurements are desirable, e.g. SQUID magnetometry, EPR and µSR spectroscopies, at ultra-low temperatures (in the millikleivin regime) to verify, whether $Cs(C_{14}H_{10})$ indeed does not undergo a long-range magnetic ordering and in this way unambiguously confirm or disprove the statement that this material is a quantum spin liquid.

4.4 The $K_2(C_{14}H_{10})_2$(THF) and $Rb_2(C_{14}H_{10})_2$(THF) structures and the triangle-like motif in A-PAHs

The triangle-like motif observed in the isostructural $K_2(C_{14}H_{10})_2$(THF) and $Rb_2(C_{14}H_{10})_2$(THF) compounds is a quite common arrangement of constituents in the crystal structures of small alkali-metal reduced PAHs. For instance, it is found in THF-containing potassium reduced naphthalene ($K_2(C_{10}H_8)_2$(THF)) [71], anthracene ($K_2(C_{14}H_{10})_2$(THF)$_3$) [72] and fluorene ($K_2(C_{13}H_9)_2$(THF)) [156] as shown in Figure 99. The naphthalene salt $K_2(C_{10}H_8)_2$(THF) crystallises in a monoclinic crystal system in contrast to an orthorhombic one, found in potassium and rubidium phenanthrides. By projecting naphthalide and phenanthride analogues along the [010] and [001] crystallographic directions, (Figure 99a and b), a distinct difference can be observed. Potassium cations interact with two neighbouring naphthalides instead of three phenanthrides, forming 1D chains along the [100] direction rather than a 3D polymeric network. The observation of these chains in the crystal structure obtained from data collected at 213 K contrast the long-range antiferromagnetic ordering, with T_N = 28.6 K, reported in this material [71]. Perhaps the considerable contraction of the unit cell, bringing naphthalides units closer together, could enable interactions in all three crystallographic directions. A structural phase transition upon further cooling could also be another possible explanation for the observed long-range magnetic ordering.

The triangle-motif in potassium reduced anthracene, $K_2(C_{14}H_{10})_2$(THF)$_3$, consists of two potassium cations, two anthracide ions and one disordered THF molecule, with its oxygen atom acting as a bridging ligand (Figure 99c). Two additional THF molecules acting as terminal ligands complete the coordination sphere of potassium cations and effectively encapsulating them. The number of THF molecules and possibly the shape of anthracene (acene *vs*. phenacene) prevent additional interactions along any crystallographic directions, and therefore form isolated anthracide dimers. It should be noted that the amount of solvent in anthracides apparently plays a vital role in magnetic exchange interactions. According to the literature [101, 102, 103, 104] low-dimensional magnetism was reported in potassium-reduced anthracene. The authors reacted equimolar (1:1) amounts of anthracene with potassium metal at temperatures considerably lower than the melting point of anthracene by utilising a solid-state

technique. At this point it can be concluded that low-dimensional magnetism is quite common in alkali-metal reduced PAHs, as it was found in caesium phenanthride, potassium triphenylide and potassium anthracide.
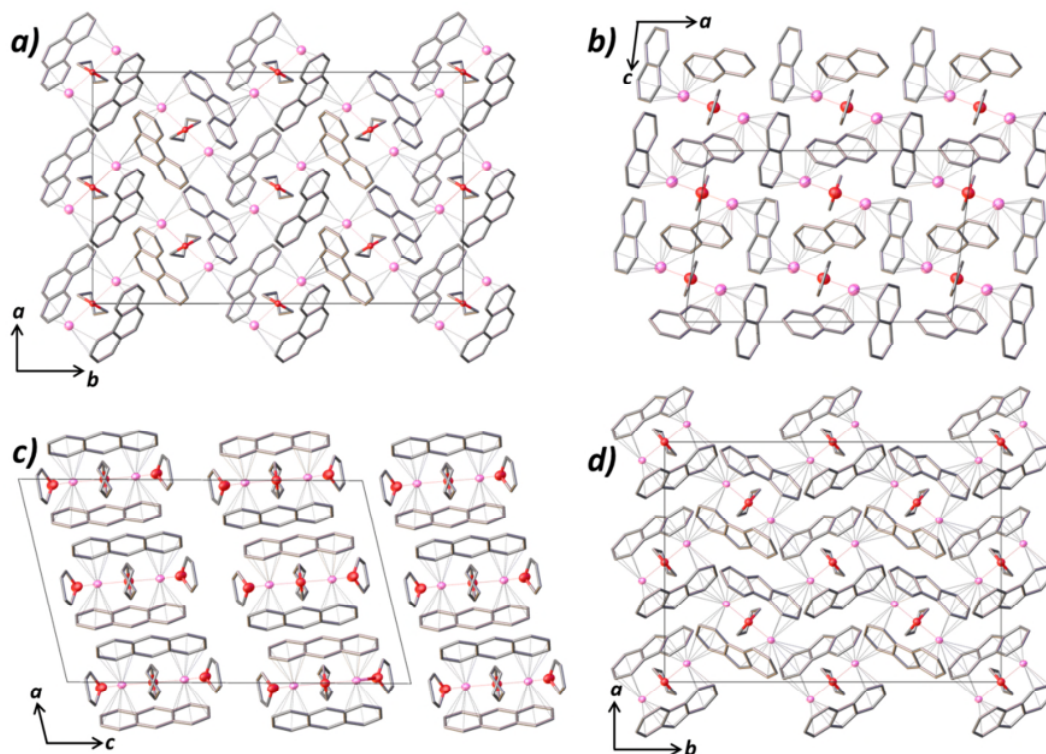
Figure 99: The triangle-like motif is presented in a) $K_2(C_{14}H_{10})_2$(THF) and d) $K_2(C_{13}H_9)_2$(THF) structures projected along [001], and c) $K_2(C_{10}H_8)_2$(THF) and d) $K_2(C_{14}H_{10})_2$(THF)$_3$ structures projected along [010] crystallographic directions. Colour code: K lilac, C grey and O red. PAH molecular units and THF molecules are depicted as tubes, and hydrogen atoms are omitted for clarity.

The potassium reduced fluorene, $K_2(C_{13}H_9)_2$(THF), contains the same number of constituents and crystallises in the same orthorhombic *Fdd*2 space group as the compounds $K_2(C_{14}H_{10})_2$(THF) and $Rb_2(C_{14}H_{10})_2$(THF). Therefore, all three materials are isostructural. The packing motif of the $K_2(C_{14}H_{10})_2$(THF) and $K_2(C_{13}H_9)_2$(THF) structures (Figure 99a and d) seems, at first look, practically identical. However, a more detailed examination of the interactions reveals subtle but noticeable differences as shown in Figure 100. It can be seen that in between the dimers (the central molecular units in Figure 100), the potassium cation interacts with one peripheral benzene ring plane (η^4) and central five-member ring plane (η^4) in the $K_2(C_{13}H_9)_2$(THF) structure, in contrast to one peripheral benzene ring plane (η^3) and rim sharing another peripheral and central

161

benzene ring plane (η^3) in $K_2(C_{14}H_{10})_2$(THF). Furthermore, the interaction between the potassium cation and the neighbouring dimers (molecular units in the left hand and right hand side) goes through the peripheral benzene ring plane (η^6) in the fluorenyl ion, while in the case of the phenanthride ion, the interaction goes through the central benzene ring plane (η^4).
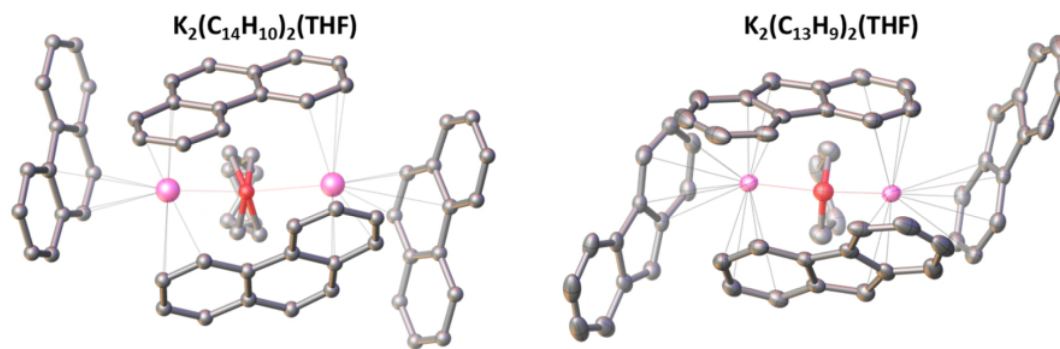
Figure 100: Coordination environment of K^+ ions in $K_2(C_{14}H_{10})_2$(THF), left panel, and $K_2(C_{13}H_9)_2$(THF) compound, right panel. Black dotted lines and red dotted lines represent $K^+\cdots C$ and $K^+\cdots O$ coordination interactions respectively. Colour code: K lilac; O red and C grey. Hydrogen atoms are omitted for clarity.

Even though the differences are subtle, and most likely originate from the substitution of a six-member for a five-member ring, they could have immense impact on magnetism. Therefore, we would like to reproduce the $K_2(C_{13}H_9)_2$(THF) compound, to study how these changes influence the canted antiferromagnetism observed in $K_2(C_{14}H_{10})_2$(THF). We would also like to elucidate the impact of the above described changes on negative thermal expansion, thus far unprecedented in alkali-metal reduced PAHs. Moreover, the extension of the fluorenyl family with a rubidium analogue and the reproduction of already-reported compounds would undoubtedly expand our understanding of the structure-magnetism relationships in alkali-metal phenanthrides.

4.5 Mixed valence compounds

Mixed valence compounds are rare in alkali-metal reduced PAHs and were until now found in sodium-reduced perylene, $Na(C_{20}H_{12})_2(triglyme)_2$ [152] and potassium-reduced anthracene, $K_4(C_{14}H_{10})_3(THF)_6$ [72]. The former consists of one radical monoanion and one neutral perylene, yielding a molecular formula of $[\{Na(triglyme)_2\}(C_{20}H_{12})^-(C_{20}H_{12})]$, while the latter consists of two radical monoanions and one dianion of anthracene with a $[\{K_4(THF)_6\}(C_{14}H_{10})^-_2(C_{14}H_{10})^{2-}]$ molecular formula, which is exactly the same mixed valence state as observed in potassium reduced phenanthrene, $[\{K(THF)\}_4(C_{14}H_{10})^-_2(C_{14}H_{10})^{2-}]$. Despite the same mixed valence state and space group ($P\bar{1}$), the arrangement of constituents in the crystal structure is different (Figure 101). While in the phenanthride anion-containing structure the interaction between potassium and phenanthrene radical ions is retained in all three crystallographic directions, the trimers in the anthracide-anion-containing structure are solvent-separated and no interactions between them can be observed. The structural differences imply a difference in magnetism. In contrast to our results which clearly indicate that the spins on the phenanthrene dianions are in a singlet state, the authors [72] reported a triplet state of spins on the anthracene dianion. This is an interesting finding because alkali-metal reduced PAHs with spins in a triplet state and strong intermolecular magnetic exchange interaction might host a metallic or potentially even a superconducting state.

A potential future direction is the low-temperature isolation and full characterisation of the rubidium analogue, $Rb_4(C_{14}H_{10})_3(THF)_4$, which at the moment remains not fully characterised due to its fast transformation from a solvent-rich, $Rb_4(C_{14}H_{10})_3(THF)_4$, to a solvent-poor $Rb_2(C_{14}H_{10})_2(THF)$ phase. In addition, we would like to understand the transformation process in order to confirm or disprove our proposed mechanism. Moreover, we would like to expand the search for mixed valence compounds in new families of alkali-metal reduced PAHs, as these materials could exhibit desirable magnetic and electronic properties.

$[\{K(THF)\}_4(C_{14}H_{10})^-{}_2(C_{14}H_{10})^{2-}]$ $[\{K_4(THF)_6\}(C_{14}H_{10})^-{}_2(C_{14}H_{10})^{2-}]$
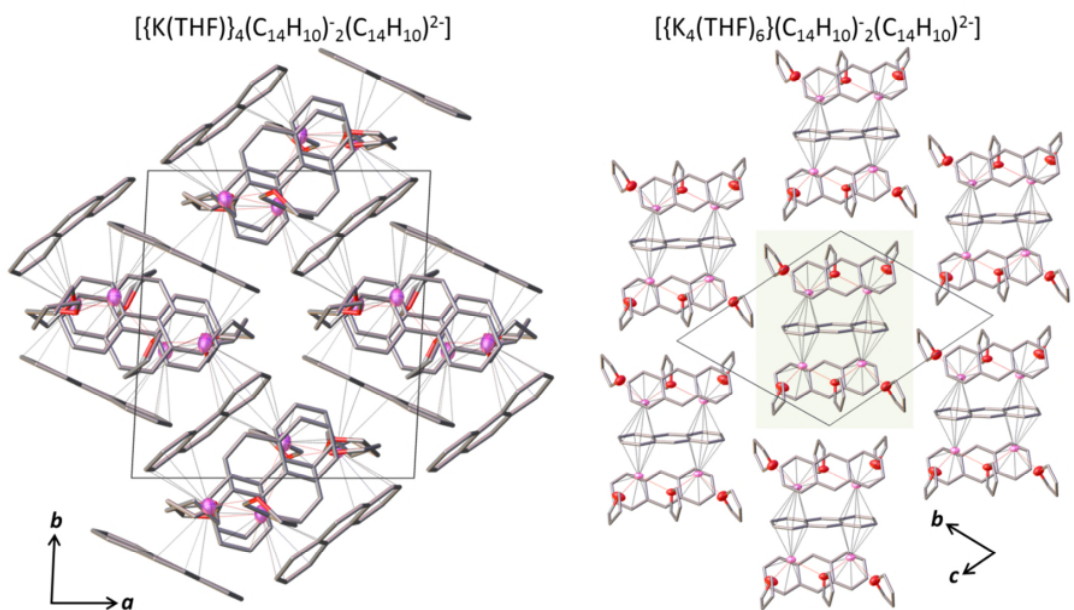
Figure 101:   Projection of $K_4(C_{14}H_{10})_3(THF)_4$, left panel, and $K_4(C_{14}H_{10})_3(THF)_6$, right panel; structures are projected along [001] and [100] crystallographic directions, respectively. The pale green square represents an anthracide trimer. Colour code: K lilac, C grey and O red. Phenanthrene/anthracene molecular units and THF molecules are depicted as tubes, and hydrogen atoms are omitted for clarity.

4.6 Towards new solvent-free compounds and observed ferromagnetism

As discussed in the Results section the amount of solvent in the crystal structure plays a decisive role in determining the crystal structure and magnetic properties, and its amount can be, to some extent, controlled by changing the temperature during the crystal growth process. Compounds where higher temperatures were utilised during the synthesis, or compounds which were heat treated, contain less solvent than those where lower temperatures were used. The second factor, which determines the amount of solvent in the structure, is the size of cation. Smaller cations favour more solvent in their coordination sphere, while larger ones favour less solvent in the crystal structure [180]. For instance, we did not succeed in obtaining the solvent-rich $Cs_4(C_{14}H_{10})_3(THF)_4$ compound and we were also unsuccessful in the isolation of phase-pure $K(C_{14}H_{10})$ and $Rb(C_{14}H_{10})$ compounds. Based on the obtained results, the $A^+ \cdots \pi^-$ interactions are strong, so the negatively charged PAH molecular unit is going to be positioned in such a way as to achieve the optimum interaction with the cation. This can lead to voids, which would inevitably be filled with coordinating solvent molecules, where the coordination between cation and electron pairs on *e.g.* oxygen will stabilise the structure. The size of these voids depends on the size of the cation. Therefore it seems that the interplay of the PAH and the cation size determines the amount of solvent in the structure at a specific temperature.

The high-temperature powder X-ray diffraction experiments performed on $K_4(C_{14}H_{10})_3(THF)_4$ and $K_2(C_{14}H_{10})_2(THF)$ clearly indicate the existence of another crystalline phase accessible at higher temperatures. Therefore, we decided to perform the preliminary synthesis of potassium and rubidium compounds under the same conditions used for the preparation of solvent-free caesium phenanthride, $Cs(C_{14}H_{10})$. The results, shown in Figure 102 and 103, evidence a formation of new crystalline phases at elevated temperatures. The Bragg diffraction peaks corresponding to new phases were observed by powder X-ray diffraction and are denoted with orange and olive-green asterisks for potassium- and rubidium-reduced phenanthrene, respectively (Figure 102 and 103 upper panels). According to elemental analysis, the potassium reduced sample contains approximately 20% solvent-free and 80% $K_2(C_{14}H_{10})_2(THF)$

phase, and the rubidium reduced sample ca. 60% solvent-free and 40% $Rb_2(C_{14}H_{10})_2$(THF) phase. These results confirm our observation that compounds containing larger cations tend to liberate solvent more easily than those containing smaller cations.
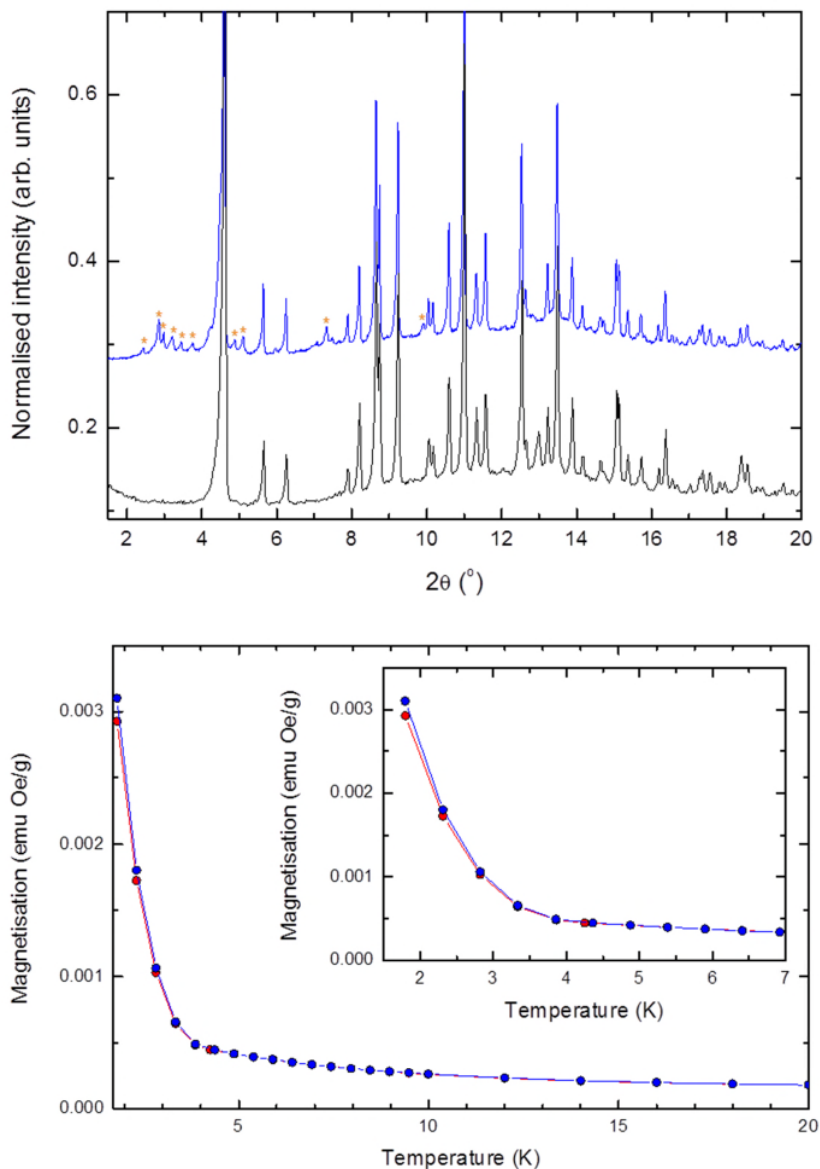
Figure 102: The upper panel is presenting powder X-ray diffractograms of the phase-pure $K_2(C_{14}H_{10})_2$(THF) compound (black solid line) and sample containing ~20% solvent-free and 80% $K_2(C_{14}H_{10})_2$(THF) phase (blue solid line), respectively. The orange asterisks are denoting the most intense peaks of newly formed crystalline potassium containing solvent-free phase. The temperature dependent magnetisation measurements at $H = 1$ mT of sample containing solvent-free and $K_2(C_{14}H_{10})_2$(THF) phases is depicted on the lower panel and the inset is showing a low temperature region. The measurements were performed under ZFC (red circles) and FC (blue circles) protocols. All measurements were collected upon heating.
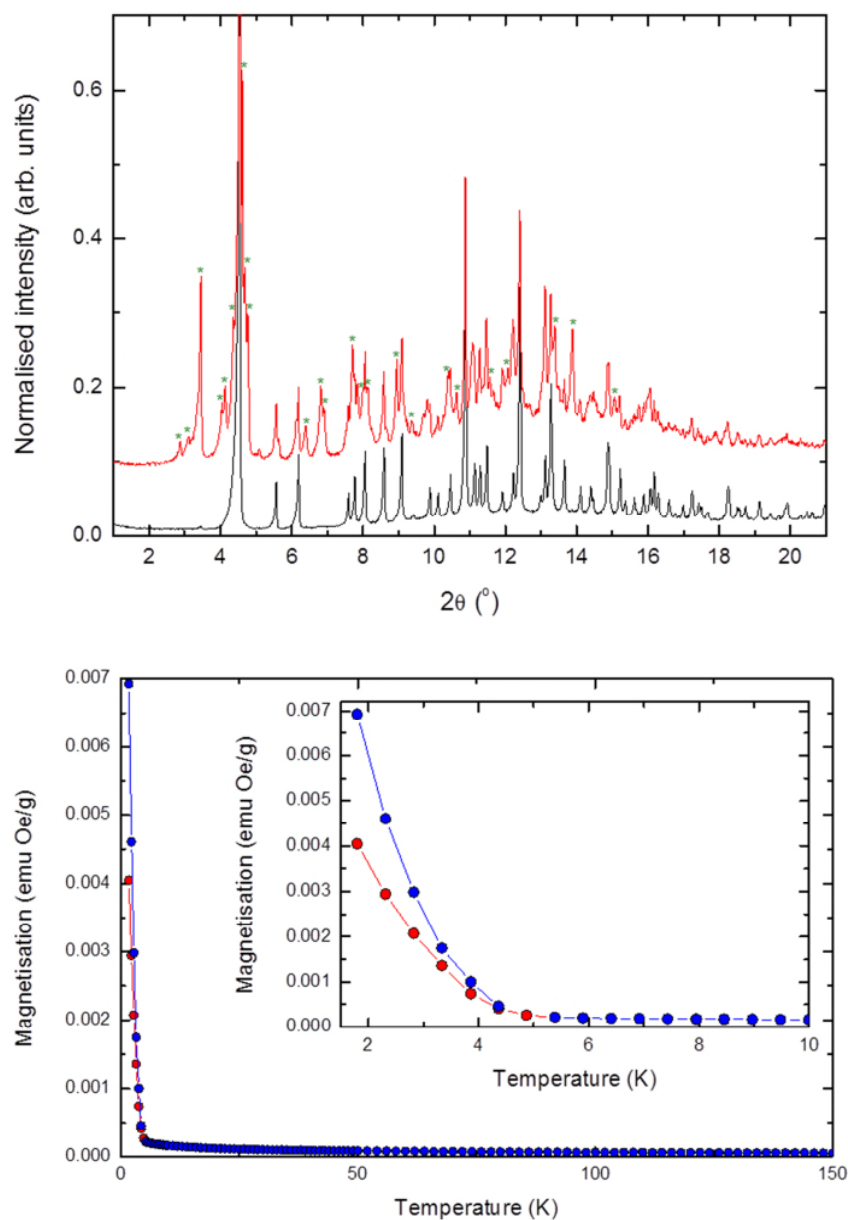
Figure 103: The upper panel shows the diffraction profiles of the phase-pure $Rb_2(C_{14}H_{10})_2(THF)$ sample (black solid line) and sample containing a mixture of solvent-free and $Rb_2(C_{14}H_{10})_2(THF)$ in 60:40 ratio (red solid curve). The olive-green asterisks are denoting the most intense peaks of newly formed crystalline rubidium containing solvent-free phase. The temperature dependent magnetisation measurements at $H = 1$ mT of the sample containing solvent-free and $Rb_2(C_{14}H_{10})_2(THF)$ phase are presented on the lower panel. The inset is showing a low temperature region. The measurements were performed under ZFC (red circles) and FC (blue circles) protocols. All measurements were collected upon heating.

The magnetisation measurements revealed a sharp magnetisation upturn at low temperatures in both samples, which is a hallmark for long-range ferromagnetic

ordering. These remarkable results open up a new pathway in the synthesis of organic ferromagnets based on alkali-metal reduced PAHs. Therefore the optimisation of the synthesis and crystallisation process is planned in order to produce well crystalline, preferably single crystalline, phase-pure organic ferromagnets.

In our first solvent-free samples of potassium phenanthride (samples containing ca. 5% of solvent-free phase or less) we observed a very strong diamagnetic response, resembling a superconducting state, which vanished under applying fields higher than 10 mT or after performing a proper re-zeroing of the SQUID magnetometer. This finding raised a very important question. Is it possible that the authors who reported superconductivity in alkali-metal reduced PAHs [76, 77, 78, 79] measured ferromagnetic impurities associated with a $A^{+}\cdots PAH^{\bullet-}$ phase instead of a superconducting phase? The high temperature solid-solid state reactions between PAHs and strong reducing agents such as alkali-metals tend to subtract hydrogen from the PAH molecule, forming alkali hydride and a PAH radical which is an extremely reactive species. Most of the researchers in this field detected alkali-hydrides by powder X-ray diffraction, as discussed in the Introduction. If this was the case then the formation of the reported A_3-PAH phase would have been impossible, suggesting that most likely the decomposition products with some A_2-PAH or even the A-PAH phases were formed. Moreover, the Raman spectrum of the reported [77] superconducting $Rb_3(C_{14}H_{10})$ phase is nearly identical to the spectrum of phase-pure $Cs_2(C_{14}H_{10})$ as shown in Figure 104. And finally the shielding fractions, which indicate the percentage of the superconducting phase, in the majority of the superconducting samples, are smaller than 1% (see Table 2). Based on these observations and the findings reported in the literature [181, 182] the answer to our question would be yes: ferromagnetic impurities caused the exciting magnetic response, but without more solid evidence this cannot be proved.
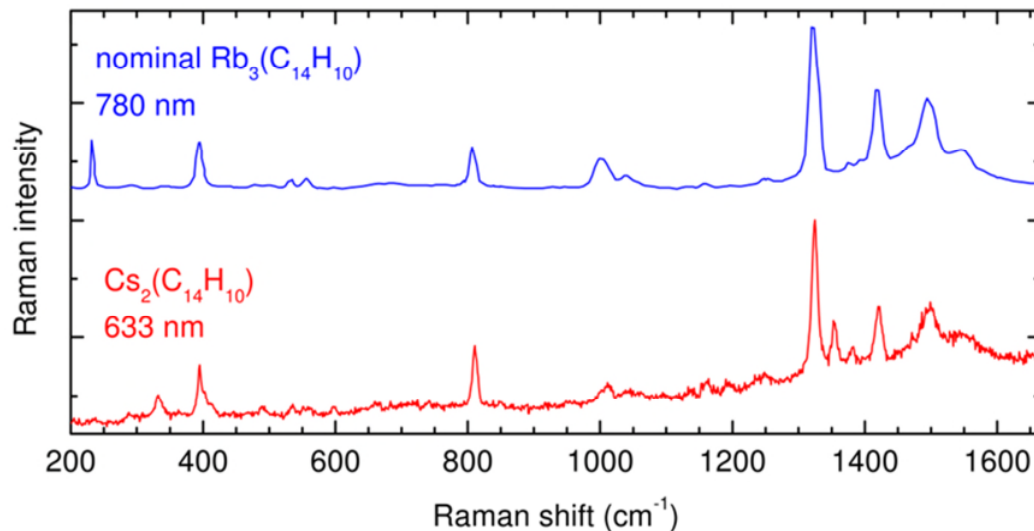
Figure 104: Comparison of the Raman spectrum of the $Cs_2(C_{14}H_{10})$ obtained with 633 nm excitation (red solid line) with that of a sample with nominal composition $Rb_3(C_{14}H_{10})$ obtained with 780 nm excitation [77] (blue solid line). The latter spectrum is reproduced from [77]. The Raman spectrum of CsPhen with 633 nm excitation contains peaks with differing intensity from those with 532 nm excitation (with same centre frequency), because the visibly green material exhibits resonance enhancement for absorption in red. The benefit of considering the Raman spectra with 532 nm excitation throughout the thesis is the higher number of appearing peaks.

It is necessary to note that various attempts to synthesise lithium and sodium phenanthrides in THF were made, however all of them were unsuccessful. The deep olive-green coloration of the THF solution was observed when reacting equimolar amounts of phenanthrene and lithium or sodium metal, signalling the appearance of phenanthride anions. Moreover, the reaction proceeded to completion, because no lithium or sodium metal remained in the left hand side after filtering the solution into the right hand side of the reaction vessel. However, upon layering the olive green solution with *n*-hexane, some tiny crystal-like material of metallic colour started to form on the walls of the reaction vessel and the dark olive-green solution started to become colourless. After isolation, a mixture of white and metal-like powder was observed under the microscope. The diffractogram of that mixture of powders corresponds to pristine phenanthrene. We believe that the coordination strength of THF is not sufficient to form or retain the small cations (lithium and sodium) in the crystal structure. Perhaps by using multidentate ligands, *e.g.* DME, diglyme, triglyme,

crown ethers, or aprotic coordinating solvents containing, e.g. nitrogen, phosphorus or sulphur, we would be able to grow single crystals of lithium/sodium phenanthrides.

Finally I would like to conclude that the results presented in this work form only a small part in the puzzle, which is building in this exciting and promising research topic of alkali-metal reduction chemistry of PAHs. However, every new finding is an extremely valuable piece of information on the path towards the understanding of this topic. Despite the fact that we did not manage to synthesise materials which would exhibit superconducting behaviour we found a variety of interesting magnetic behaviours in these materials. By taking into account the vast number of known PAHs it can be concluded that there are numerous possibilities and combinations in synthesising alkali-metal reduced PAHs with potentially intriguing magnetic and electronic properties. I believe that all the research done on this topic is just a scratch of the surface and we can only start to imagine what this field is capable of offering.

5 Bibliography

[1] IUPAC. *Nomenclature of Organic Chemistry: Blue Book*, IUPAC Publications, Pergamon Press, Oxford, 1979.

[2] Wasserfallen, D.; Kastler, M.; Pisula, W.; Hofer, W. A.; Fogel, Y.; Wang, Z. H.; Müllen, K., Suppressing Aggregation in a Large Polycyclic Aromatic Hydrocarbon. *J. Am. Chem. Soc.* (2006), **128**, 1334-1339.

[3] Dötz, F.; Brand, J. D.; Ito, S.; Gherghel, L.; Müllen, K., Synthesis of Large Polycyclic Aromatic Hydrocarbons: Variation of Size and Periphery. *J. Am. Chem. Soc.* (2000), **122**, 7707-7717.

[4] Tomović, Ž.; Watson, M. D.; Müllen, K., Superphenalene-Based Columnar Liquid Crystals. *Angew. Chem. Int. Ed.* (2004), **43**, 755-758.

[5] Kekulé, A., Sur la constitution des substances aromatiques. *Bull. Soc. Chim. Fr.* (1865), **3**, 98-110.

[6] Kekulé, A., Ueber einige Condensationsproducte des Aldehyds. *Ann. Chem.* (1872), **162**, 77-124.

[7] Rocke, A. J., It Began with a Daydream: The 150th Anniversary of the Kekulé Benzene Structure. *Angew. Chem. Int. Ed.* (2015), **54**, 46-50.

[8] Randić, M., Aromaticity of Polycyclic Conjugated Hydrocarbons. *Chem. Rev.*(2003), **103**, 3449-3605.

[9] Schleyer, P. von R.; Jiao, H., What is aromaticity? *Pure Appl. Chem.* (1996), **68**, 209-218.

[10] El-Basil, S., Additivity of resonance energy in benzenoid hydrocarbons. *Int. J. Quantum Chem.* (1981), **19**, 593-609.

[11] Alexandru T. Balaban, A. T., Using Clar sextets for two- and three-dimensional aromatic systems. *Phys. Chem. Chem. Phys.* (2011), **13**, 20649-20658.

[12] Firouzi, R., The degeneracy of the Hessian eigenvalues of the π-electron density: A new manifestation of aromaticity. *Chem. Phys. Lett.* (2014), **595**, 48-54.

[13] Poranne, R. G.; Amnon Stanger, A., Magnetic criteria of aromaticity. *Chem. Soc. Rev.* (2015),

44, 6597-6615.

[14] Clar, E., *The Aromatic Sextet, Chapter 6*. J. Wiley & Sons, London, 1972.

[15] Rieger, R.; Müllen, K., Forever young: polycyclic aromatic hydrocarbons as model cases for structural and optical studies. *J. Phys. Org. Chem.* (2010), **23**, 315-325.

[16] Rivera-Figueroa, A. M.; Ramazan, K. A.; Finlayson-Pitts, B. J., Fluorescence, Absorption, and Excitation Spectra of Polycyclic Aromatic Hydrocarbons as a Tool for Quantitative Analysis. J. Chem. Educ. (2004), **81**, 242-245.

[17] Draine, B. T., Interstellar Dust Grains. *Annu. Rev. Astron. Astrophys.* (2003), **41**, 241-289.

[18] Tiekink, E. R. T.; Zukerman-Schpector, J., *The Importance of Pi-Interactions in Crystal Engineering: Frontiers in Crystal Engineering, Chapter 4*. J. Wiley & Sons, 2012.

[19] Hunter, C. A.; Sanders, J. K. M., The Nature of π-π Interactions. *J. Am. Chem. Soc.* (1990), **112**, 5525-5534.

[20] Waters, M. L., Aromatic interactions in model systems. *Curr. Opin. Chem. Biol.* (2002), **6**, 736-741.

[21] Desiraju, G. R.; Gavezzotti, A., Crystal Structures of Polynuclear Aromatic Hydrocarbons. Classification, Rationalization and Prediction from Molecular Structure. *Acta Cryst.* (1989), **B45**, 473-482.

[22] Guijarro, A.; Vergés, J. A.; San-Fabián, E.; Chiappe, G.; Louis, E., Herringbone Pattern and CH–π Bonding in the Crystal Architecture of Linear Polycyclic Aromatic Hydrocarbons. *ChemPhysChem* (2016), **17**, 3548-3557.

[23] Herrmann, A.; Müllen, K., From Industrial Colorants to Single Photon Sources

and Biolabels: The Fascination and Function of Rylene Dyes. *Chem. Lett.* (2006), **35**, 978-985.

[24] Chen, Z.; Stepanenko, V.; Dehm, V.; Prins, P.; Siebbeles, L. D. A.; Seibt, J.; Marquetand, P.; Engel, V.; Würthner, F., Photoluminescence and Conductivity of Self-Assembled π–π Stacks of

Perylene Bisimide Dyes. *Chem. Eur. J.* (2007), **13**, 436-449.

[25] Dorlars, A.; Schellhammer, C.; Schroeder, J., Heterocycles as Structural Units in New Optical Brighteners. *Angew. Chem. Internat. Edit.* (1975), **14**, 665-679.

[26] Adam, D.; Schuhmacher, P.; Simmerer, J.; Häussling, L.; Siemensmeyer, K.; Etzbachi, K. H.; Ringsdorf, H.; Haarer, D., Fast photoconduction in the highly ordered columnar phase of a discotic liquid crystal. *Nature* (1994), **371**, 141-143.

[27] Kumar, S., Self-organization of disc-like molecules: chemical aspects. *Chem. Soc. Rev.* (2006), **35**, 83-109.

[28] Feng, X.; Marcon, V.; Pisula, W.; Hansen, M. R.; Kirkpatrick, J.; Grozema, F.; Andrienko, D.; Kremer, K.; Müllen, K., Towards high charge-carrier mobilities by rational design of the shape and periphery of discotics. *Nat. Mater.* (2009), **8**, 421-426.

[29] Wu, J.; Pisula, W.; Müllen, K., Graphenes as Potential Material for Electronics. *Chem. Rev.* (2007), **107**, 718-747.

[30] Anthony, J. E., The Larger Acenes: Versatile Organic Semiconductors. *Angew. Chem. Int. Ed.* (2008), **47**, 452-483.

[31] Guo, X.; Baumgarten, M.; Müllen, K., Designing π-conjugated polymers for organic electronics. *Prog. Polym. Sci.* (2013), **38**, 1832-1908.

[32] Cui, X.; Xiao, C.; Zhang, L.; Li, Y.; Wang, Z., Polycyclic aromatic hydrocarbons with orthogonal tetraimides as n-type semiconductors. *Chem. Commun.* (2016), **52**, 13209-13212.

[33] Bian, L.; Zhu, E.; Tang, J.; Tang, W.; Zhang, F., Recent progress in the design of narrow bandgap conjugated polymers for high-efficiency organic solar cells. *Prog. Polym. Sci.* (2012), **37**, 1292-1331.

[34] Osella, S.; Narita, A.; Schwab, M. G.; Hernandez, Y.; Feng, X.; Müllen, K.; David Beljonne, D., Graphene Nanoribbons as Low Band Gap Donor Materials for Organic Photovoltaics: Quantum Chemical Aided Design. *ACS Nano* (2012), **6**, 5539-5548.

[35] Wang, C.; Dong, H.; Hu, W.; Liu, Y.; Zhu, D., Semiconducting π-Conjugated Systems in Field-Effect Transistors: A Material Odyssey of Organic Electronics. *Chem. Rev.* (2012), **112**, 2208-2267.

[36] Zhou, K.; Dong, H.; Zhang, H.; Hu, W., High performance n-type and ambipolar small organic semiconductors for organic thin film transistors. *Phys. Chem. Chem. Phys.* (2014), **16**, 22448-22457.

[37] Saleh, M.; Park, Y.; Baumgarten, M.; Kim, J.; Müllen, M., Conjugated Triphenylene Polymers for Blue OLED Devices. *Macromol. Rapid Commun.* (2009), **30**, 1279-1283.

[38] Kamtekar, K. T.; Monkman, A. P.; Bryce. M. R., Recent Advances in White Organic Light-Emitting

Materials and Devices (WOLEDs). *Adv. Mater.* (2010), **22**, 572-582.

[39] Xue, J. Y.; Izumi, T.; Yoshii, A.; Ikemoto, K.; Koretsune, T.; Akashi, R.; Arita, R.; Taka, H.; Kita, H.; Sato, S.; Isobe, H., Aromatic hydrocarbon macrocycles for highly efficient organic light-emitting devices with singlelayer architecture. *Chem. Sci.* (2016), 7, 896-904.

[40] Molecules Get Wired. *Science* (2001), **294**, 2442-2443.

[41] Blum, A. S.; Kushmerick, J. G.; Long, D. P.; Patterson, C. H.; Yang, J. C.; Henderson, J. C.; Yao, Y.; Tour, J. M.; Shashidhar, R.; Ratna, B. R., Molecularly inherent voltage-controlled conductance switching. *Nat. Mater.* (2005), **4**, 167-172.

[42] Haiss, W.; Wang, C.; Grace, I.; Batsanov, A. S.; Schiffrin, D. J.; Higgins, S. J.; Bryce, M. R.; Lambert, C. J.; Nichols, R. J., Precision control of single-molecule electrical junctions. *Nat. Mater.* (2006), **5**, 995-1002.

[43] Davidson, R.; Al-Owaedi, O. A.; Milan, D. C.; Zeng, Q.; Tory, J.; Hartl, F.; Higgins, S. J.; Nichols, R. J.; Lambert, C. J.; Low, P. J., Effects of Electrode–Molecule Binding and Junction Geometry on the Single-Molecule Conductance of bis-2,2':6',2''-Terpyridine-based Complexes. *Inorg. Chem.* (2016), **55**, 2691-2700.

[44] Santiago Marqués-González, S. M.; Low, P. J., Molecular Electronics: History and Fundamentals. *Aust. J. Chem.* (2016), **69**, 244-253.

[45] Pott, P., "Chirurgical Observations" (1775), Reprinted in *National Cancer Inst. Monogr* (1963), **10**, 7-13.

[46] Baird, W. M.; Hooven, L. A.; Mahadevan, B., Carcinogenic Polycyclic Aromatic Hydrocarbon-DNA

Adducts and Mechanism of Action. *Environ. Mol. Mutagen.* (2005), **45**, 106-114

[47] Boström, C. E.; Gerde, P.; Hanberg , A.; Jernström, B.; Johansson, C.; Kyrklund, T.; Rannug, A.; Törnqvist, M.; Victorin, V.; Westerholm, R., Cancer Risk Assessment, Indicators, and Guidelines for

Polycyclic Aromatic Hydrocarbons in the Ambient Air. *Environ. Health Perspect*. (2002), **110**, 451-488.

[48] Dipple, A., Polycyclic Aromatic Hydrocarbon Carcinogenesis. *ACS Symposium Series* (1985), **283**, 1-17.

[49] Xue, W.; Warshawsky, D., Metabolic activation of polycyclic and heterocyclic aromatic hydrocarbons and DNA damage: A review. *Toxicol. Appl. Pharmacol.* (2005), **206**, 73-93.

[50] Nebert, D. W.; Dalton, T. P.; Okey, A. B.; Gonzalez, F. J., Role of Aryl Hydrocarbon

Receptor-mediated Induction of the CYP1 Enzymes in Environmental Toxicity and Cancer. *J. Biol. Chem*. (2004), **279**, 23847-23850.

[51] Pradhan, P.; Tirumala, S.; Liu, X.; Sayer, J.M.; Jerina, D.M.; Yeh, H.J., Solution structure of a trans-opened (10S)-dA adduct of (+)-(7S,8R,9S,10R)-7,8-dihydroxy-9,10-epoxy-7,8,9,10 tetrahydrobenzo[a]pyrene in a fully complementary DNA duplex: evidence for a major syn conformation. *Biochemistry* (2001), **40**, 5870-5881.

[52] Ramesh, A.; Walker, S. A.; Hood, D. B.; Guillén, M. D.; Schneider, K.; Weyand, E. H., Bioavailability and Risk Assessment of Orally Ingested Polycyclic Aromatic Hydrocarbons. *Int. J. Toxicol.* (2004), **23**, 301-333.

[53] Ramesh, A.; Archibong, A. E.; Hood, D. B.; Guo, Z.; Loganathan, B. G., *Global Environmental*

Distribution and Human Health Effects of Polycyclic Aromatic Hydrocarbons. CRC Press (2011), 97-126.

[54] Luch, A., *The Carcinogenic Effects of Polycyclic Aromatic Hydrocarbons*. Imperial College Press, London, 2005.

[55] Schlenk, W.; Appenrodt, J.; Michael, A.; Thal, A., Über Metalladditionen an mehrfache Bindungen. *Ber. Dtsch. Chem. Ges.* (1914), **47**, 473-490.

[56] Schlenk, W., Methoden Org. Chem. *Houben-Weyl* (1924), **4**, 720-978.

[57] Tidwell, T. T., Wilhelm Schlenk: The Man Behind the Flask. *Angew. Chem. Int. Ed.* (2001), **40**, 331-337.

[58] Wooster, C. B.; Smith, F. B., The Reduction of Naphthalene by Alkali Metals in Liquid Ammonia. *J. Am. Chem. Soc.* (1931), **53**, 179-187.

[59] Wooster, C. B., Organo-alkali Compounds. *Chem. Rev.* (1932), **11**, 1-91.

[60] Scott, N. D.; Walker, J. F.; Hansley, V. L., Sodium Naphthalene. I. A New Method for the Preparation of Addition Compounds of Alkali Metals and Polycyclic Aromatic Hydrocarbons. *J. Am. Chem. Soc.* (1936), **58**, 2442-2444.

[61] Paul, D. E.; Lipkin, D.; Weissman, S. I., Reaction of Sodium Metal with Aromatic Hydrocarbons. *J. Am. Chem. Soc.* (1956), **78**, 116-120.

[62] Bergman, I., The polarography of polycyclic aromatic hydrocarbons; the relationship between their half-wave potentials and absorption spectra. *Trans. Faraday Soc.* (1956), **52**, 690-696.

[63] Shida, T.; Iwata, S., Electronic spectra of ion radicals and their molecular orbital interpretation. III. Aromatic hydrocarbons. *J. Am. Chem. Soc.* (1973), **95**, 3473-3483.

[64] Holy, N. L., Reactions of the radical anions and dianions of aromatic hydrocarbons. *Chem. Rev.* (1974), **74**, 243-277.

[65] Jensen, B. S.; Parker, V. D., Reactions of aromatic anion radicals and dianions. II. Reversible reduction of anion radicals to dianions. *J. Am. Chem. Soc.* (1975), **97**, 5211-5217.

[66] Ashby, E. C.; Goel, A. B.; DePriest, R. N.; Prasad, H. S., Metal hydride reductions via single electron transfer. 2. Evidence for an electron transfer pathway in the reactions of simple and complex metal hydrides of the main group metals with polynuclear hydrocarbons. *J. Am. Chem. Soc.* (1981), **103**, 973-975.

[67] Stevenson, G. R.; Wiedrich, C. R.; Zigler, S. S.; Echegoyen, L.; Maldonado, R., The thermochemistry of solid naphthalene anion salts and their interaction with water. *J. Phys. Chem.* (1983), **87**, 4995-4998.

[68] Birch, A. J., The reduction of organic compounds by metal-ammonia solutions. *Q. Rev. Chem. Soc.* (1950), **4**, 69-93.

[69] Smith, J. D., Organometallic compounds of the heavier alkali metals. *Adv. Organomet. Chem*. 1999, **43**, 267–348.

[70] Zabula, A. V., Petrukhina, M. A.; Structural perspective on aggregation of alkali metal ions with charged planar and curved carbon π-surfaces. *Adv. Organomet. Chem.* 2013, **61**, 375–462.

[71] A. Scott, T. A.; Ooro, B. A.; Collins, D. J.; Shatruk, M.; Yakovenko, A.; Dunbarc, K. R.; and Zhou, H. C., After 118 years, the isolation of two common radical anion reductants as simple, stable solids. *Chem. Commun.* (2009), 65-67.

[72] Bock, H.; Gharagozloo-Hubmann, K.; Sievert, M.; Prisner, T.; Havlas, Z., Single crystals of an ionic anthracene aggregate with a triplet ground state. *Nature* (2000), **404**, 267-269.

[73] Hebard, A. F.;Rosseinsky, M. J.; Haddon, R. C.; Murphy, D. W.; Glarum, S. H.; Palstra, T. T. M.; Ramirez, A. P.; Kortan, A. R., Superconductivity at 18 K in potassium-doped C_{60}. *Nature* (1991), **350**, 600-601.

[74] Mori, T.; Ikehata, S., ESR study on potassium doped pentacene. *Solid State Commun.* (1997), **101**, 213-218.

[75] Devos, A.; Lannoo, M., Electron-phonon coupling for aromatic molecular crystals: Possible consequences for their superconductivity. *Phys. Rev. B* (1998) **58**, 8236-8239.

[76] Mitsuhashi, R.; Suzuki, Y.; Yamanari, Y.; Mitamura, H.; Kambe, T.; Ikeda, N.;

Okamoto, H.; Fujiwara, A.; Yamaji, M.; Kawasaki, N.; Maniwa, Y.; Kubozono, Y., Superconductivity in alkali-metal-doped picene. *Nature* (2010), **464**, 76-79.

[77] Wang, X. F.; Liu, R. H.; Gui, Z.; Xie, Y.L.; Yan, Y. J.; Ying, J. J.; Luo, X. G.; Chen, X. G., Superconductivity at 5 K in alkali-metal-doped phenanthrene. *Nat. Commun.* (2011), **2:507**, 1-7.

[78] Kubozono, Y.; Mitamura, H.; Lee, X.; He, X.; Yamanari, Y.; Takahashi, Y.; Suzuki, Y.; Kaji, Y.; Eguchi, R.; Akaike, K.; Kambe, T.; Okamoto, H.; Fujiwara, A.; Kato, T.; Kosugig, T.; Aoki, H., Metal-intercalated aromatic hydrocarbons: a new class of carbon-based superconductors. *Phys. Chem. Chem. Phys.* (2011) **13**, 16476–16493.

[79] Xue, M.; Cao, T.; Wang, D.; Wu, Y.; Yang, H.; Dong, X.; He, J.; Li, F.; Chen, G. F., Superconductivity above 30 K in alkali-metal-doped hydrocarbon. *Sci. Rep.* (2012), **2:389**.

[80] Artioli, G. A.; Hammerath, F.; Mozzati, M, C.; Carretta, P.; Corana, F.; Mannucci, B.; Margadonna, S.; Malavasi, L., Superconductivity in Sm-doped [n]phenacenes (n = 3, 4, 5). *Chem. Commun.* (2015), **51**, 1092-1095.

[81] Wang, X. F.; Yan, Y. J.; Gui, Z.; Liu, R. H.; Ying, J. J.; Luo, X. G.; Chen, X. H., Superconductivity in $A_{1.5}$phenanthrene (A=Sr,Ba). *Phys. Rev. B* (2011) **84**, 214523-214524.

[82] Hillesheim, D.; Gofryk, K.; Sefat, A. S., On the nature of filamentary superconductivity in metal-doped hydrocarbon organic materials. *Nov. Supercond. Mater.* (2014), **1**, 12-14.

[83] Nakagawa, T.; Yuan, Z.; Zhang, J.; Yusenko, K. V.; Drathen, C.; Liu, Q.; Margadonna, S.; Jin, C., Structure and magnetic property of potassium intercalated pentacene: observation of superconducting phase in $K_xC_{22}H_{14}$. *J. Phys.: Condens. Matter* (2016) 28, 484001.

[84] Wang, R. S.; Gao, Y.; Huang, Z. B.; Chen, X. J., Superconductivity above 120 kelvin in a chain link molecule. arXiv:1703.06641v1 (2017).

[85] Kosugi, T.; Miyake, T.; Ishibashi, S.; Arita, R.; Aoki, H., Ab initio electronic structure of solid coronene: Differences from and commonalities to picene. *Phys. Rev. B* (2011) **84**, 020507-020511.

[86] Naghavi, S. S.; Fabrizio, M.; Qin, T.; Tosatti, E., Electron-doped organics: Charge disproportionate insulators and Hubbard-Fröhlich metals, *Phys. Rev. B* (2013) **88**, 115106-115114.

[87] Yan, X.; Huang, Z,; Lin, H., Van der Waals density functional study of the structural and electronic properties of La-doped phenanthrene. *J. Chem. Phys.* (2013) **139**, 204709.

[88] Naghavi, S. S.; Tosatti, E., Crystal structure search and electronic properties of alkali-doped phenanthrene and picene. *Phys. Rev. B* (2014) **90**, 075143-075151.

[89] Yan, X.; Huang, Z.; Lin, H., Identification of the crystal structures of two superconducting phases for potassium-doped picene. arXiv:1407.0747 (2014).

[90] Yan, X.; Wang, Y.; Gao, M.; Ma, D.; Huang, Z., Magnetic and Electronic Properties of Samarium-Doped Phenanthrene from First-Principles Study. *J. Phys. Chem. C* (2016), **120**, 22565–22570.

[91] Yan, X.; Zhang, C.; Zhong, G.; Ma, D.; Gao, M., The atomic structures and electronic properties of potassium-doped phenanthrene from a first-principles study. *J. Mater. Chem. C* (2016), **4**, 11566-11571.

[92] Kubozono, Y.; Goto, H.; Jabuchi, T.; Yokoya, T.; Kambe, T.; Sakai, Y.; Izumi, M.; Zheng, L.; Hamao, S.; Nguyen, H. L. T.; Sakata, M.; Kagayama, T.; Shimizu, K., Superconductivity in aromatic hydrocarbons. Physica C (2015), 514, 199-205.

[93] Tanigaki, K.; Ebbesen, T. W.; Saito, S.; Mizuki, J.; Tsai, J. S.; Kubo, Y.; Kuroshima, S., Superconductivity at 33 K in $Cs_xRb_yC_{60}$. *Nature* (1991), **352**, 222-223.

[94] Kortan, A. R.; Kopylov, N.; Glarium, S. H.; Gyorgy, E. M.; Ramirez, A. P.; Fleming, R. M.; Haddon, R. C., Superconductivity in barium fulleride. *Nature* (1992), **360**, 566-568.

[95] Kortan, A. R.; Kopylov, N.; Özdas, E.; Ramirez, A. P.; Fleming, R. M.; Haddon, R. C., Strontium doped fullerite compounds. *Chem. Phys. Lett.* (1994), **5-6**, 501-505.

[96] Ganin, A. Y.; Takabayashi, Y.; Khimyak, Y. Z.; Margadonna, S.; Tamai, A.; Rosseinsky, M. J.; Prassides, K., Bulk superconductivity at 38 K in a molecular system. *Nature Materials* (2008), **7**, 367-371.

[97] Takabayashi, Y.; Ganin, A. Y.; Jeglic, P.; Arcon, D.; Takano, T.; Iwasa, Y.; Ohishi, Y.; Takata, M.; Takashita, N.; Prassides, K.; Rosseinsky, M. J., The disorder-free non-BCS superconductor Cs_3C_{60} emerges from an antiferromagnetic insulator parent state. *Science* (2009), **323**, 1585-1590.

[98] Zadik, R. H.; Takabayashi, Y.; Klupp, G.; Colman, R. H.; Ganin, A. Y.; Potočnik, A.; Jeglič, P.; Arčon, D.; Matus, P.; Kamarás, K.; Kasahara, Y.; Iwasa, Y.; Fitch, A. N.; Ohishi, Y.; Garbarino, G.; Kato, K.; Rosseinsky, M. J.; Prassides, K., Optimized unconventional superconductivity in a molecular Jahn-Teller metal. *Sci. Adv.* (2015), 1:e1500059.

[99] Hannay, N. B.; Geballe, T. H.; Matthias, B. T.; Andres, K.; Schmidt, P.; MacNair, D., Superconductivity in Graphitic Compounds. *Phys. Rev. Lett.* (1965), **14**, 225-226.

[100] Weller, T. E.; Ellerby, M.; Saxena, S. S.; Smith, R. P.; Skipper, N. T., Superconductivity in the intercalated graphite compounds C_6Yb and C_6Ca. *Nature Physics* (2005), **1**, 39-41.

[101] Phan, Q. T. N.; Heguri, S.; Tanabe, Y.; Shimotani, H.; Tanigaki, K., Systematic Study of the Electronic States in Electron-Doped Polyacenes. *Eur. J. Inorg. Chem.* (2014), 4033–4038.

[102] Phan, Q. T. N.; Heguri, S.; Tanabe, Y.; Shimotani, H.; Nakano, T.; Nozue, Y.; Tanigaki, K., Tuning of the ground state in electron doped anthracene. *Dalton Trans.* (2014), **43**, 10040-10045.

[103] Phan, Q. T. N.; Heguri, S.; Tamura, H.; Nakano, T.; Nozue, Y.; Tanigaki, K., Two different ground states in K-intercalated polyacenes. *Phys. Rev. B* (2016) **93**, 075130-075136.

[104] Phan, Q. T. N.; Oikawa, S.; Heguri, S.; Matsuda, Y.; Tanigaki, K., Crossover from localized to itinerant states in hydrocarbon Mott insulators. *Dalton Trans.* (2017), **46**, 6715-6722.

[105] Romero, F. D.; Pitcher, M. J.; Hiley, C. I.; Whitehead, G. F. S.; Kar, S.; Ganin, A. Y.; Antypov, D.; Collins, C.; Dyer, M. S.; Klupp, G.; Colman, R. H.; Prassides, K.; Rosseinsky, M. J., Redox-controlled potassium intercalation into two polyaromatic hydrocarbon solids. *Nat. Chem.* (2017), 9, 644-652.

[106] Petřiček, V.; Císařova, I.; Hummel, L.; Kroupa, J.; Březina, B., Orientational Disorder in Phenanthrene. Structure Determination at 248, 295, 339 and 344 K. *Acta Cryst.* (1990), **B46**, 830-832.

[107] Jenny Pickworth Glusker, J. P.; Kenneth N. Trueblood, K. N., *Crystal Structure Analysis, A Primer, Third Edition. IUCr, Oxford University Press*, 2010.

[108] Massa, W., *Crystal Structure Determination*. Springer-Verlag Berlin Heidelberg, 2004.

[109] Hammond, C., *The basics of crystallography and diffraction, Third Edition.* IUCr, Oxford University Press*, 2009.

[110] Clegg, W., *Crystal Structure Analysis, Principles and Practice, Second Edition.* IUCr, Oxford University Press, 2009.

[111] Kittel, C., *Introduction to Solid State Physics. 8th Edition.* John Wiley & Sons, 2005.

[112] Clegg, W., *X-Ray Crystallography, Second Edition*. Oxford University Press*, 2015.

[113]] Le Bail, A.; Duroy, H.; Fourquet, J. L., Ab-initio structure determination of $LiSbWO_6$ by X-ray powder diffraction. *Mater. Res. Bull.*, (1988), **23**, 447-452.

[114] Rietveld, H. M., A profile refinement method for nuclear and magnetic structures. *J. Appl. Cryst.* (1969), **2**, 65-71.

[115] Young, R. A., *Introduction to the Rietveld Method, in The Rietveld Method*. Oxford University Press, 1995.

[116] Altomare, A.; Caliandro, R.; Cuocci, C.; Giacovazzo, C.; Moliterni, A. G. G.; Rizzi, R.; Platteau, C., Direct methods and simulated annealing: a hybrid approach for powder diffraction data. *J. Appl. Cryst.* (2008), **41**, 56-61.

[117] Dolomanov, O. V.; Bourhis, L. J.; Gildea, R. J.; Howard, J. A. K.; Puschmann, H., OLEX2: a complete structure solution, refinement and analysis program. *J. Appl. Cryst.* (2009), **42**, 339-341.

[118] Sheldrick, G. M., SHELXT - Integrated space-group and crystal-structure determination. *Acta Cryst.* (2015), **A71**, 3-8.

[119] Altomare, A.; Cuocci, C.; Giacovazzo, C.; Moliterni, A.; Rizzi, R.; Corriero, N.; Falcicchio, A., EXPO2013: a kit of tools for phasing crystal structures from powder data. *J. Appl. Crystallogr.* (2013), **46**, 1231-1235.

[120] Coelho, A. A., *TOPAS Academic: General Profile and Structure Analysis Software for Powder Diffraction Data, 5th edition*. Bruker AXS, Karlsruhe, Germany, 2012.

[121] Boultif, A.; Louer, D., Powder pattern indexing with the dichotomy method. *J. Appl. Cryst.* (2004), **37**, 724-731.

[122] Altomare, A.; Giacovazzo, C.; Guagliardi, A.; Moliterni, A. G. G.; Rizzi, R.; Werner, P. E., New techniques for indexing: N-TREOR in EXPO. *J. Appl. Cryst.* (2000), **33**, 1180-1186.

[123] Blundell, S., *Magnetism in Condensed Matter*, Oxford University Press, 2001.

[124] Landee, C. P.; Turnbull, M. M., Review: A gentle introduction to magnetism: units, fields, theory, and experiment. *J. Coord. Chem.* (2014), **67**, 375-439.

[125] Pratt, F. L.; Baker, P. J.; Blundell, S. J.; Lancaster, T.; Ohira-Kawamura, S.; Baines, C.; Shimizu, Y.; Kanoda, K.; Watanabe, I.; Saito, G., Magnetic and non-magnetic phases of a quantum spin liquid. *Nature* (2011), **471**, 612-616.

[126] Zhou, D. H.; Choi, E. S.; Li, G.; Balicas, L.; Weibe, C. R.; Qui, Y.; Copley, J. R. D.; Gardner, J. S., Spin liquid state in the S = 1/2 triangular lattice $Ba_3CuSb_2O_9$. *Phys. Rev. Lett.* (2011), **106**, 147204-147208.

[127] Han, T. H.; Helton, J. H.; Chu, S.; Nocera, D. G.; Rodriguez-Rivera, J. A.; Broholm, C.; Lee, Y. S, Fractionalized excitations in the spin-liquid state of a kagome-lattice antiferromagnet. *Nature* (2012), 492, 406-410.

[128] Okamoto, Y.; Yoshida, H.; Hiroi, Z., Vesignieite $BaCu_3V_2O_8(OH)_2$ as a Candidate Spin-1/2 Kagome Antiferromagnet. *J. Phys. Soc. Jpn.* (2009), **78**, 033701-033705.

[129] Balents, L., Spin liquids in frustrated magnets. *Nature* (2010) **464**, 199-208.

[130] Blundell, S. J.; Pratt, F. L., Organic and molecular magnets. *J. Phys.: Condens. Matter* (2004), **16**, 771-828.

[131] Blundell, S. J., Molecular magnets. *Contemp. Phys.* (2007), **48**, 275-290.

[132] Lancaster, T.; Blundell, S. J.; Pratt, F. L.; *Phys. Scr.* (2013), **88**, 068506-068516.

[133] *Magnetic Property Measurement System MPMS XL, Hardware Reference Manual.* Quantum Design, San Diego, CA, 1996.

[134] Bonner, J. C.; Fisher, M. E.; Linear magnetic chains with anisotropic coupling; *Phys. Rev.* (1964), **135**, A640-A658.

[135] Johnston, D. C.; Kremer, R. K.; Troyer, M.; Wang, X.; Klümper, A.; Bud'ko, S. L.; Panchula, A. F.; Canfield, P. C.; Thermodynamics of spin S = ½ antiferromagnetic uniform and alternating-exchange Heisenberg chains. *Phys. Rev. B* (2000), **61**, 9558-9606.

[136] Zabula, A.V.; Sumner, N. J.; Filatov, A. S.; Spisak, S. N.; Grigoryants, V. M.; Petrukhina, M. A., Reshaping rubrene by controlled reduction with alkali metals. *Eur. J. Inorg. Chem*. (2012), **29**, 4675-4683.

[137] Spisak, S. N.; Sumner, N. J.; Zabula, A. V.; Filatov, A. S.; Rogachev, A. Y.; Petrukhina, M. A., Tuning binding of rubidium ions to planar and curved negatively charged p surfaces. *Organometallics* (2013), **32**, 3773-3779.

[138] Neander, S.; Tio, F. E.; Buschmann, R.; Behrens, U.; Olbrich, F., Cyclopentadienyl, indenyl, fluorenyl, and pentamethylcyclopentadienyl complexes of potassium with 18-crown-6. *J. Organomet. Chem.* (1999), **582**, 58-65.

[139] Neander, S.; Behrens, U.; Olbrich, F., Novel 18-crown-6 organometallic rubidium and cesium complexes containing cyclopentadienyl, indenyl, pentamethylcyclopentadienyl, and fluorenyl as carbanions. *J. Organomet. Chem.* (2000), **604**, 59-67.

[140] Neander, S.; Körnich, J.; Olbrich, F., Novel fluorenyl alkali metal DIGLYME complexes: synthesis and solid state structures. *J. Organomet. Chem.* (2002), **656**, 89-96.

[141] Hoffmann, D.; Hampel, F.; von Ragué Schleyer, P.; Fluorenylrubidium N, N, N', N'', N''-pentamethyldiethylenetriamine: a square-wave-like polymeric chain in the solid state. *J. Organomet. Chem.* (1993), **456**, 13-17.

[142] Spisak, S. N.; Zabula, A. V.; Filatov, A. S.; Rogachev, A. Y.; Petrukhina, M. A., Selective endo and exo binding of alkali metals to corannulene. Angew. *Chem. Int. Ed.* (2011), **50**, 8090-8094.

[143] Bienenstock, A.; Burley G. J., Thermal expansion of silver iodide. *Phys. Chem. Solids* (1963), **24**, 1271-1278.

[144] Barrera, G. D.; Bruno J. A. O.; Barron T. H. K.; Allan N. L., Negative thermal expansion. *J. Phys. Condens. Matter* (2005), **17**, R217-R252.

[145] Evans, J. S. O., Negative thermal expansion materials. *J. Chem. Soc., Dalton Trans.* (1999), **19**, 3317-3326.

[146] Chan, C. T.; Ho, K. M.; Kamitakahara, W. A.; Zone-center phonon frequencies for graphite and graphite intercalation compounds: Charge-transfer and intercalate-coupling effects; *Phys. Rev. B* (1987), **36**, R3499-R3502.

[147] Kuzmany, H.; Matus, M.; Burger, B.; Winter, J.; Raman Scattering in C_{60} fullerenes and fullerides; *Adv. Mater*. (1994), *6*, 731-745.

[148] Kamarás, K.; Hadjiev, V. G.; Thomsen, C.; Pekker, S.; Fodor-Csorba, K.; Faigel, G.; Tegze, M.; Infrared and raman spectra of $C_{60} \cdot n$-pentane clathrate crystals; *Chem. Phys. Lett.* (1993), **202**, 325-329.

[149] Huang, Q.; Zhong, G.; Zhang, J.; Xiao-Miao Zhao, X.; Zhang, C.; Lin, H.; and Chen, X., Constraint on the potassium content for the superconductivity of potassium-intercalated phenanthrene. *J. Chem. Phys.* (2014) **140**, 114301-114306.

[150] Štefančič, A.; Klupp, G.; Yufit, D. S.; Potočnik, A.; Arčon, D.; Prassides, K., Rubidium Phenanthrenide: a Molecular Canted Antiferromagnet. *To be submitted.*

[151] Bock, H.; Gharagozloo-Hubmann, K.; Holl, S.; Sievert, M., The influence of alkaline metal reduction potentials on the formation of their contact ion multiples with tetracene and decacyclene polyanions. *Z. Naturforsch.* (2000), **55**, 1163-1178.

[152] Näther, C.; Bock, H.; Havlas, Z.; Hauck, T., Solvent-shared and solvent-separated ion multiples of perylene radical anions and dianions: an exemplary case of alkali metal cation solvation. *Organometallics*. (1998), **17**, 4707-4715.

[153] Janiak, C.; Hemling, H., Coronene-potassium$(THF)_2$(tmeda): X-ray structure and MNDO calculations of a half-sandwich contact ion pair as a model for potassium (adsorbate)-graphite surface interactions. *Chem. Ber*. (1994), **127**, 1251-1253.

[154] Jordan, V.; Behrens, U.; Olbrich, F.; Weiss. E,; Metal alkyl and aryl compounds. LV. Cyclopentadienyl and indenyl compounds of potassium and sodium. *J. Organomet. Chem.* (1996), **517**, 81-88.

[155] Michel, R.; Nack, T.; Neufeld, R.; Dieterich, J. M.; Mata, R. A.; Stalke, D., The layered structure of $[Na(NH_3)_4]$[Indenide] containing a square-planar $Na(NH_3)_4^+$ cation. *Angew. Chem. Int. Ed*. (2013), **52**, 734-738.

[156] Dinnebier, R. E.; Neander, S.; Behrens, U.; Olbrich, F., Solid-state structures of base-free indenyllithium and fluorenylsodium. Organometallics. (1999), **18**, 2915-2918.

[157] Zerger, R.; Rhine, W.; Stucky, G. D., π groups inion pair bonding. The effect of the cation on the structural and spectroscopic properties of fluorenyl ion pairs. *J. Am. Chem. Soc.* (1974), **96**, 5441-5448.

[158] Liu, Y.; Ballweg. D.; Müller, T.; Guzei, I. A.; Clark, R. W.; West, R., Chemistry of the aromatic 9-germafluorenyl dianion and some related silicon and carbon species. *J. Am. Chem. Soc.* (2002), **124**, 12174-12181.

[159] Arriola, D. J.; Bokota, M.; Campbell Jr, R. E.; Klosin, J.; LaPointe, R. E.; Redwine, O. D.; Shankar, R. B.; Timmers, F. B.; Abboud, K. A., Penultimate effect in ethylene-styrene copolymerization and the discovery of highly active ethylene-styrene catalysts with increased styrene reactivity. *J. Am. Chem. Soc.* (2007), **129**, 7065-7076.

[160] Zabula, A. V.; Spisak, S. N.; Filatov, A. S.; Grigoryants, V. M.; Petrukhina, M. A., How charging corannulene with one and two electrons affects its geometry and aggregation with sodium and potassium cations. *Chem. Eur J.* (2012), **18**, 6476-6484.

[161] Spisak, S. N.; Wie, Z.; O'Neil, N. J.; Rogachev, A. Y.; Amaya, T.; Hirao, T.; Petrukhina M. A., Convex and Concave Encapsulation of Multiple Potassium Ions by Sumanenyl Anions. *J. Am. Chem. Soc.* (2015), **137**, 9768-9771.

[162] Zabula, A. V.; Filatov, A. S.; Xia, J.; Jasti, R.; Petrukhina M. A., Tightening of the nanobelt upon multielectron reduction. *Angew. Chem. Int. Ed.* (2013), **52**, 5033-5036.

[163] Rosokha, S. V.; Kochi, J. K., The question of aromaticity in open-shell cations and anions as ion-radical offsprings of polycyclic aromatic and antiaromatic hydrocarbons. *J. Org. Chem.* (2006), **71**, 9357-9365.

[164] Spisak, S. N.; Zabula, A. V.; Filatov, A. S.; Petrukhina, M. A.; Self-assembly of charged corannulene with cesium ions: Always in the bowl. *J. Organomet. Chem.* (2015), **784**, 69-74.

[165] Takabayashi, Y.; Menelaou, M.; Tamura, H.; Takemori, N.; Koretsune, T.; Štefančič, A.; Klupp, G.; Buurma, A. J. C.; Nomura, Y.; Arita, R.; Arčon, D.; Rosseinsky, M. J.; Prassides, K.; π-electron S =½ quantum spin-liquid state in anionic polyaromatic hydrocarbon; *Nat. Chem.* (2017), **9**, 635-643.

[166] Dougherty, D. A.; Ma, J. C., The Cation-π Interaction. *Chem. Rev.* (1997), **97**, 1303-1324.

[167] Amicangelo, J. C.; Armentrout, P. B., Absolute Binding Energies of Alkali-Metal Cation Complexes with Benzene Determined by Threshold Collision-Induced Dissociation Experiments and ab Initio Theory. *J. Phys. Chem. A.* (2000), **104**, 1142-11432.

[168] M. M. Gromiha, M. M.; Santhosh, C.; Ahmad, S., Structural analysis of cation-π interactions in DNA binding proteins. *Int. J. Biol. Macromol.* (2004), **34**, 203–211.

[169] Tsuzuki, S.; Yoshida, M.; Uchimaru, T.; Mikami, M., The Origin of the Cation/π Interaction: The Significant Importance of the Induction in Li+and Na+Complexes. *J. Phys. Chem. A.* (2001) ,**105**, 769-773.

[170] Mecozzi, S.; West, A. P.; Dougherty, D. A., Cation-π Interactions in Simple Aromatics: Electrostatics Provide a Predictive Tool. *J. Am. Chem. Soc.* (1996), **118**, 2307–2308.

[171] Wheeler, S. E.; Houk, K. N., Substituent Effects in Cation/π Interactions and Electrostatic Potentials above the Center of Substituted Benzenes Are Due Primarily to through-Space Effects of the Substituents. *J. Am. Chem. Soc.* (2009), **131**, 3126-3127.

[172] Brocchieri, L.; Karlin, S., Geometry of interplanar residue contacts in protein structures. *Proc. Natl. Acad. Sci. USA.* (1994), **91**, 9297-9301.

[173] Gallivan, J. P.; Dougherty, D. A., A Computational Study of Cation–π Interactions vs Salt Bridges in Aqueous Media: Implications for Protein Engineering. *J. Am*. *Chem*. *Soc*. (2000), **122,** 870-874.

[174] Marshall, M. S.; Steele, R. P.; Thanthiriwatte, K. S.; Sherrill, C. D., Potential Energy Curves for Cation–π Interactions: Off-Axis Configurations Are Also Attractive. *J. Phys*. *Chem*. *A*. (2009), **113**, 13628-13632.

[175] Dinnebier, R. E.; Behrens, U.; Olbrich, F., Solid State Structures of Cyclopentadienyllithium, -sodium, and -potassium. Determination by High-Resolution Powder Diffraction. *Organometallics* (1997), **16**, 3855-3858.

[176] Dinnebier, R. E.; Olbrich, F.; Bendele, G. M., Cyclopentadienylcaesium by High-Resolution X-ray Powder Diffraction. *Acta Cryst.* (1997), **C53**, 699-701.

[177] Jost, W.; Adam, M.; Enkelmann, V.; Miillen, K., The Crystal Structure of [(Pyrene$^{\bullet-}$){Na$^+$[(C$_2$H$_5$)$_2$O]}] : A Model for Stacked Radical Anion Salts. *Angew. Chem. Inr. Ed. Engl.* (1992), **31**, 878-879.

[178] Janiak, C., A Second Modification of Potassium Fluorenide and the Structure of Potassium 9-tert-Butylfluorenide: Effect of Crystallization Conditions and Substituents on Solid-state Contact Ion Pair Interactions. *Chem. Bet.* (1993), **126**, 1603- 1607.

[179] Štefančič, A.; Klupp, G.; Knaflič, T.; Yufit, D. S.; Tavčar, G.; Potočnik, A.; Beeby, A.; Arčon, A., Triphenylide-based molecular solid – a new candidate for a quantum spin-liquid compound. *J. Phys*. *Chem*. *C*. (2017), **121**, 14864-14871.

[180] Bock, H.; Naether, C.; Rupper, K.; Havlas, Z., Tetraphenylbutadiene disodium dimethoxyethane: solvent-shared and solvent-separated ion triples within a single crystal. *J. Am. Chem. Soc.* (1992), **114**, 6907–6908.

[181] Heguri, S.; Phan, Q. T. N.; Tanabe, Y.; Tanigaki, K., Thermodynamics and existing phase of Ba-phenanthrene. *Phys. Rev. B* (2014) **90**, 134519-134526.

[182] Heguri, S.; Kobayashi, M.; Tanigaki, K., Questioning the existence of superconducting potassium doped phases for aromatic hydrocarbons. *Phys. Rev. B* (2015) **92**, 014502-014510.

6 Appendix

6.1 [{Rb$^+$(THF)$_{0.5}$}(C$_{14}$H$_{10}$)] at 120K

Table 20: Basic refinement information.

Empirical formula	Rb(C$_{14}$H$_{10}$)(C$_4$H$_8$O)$_{0.5}$
Formula weight (g/mol)	299.74
Temperature (K)	120
Crystal system	orthorhombic
Space group	*Fdd*2
a (Å)	17.3215(13)
b (Å)	26.4735(19)
c (Å)	11.1807(9)
α (°)	90.00
β (°)	90.00
γ (°)	90.00
Volume/Å^3	5127.0(7)
Z	16
ρ$_{calc}$ (mg/mm^3)	1.553
m/mm^{-1}	3.841
F(000)	2416.0
Crystal size (mm^3)	0.2 × 0.2 × 0.1
Radiation	MoKα (λ = 0.71073 Å)
2Θ range for data collection	4.6 to 55.98°
Index ranges	-22 ≤ h ≤ 22, -34 ≤ k ≤ 34, -14 ≤ l ≤ 14
Reflections collected	15466
Independent reflections	3102 [R$_{int}$ = 0.0993, R$_{sigma}$ = 0.0732]
Data/restraints/parameters	3102/1/157
Goodness-of-fit on F^2	1.017
Final R indexes [I>=2σ (I)]	R$_1$ = 0.0636, wR$_2$ = 0.1460
Final R indexes [all data]	R$_1$ = 0.0823, wR$_2$ = 0.1587
Largest diff. peak/hole (e Å^{-3})	1.45/-0.52
Flack parameter	0.093(19)

Table 21: Fractional atomic coordinates, isotropic displacement parameters and occupancy.

Atom	x	y	z	U_{eq} (Å^2)	N
Rb1	0.39890(3)	0.56037(2)	0.47417(9)	0.0461(2)	1
O3	0.5000	0.5000	0.3290(5)	0.0524(17)	1
C15A	0.5573(10)	0.5207(7)	0.2522(14)	0.056(4)	0.5
C15B	0.5405(7)	0.5372(5)	0.2530(9)	0.031(2)	0.5
C16A	0.5489(8)	0.5048(5)	0.1364(10)	0.038(2)	0.5
C16B	0.5234(12)	0.5251(7)	0.1352(15)	0.066(4)	0.5
C1	0.5545(4)	0.3623(2)	0.6919(8)	0.060(2)	1
C2	0.5811(4)	0.3801(3)	0.7974(8)	0.0593(19)	1
C3	0.5421(4)	0.4174(2)	0.8593(7)	0.0519(16)	1
C4	0.4761(4)	0.4390(2)	0.8098(6)	0.0423(13)	1
C5	0.3403(3)	0.4875(2)	0.6913(6)	0.0420(15)	1
C6	0.2743(4)	0.5077(3)	0.6398(6)	0.0506(16)	1
C7	0.2470(4)	0.4869(3)	0.5335(6)	0.0536(17)	1
C8	0.2833(4)	0.4465(2)	0.4837(8)	0.0534(16)	1
C9	0.3894(5)	0.3837(2)	0.4807(8)	0.0537(17)	1
C10	0.4565(5)	0.3642(3)	0.5310(7)	0.0563(19)	1
C11	0.4869(4)	0.3822(2)	0.6388(6)	0.0460(15)	1
C12	0.4483(3)	0.42286(19)	0.7001(5)	0.0383(13)	1
C13	0.3794(4)	0.44599(19)	0.6438(5)	0.0357(11)	1
C14	0.3510(4)	0.4242(2)	0.5333(6)	0.0444(14)	1
H15A	0.6030	0.4983	0.2494	0.068	0.5
H15B	0.5738	0.5543	0.2816	0.068	0.5
H15C	0.5913	0.5468	0.2866	0.037	0.5
H15D	0.5091	0.5680	0.2395	0.037	0.5
H16A	0.5792	0.4734	0.1477	0.045	0.5
H16B	0.5677	0.5241	0.665	0.045	0.5
H16C	0.5629	0.5259	0.712	0.080	0.5
H16D	0.4895	0.5551	0.1284	0.080	0.5
H1	0.5817	0.3359	0.6527	0.071	1
H2	0.6275	0.3667	0.8297	0.071	1
H3	0.5602	0.4283	0.9353	0.062	1
H4	0.4499	0.4651	0.8517	0.051	1
H5	0.3598	0.5026	0.7622	0.050	1
H6	0.2482	0.5352	0.6765	0.061	1
H7	0.2029	0.5010	0.4957	0.064	1
H8	0.2626	0.4326	0.4123	0.064	1
H9	0.3695	0.3692	0.4093	0.064	1
H10	0.4826	0.3376	0.4907	0.068	1

Table 22: Atom to atom bond distances.

Atoms	Bond length (Å)	Atoms	Bond length (Å)
O3- C15A[1]	1.422(17)	C4-C12	1.385(9)
O3- C15A	1.422(17)	C5-C6	1.386(9)
O3- C15B[1]	1.479(11)	C5-C13	1.395(8)
O3-C15B	1.479(11)	C6-C7	1.392(10)
C15A-C16B	1.44(2)	C7-C8	1.360(11)
C15B-C16A	1.568(16)	C8-C14	1.425(10)
C16A-C16A[1]	1.71(3)	C9-C10	1.390(12)
C16B-C16B[1]	1.56(3)	C9-C14	1.393(9)
C1-C2	1.351(12)	C10-C11	1.400(11)
C1-C11	1.414(11)	C11-C12	1.441(8)
C2-C3	1.383(11)	C12-C13	1.482(9)
C3-C4	1.392(9)	C13-C14	1.450(9)

Table 23: Bond angles.

Atoms	Bond angle (°)	Atoms	Bond angles (°)
C15A[1]-O3-C15A	105.7(13)	C8-C7-C6	120.2(7)
C15A-O3-C15B	20.8(7)	C7-C8-C14	123.1(7)
C15A-O3-C15B[1]	104.0(8)	C10-C9-C14	121.0(8)
C15A[1]-O3-C15B	104.0(8)	C9-C10-C11	122.5(6)
C15A[1]-O3-C15B[1]	20.8(7)	C1-C11-C12	117.6(7)
C15B[1]-O3-C15B	109.9(9)	C10-C11-C1	123.2(6)
O3-C15A-C16B	107.2(13)	C10-C11-C12	119.3(6)
O3-C15B-C16A	98.9(8)	C4-C12-C11	119.3(5)
C15B-C16A-C16A[1]	89.4(9)	C4-C12-C13	121.9(5)
C15A-C16B-C16B[1]	98.2(12)	C11-C12-C13	118.8(6)
C2-C1-C11	121.3(7)	C5-C13-C12	123.7(5)
C1-C2-C3	121.3(7)	C5-C13-C14	118.2(6)
C2-C3-C4	119.7(7)	C14-C13-C12	118.1(5)
C12-C4-C3	120.7(6)	C8-C14-C13	116.5(6)
C6-C5-C13	123.0(6)	C9-C14-C8	123.2(7)
C5-C6-C7	118.9(6)	C9-C14-C13	120.3(7)

6.2 [{Rb$^+$(THF)$_{0.5}$}(C$_{14}$H$_{10}$)] at 290K

Table 24: Basic refinement information.

Empirical formula	Rb(C$_{14}$H$_{10}$)(C$_4$H$_8$O)$_{0.5}$
Formula weight (g/mol)	299.74
Temperature (K)	290
Crystal system	orthorhombic
Space group	Fdd2
a (Å)	17.2193(16)
b (Å)	27.184(3)
c (Å)	11.2850(11)
α (°)	90.00
β (°)	90.00
γ (°)	90.00
Volume/Å^3	5282.3(9)
Z	16
ρ$_{calc}$ (mg/mm^3)	1.508
m/mm^{-1}	3.728
F(000)	2416.0
Crystal size (mm^3)	0.2 × 0.2 × 0.1
Radiation	MoKα (λ = 0.71073 Å)
2Θ range for data collection	4.56 to 55.98^o
Index ranges	-22 ≤ h ≤ 22, -34 ≤ k ≤ 34, -14 ≤ l ≤ 14
Reflections collected	16866
Independent reflections	3177 [R$_{int}$ = 0.1004, R$_{sigma}$ = 0.0813]
Data/restraints/parameters	3177/1/157
Goodness-of-fit on F^2	0.962
Final R indexes [I>=2σ (I)]	R$_1$ = 0.0643, wR$_2$ = 0.1503
Final R indexes [all data]	R$_1$ = 0.1274, wR$_2$ = 0.1861
Largest diff. peak/hole (e Å^{-3})	0.88/-0.32
Flack parameter	0.11(2)

Table 25: Fractional atomic coordinates, isotropic displacement parameters and occupancy.

Atom	x	y	z	U_{eq} (Å^2)	N
Rb1	0.59875(4)	0.56078(3)	0.27408(13)	0.0967(3)	1
O3	0.5000	0.5000	0.4244(7)	0.097(2)	1
C15A	0.5571(10)	0.4796(6)	0.4980(15)	0.079(4)	0.5
C15B	0.5356(11)	0.4606(7)	0.4990(15)	0.087(5)	0.5
C16A	0.5456(11)	0.4950(7)	0.6117(16)	0.089(4)	0.5
C16B	0.5208(11)	0.4715(7)	0.6135(15)	0.093(5)	0.5
C1	0.5525(8)	0.6375(4)	0.568(16)	0.131(5)	1
C2	0.5786(8)	0.6208(5)	-0.435(16)	0.136(4)	1
C3	0.5426(6)	0.5828(3)	-0.1015(12)	0.120(3)	1
C4	0.4776(5)	0.5616(3)	-0.517(9)	0.093(2)	1
C5	0.3405(4)	0.5138(3)	0.654(8)	0.086(2)	1
C6	0.2743(5)	0.4939(4)	0.1158(9)	0.104(3)	1
C7	0.2464(7)	0.5137(5)	0.2191(11)	0.120(3)	1
C8	0.2828(7)	0.5529(4)	0.2691(12)	0.126(4)	1
C9	0.3883(9)	0.6159(4)	0.2709(14)	0.125(4)	1
C10	0.4539(9)	0.6345(4)	0.2194(11)	0.126(4)	1
C11	0.4849(6)	0.6189(3)	0.1154(11)	0.106(3)	1
C12	0.4473(4)	0.5779(2)	0.548(8)	0.085(2)	1
C13	0.3788(5)	0.5548(2)	0.1122(7)	0.0799(19)	1
C14	0.3508(6)	0.5751(3)	0.2203(8)	0.097(3)	1
H15A	0.6017	0.5024	0.5056	0.095	0.5
H15B	0.5761	0.4481	0.4647	0.095	0.5
H15C	0.5857	0.4486	0.4672	0.104	0.5
H15D	0.5000	0.4326	0.5134	0.104	0.5
H16A	0.5643	0.4775	0.6830	0.107	0.5
H16B	0.5772	0.5248	0.5963	0.107	0.5
H16C	0.5589	0.4668	0.6782	0.111	0.5
H16D	0.4824	0.4444	0.6130	0.111	0.5
H1	0.5800	0.6637	0.935	0.157	1
H2	0.6237	0.6352	-0.774	0.163	1
H3	0.5623	0.5712	-0.1751	0.143	1
H4	0.4529	0.5350	-0.916	0.112	1
H5	0.3608	0.4989	-0.42	0.103	1
H6	0.2485	0.4670	0.793	0.125	1
H7	0.2016	0.5000	0.2556	0.144	1
H8	0.2619	0.5662	0.3401	0.152	1
H9	0.3681	0.6306	0.3408	0.150	1
H10	0.4799	0.6604	0.2596	0.151	1

Table 26: Atom to atom bond distances.

Atoms	Bond length (Å)	Atoms	Bond length (Å)
O3- C15A[1]	1.401(17)	C4-C12	1.383(13)
O3- C15A	1.401(17)	C5-C6	1.384(12)
O3- C15B[1]	1.495(17)	C5-C13	1.399(10)
O3-C15B	1.495(17)	C6-C7	1.370(15)
C15A-C16B	1.46(3)	C7-C8	1.360(17)
C15B-C16A	1.59(3)	C8-C14	1.428(16)
C16A-C16A[1]	1.59(4)	C9-C10	1.366(19)
C16B-C16B[1]	1.71(3)	C9-C14	1.406(15)
C1-C2	1.300(18)	C10-C11	1.358(18)
C1-C11	1.431(19)	C11-C12	1.460(12)
C2-C3	1.371(17)	C12-C13	1.485(12)
C3-C4	1.380(13)	C13-C14	1.423(13)

Table 27: Bond angles.

Atoms	Bond angle (°)	Atoms	Bond angles (°)
C15A[1]-O3-C15A	107.3(14)	C8-C7-C6	119.9(12)
C15A-O3-C15B	103.7(9)	C7-C8-C14	123.3(11)
C15A-O3-C15B[1]	25.2(8)	C10-C9-C14	119.9(12)
C15A[1]-O3-C15B	25.2(8)	C9-C10-C11	125.2(10)
C15A[1]-O3-C15B[1]	103.7(9)	C1-C11-C12	114.5(12)
C15B[1]-O3-C15B	111.4(14)	C10-C11-C1	127.5(12)
O3-C15A-C16B	106.8(12)	C10-C11-C12	118.0(11)
O3-C15B-C16A	94.1(12)	C4-C12-C11	119.0(8)
C15B-C16A-C16A[1]	89.6(14)	C4-C12-C13	122.9(6)
C15A-C16B-C16B[1]	92.4(12)	C11-C12-C13	118.1(9)
C2-C1-C11	124.1(12)	C5-C13-C12	123.1(8)
C1-C2-C3	121.5(12)	C5-C13-C14	118.3(8)
C2-C3-C4	119.2(12)	C14-C13-C12	118.6(7)
C12-C4-C3	121.7(8)	C8-C14-C13	116.4(9)
C6-C5-C13	122.9(8)	C9-C14-C8	123.6(11)
C5-C6-C7	119.1(9)	C9-C14-C13	120.0(11)

6.3 [{K⁺(THF)$_{0.5}$}(C$_{14}$H$_{10}$)] at 295K

Table 28: Basic refinement information.

Empirical formula	$K(C_{14}H_{10})(C_4H_8O)_{0.5}$
Formula weight (g/mol)	253.37
Temperature (K)	295
Crystal system	orthorhombic
Space group	*Fdd*2
a (Å)	16.9460(3)
b (Å)	27.2106(3)
c (Å)	11.12572(19)
α (°)	90.00
β (°)	90.00
γ (°)	90.00
Volume/Å^3	5130.19(13)
Z	16
Radiation	Synchrotron (λ = 0.39959(4) Å)
2Θ range of refined data (°)	2 - 13
R_p	5.357
R_{wp}	7.649
R_{exp}	3.757
χ^2	4.145
Background model	Chebyshev polynomial (20 parameters)
Zero	-0.00003(3)°
Scale	0.0000005937
Profile shape function	Pearson VII
U	0.0246(6)
V	0.001789990
W	0.0000774(13)
beta0	0.99(10)
beta 1	-0.2(8)
beta2	2.5(14)
asymmetry	-0.222(15)

Table 29: Fractional atomic coordinates, isotropic temperature factors and occupancy.

Atom	x	y	z	B_{iso} (Å^2)	N
K1	0.0942(3)	0.5636(2)	-0.2259(2)	5.9(3)	1
O3	0.0000	0.5000	-0.0756	2.6(9)	1
C15A	0.0571	0.4796	-0.0020	5.7(3)	0.5
C15B	0.0356	0.4606	-0.0010	5.7(3)	0.5
C16A	0.0456	0.4950	0.1117	5.7(3)	0.5
C16B	0.0208	0.4715	0.1135	5.7(3)	0.5
C1	0.5525	0.6375	0.0568	5.7(3)	1
C2	0.5786	0.6208	-0.0435	5.7(3)	1
C3	0.5426	0.5828	-0.1015	5.7(3)	1
C4	0.4776	0.5616	-0.0517	5.7(3)	1
C5	0.3405	0.5138	0.0654	5.7(3)	1
C6	0.2743	0.4939	0.1158	5.7(3)	1
C7	0.2464	0.5137	0.2191	5.7(3)	1
C8	0.2828	0.5529	0.2691	5.7(3)	1
C9	0.3883	0.6159	0.2709	5.7(3)	1
C10	0.4539	0.6345	0.2194	5.7(3)	1
C11	0.4849	0.6189	0.1154	5.7(3)	1
C12	0.4473	0.5779	0.0548	5.7(3)	1
C13	0.3788	0.5548	0.1122	5.7(3)	1
C14	0.3508	0.5751	0.2203	5.7(3)	1
H15A	0.1017	0.5024	0.0056	8	0.5
H15B	0.0761	0.4481	-0.0353	8	0.5
H15C	0.0857	0.4486	-0.0328	8	0.5
H15D	0.0000	0.4326	0.0134	8	0.5
H16A	0.0643	0.4775	0.1830	8	0.5
H16B	0.0772	0.5248	0.0963	8	0.5
H16C	0.0589	0.4668	0.1782	8	0.5
H16D	-0.0176	0.4444	0.1130	8	0.5
H1	0.5800	0.6637	0.0935	8	1
H2	0.6237	0.6352	-0.0774	8	1
H3	0.5623	0.5712	-0.1751	8	1
H4	0.4529	0.5350	-0.0916	8	1
H5	0.3608	0.4989	-0.0042	8	1
H6	0.2485	0.4670	0.0793	8	1
H7	0.2016	0.5000	0.2556	8	1
H8	0.2619	0.5662	0.3401	8	1
H9	0.3681	0.6306	0.3408	8	1
H10	0.4799	0.6604	0.2596	8	1

Table 30: Atom to atom bond distances.

Atoms	Bond length (Å)	Atoms	Bond length (Å)
O3-C15A[1]	1.38381	C4-C12	1.36540
O3-C15A	1.38381	C5-C6	1.36607
O3-C15B[1]	1.48398	C5-C13	1.39176
O3-C15B	1.48398	C6-C7	1.35450
C15A-C16B	1.44162	C7-C8	1.35192
C15B-C16A	1.57388	C8-C14	1.40981
C16A-C16A[1]	1.56925	C9-C10	1.34916
C16B-C16B[1]	1.70369	C9-C14	1.39760
C1-C2	1.28350	C10-C11	1.33977
C1-C11	1.41192	C11-C12	1.45093
C2-C3	1.36299	C12-C13	1.46642
C3-C4	1.36126	C13-C14	1.40596

Table 31: Bond angles.

Atoms	Bond angle (°)	Atoms	Bond angles (°)
K1-O3-C15A	101.3	C5-C13-C12	123.4
O3-C15A-C16B	106.9	C5-C13-C14	118.5
C2-C1-C11	123.7	C6-C7-C8	120.2
C1-C2-C3	121.7	C7-C8-C14	123.5
C1-C11-C10	127.1	C8-C14-C9	123.8
C1-C11-C12	114.7	C8-C14-C13	115.9
C2-C3-C4	119.4	C10-C9-C14	120.1
C3-C4-C12	121.3	C9-C10-C11	124.8
C4-C12-C11	119.2	C9-C14-C13	120.2
C4-C12- C13	122.4	C10-C11-C12	118.2
C6-C5- C13	123.2	C11-C12-C13	118.3
C5-C6- C7	118.5	C12-C13-C14	118.1

6.4 [{Cs$^+$(THF)$_{0.5}$}(C$_{14}$H$_{10}$)] at 120K

Table 32: Basic refinement information.

Empirical formula	Cs(C$_{14}$H$_{10}$)(C$_4$H$_8$O)$_{0.5}$
Formula weight (g/mol)	347.18
Temperature (K)	120.0
Crystal system	monoclinic
Space group	*Cc*
a (Å)	10.6212(7)
b (Å)	25.0224(15)
c (Å)	20.1555(12)
α (°)	90.00
β (°)	92.284(2)
γ (°)	90.00
Volume/Å^3	5352.4(6)
Z	16
ρ$_{calc}$ (mg/mm^3)	1.723
m/mm^{-1}	2.747
F(000)	2704.0
Crystal size (mm^3)	0.77 × 0.55 × 0.28
Radiation	MoKα (λ = 0.71073 Å)
2Θ range for data collection	4.56 to 60°
Index ranges	-14 ≤ h ≤ 14, -35 ≤ k ≤ 35, -28 ≤ l ≤ 28
Reflections collected	41609
Independent reflections	15447 [R$_{int}$ = 0.0628, R$_{sigma}$ = 0.0662]
Data/restraints/parameters	15447/2/631
Goodness-of-fit on F^2	0.995
Final R indexes [I>=2σ (I)]	R$_1$ = 0.0373, wR$_2$ = 0.0736
Final R indexes [all data]	R$_1$ = 0.0479, wR$_2$ = 0.0770
Largest diff. peak/hole (e Å^{-3})	1.52/-0.56
Flack parameter	0.005(12)

Table 33: Fractional atomic coordinates, isotropic displacement parameters and occupancy.

Atom	x	y	z	U_{eq} (Å^2)	N
Cs1	0.496563(19)	0.615337(12)	0.409985(12)	0.02935(6)	1
Cs2	0.50454(2)	0.777826(13)	0.292898(13)	0.03619(7)	1
Cs3	0.99044(2)	0.538813(11)	0.268908(12)	0.02763(6)	1
Cs4	0.99116(2)	0.704723(11)	0.142438(12)	0.02901(6)	1
O1	0.10125(3)	0.58394(14)	0.12729(14)	0.0386(8)	1
C1S	0.9089(5)	0.5572(2)	0.961(3)	0.0496(13)	1
C2S	0.9411(6)	0.5544(3)	0.242(2)	0.0596(17)	1
C3S	0.10807(5)	0.5469(2)	0.266(2)	0.0510(14)	1
C4S	0.11234(5)	0.5709(3)	0.919(3)	0.0570(16)	1
O2	0.5248(4)	0.53711(16)	0.5323(2)	0.0602(11)	1
C5S	0.4195(6)	0.5080(3)	0.5544(3)	0.0643(17)	1
C6S	0.4392(5)	0.4495(3)	0.5381(3)	0.0581(16)	1
C7S	0.5710(6)	0.4489(3)	0.5131(3)	0.0611(16)	1
C8S	0.6254(5)	0.5015(2)	0.5384(3)	0.0540(15)	1
C1	0.8138(4)	0.73071(18)	0.2924(2)	0.0299(10)	1
C2	0.8154(5)	0.7790(2)	0.2588(3)	0.0388(12)	1
C3	0.7539(5)	0.7823(2)	0.1964(3)	0.0437(13)	1
C4	0.6932(5)	0.7387(2)	0.1689(2)	0.0395(12)	1
C5	0.6369(4)	0.6428(2)	0.1729(2)	0.0323(10)	1
C6	0.6350(4)	0.59459(19)	0.20659(19)	0.0298(10)	1
C7	0.6856(4)	0.54032(17)	0.3079(2)	0.028(1)	1
C8	0.7428(4)	0.53515(19)	0.3694(2)	0.0324(11)	1
C9	0.8046(4)	0.5786(2)	0.3991(2)	0.0304(10)	1
C10	0.8080(4)	0.62751(19)	0.3662(2)	0.0250(9)	1
C11	0.7519(3)	0.63386(17)	0.30275(18)	0.0222(8)	1
C12	0.7556(3)	0.68502(18)	0.26690(19)	0.0234(8)	1
C13	0.6939(4)	0.6886(2)	0.2015(2)	0.0296(10)	1
C14	0.6884(4)	0.58918(17)	0.2713(2)	0.0244(9)	1
C1A	0.9013(5)	0.40553(18)	0.1187(2)	0.0359(10)	1
C2A	0.10063(5)	0.4065(2)	0.800(2)	0.0391(11)	1
C3A	0.11241(5)	0.4126(2)	0.1100(3)	0.0418(12)	1
C4A	0.11376(5)	0.41539(19)	0.1778(3)	0.0406(11)	1
C5A	0.10470(5)	0.4122(2)	0.2892(2)	0.0405(11)	1
C6A	0.9426(6)	0.40911(19)	0.3287(2)	0.0429(13)	1
C7A	0.7119(6)	0.39912(19)	0.3391(3)	0.0443(13)	1
C8A	0.5931(5)	0.3975(2)	0.3111(3)	0.0494(14)	1
C9A	0.5724(5)	0.4023(2)	0.2434(3)	0.0464(13)	1
C10A	0.6754(4)	0.40635(19)	0.2033(2)	0.0367(11)	1
C11A	0.7997(5)	0.40686(17)	0.2296(2)	0.0342(10)	1
C12A	0.9103(4)	0.40840(17)	0.1881(2)	0.0296(9)	1
C13A	0.10334(5)	0.41169(18)	0.2197(2)	0.0334(10)	1
C14A	0.8194(5)	0.40452(18)	0.3006(2)	0.0362(11)	1
C1B	0.3189(4)	0.6705(2)	0.1993(2)	0.0294(9)	1
C2B	0.3212(4)	0.7175(2)	0.1645(2)	0.0347(11)	1
C3B	0.2621(5)	0.7633(2)	0.1880(2)	0.0399(11)	1
C4B	0.2022(4)	0.7618(2)	0.2471(2)	0.0361(11)	1
C5B	0.1375(4)	0.7112(2)	0.3451(2)	0.0381(11)	1

C6B	0.1353(4)	0.6651(2)	0.3812(2)	0.0411(12)	1
C7B	0.1912(4)	0.5699(2)	0.3984(2)	0.0366(12)	1
C8B	0.2503(4)	0.5241(2)	0.3775(2)	0.0382(11)	1
C9B	0.3100(4)	0.5245(2)	0.3174(2)	0.0336(10)	1
C10B	0.3117(4)	0.5694.4(19)	0.2787(2)	0.0292(10)	1
C11B	0.2542(4)	0.6180.9(18)	0.2992(2)	0.0268(9)	1
C12B	0.2569(4)	0.66660(18)	0.26125(19)	0.0261(9)	1
C13B	0.1986(4)	0.71408(19)	0.2847(2)	0.0298(10)	1
C14B	0.1923(4)	0.61699(19)	0.3604(2)	0.0293(10)	1
C1C	0.5776(4)	0.6833(2)	0.5488(2)	0.0363(11)	1
C2C	0.4549(5)	0.6663(2)	0.5613(2)	0.0453(13)	1
C3C	0.3529(5)	0.6938(2)	0.5327(2)	0.0467(13)	1
C4C	0.3696(5)	0.7372(2)	0.4945(2)	0.0428(13)	1
C5C	0.5122(5)	0.8056(2)	0.4511(2)	0.0464(13)	1
C6C	0.6349(6)	0.8254(2)	0.4409(2)	0.0576(16)	1
C7C	0.8651(7)	0.8150(3)	0.4522(3)	0.0660(18)	1
C8C	0.9657(6)	0.7862(3)	0.4734(3)	0.070(2)	1
C9C	0.9556(5)	0.7366(3)	0.5033(3)	0.0550(15)	1
C10C	0.8335(5)	0.7165(2)	0.5136(2)	0.0456(13)	1
C11C	0.7263(5)	0.7457(2)	0.4948(2)	0.0371(11)	1
C12C	0.5986(4)	0.72624(19)	0.5092(2)	0.0326(10)	1
C13C	0.4944(5)	0.7575(2)	0.4828(2)	0.0412(12)	1
C14C	0.7391(5)	0.7963(2)	0.4618(2)	0.0479(14)	1
H1SA	0.8315	0.5771	0.1015	0.059	1
H1SB	0.8992	0.5217	0.1145	0.059	1
H2SA	0.8988	0.5246	0.0021	0.072	1
H2SB	0.9176	0.5872	0.0011	0.072	1
H3SA	1.1187	0.5652	-0.0100	0.061	1
H3SB	1.1024	0.5093	0.0248	0.061	1
H4SA	1.1752	0.5457	0.1172	0.068	1
H4SB	1.1727	0.6029	0.0847	0.068	1
H5SA	0.3426	0.5210	0.5323	0.077	1
H5SB	0.4122	0.5126	0.6019	0.077	1
H6SA	0.4328	0.4273	0.5773	0.070	1
H6SB	0.3785	0.4373	0.5042	0.070	1
H7SA	0.5700	0.4472	0.4650	0.073	1
H7SB	0.6187	0.4188	0.5312	0.073	1
H8SA	0.6554	0.4984	0.5843	0.065	1
H8SB	0.6945	0.5129	0.5117	0.065	1
H1	0.8538	0.7288	0.3342	0.036	1
H2	0.8565	0.8085	0.2774	0.047	1
H3	0.7542	0.8144	0.1731	0.052	1
H4	0.6506	0.7422	0.1279	0.047	1
H5	0.5998	0.6449	0.1304	0.039	1
H6	0.5974	0.5651	0.1860	0.036	1
H7	0.6435	0.5111	0.2892	0.034	1
H8	0.7405	0.5026	0.3915	0.039	1
H9	0.8437	0.5750	0.4409	0.036	1
H10	0.8483	0.6564	0.3868	0.030	1
H1A	0.8218	0.4029	0.0978	0.043	1
H2A	0.9972	0.4029	0.0341	0.047	1

H3A	1.1946	0.4149	0.0842	0.050	1
H4A	1.2179	0.4199	0.1971	0.049	1
H5A	1.1271	0.4147	0.3093	0.049	1
H6A	0.9545	0.4101	0.3747	0.051	1
H7A	0.7225	0.3966	0.3850	0.053	1
H8A	0.5249	0.3932	0.3381	0.059	1
H9A	0.4908	0.4027	0.2249	0.056	1
H10A	0.6615	0.4088	0.1576	0.044	1
H1B	0.3583	0.6405	0.1825	0.035	1
H2B	0.3626	0.7190	0.1248	0.042	1
H3B	0.2633	0.7948	0.1636	0.048	1
H4B	0.1635	0.7924	0.2625	0.043	1
H5B	0.0975	0.7414	0.3608	0.046	1
H6B	0.0946	0.6653	0.4212	0.049	1
H7B	0.1500	0.5696	0.4383	0.044	1
H8B	0.2501	0.4933	0.4034	0.046	1
H9B	0.3497	0.4937	0.3033	0.040	1
H10B	0.3509	0.5683	0.2382	0.035	1
H1C	0.6459	0.6650	0.5679	0.044	1
H2C	0.4420	0.6368	0.5884	0.054	1
H3C	0.2715	0.6821	0.5401	0.056	1
H4C	0.2996	0.7545	0.4753	0.051	1
H5C	0.4426	0.8253	0.4361	0.056	1
H6C	0.6451	0.8581	0.4200	0.069	1
H7C	0.8771	0.8475	0.4309	0.079	1
H8C	1.0457	0.8002	0.4678	0.084	1
H9C	1.0270	0.7171	0.5161	0.066	1
H10C	0.8246	0.6832	0.5334	0.055	1

Table 34: Atom to atom bond distances.

Atoms	Bond length (Å)	Atoms	Bond length (Å)
O1-C1S	1.414(6)	C9A-C10A	1.389(6)
O1-C4S	1.438(6)	C10A-C11A	1.402(7)
C1S-C2S	1.505(7)	C11A-C12A	1.469(6)
C2S-C3S	1.494(8)	C11A-C14A	1.441(6)
C3S-C4S	1.502(8)	C12A-C13A	1.435(7)
O2-C5S	1.421(7)	C1B-C2B	1.369(6)
O2-C8S	1.393(6)	C1B-C12B	1.439(5)
C5S-C6S	1.518(9)	C2B-C3B	1.398(7)
C6S-C7S	1.507(8)	C3B-C4B	1.372(7)
C7S-C8S	1.516(8)	C4B-C13B	1.416(7)
C1-C2	1.385(6)	C5B-C6B	1.364(7)
C1-C12	1.388(6)	C5B-C13B	1.402(6)
C2-C3	1.397(7)	C6B-C14B	1.418(7)
C3-C4	1.372(7)	C7B-C8B	1.380(7)
C4-C13	1.417(7)	C7B-C14B	1.406(7)
C5-C6	1.384(6)	C8B-C9B	1.390(6)
C5-C13	1.409(7)	C9B-C10B	1.369(6)
C6-C14	1.408(6)	C10B-C11B	1.431(6)
C7-C8	1.364(6)	C11B-C12B	1.436(6)
C7-C14	1.429(6)	C11B-C14B	1.421(6)
C8-C9	1.394(7)	C12B-C13B	1.429(6)
C9-C10	1.392(6)	C1C-C2C	1.404(7)
C10-C11	1.399(5)	C1C-C12C	1.360(7)
C11-C12	1.471(5)	C2C-C3C	1.390(7)
C11-C14	1.439(6)	C3C-C4C	1.347(8)
C12-C13	1.451(6)	C4C-C13C	1.448(8)
C1A-C2A	1.387(7)	C5C-C6C	1.416(8)
C1A-C12A	1.398(6)	C5C-C13C	1.378(7)
C2A-C3A	1.377(7)	C6C-C14C	1.377(8)
C3A-C4A	1.371(7)	C7C-C8C	1.345(10)
C4A-C13A	1.422(7)	C7C-C14C	1.438(8)
C5A-C6A	1.392(7)	C8C-C9C	1.386(9)
C5A-C13A	1.402(6)	C9C-C10C	1.414(8)
C6A-C14A	1.410(7)	C10C-C11C	1.392(7)
C7A-C8A	1.362(8)	C11C-C12C	1.481(7)
C7A-C14A	1.412(7)	C11C-C14C	1.439(8)
C8A-C9A	1.379(8)	C12C-C13C	1.440(6)

Table 35: Bond angles.

Atoms	Bond angle (°)	Atoms	Bond angles (°)
C1S-O1-C4S	108.1(4)	C5A-C13A-C4A	122.8(5)
O1-C1S-C2S	104.3(4)	C5A-C13A-C12A	120.0(4)
C3S-C2S-C1S	103.8(4)	C6A-C14A-C7A	123.1(5)
C2S-C3S-C4S	104.0(4)	C6A-C14A-C11A	119.4(4)
O1-C4S-C3S	107.5(4)	C7A-C14A-C11A	117.5(5)
C8S-O2-C5S	104.8(4)	C2B-C1B-C12B	121.4(4)
O2-C5S-C6S	108.0(4)	C1B-C2B-C3B	120.9(4)
C7S-C6S-C5S	102.7(5)	C4B-C3B-C2B	120.0(5)
C6S-C7S-C8S	103.1(5)	C3B-C4B-C13B	120.8(5)
O2-C8S-C7S	104.2(5)	C6B-C5B-C13B	121.7(5)
C2-C1-C12	123.5(4)	C5B-C6B-C14B	122.9(4)
C1-C2-C3	118.5(5)	C8B-C7B-C14B	121.1(4)
C4-C3-C2	120.8(5)	C7B-C8B-C9B	119.2(5)
C3-C4-C13	121.5(5)	C10B-C9B-C8B	121.4(5)
C6-C5-C13	121.5(4)	C9B-C10B-C11B	121.2(4)
C5-C6-C14	121.7(4)	C10B-C11B-C12B	123.2(4)
C8-C7-C14	122.2(4)	C14B-C11B-C10B	116.9(4)
C7-C8-C9	120.1(4)	C14B-C11B-C12B	119.9(4)
C10-C9-C8	120.2(4)	C11B-C12B-C1B	122.7(4)
C9-C10-C11	121.1(4)	C13B-C12B-C1B	116.8(4)
C10-C11-C12	122.0(4)	C13B-C12B-C11B	120.5(4)
C10-C11-C14	119.3(4)	C4B-C13B-C12B	120.1(4)
C14-C11-C12	118.7(3)	C5B-C13B-C4B	122.2(4)
C1-C12-C11	123.7(4)	C5B-C13B-C12B	117.7(4)
C1-C12-C13	117.6(4)	C6B-C14B-C11B	117.2(4)
C13-C12-C11	118.6(4)	C7B-C14B-C6B	122.6(4)
C4-C13-C12	118.0(4)	C7B-C14B-C11B	120.2(4)
C5-C13-C4	122.4(4)	C12C-C1C-C2C	121.4(5)
C5-C13-C12	119.6(4)	C3C-C2C-C1C	119.2(5)
C6-C14-C7	123.0(4)	C4C-C3C-C2C	121.2(5)
C6-C14-C11	119.8(4)	C3C-C4C-C13C	121.2(5)
C7-C14-C11	117.1(4)	C13C-C5C-C6C	121.0(5)
C2A-C1A-C12A	122.5(5)	C14C-C6C-C5C	120.3(5)
C3A-C2A-C1A	119.4(4)	C8C-C7C-C14C	121.0(7)
C4A-C3A-C2A	120.1(5)	C7C-C8C-C9C	122.9(6)
C3A-C4A-C13A	122.4(5)	C8C-C9C-C10C	118.1(6)
C6A-C5A-C13A	121.2(5)	C11C-C10C-C9C	121.2(6)
C5A-C6A-C14A	121.5(4)	C10C-C11C-C12C	121.3(5)
C8A-C7A-C14A	122.1(5)	C10C-C11C-C14C	119.7(5)
C7A-C8A-C9A	121.1(5)	C14C-C11C-C12C	118.9(4)
C8A-C9A-C10A	118.9(5)	C1C-C12C-C11C	123.1(4)
C9A-C10A-C11A	122.2(5)	C1C-C12C-C13C	120.3(4)
C10A-C11A-C12A	123.2(4)	C13C-C12C-C11C	116.4(4)
C10A-C11A-C14A	118.1(4)	C5C-C13C-C4C	121.7(5)
C14A-C11A-C12A	118.7(4)	C5C-C13C-C12C	121.9(5)
C1A-C12A-C11A	122.9(4)	C12C-C13C-C4C	116.3(5)
C1A-C12A-C13A	118.2(4)	C6C-C14C-C7C	121.8(6)
C13A-C12A-C11A	118.9(4)	C6C-C14C-C11C	121.1(5)
C4A-C13A-C12A	117.2(4)	C7C-C14C-C11C	117.1(6)

198

6.5 [Cs(C$_{14}$H$_{10}$)] at 295K

Table 36: Basic refinement information.

Empirical formula	Cs$_2$(C$_{14}$H$_{10}$)$_2$
Formula weight (g/mol)	622.27
Temperature (K)	295
Crystal system	orthorhombic
Space group	$P2_12_12_1$
a (Å)	14.69611(17)
b (Å)	15.11696(17)
c (Å)	10.22027(11)
α (°)	90.00
β (°)	90.00
γ (°)	90.00
Volume/Å^3	2270.54(4)
Z	4
Radiation	CuKα (λ = 1.540560 Å)
2Θ range of refined data (^{o})	5 - 70°
R$_p$	1.950
R$_{wp}$	2.569
R$_{exp}$	2.397
χ^2	1.149
Background model	Chebyshev polynomial (20 parameters)
Zero	-0.008334901
Scale	0.000069940
Profile shape function	Pearson VII
U	0.540(3)
V	0.03582651
W	0.00884(6)
beta0	5.99(16)
beta 1	-75(3)
beta2	316.8(17)
asymmetry	-0.603(8)

Table 37: Fractional atomic coordinates, isotropic temperature factors and occupancy.

Atom	x	y	z	B_{iso} (Å^2)	N
C1	0.5533	0.5613	0.7538	1.6(1)	1
C2	0.5956	0.4884	0.6954	1.6(1)	1
C3	0.5469	0.4114	0.6739	1.6(1)	1
C4	0.4560	0.4042	0.7100	1.6(1)	1
C5	0.2651	0.3939	0.8002	1.6(1)	1
C6	0.1744	0.3929	0.8429	1.6(1)	1
C7	0.1353	0.4674	0.9020	1.6(1)	1
C8	0.1865	0.5434	0.9156	1.6(1)	1
C9	0.3302	0.6266	0.8894	1.6(1)	1
C10	0.4181	0.6298	0.8507	1.6(1)	1
C11	0.4607	0.5546	0.7925	1.6(1)	1
C12	0.4113	0.4752	0.7718	1.6(1)	1
C13	0.3169	0.4700	0.8149	1.6(1)	1
C14	0.2767	0.5456	0.8717	1.6(1)	1
H1	0.5905	0.6231	0.7722	3.2	1
H2	0.6633	0.4912	0.6648	3.2	1
H3	0.5778	0.3543	0.6236	3.2	1
H4	0.4206	0.3442	0.6902	3.2	1
H5	0.2916	0.3322	0.7603	3.2	1
H6	0.1344	0.3318	0.8316	3.2	1
H7	0.0662	0.4622	0.9323	3.2	1
H8	0.1583	0.6027	0.9640	3.2	1
H9	0.2970	0.6797	0.9332	3.2	1
H10	0.4557	0.6885	0.8680	3.2	1
C1a	-0.1743	0.3551	0.7385	1.6(1)	1
C2a	-0.1900	0.3453	0.6043	1.6(1)	1
C3a	-0.1355	0.2894	0.5308	1.6(1)	1
C4a	-0.0641	0.2426	0.5876	1.6(1)	1
C5a	0.0900	0.1519	0.7163	1.6(1)	1
C6a	0.1612	0.1093	0.7825	1.6(1)	1
C7a	0.1747	0.1220	0.9169	1.6(1)	1
C8a	0.1155	0.1757	0.9854	1.6(1)	1
C9a	-0.0175	0.2755	0.9954	1.6(1)	1
C10a	-0.0865	0.3184	0.9347	1.6(1)	1
C11a	-0.1011	0.3084	0.7976	1.6(1)	1
C12a	-0.0446	0.2521	0.7217	1.6(1)	1
C13a	0.0311	0.2065	0.7849	1.6(1)	1
C14a	0.0434	0.2176	0.9208	1.6(1)	1
H1a	-0.2165	0.3992	0.7988	3.2	1
H2a	-0.2435	0.3779	0.5578	3.2	1
H3a	-0.1486	0.2781	0.4260	3.2	1
H4a	-0.0244	0.1995	0.5281	3.2	1
H5a	0.0864	0.1416	0.6110	3.2	1
H6a	0.2079	0.0668	0.7265	3.2	1
H7a	0.2301	0.0878	0.9610	3.2	1
H8a	0.1252	0.1884	1.0909	3.2	1
H9a	-0.0042	0.2816	1.0950	3.2	1
H10a	-0.1279	0.3617	0.9906	3.2	1
Cs1	0.2527(1)	0.34720(7)	0.1164(1)	1.86(3)	1

Cs2	-0.00328(9)	-0.02343(7)	0.8874(1)	1.86(3)	1

Table 38: Atom to atom bond distances.

Atoms	Bond length (Å)	Atoms	Bond length (Å)
C1-C11	1.421144	C1a-C11a	1.421682
C1-C2	1.399118	C1a-C2a	1.398738
C10-C11	1.427743	C10a-C11a	1.425607
C10-C9	1.352188	C10a-C9a	1.353272
C11-C12	1.418794	C11a-C12a	1.419009
C12-C13	1.458050	C12a-C13a	1.459722
C12-C4	1.408138	C12a-C4a	1.407569
C13-C14	1.410937	C13a-C14a	1.410699
C13-C5	1.386995	C13a-C5a	1.386580
C14-C8	1.400198	C14a-C8a	1.400184
C14-C9	1.465763	C14a-C9a	1.465937
C2-C3	1.384152	C2a-C3a	1.385764
C3-C4	1.390507	C3a-C4a	1.391453
C5-C6	1.402984	C5a-C6a	1.402861
C6-C7	1.401336	C6a-C7a	1.401111
C7-C8	1.380546	C7a-C8a	1.380776

6.6 [{K$^+_4$(THF)}$_4$(C$_{14}$H$_{10}$)$_3$] at 120K

Table 39: Basic refinement information.

Empirical formula	K(C$_{14}$H$_{10}$)$_{0.75}$(C$_4$H$_8$O)
Formula weight (g/mol)	244.87
Temperature (K)	120
Crystal system	triclinic
Space group	*P*-1
a (Å)	12.271(3)
b (Å)	13.346(3)
c (Å)	15.313(3)
α (°)	89.455(3)
β (°)	85.581(2)
γ (°)	86.967(3)
Volume/Å^3	2496.8(10)
Z	8
ρ$_{calc}$ (mg/mm^3)	1.303
m/mm^{-1}	0.374
F(000)	1036.0
Crystal size (mm^3)	0.26 × 0.12 × 0.10
Radiation	Synchrotron (λ = 0.688900 Å)
2Θ range for data collection	2.58 to 50°
Index ranges	-15 ≤ h ≤ 15, -13 ≤ k ≤ 16, -18 ≤ l ≤ 18
Reflections collected	21229
Independent reflections	9285 [R(int) = 0.0353]
Data/restraints/parameters	9285/0/523
Goodness-of-fit on F^2	1.044
Final R indexes [I>=2σ (I)]	R$_1$ = 0.0701, wR$_2$ = 0.1877
Final R indexes [all data]	R$_1$ = 0.0893, wR$_2$ = 0.2015
Largest diff. peak/hole (e Å^{-3})	0.72/-0.39

Table 40: Fractional atomic coordinates, isotropic displacement parameters and occupancy.

Atom	x	y	z	U_{eq} (Å^2)	N
K1	0.9556(6)	0.41236(6)	0.30197(5)	0.0483(2)	1
K2	0.23517(7)	0.43861(8)	0.65044(6)	0.0647(3)	1
K3	0.53392(6)	0.11754(7)	0.79226(5)	0.0507(2)	1
K4	0.72123(6)	0.09243(6)	0.11872(5)	0.0481(2)	1
O1	0.9513(2)	0.55778(19)	0.23787(16)	0.0533(6)	1
C1S	1.0000(4)	0.6544(3)	0.2349(3)	0.0716(12)	1
C2S	1.0422(4)	0.6709(4)	0.1434(3)	0.0774(13)	1
C3S	0.9644(5)	0.6159(4)	0.0915(3)	0.0795(14)	1
C4S	0.9265(4)	0.5346(4)	0.1508(3)	0.0709(12)	1
O2A	0.2260(5)	0.4634(5)	0.1604(4)	0.0517(14)	0.5
C5SB	0.3396(7)	0.4540(8)	0.1752(6)	0.064(2)	0.5
C6SA	0.3746(7)	0.5126(7)	0.0834(5)	0.061(2)	0.5
C7SB	0.3313(10)	0.4457(10)	0.0246(8)	0.070(3)	0.5
C8SA	0.2211(8)	0.4296(8)	0.0695(6)	0.065(2)	0.5
O2B	0.2380(5)	0.4219(5)	0.1676(4)	0.0526(14)	0.5
C5SA	0.3271(6)	0.5076(7)	0.1712(5)	0.0514(17)	0.5
C6SB	0.4008(8)	0.4587(8)	0.0934(6)	0.067(2)	0.5
C7SA	0.3023(10)	0.4646(9)	0.0244(7)	0.065(3)	0.5
C8SB	0.2469(9)	0.3818(8)	0.0864(7)	0.078(3)	0.5
O3	0.54901(19)	0.0672(2)	0.24530(16)	0.0512(6)	1
C9S	0.5954(3)	0.0860(4)	0.3255(3)	0.0719(13)	1
C10S	0.5043(4)	0.1236(4)	0.3892(3)	0.0780(14)	1
C11S	0.4117(4)	0.1541(4)	0.3326(3)	0.0803(14)	1
C12S	0.4625(3)	0.1431(3)	0.2396(3)	0.0626(10)	1
O4B	0.6999(4)	0.0823(5)	0.6690(3)	0.0498(13)	0.5
C13A	0.6807(8)	0.0887(9)	0.5777(6)	0.070(2)	0.5
C13B	0.6861(6)	0.1473(6)	0.5814(4)	0.0462(16)	0.5
C14A	0.7697(8)	0.1255(10)	0.5310(7)	0.077(3)	0.5
C14B	0.7746(7)	0.0750(8)	0.5318(6)	0.058(2)	0.5
C15B	0.8670(8)	0.0761(9)	0.5822(7)	0.060(3)	0.5
C16B	0.8156(8)	0.0926(8)	0.6756(6)	0.050(3)	0.5
C1	1.0716(3)	0.1998(3)	0.1794(3)	0.0682(12)	1
C2	1.1267(4)	0.1725(4)	0.2502(4)	0.0774(14)	1
C3	1.0784(4)	0.1832(4)	0.3335(3)	0.0725(12)	1
C4	0.9712(3)	0.2243(3)	0.3458(3)	0.0557(9)	1
C5	0.7496(3)	0.3256(3)	0.3692(3)	0.0622(10)	1
C6	0.6425(4)	0.3691(4)	0.3792(4)	0.0837(15)	1
C7	0.5886(4)	0.3922(4)	0.3048(4)	0.0857(16)	1
C8	0.6372(4)	0.3737(4)	0.2233(4)	0.0794(14)	1
C9	0.7956(4)	0.3061(3)	0.1271(3)	0.0672(12)	1
C10	0.9022(4)	0.2647(3)	0.1158(2)	0.0617(11)	1
C11	0.9608(3)	0.2405(3)	0.1878(2)	0.0511(9)	1
C12	0.9118(3)	0.2556(3)	0.2757(2)	0.0449(8)	1
C13	0.8014(3)	0.3032(3)	0.2876(2)	0.0470(8)	1
C14	0.7443(3)	0.3279(3)	0.2101(3)	0.0557(9)	1
C21	0.4150(3)	0.2636(3)	0.6243(3)	0.0645(11)	1
C22	0.4675(3)	0.3280(3)	0.6766(4)	0.0705(12)	1

C23	0.4355(3)	0.3384(3)	0.7635(4)	0.0709(12)	1
C24	0.3514(3)	0.2812(3)	0.8017(3)	0.0577(9)	1
C25	0.1898(4)	0.1434(3)	0.8825(3)	0.0611(10)	1
C26	0.1073(4)	0.0856(3)	0.9183(3)	0.0755(13)	1
C27	0.0499(4)	0.0288(3)	0.8643(4)	0.0749(13)	1
C28	0.0739(3)	0.0288(3)	0.7766(3)	0.0617(11)	1
C29	0.1811(3)	0.0907(3)	0.6465(3)	0.0602(10)	1
C30	0.2660(4)	0.1461(3)	0.6098(3)	0.0614(10)	1
C31	0.3273(3)	0.2066(3)	0.6605(3)	0.0529(9)	1
C32	0.2986(3)	0.2127(3)	0.7524(2)	0.0473(8)	1
C33	0.2153(3)	0.1485(3)	0.7916(2)	0.0470(8)	1
C34	0.1565(3)	0.0886(3)	0.7357(3)	0.0491(8)	1
C49	0.6734(8)	-0.0651(7)	0.9419(6)	0.071(2)	0.5
C50	0.6050(8)	-0.1426(8)	0.9697(6)	0.074(2)	0.5
C51	0.4859(3)	-0.1209(4)	1.0043(3)	0.0501(17)	0.5
C41	0.4140(4)	-0.1941(3)	1.0315(4)	0.064(2)	0.5
C42	0.3103(3)	-0.1664(3)	1.0693(3)	0.0406(14)	0.5
C43	0.2785(3)	-0.0655(4)	1.0801(3)	0.0391(14)	0.5
C44	0.3504(3)	0.0077(3)	1.0529(3)	0.0266(11)	0.5
C52	0.4541(3)	-0.0200(3)	1.0151(3)	0.0328(12)	0.5
C54	0.6408(4)	0.0380(4)	0.9490(3)	0.0454(16)	0.5
C48	0.7091(3)	0.1143(5)	0.9227(3)	0.0483(16)	0.5
C47	0.6722(4)	0.2140(4)	0.9335(4)	0.066(2)	0.5
C46	0.5671(5)	0.2374(4)	0.9707(4)	0.085(3)	0.5
C45	0.4988(4)	0.1611(4)	0.9970(4)	0.059(2)	0.5
C53	0.5357(3)	0.0613(4)	0.9861(3)	0.0460(16)	0.5
C67	0.2824(3)	0.4811(4)	0.4222(4)	0.0600(19)	0.5
C66	0.2300(4)	0.5740(4)	0.4077(4)	0.074(2)	0.5
C65	0.1203(4)	0.5914(3)	0.4360(4)	0.0541(18)	0.5
C73	0.0630(3)	0.5159(4)	0.4789(3)	0.0453(15)	0.5
C74	0.1154(4)	0.4230(4)	0.4934(3)	0.0505(17)	0.5
C68	0.2251(4)	0.4056(4)	0.4651(4)	0.067(2)	0.5
C69	0.0523(8)	0.3446(8)	0.5340(7)	0.077(2)	0.5
C70	-0.0631(8)	0.3601(7)	0.5595(6)	0.069(2)	0.5
C71	-0.1204(3)	0.4555(3)	0.5433(3)	0.0450(15)	0.5
C72	-0.0581(2)	0.5331(3)	0.5100(3)	0.0411(14)	0.5
C64	-0.1056(3)	0.6295(3)	0.5039(3)	0.0358(13)	0.5
C63	-0.2154(3)	0.6483(3)	0.5311(3)	0.0529(17)	0.5
C62	-0.2777(3)	0.5707(4)	0.5645(3)	0.0479(16)	0.5
C61	-0.2302(3)	0.4743(3)	0.5705(3)	0.0600(19)	0.5
O4A	0.7005(4)	0.1272(4)	0.6712(3)	0.0432(12)	0.5
C16A	0.8103(9)	0.1222(9)	0.6808(7)	0.059(3)	0.5
C15A	0.8686(9)	0.1063(10)	0.5929(7)	0.067(3)	0.5

Table 41: Atom to atom bond distances.

Atoms	Bond length (Å)	Atoms	Bond length (Å)
O1-C1S	1.448(5)	C22-C23	1.364(7)
O1-C4S	1.430(5)	C23-C24	1.404(6)
C1S-C2S	1.476(7)	C24-C32	1.406(5)
C2S-C3S	1.511(7)	C25-C26	1.382(6)
C3S-C4S	1.479(6)	C25-C33	1.405(5)
O2A-C5SB	1.428(10)	C26-C27	1.383(7)
O2A-C8SA	1.474(10)	C27-C28	1.353(7)
C5SB-C6SA	1.642(12)	C28-C34	1.426(5)
C6SA-C7SB	1.423(15)	C29-C30	1.389(6)
C7SB-C8SA	1.494(15)	C29-C34	1.376(6)
O2B-C5SA	1.628(10)	C30-C31	1.410(5)
O2B-C8SB	1.353(11)	C31-C32	1.426(5)
C5SA-C6SB	1.565(12)	C32-C33	1.458(5)
C6SB-C7SA	1.664(15)	C33-C34	1.436(5)
C7SA-C8SB	1.596(15)	C49-C50	1.409(13)
O3-C9S	1.422(4)	C49-C54	1.414(10)
O3-C12S	1.435(5)	C50-C51	1.530(10)
C9S-C10S	1.496(6)	C51-C41	1.3900
C10S-C11S	1.517(6)	C51-C52	1.3900
C11S-C12S	1.516(6)	C41-C42	1.3900
O4B-C13B	1.606(9)	C42-C43	1.3900
O4B-C16B	1.445(11)	C43-C44	1.3900
C13A-C14A	1.369(14)	C44-C52	1.3900
C13A-O4A	1.567(11)	C52-C53	1.554(5)
C13B-C14B	1.569(12)	C54-C48	1.3900
C14A-C15B	1.589(15)	C54-C53	1.3900
C14B-C15A	1.613(14)	C48-C47	1.3900
C15B-C16A	1.717(15)	C47-C46	1.3900
C16B-C15A	1.393(15)	C46-C45	1.3900
C1-C2	1.359(7)	C45-C53	1.3900
C1-C11	1.434(6)	C67-C66	1.3900
C2-C3	1.370(7)	C67-C68	1.3900
C3-C4	1.398(6)	C66-C65	1.3900
C4-C12	1.392(5)	C65-C73	1.3900
C5-C6	1.406(6)	C73-C74	1.3900
C5-C13	1.385(5)	C73-C72	1.531(4)
C6-C7	1.384(8)	C74-C68	1.3900
C7-C8	1.361(8)	C74-C69	1.442(10)
C8-C14	1.420(6)	C69-C70	1.444(13)
C9-C10	1.391(6)	C70-C71	1.449(10)
C9-C14	1.401(6)	C71-C72	1.3900
C10-C11	1.389(6)	C71-C61	1.3900
C11-C12	1.443(5)	C72-C64	1.3900
C12-C13	1.465(5)	C64-C63	1.3900
C13-C14	1.451(5)	C63-C62	1.3900
C21-C22	1.395(6)	C62-C61	1.3900
C21-C31	1.425(6)	O4A-C16A	1.365(12)

Table 42: Bond angles.

Atoms	Bond angle (°)	Atoms	Bond angles (°)
C4S-O1-C1S	107.7(3)	C21-C31-C32	118.4(3)
O1-C1S-C2S	106.7(4)	C30-C31-C21	123.3(4)
C1S-C2S-C3S	103.1(4)	C30-C31-C32	118.3(4)
C4S-C3S-C2S	104.4(4)	C24-C32-C31	118.5(3)
O1-C4S-C3S	108.5(4)	C24-C32-C33	122.5(4)
C5SB-O2A-C8SA	104.4(6)	C31-C32-C33	119.0(3)
O2A-C5SB-C6SA	92.4(6)	C25-C33-C32	122.3(3)
C7SB-C6SA-C5SB	98.1(8)	C25-C33-C34	118.5(3)
C6SA-C7SB-C8SA	101.5(9)	C34-C33-C32	119.2(3)
O2A-C8SA-C7SB	105.9(7)	C28-C34-C33	117.4(4)
C8SB-O2B-C5SA	108.6(6)	C29-C34-C28	122.9(4)
C6SB-C5SA-O2B	91.9(6)	C29-C34-C33	119.7(3)
C5SA-C6SB-C7SA	94.4(7)	C50-C49-C54	123.4(9)
C8SB-C7SA-C6SB	85.2(7)	C49-C50-C51	121.7(8)
O2B-C8SB-C7SA	105.3(8)	C41-C51-C50	124.4(5)
C9S-O3-C12S	105.2(3)	C41-C51-C52	120.0
O3-C9S-C10S	107.3(3)	C52-C51-C50	115.4(5)
C9S-C10S-C11S	104.4(3)	C42-C41-C51	120.0
C12S-C11S-C10S	104.3(3)	C43-C42-C41	120.0
O3-C12S-C11S	104.5(3)	C44-C43-C42	120.0
C16B-O4B-C13B	98.5(6)	C43-C44-C52	120.0
C14A-C13A-O4A	99.7(8)	C51-C52-C53	119.6(4)
C14B-C13B-O4B	89.0(6)	C44-C52-C51	120.0
C13A-C14A-C15B	101.1(9)	C44-C52-C53	120.3(4)
C13B-C14B-C15A	92.4(7)	C48-C54-C49	123.2(5)
C14A-C15B-C16A	92.1(8)	C48-C54-C53	120.0
C15A-C16B-O4B	110.5(8)	C53-C54-C49	116.8(5)
C2-C1-C11	122.0(4)	C47-C48-C54	120.0
C1-C2-C3	121.1(4)	C46-C47-C48	120.0
C2-C3-C4	119.4(4)	C47-C46-C45	120.0
C12-C4-C3	121.9(4)	C53-C45-C46	120.0
C13-C5-C6	122.0(4)	C54-C53-C52	122.8(4)
C7-C6-C5	118.6(5)	C45-C53-C52	117.2(4)
C8-C7-C6	121.3(5)	C45-C53-C54	120.0
C7-C8-C14	122.0(5)	C66-C67-C68	120.0
C10-C9-C14	122.1(4)	C67-C66-C65	120.0
C11-C10-C9	120.6(4)	C66-C65-C73	120.0
C1-C11-C12	116.7(4)	C65-C73-C72	120.9(4)
C10-C11-C1	122.5(4)	C74-C73-C65	120.0
C10-C11-C12	120.7(4)	C74-C73-C72	119.1(4)
C4-C12-C11	118.8(3)	C73-C74-C68	120.0
C4-C12-C13	122.6(3)	C73-C74-C69	118.6(5)
C11-C12-C13	118.7(3)	C68-C74-C69	121.3(5)
C5-C13-C12	123.0(3)	C74-C68-C67	120.0
C5-C13-C14	118.9(4)	C74-C69-C70	121.8(8)
C14-C13-C12	118.1(3)	C69-C70-C71	120.7(8)
C8-C14-C13	117.1(4)	C72-C71-C70	117.3(5)

C9-C14-C8	123.3(4)	C72-C71-C61	120.0
C9-C14-C13	119.6(4)	C61-C71-C70	122.1(5)
C22-C21-C31	120.8(4)	C71-C72-C73	121.9(4)
C23-C22-C21	120.7(4)	C71-C72-C64	120.0
C22-C23-C24	120.0(4)	C64-C72-C73	118.1(4)
C23-C24-C32	121.5(4)	C72-C64-C63	120.0
C26-C25-C33	121.6(4)	C62-C63-C64	120.0
C25-C26-C27	119.8(4)	C63-C62-C61	120.0
C28-C27-C26	120.7(4)	C62-C61-C71	120.0
C27-C28-C34	122.0(4)	C16A-O4A-C13A	108.8(6)
C34-C29-C30	121.0(3)	O4A-C16A-C15B	103.9(7)
C29-C30-C31	122.4(4)	C16B-C15A-C14B	100.3(8)

6.7 [{Rb$^+_4$(THF)}$_4$(C$_{14}$H$_{10}$)$_3$] at 120K

Table 43: Basic refinement information.

Empirical formula	Rb(C$_{14}$H$_{10}$)$_{0.75}$(C$_4$H$_8$O)
Formula weight (g/mol)	291.24
Temperature (K)	120
Crystal system	triclinic
Space group	*P*-1
a (Å)	12.3669(8)
b (Å)	13.4681(9)
c (Å)	15.4725(11)
α (°)	90.366(2)
β (°)	93.996(2)
γ (°)	93.795(2)
Volume/Å^3	2565.0(3)
Z	8
ρ$_{calc}$ (mg/mm^3)	1.508
m/mm^{-1}	3.839
F(000)	1180.0
Crystal size (mm^3)	1.02 × 0.203 × 0.056
Radiation	MoKα (λ = 0.71073 Å)
2Θ range for data collection	4.64 to 58°
Index ranges	-16 ≤ h ≤ 16, -18 ≤ k ≤ 18, -21 ≤ l ≤ 21
Reflections collected	39148
Independent reflections	13588 [R$_{int}$ = 0.0518, R$_{sigma}$ = 0.0665]
Data/restraints/parameters	13588/42/511
Goodness-of-fit on F^2	1.071
Final R indexes [I>=2σ (I)]	R$_1$ = 0.0524, wR$_2$ = 0.1250
Final R indexes [all data]	R$_1$ = 0.0895, wR$_2$ = 0.1405
Largest diff. peak/hole (e Å^{-3})	1.34/-0.95

Table 44: Fractional atomic coordinates, isotropic displacement parameters and occupancy.

Atom	x	y	z	U_{eq} (Å^2)	N
Rb1	-0.03578(3)	0.62020(3)	0.029452(2)	0.03417(10)	1
Rb2	0.22130(3)	0.40831(3)	0.36830(2)	0.03153(10)	1
Rb3	0.26538(3)	-0.04775(3)	0.15347(3)	0.04148(11)	1
Rb4	0.59791(3)	0.10012(3)	0.19936(2)	0.03389(10)	1
O1	-0.2084(2)	0.6247(3)	0.16823(19)	0.0642(10)	1
C1S	-0.1913(4)	0.6343(5)	0.0790(3)	0.0695(15)	1
C2S	-0.2837(4)	0.5789(4)	0.0345(3)	0.0643(14)	1
C3S	-0.3760(4)	0.5986(4)	0.0879(3)	0.0706(15)	1
C4S	-0.3202(4)	0.6221(5)	0.1768(3)	0.0695(15)	1
O2	0.0391(2)	0.4296(2)	0.24182(18)	0.0443(7)	1
C5S	-0.0490(4)	0.3562(3)	0.2476(3)	0.0489(11)	1
C6S	-0.1078(4)	0.3538(4)	0.1584(3)	0.0650(14)	1
C7S	-0.0186(4)	0.3768(4)	0.0994(3)	0.0609(13)	1
C8S	0.0755(4)	0.4180(4)	0.1560(3)	0.0654(15)	1
O3	0.4584(2)	-0.05557(19)	0.26770(17)	0.0419(6)	1
C9D	0.4496(9)	-0.0264(6)	0.3577(3)	0.046(3)	0.5
C9S	0.4238(7)	-0.0554(8)	0.3558(3)	0.043(2)	0.5
C10D	0.4687(8)	-0.1159(6)	0.4137(5)	0.044(2)	0.5
C10S	0.5122(8)	-0.1113(7)	0.4027(6)	0.059(3)	0.5
C11D	0.5531(7)	-0.1657(7)	0.3657(5)	0.044(2)	0.5
C11S	0.5542(7)	-0.1760(7)	0.3336(5)	0.046(2)	0.5
C12D	0.5120(7)	-0.1493(5)	0.2727(5)	0.036(2)	0.5
C12S	0.4949(8)	-0.1536(5)	0.2478(6)	0.046(3)	0.5
O4	0.7350(5)	0.0554(6)	0.3457(4)	0.056(2)	0.5
C13D	0.7309(7)	0.0855(8)	0.4322(5)	0.055(3)	0.5
C14D	0.8311(9)	0.0548(9)	0.4810(6)	0.049(3)	0.5
C15D	0.8638(9)	-0.0205(7)	0.4191(5)	0.055(3)	0.5
C16D	0.8271(6)	0.0052(7)	0.3294(5)	0.045(2)	0.5
O4A	0.7517(5)	0.0923(6)	0.3372(4)	0.0522(19)	0.5
C13S	0.7654(10)	0.1258(8)	0.4225(5)	0.066(3)	0.5
C14S	0.8071(11)	0.0399(10)	0.4720(8)	0.083(6)	0.5
C15S	0.8941(8)	0.0180(8)	0.4141(5)	0.054(3)	0.5
C16S	0.8505(7)	0.0521(8)	0.3289(6)	0.063(3)	0.5
C1	0.1535(3)	0.7895(3)	0.3100(3)	0.0380(9)	1
C2	0.0701(3)	0.8442(3)	0.2723(3)	0.0443(10)	1
C3	0.0364(3)	0.8292(3)	0.1865(3)	0.0476(11)	1
C4	0.0878(3)	0.7631(3)	0.1350(3)	0.0433(10)	1
C5	0.2330(3)	0.6458(3)	0.1211(3)	0.0404(9)	1
C6	0.3171(3)	0.5930(3)	0.1572(3)	0.0408(9)	1
C7	0.4270(3)	0.5390(3)	0.2842(3)	0.0416(10)	1
C8	0.4521(3)	0.5415(3)	0.3716(3)	0.0492(11)	1
C9	0.3941(4)	0.5991(3)	0.4256(3)	0.0488(11)	1
C10	0.3125(3)	0.6546(3)	0.3908(3)	0.0412(9)	1
C11	0.2862(3)	0.6575(3)	0.3006(2)	0.0306(8)	1
C12	0.2044(3)	0.7204(3)	0.2618(2)	0.0298(8)	1
C13	0.1746(3)	0.7087(3)	0.1720(2)	0.0342(8)	1
C14	0.3438(3)	0.5963(3)	0.2455(3)	0.0335(8)	1

C1A	0.4638(3)	0.2911(3)	0.1533(3)	0.0394(9)	1
C2A	0.5676(3)	0.3341(3)	0.1656(3)	0.0494(11)	1
C3A	0.6173(4)	0.3421(3)	0.2482(3)	0.0527(12)	1
C4A	0.5623(3)	0.3082(3)	0.3177(3)	0.0460(11)	1
C5A	0.3976(4)	0.2318(3)	0.3780(2)	0.043(1)	1
C6A	0.2937(4)	0.1870(3)	0.3663(3)	0.0454(11)	1
C7A	0.1335(4)	0.1275(3)	0.2695(3)	0.0532(12)	1
C8A	0.0821(4)	0.1161(3)	0.1889(4)	0.0588(13)	1
C9A	0.1343(4)	0.1467(3)	0.1163(3)	0.0556(12)	1
C10A	0.2395(3)	0.1917(3)	0.1270(3)	0.0424(9)	1
C11A	0.2941(3)	0.2066(3)	0.2083(2)	0.0314(8)	1
C12A	0.4040(3)	0.2547(3)	0.2218(2)	0.0298(8)	1
C13A	0.4552(3)	0.2644(3)	0.3079(2)	0.0362(9)	1
C14A	0.2402(3)	0.1729(3)	0.2839(3)	0.0379(9)	1
C5B	-0.1642(9)	0.4169(8)	0.4408(7)	0.068(3)	0.5
C6B	-0.0875(8)	0.3438(8)	0.4648(7)	0.065(3)	0.5
C11B	0.0490(4)	0.4743(4)	0.5147(4)	0.0262(18)	0.5
C10B	0.1502(4)	0.5085(3)	0.5522(3)	0.0210(14)	0.5
C9B	0.2269(3)	0.4412(4)	0.5768(3)	0.0329(17)	0.5
C8B	0.2024(4)	0.3398(4)	0.5639(4)	0.0287(16)	0.5
C7B	0.1012(4)	0.3056(3)	0.5265(4)	0.0391(19)	0.5
C14B	0.0245(4)	0.3728(4)	0.5019(4)	0.041(2)	0.5
C12B	-0.0371(4)	0.5498(4)	0.4910(4)	0.031(2)	0.5
C13B	-0.1396(4)	0.5220(3)	0.4524(4)	0.0324(18)	0.5
C4B	-0.2118(3)	0.5941(4)	0.4304(3)	0.0300(16)	0.5
C3B	-0.1814(4)	0.6940(4)	0.4470(4)	0.0360(18)	0.5
C2B	-0.0789(4)	0.7218(3)	0.4856(4)	0.044(2)	0.5
C1B	-0.0068(4)	0.6496(4)	0.5076(4)	0.0292(17)	0.5
C5C	0.4730(7)	-0.1615(7)	0.0364(6)	0.0496(6)	0.5
C6C	0.5820(7)	-0.1317(7)	0.0573(6)	0.0496(6)	0.5
C11C	0.5567(4)	0.0360(4)	0.0056(5)	0.0496(6)	0.5
C10C	0.5927(4)	0.1354(4)	-0.0019(5)	0.0496(6)	0.5
C9C	0.7003(5)	0.1659(3)	0.0218(5)	0.0496(6)	0.5
C8C	0.7719(4)	0.0971(4)	0.0531(5)	0.0496(6)	0.5
C7C	0.7359(4)	-0.0023(4)	0.0606(5)	0.0496(6)	0.5
C14C	0.6283(5)	-0.0328(3)	0.0369(5)	0.0496(6)	0.5
C12C	0.4378(4)	-0.0049(4)	-0.0137(5)	0.0496(6)	0.5
C1C	0.3671(5)	0.0632(4)	-0.0480(5)	0.0496(6)	0.5
C2C	0.2591(4)	0.0330(4)	-0.0704(5)	0.0496(6)	0.5
C3C	0.2217(4)	-0.0653(4)	-0.0585(5)	0.0496(6)	0.5
C4C	0.2923(5)	-0.1333(3)	-0.0242(5)	0.0496(6)	0.5
C13C	0.4004(4)	-0.1031(4)	-0.0018(5)	0.0496(6)	0.5

Table 45: Atom to atom bond distances.

Atoms	Bond length (Å)	Atoms	Bond length (Å)
O1-C1S	1.417(5)	C1A-C12A	1.406(5)
O1-C4S	1.396(5)	C2A-C3A	1.380(6)
C1S-C2S	1.452(7)	C3A-C4A	1.377(6)
C2S-C3S	1.491(7)	C4A-C13A	1.412(6)
C3S-C4S	1.518(7)	C5A-C6A	1.383(6)
O2-C5S	1.430(5)	C5A-C13A	1.396(5)
O2-C8S	1.443(5)	C6A-C14A	1.401(6)
C5S-C6S	1.515(6)	C7A-C8A	1.363(7)
C6S-C7S	1.499(6)	C7A-C14A	1.420(6)
C7S-C8S	1.482(6)	C8A-C9A	1.386(7)
O3-C9D	1.458(5)	C9A-C10A	1.397(6)
O3-C9S	1.458(5)	C10A-C11A	1.392(5)
O3-C12D	1.464(4)	C11A-C12A	1.468(5)
O3-C12S	1.461(5)	C11A-C14A	1.446(5)
C9D-C10D	1.511(5)	C12A-C13A	1.437(5)
C9S-C10S	1.515(5)	C5B-C6B	1.444(14)
C10D-C11D	1.512(5)	C5B-C13B	1.435(12)
C10S-C11S	1.516(5)	C6B-C14B	1.489(11)
C11D-C12D	1.515(5)	C11B-C10B	1.3900
C11S-C12S	1.514(5)	C11B-C14B	1.3900
O4-C13D	1.400(5)	C11B-C12B	1.548(4)
O4-C16D	1.400(5)	C10B-C9B	1.3900
C13D-C14D	1.490(6)	C9B-C8B	1.3900
C14D-C15D	1.485(6)	C8B-C7B	1.3900
C15D-C16D	1.479(5)	C7B-C14B	1.3900
O4A-C13S	1.388(5)	C12B-C13B	1.3900
O4A-C16S	1.383(5)	C12B-C1B	1.3900
C13S-C14S	1.492(6)	C13B-C4B	1.3900
C14S-C15S	1.490(6)	C4B-C3B	1.3900
C15S-C16S	1.476(6)	C3B-C2B	1.3900
C1-C2	1.403(5)	C2B-C1B	1.3900
C1-C12	1.397(5)	C5C-C6C	1.396(12)
C2-C3	1.373(6)	C5C-C13C	1.341(10)
C3-C4	1.402(6)	C6C-C14C	1.460(10)
C4-C13	1.428(5)	C11C-C10C	1.3900
C5-C6	1.386(6)	C11C-C14C	1.3900
C5-C13	1.418(5)	C11C-C12C	1.545(4)
C6-C14	1.382(6)	C10C-C9C	1.3900
C7-C8	1.366(6)	C9C-C8C	1.3900
C7-C14	1.427(5)	C8C-C7C	1.3900
C8-C9	1.402(6)	C7C-C14C	1.3900
C9-C10	1.378(6)	C12C-C1C	1.3900
C10-C11	1.412(5)	C12C-C13C	1.3900
C11-C12	1.463(5)	C1C-C2C	1.3900
C11-C14	1.438(5)	C2C-C3C	1.3900
C12-C13	1.417(5)	C3C-C4C	1.3900
C1A-C2A	1.373(6)	C4C-C13C	1.3900

Table 46: Bond angles.

Atoms	Bond angle (°)	Atoms	Bond angles (°)
C4S-O1-C1S	107.8(4)	C5A-C6A-C14A	121.9(4)
O1-C1S-C2S	104.8(4)	C8A-C7A-C14A	122.6(4)
C1S-C2S-C3S	103.9(4)	C7A-C8A-C9A	120.5(4)
C2S-C3S-C4S	103.0(4)	C8A-C9A-C10A	119.1(5)
O1-C4S-C3S	107.2(4)	C11A-C10A-C9A	122.2(4)
C5S-O2-C8S	105.5(3)	C10A-C11A-C12A	123.5(3)
O2-C5S-C6S	104.5(3)	C10A-C11A-C14A	118.7(4)
C7S-C6S-C5S	103.5(4)	C14A-C11A-C12A	117.9(3)
C8S-C7S-C6S	105.7(4)	C1A-C12A-C11A	122.9(3)
O2-C8S-C7S	107.5(3)	C1A-C12A-C13A	117.5(4)
C9D-O3-C12D	104.7(5)	C13A-C12A-C11A	119.6(3)
C9D-O3	119.6(5)	C4A-C13A-C12A	117.8(4)
C9S-O3-C9D	19.3(5)	C5A-C13A-C4A	122.8(4)
C9S-O3-C12D	97.2(5)	C5A-C13A-C12A	119.4(4)
C9S-O3-C12S	109.0(6)	C6A-C14A-C7A	123.4(4)
C12S-O3-C12D	16.8(4)	C6A-C14A-C11A	119.6(4)
O3-C9D-C10D	108.1(5)	C7A-C14A-C11A	117.0(4)
O3-C9S-C10S	101.0(5)	C13B-C5B-C6B	123.0(10)
C9D-C10D-C11D	101.4(7)	C5B-C6B-C14B	122.0(9)
C9S-C10S-C11S	105.0(7)	C10B-C11B-C14B	120.0
C10D-C11D-C12D	100.8(6)	C10B-C11B-C12B	119.4(4)
C12S-C11S-C10S	108.0(6)	C14B-C11B-C12B	120.5(4)
O3-C12D-C11D	108.9(5)	C11B-C10B-C9B	120.0
O3-C12S-C11S	99.9(5)	C10B-C9B-C8B	120.0
C16D-O4-C13D	114.2(7)	C7B-C8B-C9B	120.0
O4-C13D-C14D	107.7(7)	C8B-C7B-C14B	120.0
C15D-C14D-C13D	99.2(8)	C11B-C14B-C6B	115.7(5)
C16D-C15D-C14D	110.2(7)	C7B-C14B-C6B	124.2(5)
O4-C16D-C15D	99.7(6)	C7B-C14B-C11B	120.0
C16S-O4A-C13S	100.3(8)	C13B-C12B-C11B	123.1(4)
O4A-C13S-C14S	104.7(9)	C13B-C12B-C1B	120.0
C15S-C14S-C13S	97.1(8)	C1B-C12B-C11B	116.9(4)
C16S-C15S-C14S	102.8(8)	C12B-C13B-C5B	115.6(6)
O4A-C16S-C15S	109.8(7)	C12B-C13B-C4B	120.0
C12-C1-C2	121.3(4)	C4B-C13B-C5B	124.4(6)
C3-C2-C1	119.8(4)	C3B-C4B-C13B	120.0
C2-C3-C4	120.7(4)	C4B-C3B-C2B	120.0
C3-C4-C13	120.2(4)	C3B-C2B-C1B	120.0
C6-C5-C13	121.7(4)	C2B-C1B-C12B	120.0
C14-C6-C5	120.8(3)	C13C-C5C-C6C	124.4(9)
C8-C7-C14	121.4(4)	C5C-C6C-C14C	122.1(8)
C7-C8-C9	120.1(4)	C10C-C11C-C14C	120.0
C10-C9-C8	120.3(4)	C10C-C11C-C12C	124.4(4)
C9-C10-C11	121.7(4)	C14C-C11C-C12C	115.6(4)
C10-C11-C12	122.7(3)	C9C-C10C-C11C	120.0
C10-C11-C14	118.0(3)	C10C-C9C-C8C	120.0
C14-C11-C12	119.4(3)	C7C-C8C-C9C	120.0

C1-C12-C11	122.6(4)	C14C-C7C-C8C	120.0
C1-C12-C13	119.3(3)	C11C-C14C-C6C	117.3(5)
C13-C12-C11	118.1(3)	C7C-C14C-C6C	121.9(5)
C5-C13-C4	121.9(4)	C7C-C14C-C11C	120.0
C12-C13-C4	118.6(3)	C1C-C12C-C11C	115.5(4)
C12-C13-C5	119.5(3)	C1C-C12C-C13C	120.0
C6-C14-C7	121.6(4)	C13C-C12C-C11C	124.5(4)
C6-C14-C11	119.9(3)	C2C-C1C-C12C	120.0
C7-C14-C11	118.5(4)	C1C-C2C-C3C	120.0
C2A-C1A-C12A	123.0(4)	C2C-C3C-C4C	120.0
C1A-C2A-C3A	119.5(4)	C13C-C4C-C3C	120.0
C4A-C3A-C2A	120.0(4)	C5C-C13C-C12C	115.4(6)
C3A-C4A-C13A	122.2(4)	C5C-C13C-C4C	124.4(6)
C6A-C5A-C13A	121.5(4)	C4C-C13C-C12C	120.0

6.8 [Cs$_2$(C$_{14}$H$_{10}$)] at 295K

Table 47: Basic refinement information.

Empirical formula	Cs$_2$(C$_{14}$H$_{10}$)
Formula weight (g/mol)	444.04
Temperature (K)	295
Crystal system	monoclinic
Space group	$P2_1/a$
a (Å)	11.8123(2)
b (Å)	11.4666(2)
c (Å)	9.8263(2)
α (°)	90.00
β (°)	110.891(1)
γ (°)	90.00
Volume/Å^3	1243.44(4)
Z	4
Radiation	CuKα (λ = 1.540560Å)
2Θ range of refined data (°)	5 – 70°
R$_p$ (%)	1.530
R$_{wp}$ (%)	2.085
R$_{exp}$ (%)	1.975
χ^2	1.114
Background model	Chebyshev polynomial (19 parameters)
Zero	-0.01016435
Scale	0.0001043(5)
Profile shape function	Pearson VII
U	0.374(4)
V	0.03221000
W	0.00776(18)
beta0	6.8(3)
beta 1	-148(9)
beta2	947(60)
asymmetry	0.049(16)

Table 48: Fractional atomic coordinates, isotropic temperature factors and occupancy.

Atom	x	y	z	B_{iso} (Å^2)	N
C1	0.4224	0.3323	0.8380	1.6	1
C2	0.3612	0.3963	0.9088	1.6	1
C3	0.2574	0.4587	0.8265	1.6	1
C4	0.2133	0.4547	0.6739	1.6	1
C5	0.1307	0.4432	0.3525	1.6	1
C6	0.0930	0.4312	0.2020	1.6	1
C7	0.1556	0.3613	0.1380	1.6	1
C8	0.2595	0.3015	0.2248	1.6	1
C9	0.4051	0.2514	0.4660	1.6	1
C10	0.4455	0.2584	0.6130	1.6	1
C11	0.3801	0.3287	0.6856	1.6	1
C12	0.2741	0.3894	0.6027	1.6	1
C13	0.2331	0.3825	0.4442	1.6	1
C14	0.2983	0.3119	0.3788	1.6	1
H1	0.5034	0.2804	0.8996	3.2	1
H2	0.3897	0.4030	0.0243	3.2	1
H3	0.2076	0.5101	0.8816	3.2	1
H4	0.1293	0.5016	0.6180	3.2	1
H5	0.0811	0.4990	0.3975	3.2	1
H6	0.0137	0.4826	0.1357	3.2	1
H7	0.1250	0.3565	0.0247	3.2	1
H8	0.3105	0.2453	0.1766	3.2	1
H9	0.4524	0.1973	0.4168	3.2	1
H10	0.5224	0.2149	0.6804	3.2	1
Cs1	0.7327(2)	0.3642(3)	0.8029(2)	0.72(6)	1
Cs2	0.5795(2)	0.3694(3)	0.3120(2)	0.72(6)	1

Table 49: Atom to atom bond distances.

Atoms	Bond length (Å)	Atoms	Bond length (Å)
C1-C2	1.37980(2)	C7-C8	1.39906(2)
C2-C3	1.40077(2)	C8-C14	1.42112(3)
C3-C4	1.40174(3)	C14-C9	1.42690(2)
C4-C12	1.38719(2)	C9-C10	1.35242(2)
C12-C13	1.45896(3)	C10-C11	1.46580(2)
C13-C5	1.40789(2)	C11-C1	1.40011(3)
C5-C6	1.39090(2)	C11-C12	1.41009(2)
C6-C7	1.38433(2)	C13-C14	1.411932(2)

6.9 IR and Raman spectroscopy

Table 50: A tentative assignments of vibration peaks in IR spectra.

Assignment	$C_{14}H_{10}$	$Rb_2(C_{14}H_{10})_2$ (THF)	$K_2(C_{14}H_{10})_2$ (THF)	$Cs_2(C_{14}H_{10})_2$ (THF)	$Cs(C_{14}H_{10})$	$K_4(C_{14}H_{10})_3$ (THF)$_4$	$Cs_2(C_{14}H_{10})$
A_1							
A_2							
A_1	408			398	398		402
B_1	428		424	420	420		417
B_2	441			435	435		
B_1	497	484	484	482	482	486	488
A_1							
B_2	713	684	683	689	687	686	652
B_1	732	705	704	709	708	668, 707	666
B_1	818	748	747	744	743	743	746
A_1							
A_1	863	817	816	818	817	814	809
B_2							
B_1	950			904	904	866, 899	869
B_2	999	971	967	969	968	952, 972	951
A_1							
A_2							
A_1	1243	1193	1190	1192	1191	1161, 1193	1160
A_1	1348	1333	1331	1328	1329	1324, 1334	1323
A_1							
A_1	1523	1443	1440	1444	1444	1424, 1444	1419
B_2							
A_1	1600	1530	1527	1524	1524	1498, 1530	1498

Table 51: A tentative assignments of vibration peaks in Raman (532 nm) spectra.

Assignment	$C_{14}H_{10}$	$Rb_2(C_{14}H_{10})_2$ (THF)	$K_2(C_{14}H_{10})_2$ (THF)	$Cs_2(C_{14}H_{10})_2$ (THF)	$Cs(C_{14}H_{10})$	$K_4(C_{14}H_{10})_3$ (THF)$_4$	$Cs_2(C_{14}H_{10})$
A_1	250		242	240	239	240	239
A_2	397						334
A_1	409	404	405	400	402	398	395
B_1							
B_2							
B_1	498						490
A_1	710	699	700	694	697	701	
B_2							
B_1							
B_1							742
A_1	829	818		816	814	812	812
A_1							
B_2	875	860	861				848
B_1							
B_2							
A_1	1036	966	962	962	962		960
A_2	1155			1063	1064		1013
A_1	1244	1194	1194	1191	1191		
A_1	1349	1335	1334	1331	1332	1326, 1335	1325
A_1	1439		1403	1400	1398		1355
A_1	1523						1421
B_2	1567	1488	1488	1491	1498		1476
A_1	1598	1524	1527	1525	1525	1504, 1524	1499